ACTIVE MATTER IN CONFINED GEOMETRIES

BIOPHYSICS OF ARTIFICIAL MINIMAL CORTICES

DISSERTATION

for the award of the degree

Doctor rerum naturalium

of the Georg-August University Göttingen

within the doctoral program

of the Georg-August University School of Science (GAUSS)

submitted by

Hanna Hubrich

from Uelzen

Göttingen 2020

Members of the Thesis Advisory Committee

Prof. Dr. Andreas Janshoff
Institute of Physical Chemistry
Georg-August-University of Göttingen

Prof. Dr. Sarah Köster
Institute of X-Ray Physics
Georg-August-University of Göttingen

Dr. Florian Rehfeldt
Third Institute of Physics
Georg-August-University of Göttingen

Members of the Examination Board

1st Referee: *Prof. Dr. Andreas Janshoff*
Institute of Physical Chemistry
Georg-August-University of Göttingen

2nd Referee: *Prof. Dr. Sarah Köster*
Institute of X-Ray Physics
Georg-August-University of Göttingen

Further Members of the Examination Board

Dr. Sarah Adio
Institute for Microbiology and Genetics
Georg-August-University of Göttingen

Prof. Dr. Michael Meinecke
Department of Cellular Biochemistry
University Medical Center Göttingen

Prof. Dr. Jörg Großhans
Institute of Developmental Biochemistry
University Medical Center Göttingen

Prof. Dr. Silvio O. Rizzoli
Department of Neuro- and Sensory Physiology
University Medical Center Göttingen

Date of Oral Examination

7th December 2020

Declaration

I, Hanna Hubrich, hereby certify that my doctoral thesis entitled “Active matter in confined geometries – biophysics of artificial minimal cortices” has been written independently and with no other sources and aids than quoted.

Göttingen, 2020

_____

Hanna Hubrich

ABSTRACT: Essential physiological processes, such as cell motility, adhesion, growth and differentiation are determined by the ability of cells to modify their mechanical properties. Consequently, both the vitality as well as malignancy and thus the fate of the cells are often reflected in alterations of their viscoelastic properties. The viscoelasticity of cells is believed to be predominately regulated by the actin cortex, a thin transiently cross-linked actomyosin network containing several hundred actin binding proteins (ABPs), which is dynamically coupled to the plasma membrane by proteins of the ERM (ezrin-radixin-moesin) family. The multitude of different ABPs ensures on the one hand the resilience of the cell body and on the other hand, due to their transient nature, also provides sufficient fluidity to enable cell shape changes on long time scales. The highly dynamic biochemical processes in the active adaptive actin cortex and how they influence cell mechanics are still not fully understood.

In this thesis, the contribution of the actin cortex to the viscoelasticity of cells based on the concept of continuum mechanics was studied – with the focus on architecture, motor activity and membrane-attachment – using different model systems as a mimic of the cellular cortex. First experiments on purely entangled 3D actin gels showed that network architecture and mechanics can be altered by the experimental setup, such as the construction of the measuring chamber and the choice of the illumination technique of the measuring method. In bead tracking microrheology, a light-induced softening of the network was found by fluorescent imaging, while non-fluorescent imaging showed no effect. Network softening was also observed in bulk rheology measurements of 3D actin gels in presence of the motor fragment protein heavy meromyosin (HMM) under ATP consumption. In minimal cell compartments (MCCs) created by polymerization of F-actin within water-in-oil droplets, full-length myosin II motors generated non-thermal fluctuations under excess ATP. These fluidization and fluctuations are proposed to be caused by filament sliding movements induced by active motors during ATP hydrolysis, mimicking the contractility of the cell cortex. In comparison to 3D actin networks, a significant increase of the network stiffness by a factor of about 6 was found in minimal actin cortices (MACs), where a quasi-two-dimensional F-actin network was crowded by methylcellulose (MC) on a solid supported membrane (SSM) and coupled to the membrane via an active mutant of ezrin and the receptor lipid phosphatidylinositol-4,5-bisphosphate (PIP_2). In addition, actin filaments where observed to be about a quarter of the size in MACs compared to 3D networks. These results indicate that the dynamic attachment of F-actin to the membrane plays a key role in self-organization and viscoelasticity of the actin cortex.

In order to measure rheological properties of the entire actin cortex components, in absence of the crowded cytoplasm and the stiff nucleus, apical cell cortices were isolated from living MDCK II cells, deposited on porous silica matrices and locally deformed with a sharp atomic force microscope (AFM) tip. The obtained force cycle data was described with a viscoelastic cortex model using a time-dependent area compressibility modulus that obeys the same universal scaling behavior as applied for living cells. In comparison to living cells, the apical cell cortices showed a reduced fluidity, which was partially restored by addition of exogenous ATP to reactivate myosin motors. A comparison with MACs showed higher cortex fluidity due to the absence of cross-links. From this it can be concluded that viscoelasticity of cells to external deformation is mainly determined by the components of the membrane cortex, in particular the actin cortex dynamically connected to the plasma membrane and the myosin motor activity controlled in an ATP-dependent manner.

Contents

1 Introduction

The actin cortex is an important component of the cytoskeleton of eukaryotic cells and essential for many cellular processes, like changing as well as maintaining cell shape, intracellular transport processes, cell division and cell motility. In order to be motile, the thin cellular cortex (~200 nm)[1] – attached to the plasma membrane via ezrin-radixin-moesin (ERM) proteins – needs to be remodeled. To achieve this, the actin network consisting of filamentous actin (F-actin) and various actin binding proteins (ABPs) constantly needs to rearrange.[2–6] The mechanical properties of actin filaments are determined by their semiflexible nature and can be described in terms of a dashpot. In presence of active myosin motor proteins, F-actin acts as an active biological spring. Thus, the actomyosin networks is able to resist against external stresses as well as exert forces, which is significant for the force response of cells.[2,3] Until now little is known about the highly dynamic biochemical processes in the cytoskeleton and how it influences mechanical properties of cells. Therefore, future scientific research is needed to understand how the cytoskeleton controls cell physiology by regulating viscoelastic properties of the actin cortex.

1.1 Cytoskeleton

Cell mechanics, spatial organization of the cell and cell shape are mainly determined by the cytoskeleton. The cytoskeleton is a dynamic network of interacting and interlinking filamentous as well as regulatory proteins. The main building blocks of the cytoskeleton are intermediate filaments (IFs), microtubules (MTs) and actin filaments (AFs). The three cytoskeletal components differ in their mechanical properties, spatial organization and function within the cell. Various cross-linking and motor proteins as well as direct bonding control the structure and mobility of the filaments and enable crosstalk between the three subsystems in overlapping regions (see fig. 1.1).[3,4]

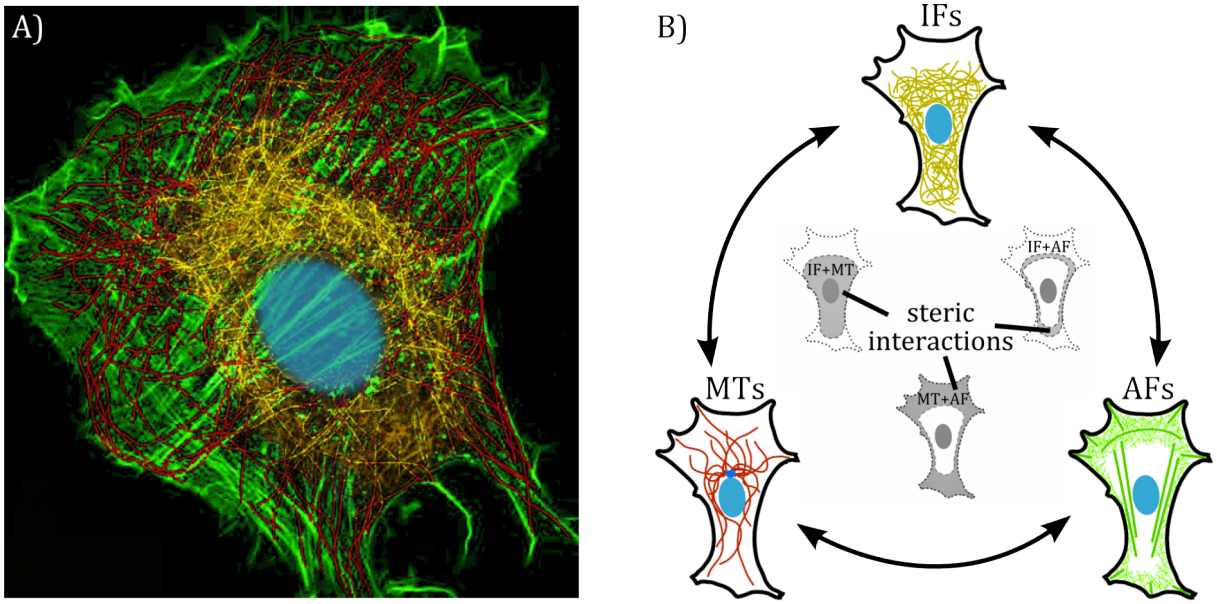

Figure 1.1: Components of the cytoskeleton in eukaryotic cells. Microtubules (MFs) are shown in red, intermediate filaments (IFs) in yellow and actin filaments (AFs) in green. The cell nucleus is shown in blue. **A)** Overlay of cytoskeleton components within a cell. Modified from *Medical School*.[7] **B)** Localization and overlapping regions of the cytoskeletal filaments within the cell. Steric interactions occur in the region of spatial overlap, shown in the center in grey. Modified from *Huber et al*.[4]

Microtubules can be found in nuclear region and disperse in the periphery of the cell. They form stiff, hollow cylinders made of globular homologous protein subunits α- and β-tubulin. With a persistence length on the order of millimeters, they contribute mainly to the rigidity of the cytoskeleton. Microtubules are essential for chromosome separation during cell division and for transport of larger cargo within the cell.[3,4,8]

Intermediate filaments are located in between the nuclear region and the cellular cortex, where they form rope-like fibers of proteins, like vimentin and keratin. They are the most flexible filaments in the cytoskeleton with a persistence length in the range of 1 µm.[4] IFs form a compliant network in the cytoplasm, where they can withstand large deformations and act as a kind of absorber of externally stresses.[3,4]

Actin filaments are located in a thin shell underneath the plasma membrane.[2] In comparison to the other cytoskeletal filaments, F-actin has an intermediate persistence length (~17 µm).[4,9,10] Therefore, the filaments have mechanical properties of a semiflexible polymer, which enable actin to fulfill various functions within the cell. On the one hand F-actin was found to be most resistant against externally applied forces and plays an important role in cell stability.[2,11] On the other hand F-actin is also essential for maintaining and creating forces required for cell motility and contraction.[6,8] Hence, the actin cortex is an essential component in cell mechanics and of special interest in current research.[2,5,6]

1.2 Actin Filaments

The building blocks of actin filaments (F-actin) are globular actin monomers (G-actin) with a length of 375 amino acids and a molecular mass of ~43 kDa.[6,12,13] Above a critical concentration (0.1 µM)[14] monomeric G-actins form filamentous actin under hydrolysis of adenosine triphosphate (ATP) to adenosine diphosphate (ADP).[15,16] Two F-actin chains entangle together and form a helical polymer with a diameter of 5 - 7 nm and a single helix length of 37 nm (see fig. 1.2).[17,18]

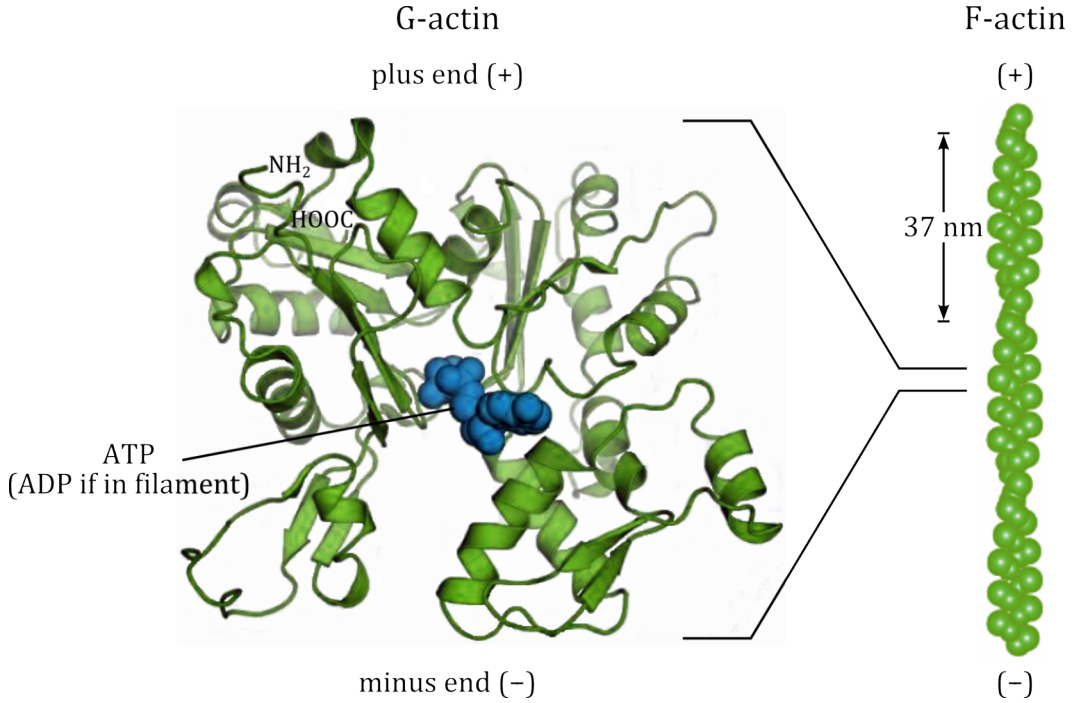

Figure 1.2: Structure of a globular actin monomer (G-actin) containing ATP in in its binding pocket and filamentous actin (F-actin). Actin monomers assemble in filamentous actin. Two single F-actin strands entangle together forming a double helix twist repeating every 37 nm. Modified from *Alberts et al.*[18]

As shown in figure 1.2, F-actin is a polar polymer, which exhibits a plus (barbed end) and a minus end (pointed end). During the self-assembling process of G-actin into the polar filamentous actin, different phases can be observed: the nucleation, growth and treadmilling phase (see fig. 1.3).[18,19]

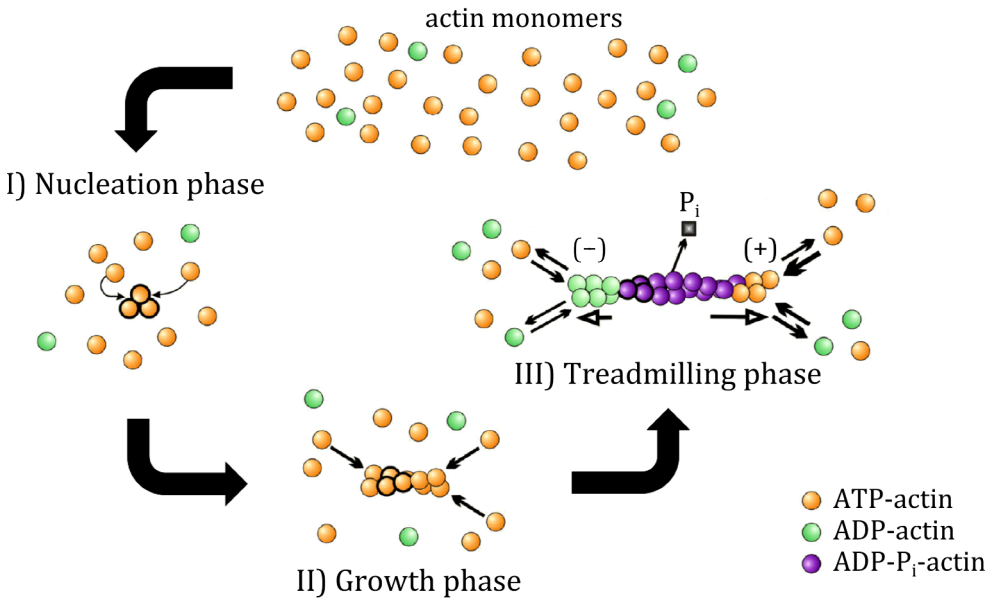

Figure 1.3: The three different phases during the self-assembling process of G-actin to F-actin. **I)** In the nucleation phase G-actin assembles in oligomers. **II)** In the growth phase oligomers elongate fast into filaments by addition of actin monomers on both ends. **III)** In the treadmilling phase the filament length and the concentration of free actin monomers remain constant. Modified from *Tharmann*.[20]

The nucleation of three or more actin monomers is initiated by binding of ATP and Mg^{2+} ions to G-actin. After overcoming the kinetic barrier of nucleation, the growth phase starts, where the polymerization rate reaches a maximum and actin monomers elongate at both sides of the forming filament. Hydrolysis of ATP-actin results in actin monomers bonded to ADP and inorganic phosphate (ADP-P_i-actin). After release of P_i, ADP-actin remains within the actin filament.[18,19] During the elongation process the monomer concentration decreases and reaches a critical concentration. At this point the filament length as well as the monomer concentration remain constant, but dynamic monomer exchange still take place. At the plus end the filament grows, because here ATP-actin accumulation is faster than ADP-actin dissociation. On the other hand, at the minus end hydrolysis of ATP to ADP is faster compared to the addition of ATP-actin and ADP-actin dissociates with higher amount, which results in a shrinking of the filament at this end. In this steady state association and dissociation of actin monomers to the actin filament are in equilibrium, the so-called treadmilling phase, which strongly depends on the ATP concentration.[14,21,22]

Furthermore, the degree of polymerization and depolymerization is regulated through a variety of actin binding proteins (ABPs), which allows to control the organization and viscoelastic properties of the cytoskeleton.[23,24]

1.3 Actin Binding Proteins on a Cellular Scale

In eukaryotic cells over one hundred actin binding proteins (ABPs) were found to regulate dynamics and mechanics of the actin cytoskeleton by cross-linking, bundling, branching and capping as well as controlling actin assembly and disassembly. This diversity of ABPs enables cells to accomplish various specialized organizations of actin networks with distinct functions and localizations. In the following different actin architectures in a moving cell and the influence of accessory proteins on network properties will be shortly described (see fig. 1.4).[2,21]

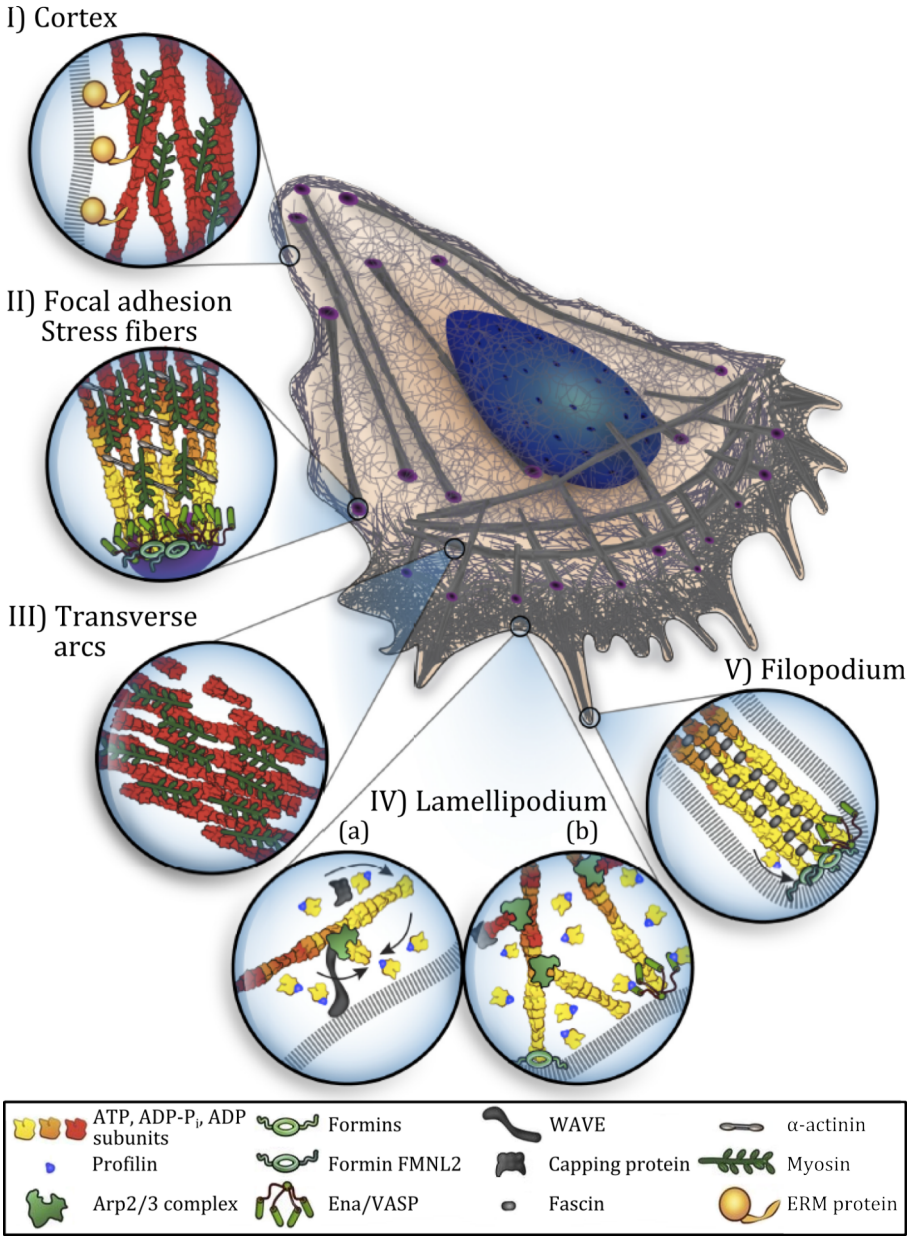

Figure 1.4: Distinct organizations of actin filaments and ABPs at special locations in the cell. **I)** The actomyosin cortex is attached to the plasma membrane via ERM proteins. **II)** Stress fibers are antiparallel contractile actin bundles formed by ABPs like α-actinin and myosin, which are connected to the plasma

membrane through focal adhesions mediated by Ena/VASP proteins and formins. Usually, they are oriented parallel in the direction of movement. **III)** Another type of contractile antiparallel bundles are transverse arcs, which are running parallel to the leading edge of the cell. **IV)** In the lamellipodium branched actin networks are formed mediated by the activation of the Arp2/3 complex via proteins of the WAVE family. Addition of the profilin/actin complex at the plus end of the actin filament leads to elongation of the network **(a)**. Filament dynamics at the plus end are regulated by VASP proteins, formin FMNL2 and capping proteins **(b)**. **V)** At the leading edge of the cell filopodia are formed. The parallel tightly packed bundles are constructed by the cross-linker fascin. Elongation of the bundles occurs in presence of actin polymerases, as well as formins and Ena/VASP proteins. Modified from *Blanchoin et al*.[2]

Cortex

The actin cortex – a thin layer of several hundred nanometer thickness underneath the plasma membrane – is a cross-linked actin meshwork with mesh sizes in the range of 50 nm to 200 nm, which plays a pivotal role in maintaining as well as changing the cell shape (see fig. 1.4, I).[2] Structure and mechanical properties of the cortex are controlled by more than hundred ABPs. Depending on the type of ABPs actin filaments form bundles (*e.g.* in presence of α-actinin, fimbrin or fascin), dendritic networks (*e.g.* with filamin or spectrin), branched networks with the Arp2/3 complex or generate contractile forces in presence of active motor proteins, like myosin II (see chpt. 1.3.1). On the one hand, this versatility of cross-linking proteins enables the cell body to withstand stresses. On the other hand, the transient nature of cross-linkers allows the actin cortex to flow slowly, which enables cell shape changes.[2,6,8,11,25] In order to communicate with the plasma membrane, the actin cortex needs to be attached to it. Proteins from the ERM (ezrin-radixin-moesin) family were found to be the most important players for this linkage.[2,26,27] More details of the ERM protein family are given in chapter 1.3.2.

Focal Adhesion Stress Fibers and Transverse Arcs

Important actin assemblies to provide cell contraction are stress fibers, which are antiparallel contractile bundles spanning the cell body. Within a migrating cell there are two types of stress fibers: the ventral stress fibers, which are oriented parallel in the direction of cell movement (see fig. 1.4, II) and the transvers arcs, which are spanning the cell parallel to its leading edge (see fig. 1.4, III). Ventral stress fibers are attached to the plasma membrane through focal adhesion sites, which are formed by Ena/VASP proteins and formins, whereas transverse arcs are not attached to focal adhesions.[2] The antiparallel stress fibers are stabilized by the cross-linking protein α-actinin, which ensures an ideal distance between actin filaments for myosin motor proteins to assemble in between and generate forces by walking along the filaments.[2,28] This myosin induced filament sliding leads to contraction and might also induce actin disassembly in

absence of cross-linking proteins, whereas cross-linking of stress fibers with α-actinin limited the extend of contraction and therefore prevent disassembly processes.[2,29–31]

Lamellipodium

At the cell's front branched and cross-linked actin networks are localized within the so-called lamellipodium (see fig. 1.4, IV), the major engine of cell movement by reorganizing and pushing against the plasma membrane through force generating assembly processes of actin. These highly dynamic branching processes are regulated by various ABPs. An important protein for construction of branched actin networks is the Arp2/3 complex, composed of seven proteins and activated trough interactions with members of the WAVE protein family.[2,32] In presence of profilin/actin complexes the branched network elongates at the plus ends of the filaments, which are in close contact to the plasma membrane (see fig. 1.4, IV, a) and therefore enable actin-based force generation for cell motility. The ABP profilin is essential for controlling actin assembly. Profilin is a G-actin binding protein and inhibits the formation of actin dimers and trimers, which are the building blocks for the formation of new actin filaments. Profilin/actin complexes can only assemble if polymerization nucleation factors like Arp2/3 are present. Furthermore, actin monomers complexed with profilin can only assemble at the fast-growing plus end, whereas polymerization at the minus end is prevented resulting in polarity of actin elongation.[2,14,33] Elongation of actin networks is also regulated by capping proteins, Ena/VASP proteins and formin FMNL2, which modulate filament dynamics at the plus end (see fig. 1.4, IV, b). Capping proteins like gelsolin block filament growing, while Ena/VASP and FMNL2 promote elongation at the plus end.[2,34]

Filopodium

Tightly packed parallel actin bundles can be found in filopodia (see fig. 1.4, V) and are formed by the cross-linking protein fascin. These finger-like bundle structures are located at the front of the cell and play an important role in cell migration, transmitting cell-cell signals, sensing the environment of the cell and initiating cell contacts. The retraction of filopodia is mainly controlled by dynamics and assembly of actin filaments and completely independent of myosin motor proteins, which on the contrary are pivotal for contractility of the cell cortex.[2]

1.3.1 Myosin Motor Proteins

Myosin motor proteins are able to convert chemical energy by means of ATP hydrolysis in kinetic energy, which enables various essential processes in cell biology, like cell motility, cell shape changes and the transport of intracellular cargoes.[6,35] Myosin motors can be divided in two broad classes: the conventional members (*e.g.* myosin II) – forming thick bipolar filaments consisting of dozens of motor proteins due to coiled-coil domains in their heavy chain – and unconventional members (*e.g.* myosin V), which do not assemble in thick bipolar myosin bundles. Conventional myosin's play a pivotal role in muscle contraction (*e.g.* muscle myosin II) and cytokinesis (*e.g.* non-muscle myosin II), while unconventional motor proteins like myosin V are important for individual cellular anchoring and trafficking events (see fig. 1.5).[36,37]

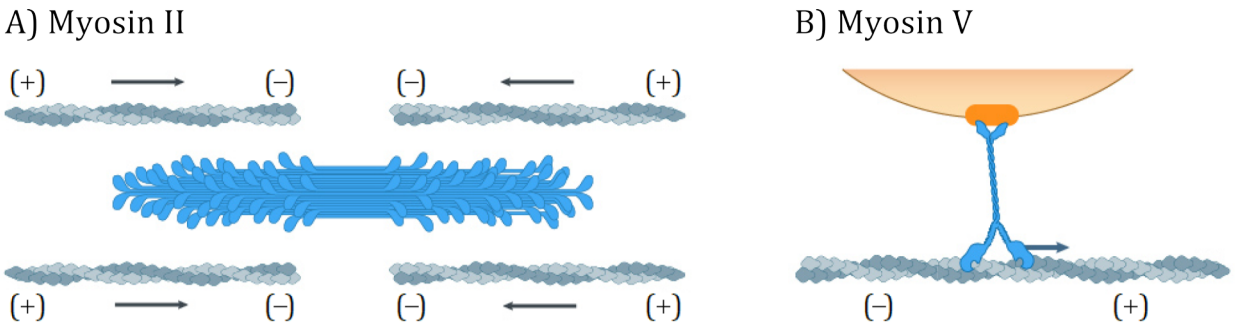

Figure 1.5: Structure and function of conventional myosin II and unconventional myosin V motor proteins. **A)** Thick bipolar bundles of myosin II (blue) slide along actin filaments (grey), which results in contraction. **B)** Myosin V (blue) is important for the transport of cargo (orange) by walking along F-actin (grey). Modified from *MBInfo*.[37]

Myosin motor proteins are mechanoenzymes consisting of ATP- and actin binding sites in their highly conserved catalytic head domain, which is crucial for motor activity. Motility of myosin motors is generated through conformational changes – more precisely the power stroke – induced by binding of ATP followed by its hydrolysis and release of inorganic phosphate (P_i). The ATPase cycle regulates the association between myosin heads and the actin filament. If ADP is bound to the head domain, a strong interaction occurs between the myosin head and F-actin. On the other hand, binding of ATP or ADP-P_i to the catalytic head leads to a drastically lower binding affinity of myosin to actin. Consequently, the release of myosin heads from actin is initiated by binding of ATP, while the release of P_i catalyzes binding of myosin heads to F-actin followed by the force generating power stroke.[35,36] The rate at which myosin heads bound to ATP and how long the heads associates with actin during the strongly bound

state per ATPase cycle (so-called duty ratio) varies for different motor proteins. Motors like myosin II have a rather low duty ratio and their heads are only associated to actin for a short time, while myosin V possesses a high duty ratio and is able to do many steps along F-actin before detachment.[36,38] The polar structure of actin filaments ensures that myosin motors generally bind in one direction and consequently only move towards the plus end of the filament. Due to the assembly of conventional myosin motors in thick bundles, numerous myosin heads are faced in opposite direction generating a sliding movement of the polar actin filaments resulting in contraction (see fig. 1.5, A), *e.g.* in muscle cells or while two daughter cells separate during cytokinesis.[28,36] On the contrary unconventional myosin motors like myosin V, operate as single molecules. Because of specific binding domains in their tail region, myosin V proteins are able to transport cargo along actin filaments (see fig. 1.5, B).[36,39]

The number of further actin-based myosin motors involved in different cellular pathways is great and their structure and function is versatile, but the best studied motor protein is muscle myosin II, which was solely used during this work and will be described in more detail in the following.

Myosin II Motor Proteins

Myosin II was the first motor protein discovered in muscle extracts by *Willy Kühne* in 1864.[36,40] As mentioned before, myosin II forms thick bundles, which are able to generate forces during muscle contraction through hydrolysis of ATP. In nature there are two states of myosin: the rigor state in absence of ATP, where myosin binds strongly to F-actin and act as permanent cross-linker and on the other hand the active state in presence of ATP, where myosin acts as a transient cross-linker between F-actin leading to sliding of filaments induced by the ATP consuming power stroke.[36,41–45] In active state the independently operating head domains of the non-processive motor protein attach and detach about 50 times per second[46], whereby a single head advances actin filaments roughly 10 nm to 15 nm and exerts a force of nearly 1 pN during the power stroke.[47] Myosin II is not only found in muscles, but also in non-muscle cells, where it is believed to be important to establish cortical tension in living cells, which is essential for shape changes during cell division and migration as well as morphogenesis.[44,48,49]

Myosin II is a dimer with a molecular mass of about 470 kDa consisting of a head, neck and tail domain build up by two heavy chains and four light chains.[50,51]

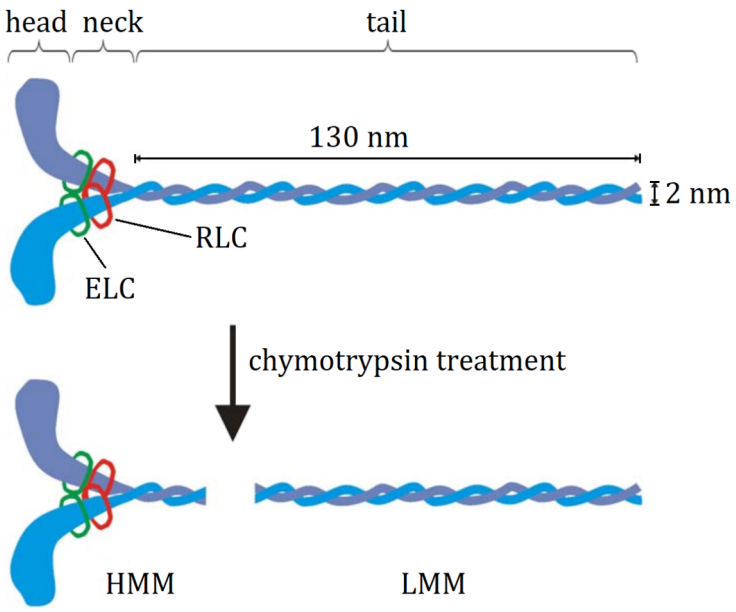

Figure 1.6: The structure and fragments of myosin II. The head domain consists of an actin and ATP binding site. The head domain activity is controlled by the neck domain composed of regulatory (red) and essential (green) light chains (RLC and ELC). Long coiled-coil domains are the building blocks of the myosin tail. Myosin II can be cleaved by the enzyme chymotrypsin in heavy meromyosin (HMM) and light meromyosin (LMM). Modified from *Lodish et al.* and *Roos et al.*[46,52]

The catalytic head domain – constructed by amino-terminal sequences of the heavy chains – contains the ATP and actin binding sites and is essential for motor activity. In association to the head region, the neck domain containing the regulatory and essential light chains (RLC and ELC) can be found. The activity of the catalytic head is regulated by the light chains. The coiled-coil tail of the myosin motors is formed by two twisted α-helices of the heavy chains and enables multimerization of myosin dimers as already mentioned before.[51,52]

By enzymatic cleavage myosin II can be split in different functional fragments. The enzyme chymotrypsin was found to cleave full-length myosin in heavy meromyosin (HMM) and light meromyosin (LMM) fragments.[52] HMM contains the head and neck domains, as well as a subfragment of the coiled-coil tail and conserves consequently full motor activity.[53] In rigor state HMM is proclaimed to build homogeneous isotopically actin networks, without any bundling structures, which are believed to be formed through the LMM subfragment. These homogeneous actin-HMM networks are ideal for the analysis of single filament models.[54]

1.3.2 The ERM Protein Ezrin

The physiological linker ezrin from the ezrin-radixin-moesin (ERM) protein family plays a pivotal role in linking the actomyosin cortex to the plasma membrane. Therefore, ezrin is also essential for the transmission of tension – generated by the actomyosin cytoskeleton – to the plasma membrane, which is important for many cellular processes such as cell motility and division, as well as endocytosis. [2,26,27,55] Ezrin consists of two domains, the *N*-terminal ERM associated domain (*N*-ERMAD) and the *C*-terminal ERM associated domain (*C*-ERMAD) connected through an α-helical domain and a linker region. *N*-ERMAD mediates the connection to the plasma membrane, while *C*-ERMAD contains a binding site for F-actin. To enable linkage between the cell membrane and the cytoskeleton, a conformational change of ezrin is necessary, which is proposed to be induced by a two-step activation process (see fig. 1.7).[26,27,56]

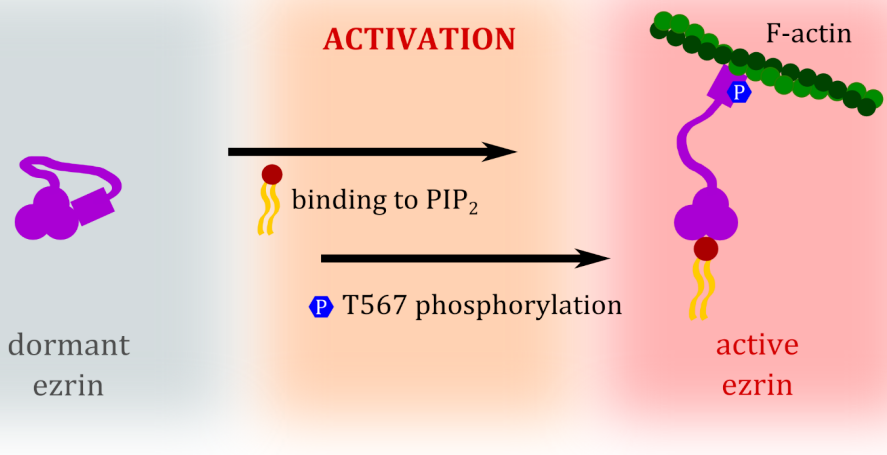

Figure 1.7: Schematic illustration of the two-step activation process of ezrin. The activation of dormant ezrin in its active state is believed to be induced by binding of PIP_2 at the *N*-terminal ERM domain followed by phosphorylation of threonine 567 localized at the F-actin binding site in the *C*-terminal ERM domain. In its active state ezrin links the PIP_2 containing plasma membrane with the actin cortex.

Cytosolic ezrin was found to be in a dormant state, where the F-actin binding site on the *C*-terminal ERM domain is masks through self-association. Activation of ezrin by conformational change is initiated by binding of *N*-ERMAD to phosphatidylinositol-4,5-bisphosphate (PIP_2) – a component of the plasma membrane – followed by the phosphorylation of threonine at position 567, which is located at the F-actin binding site on *C*-ERMAD. Ezrin in its active state acts as linker between the actin cytoskeleton and the PIP_2 containing plasma membrane.[27,56–58]

Astonishingly, the amount of the phospholipid PIP_2 within the plasma membrane is only about 1 mol%[59] even though it is an important regulator within the membrane.[60] It has been suggested that PIP_2 can be enriched locally (~5 mol%)[59] for instance through "selfish" PIP_2 synthesis, pre-concentrated platforms of PIP_2 or formation of PIP_2 "megapools", but the underlying molecular mechanism has still not been cleared up.[60,61]

In this work a permanently active pseudophosphorylated ezrin mutant (ezrin T567D) was used for construction of artificial model systems. In the ezrin T567D mutant the threonine at position 567 is replaced by a negatively charged aspartate. In several *in vitro* experiments this mutant was used for characterization of ezrin features and also a proper binding activity towards F-actin was observed.[26,58,62–66]

1.3.3 Phalloidin

Phalloidin belongs to the phallotoxins isolated from the death cap mushroom amanita phalloides.[67] The bicyclic heptapeptide is known to interact with actin filaments and stabilize them against depolymerization by binding between three actin subunits.[68–70]

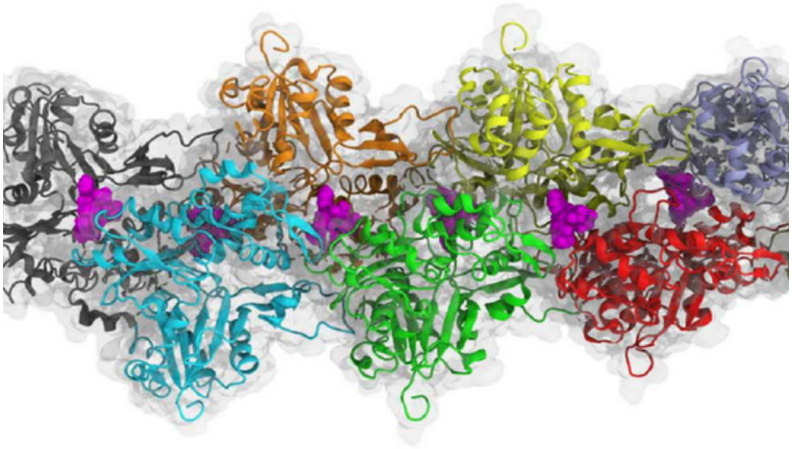

Figure 1.8: The position and orientation of phalloidin (magenta) within an actin filament. Phalloidin interacts with three different actin subunits. Modified from *Skillman et al.*[69]

Furthermore, phalloidin accelerates nucleation of actin monomers and consequently the formation of actin filaments.[68,70] These actin stabilizing properties of phalloidin as well as its fluorescent derivates provide a great possibility to characterize and visualize actin filaments in artificial model systems.[71–74]

1.4 Model Systems of Cellular Mechanics

Essential physiological processes, like cytokinesis and cell motility are governed by the ability of cells to adapt their mechanical properties. The mechanical properties of cells are mainly determined by the actin cortex, a thin layer consisting of actin filaments and several hundred ABPs dynamically connected to the plasma membrane via ERM proteins.[2–6] In order to analyze this highly complex biological meshwork, it is helpful to mimic the cytoskeletal components and plasma membrane by artificial model systems. There are two main methods to build up model systems: the bottom-up and top-down approaches (see fig. 1.9).

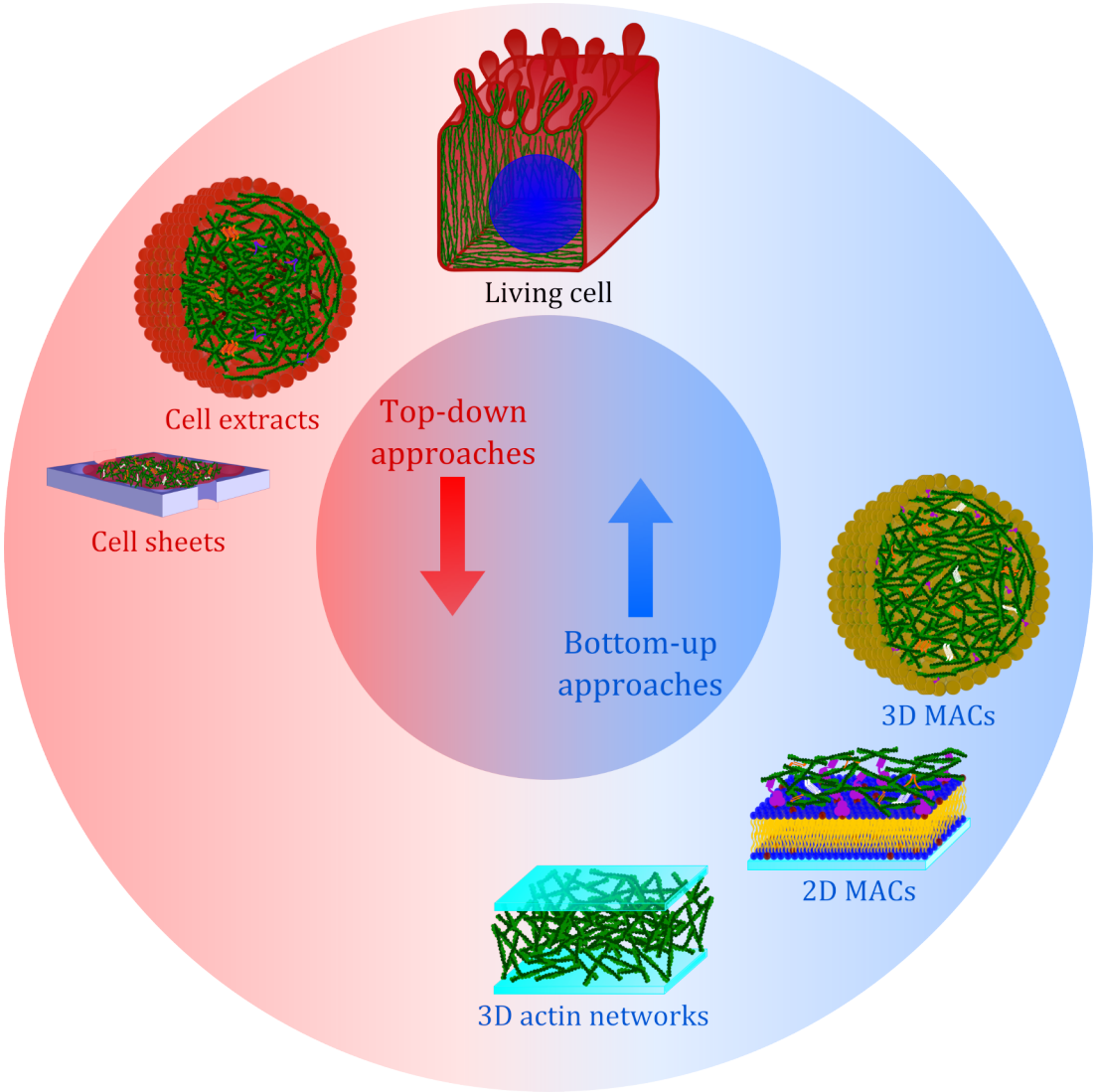

Figure 1.9: Experimental systems to study cortex mechanics. In top-down approaches (red) cellular complexity is simplified stepwise by extracting cell components, while bottom-up approaches (blue) increase complexity of the system subsequently. Exemplary top-down approaches are cell extracts and cell sheets isolated from living cells. Typical bottom-up systems are simple 3D actin networks as well as 2D and 3D minimal actin cortex (MAC) model systems.

In bottom-up approaches simple minimal systems are designed to elucidate the function of isolated single proteins, while top-down systems start with studying complex systems followed by a subsequent simplification to investigate the working mechanism of biological components within their operational environment. In this chapter an overview of bottom-up and top-down model systems for studying cortex mechanics is given.

1.4.1 Bottom-up Approaches of Cellular Mechanics

The mechanism of force generation in cells is a complex interplay of interacting and interlinking components of the actin cortex. In order to analyze the contributions and functions of separate cortex components, various studies were done using *in vitro* systems with purified proteins under controlled conditions.

Entangled F-actin Networks

For the simplest case pure 3D actin networks without cross-linkers were characterized in various studies regarding the influence of several parameters – like actin concentration, filament length and buffer conditions – on their architecture and mechanics. In oscillating rheometry studies *Xu et al.* found variations in the shear moduli of actin networks of more than two orders of magnitude depending on preparation procedure, conditions of polymerization as well as storage of G-actin.[75] *Gardel et al.* analyzed the viscoelastic properties of entangled actin networks in dependency of the actin concentration using one- and two-particle microrheology (MR). An increase of the actin concentration results in increased network stiffness, because the entanglement length between the filaments gets shorter and leads to smaller mesh sizes and consequently denser network structures.[76] Structure and mechanics of actin networks is also influenced by ions, like Mg^{2+} and Ca^{2+} leading to bundling of the negatively charged actin filaments by counter ion condensation.[77,78] These actin bundles show higher bending rigidity in comparison to single actin filaments, which also increase overall network elasticity.[77]

Cross-linked F-actin Networks

Further modifications of the architecture and viscoelastic properties of artificial actin networks were performed by administration of several cross-linking proteins. Depending on the type, binding affinity and concentration of cross-linkers a conspicuous structural polymorphism was

observed (see also chpt. 1.3) and reviewed by *Lieleg et al.*[79] Generally, a weakly cross-linked network phase occurs at low concentration of cross-linkers independent of the type of cross-linking protein. With an increasing cross-linker concentration network phase transitions arise from weakly cross-linked to composite followed by bundle networks. At very high concentrations small cross-linkers (*e.g.* fascin and espin) tend to assemble actin filaments in homogeneous bundled phases, while long and flexible cross-linkers (*e.g.* α-actinin and filamin) tend to form clusters of actin bundles.[79] An increase in cross-linker concentration is not only correlated with changes in the network microstructure, but also with enhanced elastic response of the actin network up to the 1000 fold.[79–81] This increased elastic modulus in presence of cross-linkers is important to ensure resilience of cells. On the other hand the transient nature of cross-linkers also provides an adequate fluidity enabling cell shape changes. The viscoelastic behavior of cross-linked actin networks in dependency of the frequency was analyzed in a lot of studies. Generally, at low frequencies cross-linkers have time to redistribute, because their unbinding and rebinding to actin filaments is fast at this time scale, which enables the meshwork to flow. Whereas, at high frequencies cross-linking proteins have no time to reorganize and are permanent linked to actin filaments, which leads to an increased network stiffness.[2,80,82–84]

The viscoelastic response of cross-linked actin networks is also regulated by myosin motor proteins (see chpt. 1.3.1), which are essential components for structural remodeling as well as force generation within the networks. The mechanisms of establishing contractile forces by active myosin motors in actin networks was studied in several *in vitro* experiments and reviewed by *Murrell et al.*[85] The contractile response is influenced by the architecture and connectivity (regulated by ABPs) of the actomyosin networks. *Ennomani et al.* found three different types of contractile response – local sliding, global deformation as well as massive freezing – in dependency of the network connectivity.[86]

There are numerous studies characterizing actomyosin networks in presence and absence of various ABPs, but these 3D artificial systems do not mimic the physiological conditions within a cell properly, where the actin cortex is a quasi-2D layer dynamically connected to the plasma membrane. To get a better understanding of cell cortex mechanics, F-actin as a mimic of the actin cortex had to be coupled to artificial bilayers mimicking the plasma membrane. Therefore, so-called minimal actin cortices (MACs) get more in focus of research and will be introduced in the following.

Minimal Actin Cortices

For a better imitation of the physiological situation in living cells, minimal actin cortices (MACs) – composed of an F-actin layer attached to an artificial lipid bilayer – were designed. Typical MAC setups are 2D models on a planar surface and 3D shell-like models with actin cortices linked at the outside or inside of droplets or vesicles (see fig. 1.10).[66]

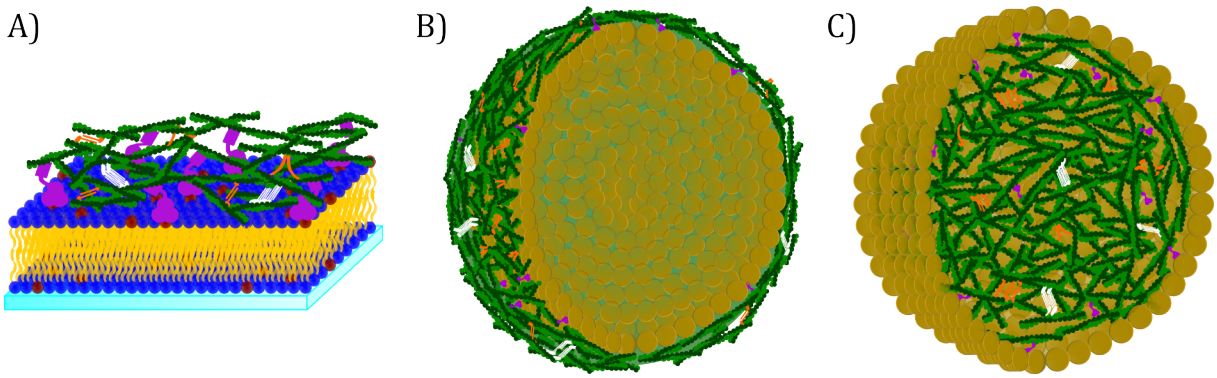

Figure 1.10: Schematic illustration of MAC setups. **A)** 2D MAC model systems are prepared by spreading a lipid bilayer on a solid support and coupling the actin cortex via a linker protein to the membrane. 3D shell-like MACs were created by linking an actin cortex **B)** at the outside or **C)** at the inner wall of a droplet or vesicle. F-actin is shown in green, myosin motor proteins in white, various other cross-linkers in orange and membrane-cortex linking proteins in magenta.

While 2D MACs model systems are useful to investigate small scale impacts on the level of single filaments, 3D MACs offer the possibility of characterizing the impact of compartmentation on mechanical properties of the actin cortex as well as the membrane.

For investigations of 2D actin networks anchored to lipid bilayers, different coupling strategies were used. *Vogel et al.* attached MACs via biotin-neutravidin binding to a bilayer. After addition of active myosin motors they observed buckling, fragmentation and compaction of actin filaments due to the strong coupling to the bilayer.[30] A more weakly attached MACs was prepared by *Murell* and *Gardel et al.* by crowding F-actin near the lipid surface with methylcellulose (MC) and attachment to the membrane provided by a His-tagged actin binding domain of fimbrin, which links to DOGS-Ni-NTA lipids embedded in the solid supported membrane. Addition of α-actinin and active myosin motor proteins drives contraction of the reconstituted actin network.[31] A more physiological approach for linking F-actin to a lipid bilayer is based on the actin binding transmembrane protein ponticulin and was applied by *Barfoot et al*. AFM height images of F-actin linked to ponticulin containing SSMs show individual filaments with an average height of (7 ± 1.6) nm and a helical pitch of

(37 ± 1.1) nm.[87] *Nöding* and *Schön et al.* used the physiological linker ezrin from the ERM protein family (see chpt. 1.3.2) to create MAC. In order to achieve this, an actin network was attached to a SSM doped with the receptor lipid PIP_2 via a permanently active pseudophosphorylated ezrin mutant (ezrin T567D).[65,66] An increasing density of attachment sites of the actin network to the bilayer – induced by higher PIP_2 concentrations – results in denser networks with raised stiffness.[65]

An increased stiffness of actin networks with higher amount of actin-membrane cross-linking was also observed by *Ershov et al*. They studied mechanics of actin networks on shell-like structures by attaching biotinylated F-actin via streptavidin to biotinylated lipids at the outside of oil-in-water droplet.[88] A more physiological MAC model system was created by *Liu* and *Fletcher et al*. using cell-sized giant unilamellar vesicles (GUVs) instead of droplets. The coupling of a dendritic actin network at the outside of the GUVs was established by incorporation of the receptor lipid PIP_2 in the bilayer and N-WASP, a physiological linking combination also found in living cells. Their results show that actin polymerization and depolymerization promote formation as well as destabilization of membrane domains by influencing lipid-lipid interaction through assembly and disassembly processes of the membrane-linked actin cortex. This suggests that membrane organization might be directly controlled by the actin cytoskeleton dynamics.[89]

To mimic the physiological situation in cell more precise, F-actin was attached at the inside of cell-sized droplets and vesicles. *Shah et al.* for example analyzed the self-organization of a dynamic actin cortex inside a water-in-oil droplet. They observed spontaneous symmetry breaking due to myosin induced actin flows, which might also play an important role during cell division and polarization of embryos.[90] *Liu et al.* coupled an actin network at the inner wall of a GUV by a His-tagged actin binding domain of the WASP protein family and DOGS-Ni-NTA. This strong coupling of the actin cortex to the membrane led to the formation of protrusions if actin polymerization is controlled by Arp2/3. They suggest that the formation of filopodium-like protrusions is a result of interactions between the elastic membrane and the growing actin network and might also drive shape changes within the cell.[91]

1.4.2 Top-down Approaches of Cellular Mechanics

To investigate mechanical properties of the whole biomolecule assembly within the actin cortex of a living cell, top-down approaches were applied. Here, the actin cortex is isolated from living organisms by different techniques.

One technique to isolate the complete cytoskeleton composition of an *in vivo* actin cortex is to use the extract from oocytes of the African clawed frog *Xenopus laevis*, which was done in several studies to investigate mechanisms controlling the cortex contraction. *Bement* and *Capco et al.* for example analyzed signal transduction mechanisms regulating cortical contraction in embryonic *Xenopus laevis* as mimic of cytokinesis.[92,93] Further characterization of the regulation of punctuated actomyosin contraction on embryonic tissues of *Xenopus* was done by *Kim* and *Davidson et al*.[94] Viscoelastic properties of cytoplasmic extract from *Xenopus laevis* oocytes were investigated by *Chaudhuri et al.* For this, a dendritic actin network – as it can be found in the lammelipodium of a moving cell – extracted from *Xenopus* eggs was polymerized between a cantilever and a surface and oscillatory microrheology experiments were performed. Interestingly, the stiffness of these dendritic networks ((985 ± 655) Pa)[95] is consistent with the stiffness found in living cells (in the range of several kPa)[96–99] and significantly higher than the stiffness of reconstituted dendritic actin networks in bottom-up approaches (~1 Pa).[100] Furthermore, a reversible elastic behavior for the dendritic actin networks extracted from *Xenopus* oocytes was observed. Based on the elastic properties found for these networks, they are believed to be important for resisting compression and are suggest to play a pivotal role in stabilizing membrane protrusions at the leading edge of a migrating cell.[95]

Another technique to investigate rheological properties of cell cortices is to remove the apical membrane-cortex components of living cells in a controlled manner by the so-called sandwich cleavage method. For this purpose, a sticky porous substrate was placed on top of a cell monolayer and ripped off after short incubation. Before, the cytoskeleton of the cells was weakened by osmotic swelling to facilitate the cleavage of the apical cortex fragments from the basal parts of the cells. This transfer of apical membranes with still attached actin cortices on macroporous substrates, allows to analyze their mechanics in absence of neighboring cells, the nucleus, cytosolic components and other cell organelles. The elastic properties of free standing apical cortex fragments obtained in this way from living Madin-Darby canine kidney cells, strain II (MDCK II) were studied by *Janshoff* and coworkers using AFM indentation experiments. They found that mechanical response of cells is dominated by the components of the membrane cortex as an interplay of accessible membrane reservoirs, adhesion to the plasma

membrane, meshwork architecture and myosin motors, while the impact of the cytosol and organelles can be neglected.[5,101] Furthermore, this top-down approach enables the administration and directly following investigation of exogenous biomolecules on the mechanics of cell cortex fragments. *Nehls et al.* for example found, that the fixation agent glutardialdehyde (GDA) – known to cross-link protein domains in the plasma membrane – reduces the accessible amount of membrane reservoirs, which results in an increased membrane-cortex stiffness. The exact opposite was observed after treating the cortex fragments with the protease pronase E, which is known to remove membrane-associated proteins and thus enlarges accessible membrane reservoirs and consequently decreases the membrane-cortex stiffness.[5]

2 Scope of the Thesis

Many cellular processes, like cell division and motility as well as cell adhesion are governed by the morphological dynamics and resilience of the cell cortex, a thin cross-linked actin network attached to the plasma membrane via proteins of the ezrin-radixin-moesin (ERM) family. The actin cortex morphology and mechanic are regulated by more than a hundred different actin binding proteins (ABPs) as well as by the dynamic coupling to the plasma membrane and is far from being understood in its complexity. In order to disentangle the highly dynamic interplay of actin cortex architecture, myosin motor activity as well as attachment to the membrane and their contribution to the viscoelasticity of cells, different model systems with representative components of the cell cortex are studied under well-defined conditions.

For this purpose, bottom-up strategies are developed, to investigate the function of isolated single proteins of the actin cortex. In a first step, artificial 3D actin networks without cross-linking proteins are analyzed regarding the influence of the experimental setup on their self-organization and viscoelasticity using fluorescence microscopy and passive microrheology (PMR). In a second step, the influence of the motor fragment protein heavy meromyosin (HMM) and the full-length myosin II motor protein − under ATP depletion and ATP excess − on the viscoelastic properties of the *in vitro* actin networks is examined by means of bulk rheology and particle tracking. For a better mimic of the physiological situation in living cells, minimal actin cortices (MACs) are crowded onto a lipid bilayer by methylcellulose (MC). In a third step, the actin cortex is attached to the lipid bilayer via an active ezrin mutant (ezrin T567D) and the receptor lipid phosphatidylinositol-4,5-bisphosphate (PIP_2). Network morphology and viscoelasticity are studied depending on the concentration of the crowding agent MC, the choice of the measuring method and the membrane-attachment points (regulated by the PIP_2 concentration) using fluorescence microscopy and PMR.

In order to investigate the entire biomolecular assembly of the cell cortex, apical cell cortices are isolated from living MDCK II cells in a top-down fashion. Viscoelastic properties of the apical cell cortices after treatment with different cortex-influencing drugs are investigated with atomic force microscopy (AFM) nanoindentation experiments. Here, the focus lies on the impact of ATP regulated myosin motor activity on the cortex fluidity. The results of the isolated apical cell cortices are compared to data obtained from intact, living MDCK II cells and from MAC model systems.

3 Materials and Methods

A detailed list of materials, devices and software used in this work and the corresponding suppliers can be found in the appendix (see chpt. 7.2 and 7.3).

3.1 Materials

3.1.1 Lipids

For the construction of 2D minimal actin cortex model systems, solid supported membranes (SSMs) were prepared to mimic the plasma membrane of living cells. To achieve this, different types and amounts of phospholipids were used.

1-Palmitoyl-2-oleoyl-*sn*-glycero-3-phosphocholine (POPC)

The synthetic phospholipid 1-palmitoyl-2-oleoyl-*sn*-glycero-3-phosphocholine (POPC) contains a zwitterionic choline head group, a palmitic acid moiety (C16:0) at first position of the glycerol backbone and an oleic acid moiety (C18:1, Δ^9) at its second position (see fig. 3.1).

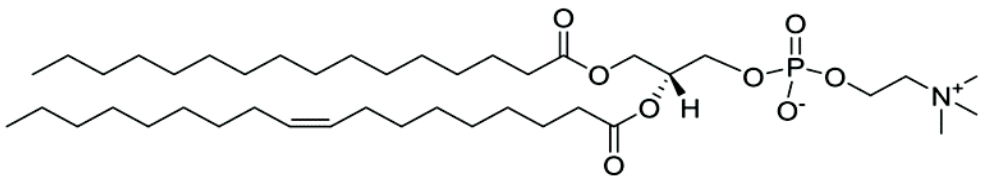

Figure 3.1: Structure of POPC with a molecular weight of M = 760.1 g/mol.[102]

Due to the *cis* configurated double bond inside the oleic acid chain, POPC possesses a low main transition temperature of −7 °C, leading to a liquid-crystalline phase at physiological conditions.[103] This neutral fatty acid ester has great similarities to lipids within mammalian cells and is therefore often used as matrix lipid in artificial lipid bilayers as in this work.[102]

L-α-Phosphatidylinositol-4,5-bisphosphate (PIP_2)

L-α-phosphatidylinositol-4,5-bisphosphate (PIP_2) is a mixture of natural lipids extracted from porcine brain with a negatively charged inositol head group phosphorylated at position 4 and 5, and a blend of different fatty acid chains. A representative structure is shown in figure 3.2.

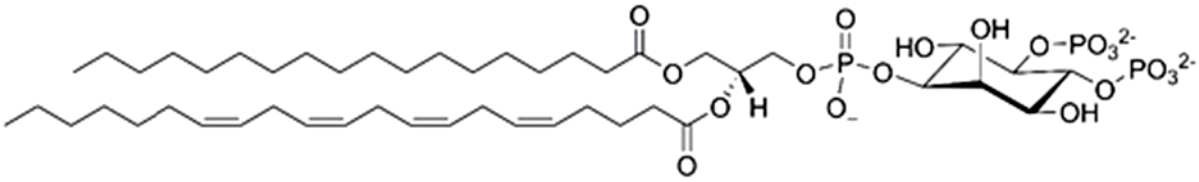

Figure 3.2: Structure of PIP_2 with a molecular weight of M = 1096.4 g/mol.[104]

Despite the fact that the amount of PIP_2 in the plasma membrane is only about 1%, it is an important receptor lipid for proteins.[60] In this work PIP_2 serves as a receptor for ezrin T567D.

3.1.2 Fluorescence Probes

In order to investigate the SSMs by means of fluorescence microscopy, the artificial membranes were doped with fluorescently labeled lipids for visualizing. For fluorescence microscopy analysis of actin network structures, a phalloidin coupled fluorescent dye was used to visualize actin filaments.

Texas Red® 1,2-dihexadecanoyl-*sn*-glycero-3-phosphoethanolamine (TxR-DHPE)

Texas Red® 1,2-dihexadecanoyl-*sn*-glycero-3-phosphoethanolamine (TxR-DHPE) is a synthetic phospholipid labeled at the head group with the red fluorescent dye Texas Red® based on sulforhodamine 101 (see fig. 3.3).

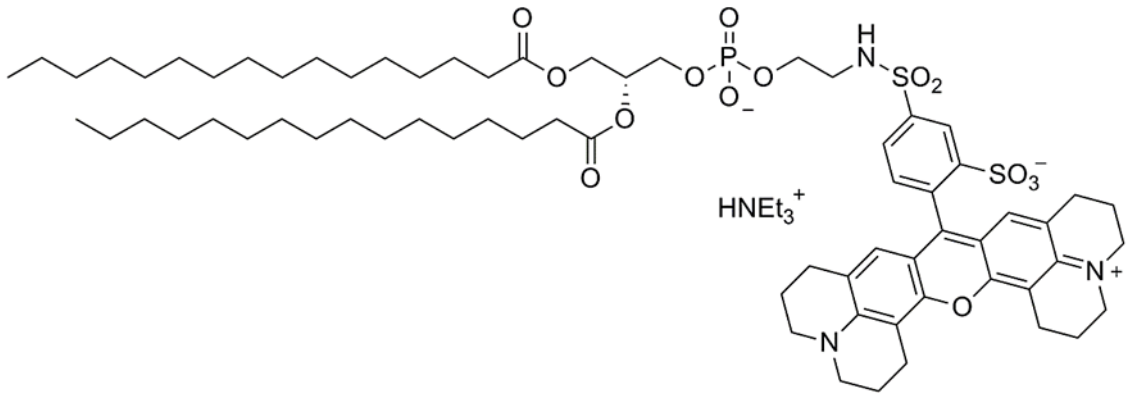

Figure 3.3: Structure of TxR-DHPE with a molecular weight of M = 1381.9 g/mol.[105]

TxR-DPHE is inserted in artificial membranes over the phospholipid anchor and therefore it can be used as fluorescence probe for characterizing membrane systems. The fluorescence excitation maxima of TxR is nearly λ_{ex} = 595 nm and the emission maxima is about λ_{em} = 615 nm.[105]

Atto 390 1,2-dioleoyl-*sn*-glycero-3-phosphoethanolamine (Atto 390-DOPE)

The fluorescent probe Atto 390 1,2-dioleoyl-*sn*-glycero-3-phosphoethanolamine (Atto 390-DOPE) is a synthetic phospholipid, whose phosphoethanolamine head group is linked via an amide bond to a fluorescent cumarin derivate (see fig. 3.4).

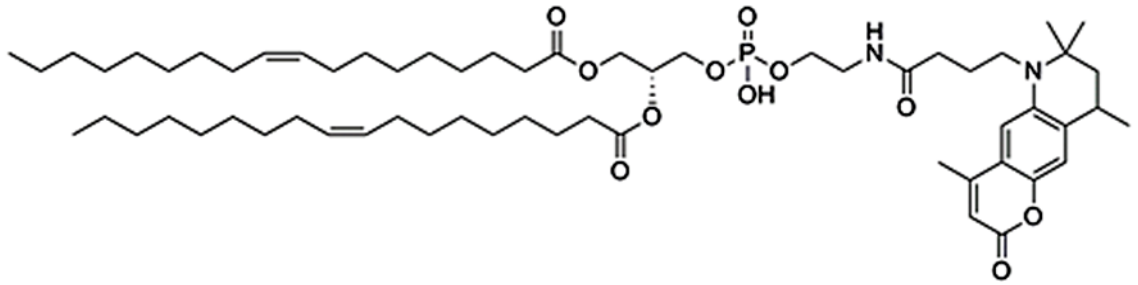

Figure 3.4: Structure of Atto 390-DOPE with a molecular weight of M = 1069 g/mol.[106]

Atto 390-DOPE can be integrated into artificial membrane systems through the fatty acid chain. The fluorescence excitation maxima of Atto 390 is at λ_{ex} = 390 nm and the emission maxima at λ_{em} = 476 nm.[107] This blue fluorescent probe was used in microrheology experiments for membrane labeling, because F-actin was already stained in green and tracer particle in red.

Alexa Fluor® 488-Phalloidin (AF 488-Phal)

The fluorescently labeled phalloidin (see chpt. 1.3.3) derivate Alexa Fluor® 488-Phalloidin (AF 488-Phal, see fig. 3.5) selectively binds to actin filaments and was used in this work for fluorescence microscopy analysis of actin networks.

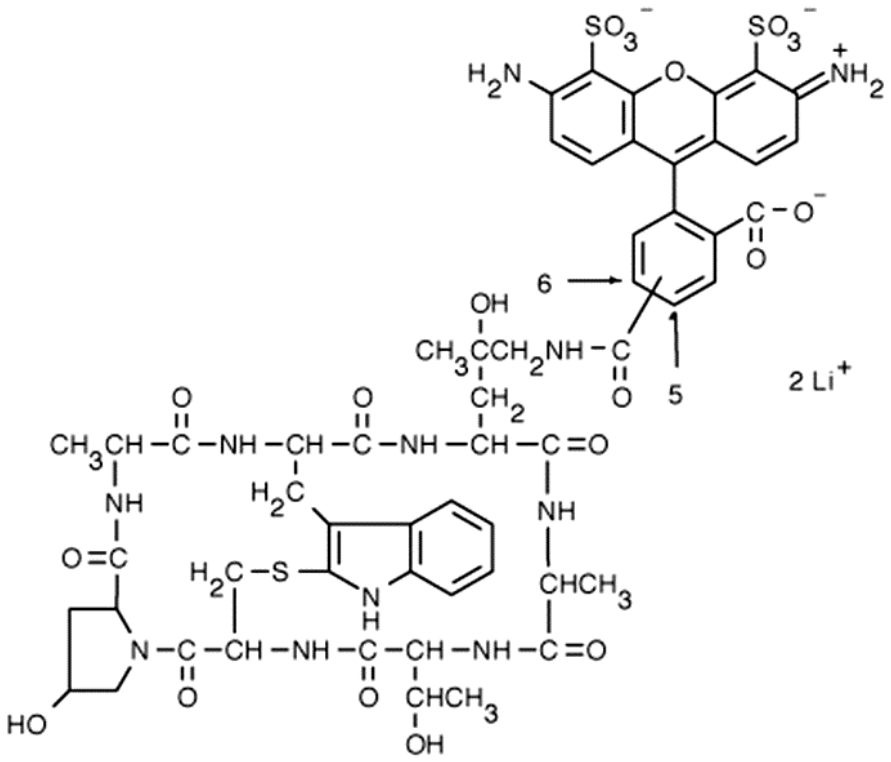

Figure 3.5: Structure of AF 488-Phal[108] with a molecular weight of $M \approx 1300$ g/mol.[109]

The absorption maximum of Alexa Fluor® 488 is at $\lambda_{ex} = 495$ nm and its emission maximum at $\lambda_{em} = 518$ nm.[108]

3.2 Preparative Methods

In this work different bottom-up and top-down approaches were prepared in order to analyze actin cortex mechanics. For bottom-up model systems, 3D actin networks were polymerized in presence of different actin binding proteins (ABPs) between glass coverslips or plates of a rheometer, as well as inside droplets. Apart from this, a 2D minimal actin cortex (MAC) model system was constructed. Furthermore, in a top-down approach apical cell cortices were isolated from MDCK II cells. The preparation procedures are described in the following. A detailed list of materials used in this work and the corresponding suppliers can be found in the appendix (see chpt. 7.2).

3.2.1 Actin Polymerization in Presence or Absence of Additional Agents

For bottom-up approaches, G-actin monomers were polymerized to generate networks of filamentous actin. For this procedure, the buffers listed below were used.

G-buffer: 5 mM Tris/HCl, 0.2 mM $CaCl_2$, 0.77 nM NaN_3, pH = 8.0

F1-buffer: 100 mM Tris/HCl, 500 mM KCl, 20 mM $MgCl_2$, 50 guanidine carbonat, pH = 7.4

F-buffer: 20 mM Tris/HCl, 50 mM KCl, 2 mM $MgCl_2$, 0.1 mM NaN_3, pH = 7.4

Lyophilized powder of muscle (rabbit skeletal muscle) or non-muscle (human platelet) G-actin was dissolved in ultrapure water and divided in aliquots of 10 µL with a concentration of 10 mg/mL (equivalent to 238 µM), which were stored at -80 °C. Before usage, G-actin was diluted in G-buffer to get actin monomer concentrations in the range of 10 µM to 24 µM. Then ATP (0.2 mM) and DTT (0.5 mM) were added and the solution was stored on ice for 1 - 2 h, followed by centrifugation (17 000 g, 4 °C, 20 min) and transfer of the supernatant into a new Eppendorf cup to ensure the removal of potential oligomers. Before initiating actin polymerization, the actin labeling component AF 488-Phal (in a ratio of 1.5% compared to G-actin) as well as tracer particles, ABPs or ATP regeneration components were added, depending on the focus of the experiment.

Polymerization of actin monomers in presence or absence of different additional agents was induced by administration of 10% (*v*/*v*) of the high salt polymerization buffer F1. Depending on the experiment, the actin solution was pipetted into different measuring chambers directly after

initiation of polymerization (see chpt. 3.2.2) or polymerization occurred within Eppendorf cups and pre-polymerized actin was used for preparation of 2D MACs (see chpt. 3.2.3). The networks were allowed to polymerize at least for 30 min before the start of measurements.

Tracer Particles

Microspheres were added to the G-actin solution for microrheology (MR) experiments. For this, stock solutions were prepared in aqueous solution – containing 0.8% solids – by centrifugation (five times, 17 000 g, 5 min) at room temperature and subsequent resuspension of the obtained particle solution in ultrapure water. The particle stock solutions were stored at 4 °C. Characteristics of tracer particles used in this work are listed in table 3.1.

Table 3.1: Overview of tracer particle characteristics used in this work.

Bead material	Bead diameter	λ_{ex}	λ_{em}
carboxylate-modified polystyrene beads	2 µm (1.9 - 2.1) µm	575 nm	610 nm
carboxylate-modified polystyrene beads	1 µm (1.05 - 1.06) µm	470 nm	505 nm

For incorporation of the beads in the actin network, 1 µL of the stock solution was added to the G-actin solution, followed by thorough mixing. Actin polymerization was initiated as described before. Carboxylate-modified beads were used, since they show on the one hand non-specifically binding to F-actin and on the other hand enable stable interaction with the actin network,[110] which is important for passive MR measurements (see chpt. 3.4.1).

Actin Binding Proteins and Additional Agents

Depending on the experiments, ABPs were added to the G-actin solution if desired. In this work distinct ABP to G-actin ratios or distinct ABP concentrations were used. Furthermore, the ATP regeneration agents creatine phosphokinase (CPK) and creatine phosphate (CP) were applied in some experiments with a certain concentration. Final ratios and concentrations of ABPs and ATP regeneration components are listed in table 3.2.

Table 3.2: Overview of ratios and concentrations of ABPs and ATP regeneration agents used in this work.

Actin binding proteins	ATP regeneration agents
r(α-actinin / actin) = 1/40	c(CPK) = 700 nM
r(HMM / actin) = 1/66	c(CP) = 1.7 mM
c(myosin II) = 770 nM	

Myosin II motor proteins (10 mg/mL) were incubated for 20 min at room temperature in F-buffer (1:5 (v/v)) to form bundles with an average length of 0.69 µm,[111] before adding to the actin solution. The actin samples were mixed thoroughly after addition of the ABPs or additional agents. Afterwards, actin polymerization was induced as aforementioned.

3.2.2 3D Actin Networks

In bottom-up approaches 3D actin networks in presence of different ABPs, like myosin II, HMM and α-actinin were polymerized (see chpt. 3.2.1) in different measuring chambers as well as inside water-in-oil droplets.

Glass Chambers

First evaluations of the of F-actin network quality were performed in different kinds of measuring chambers constructed from glass coverslips and double faced adhesive tape. A schematic illustration is shown in figure 3.6.

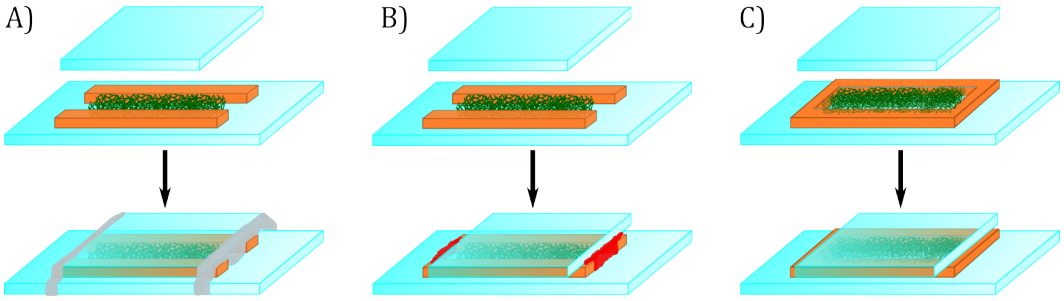

Figure 3.6: Schematic illustration of different glass chambers prepared by glass coverslips (cyan) and double faced adhesive tape (brown). Two stripes of double faced adhesive tape were glued onto a glass coverslip forming a channel. The channel chambers were filled with actin (green) after mounting a second coverslips on top. The channel chambers were either closed with **A)** Parafilm® (grey) or **B)** nail polish (red). **C)** A rectangle was cut out of the double faced adhesive tape. This construct was glued onto a coverslip, filled with actin solution (green) and closed by mounting a second coverslip on top.

For the preparation of channel chambers, two stripes of double faced adhesive tape were stuck on the upper side of a glass coverslip (No. 1, 24 x 50 mm). A second coverslip (No. 1, 22 x 22 mm) was glued on top. The actin solution was added inside the channel chambers through capillary forces and closed either with Parafilm® (see fig. 3.6, A) or nail polish (see fig. 3.6, B). A closed chamber was built by cutting out a rectangle (~0.5 x 1.0 cm) from the double faced adhesive tape with a scalpel and sticking the constructed frame of the adhesive tape onto a glass coverslip (No. 1, 24 x 50 mm). The chamber was filled with actin solution and closed by mounting a second coverslip (No. 1, 22 x 22 mm) on top (see fig. 3.6, C).

Measuring Chambers for Rheology Experiments

Rheology experiments of 3D actin networks in presence and absence of accessory proteins were performed in different measuring chambers, illustrated in figure 3.7.

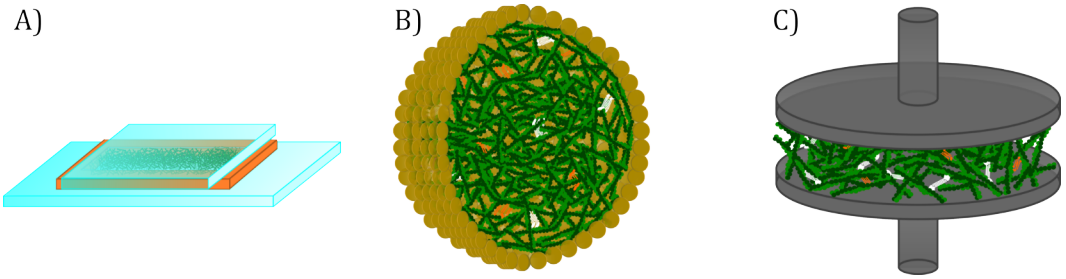

Figure 3.7: Schematic illustration of different measuring chambers for rheology experiments of 3D actin networks. **A)** Actin polymerization within glass coverslip (cyan) chambers sealed with double faced adhesive tape (brown). Polymerization of 3D actin **B)** inside a water-in-oil droplet (yellow) or **C)** between two metal plates of a rheometer (grey). F-actin is shown in green, myosin II or HMM motor proteins in white and α-actinin cross-linkers in orange.

For microrheology studies of entangled actin networks, glass coverslip chambers sealed with double faced adhesive tape were used (see fig. 3.7, A). Furthermore, viscoelastic properties of actin networks in presence of myosin II bundles, α-actinin cross-linkers and ATP regeneration agents were analyzed within oil (008-fluorosurfactant) droplets (see fig. 3.7, B). For this purpose, the aqueous actin solution was pipetted five times back and forth into an oil reservoir to produce water-oil-water droplets. The obtained droplets were put in a channel chamber (see fig. 3.6, A without Parafilm®), sealed with silicone grease and then used for microrheology measurements. For bulk rheology experiments, actin was polymerized with α-actinin and HMM between two metal plates of a rheometer (see fig. 3.7, C) as described in chapter 3.2.1.

3.2.3 2D Minimal Actin Cortices

A 2D MAC model system based on a bottom-up approach designed by *Nöding* and *Schön et al.*[65,66] was prepared. The following buffers were used for preparation and measurements.

Na-citrate buffer: 20 mM Na-citrate, 50 mM KCl, 0.1 mM EDTA, 0.1 mM NaN_3, pH = 4.8

E1-buffer: 20 mM Tris/HCl, 50 mM KCl, 0.1 mM EDTA, 0.1 mM NaN_3, pH = 7.4

F-buffer: 20 mM Tris/HCl, 50 mM KCl, 2 mM $MgCl_2$, 0.1 mM NaN_3, pH = 7.4

PBS-buffer: 1.5 mM KH_2PO_4, 8.1 mM Na_2HPO_4, 2.7 mM KCl, 137 mM NaCl, pH = 7.4

Preparation of Lipid Films

Lipid films with a total mass of 0.4 mg containing different amounts of POPC, PIP_2 and TxR-DHPE or Atto 390-DOPE were produced using lipid film compositions listed in table 3.3.

Table 3.3: Used lipid film composition with a total mass of 0.4 mg.

POPC / mol%	PIP_2 / mol%	TxR-DHPE / mol%	Atto 390-DOPE / mol%
99.6	0	0.4	0
99.1	0.5	0.4	0
96.6	3.0	0.4	0
94.6	5.0	0.4	0
99.0	0	0	1.0
98.5	0.5	0	1.0
96.0	3.0	0	1.0
94.0	5.0	0	1.0

Lipid stock solutions of the respective lipids were mixed according to their amount of substance fraction in chloroform and in presence of PIP_2 in a solution of methanol and chloroform (1:10). Evaporation in a constant stream of nitrogen for 30 min and subsequent drying in vacuum for 3 h completed the preparation. The lipid films were stored at 4 °C until use. Evaporation and drying temperature was 30 °C.

Preparation of Small Unilamellar Vesicles (SUVs)

Small unilamellar vesicles (SUVs) have a diameter of less than 100 nm and are commonly used to form planar solid supported membranes.[112] For the preparation of SUVs, the 0.4 mg lipid films were rehydrated for 30 min in 500 µL Na-citrate buffer (in presence of PIP_2) or PBS-buffer (in absence of PIP_2) to obtain a lipid concentration of 0.8 mg/mL. Thereafter, the suspension was vortexed three times for 30 s in 5 min intervals resulting in multilamellar vesicles. To form SUVs, the suspension was subsequently sonicated for 30 min (60%, cycle 4).

Preparation of Solid Supported Membranes

In this work solid supported membranes (SSMs) were prepared on a glass coverslip No. 1.5 (thickness: 0.17 mm, diameter: 14 mm) of a 35 mm MatTek-dish. For this purpose, the glass coverslip of the MatTek-dish was cleaned with HELLMANEX® III in pure water (1:100) by incubation overnight and rinsed with ultrapure water before usage. The cleaned glass coverslips were incubated for 1 h with SUVs (0.8 mg/mL). SUVs containing PIP_2 were spread in Na-citrate buffer to ensure a homogeneous distribution of the receptor lipid[109], while SUVs without PIP_2 were spread in PBS-buffer. After the spreading process a lipid bilayer was formed on the solid support (see fig. 3.8) and excess lipid material was rinsed away with Na-citrate buffer.

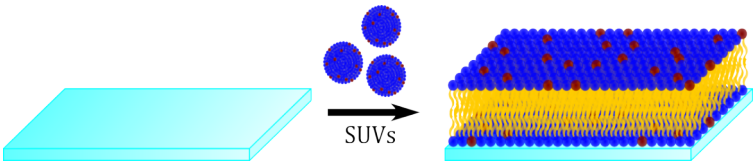

Figure 3.8: Schematic illustration of the spreading process of SUVs on a glass surface in order to prepare solid supported lipid bilayers. The lipid bilayer consists of the matrix lipid POPC (blue headgroup) and the receptor lipid PIP_2 (red headgroup).

Preparation of 2D MACs

For the formation of 2D MACs, the buffer system of the previously prepared SSMs was exchanged to E1-buffer. Thereafter, the linking protein ezrin T567D (isolated and purified by *N. L. Liebe* from the Institute of Organic and Biomolecular Chemistry of the University of Göttingen, Germany) was attached in order to connect the actin networks to the SSM (see chpt. 1.3.2). Ezrin T567D was either incubated for 2 h at room temperature or overnight at 4 °C at a concentration of roughly 1 µM. The samples stored overnight at 4 °C were conditioned to room

temperature the next morning by waiting 1 h. Unbound ezrin proteins were removed by rinsing with E1-buffer. Then, the buffer was exchanged to F-buffer, before pre-polymerized F-actin (c_A = 10 µM, see chpt. 3.2.1) and the crowding agent methylcellulose (MC, 0.02% (*w*/*v*)) were incubated for 4.5 h at room temperature to form a quasi-2D MAC system. Depending on the incubation time of the ezrin protein, pre-polymerized actin was freshly prepared (for ezrin incubation of 2 h) or was stored at 4 °C overnight (for ezrin incubation overnight). For removal of unbound actin filaments, the system was rinsed with F-buffer. A schematic illustration of the preparation steps to construct 2D MACs is shown in figure 3.9.

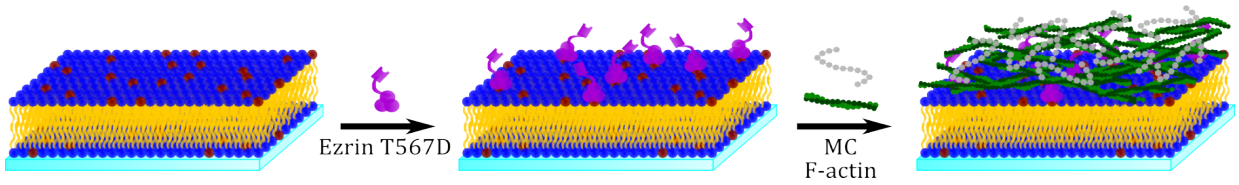

Figure 3.9: Schematic illustration of preparation steps to form 2D MACs. The permanently active mutant ezrin T567D (magenta) was attached to connect F-actin (green) onto the SSM composed of POPC (blue headgroup) and PIP_2 (red headgroup). In its active state ezrin links the membrane via the receptor lipid PIP_2 with the actin network. MC (grey) was used as crowding agent.

3.2.4 Isolated Apical Cell Cortices

In a top-down approach developed by *Janshoff* and coworkers,[5,101] apical cell cortex fragments were isolated in a controlled manner from living Madin-Darby canine kidney cells, strain II (MDCK II) by the sandwich cleavage method. For preparation and experiments the following buffer was used.

PBS-buffer: 1.5 mM KH_2PO_4, 8.1 mM Na_2HPO_4, 2.7 mM KCl, 137 mM NaCl, pH = 7.4

Cell Culture

MDCK II cells were maintained in minimum essential medium (MEM) with Earle's salts, 2.2 g/L $NaHCO_3$, 2 mM GlutaMAX™ and 10% fetal calf serum (FCS) in a humidified incubator set to 37 °C and 5% CO_2. Twice a week the cells were subcultured using Trypsin/EDTA (0.25% / 0.02%)

Isolation of Apical Cell Cortices

To obtain apical cell cortex fragments from intact, living MDCK II cells, the sandwich cleavage method was applied.[5,101] For this, glass coverslips – for STED experiments of apical cell cortices – or porous silicon substrates with a depth of 800 nm and a pore radius of 0.6 µm – for AFM indentation experiments of free-standing apical cell cortices – were used. The pores of the silicon substrate were accessible from both sides, which prevents generation of pressure differences. Before usage, the substrates were cleaned in oxygen plasma, incubated for 2 h with the positively charged polymer poly-D-lysine (PDL, 0.2 g/L) and rinsed with ultrapure water. Thereafter, the substrates were placed on top of an osmotically swollen confluent MDCK II cell monolayer (with a net negatively charged plasma membrane), incubated for 30 min and ripped off. After the cleavage, the samples were rinsed five times with phosphate-buffered saline (PBS). The obtained samples were stored in PBS and used immediately for fluorescence microscopy analysis or stored overnight at 4 °C and utilized the next day for AFM indentation experiments. AFM indentation experiments were also performed on samples treated further with ATP (7 mM, AFM measurement directly after addition) or cytochalasin D (CytD, 10 µM, AFM measurement 15 min after addition).

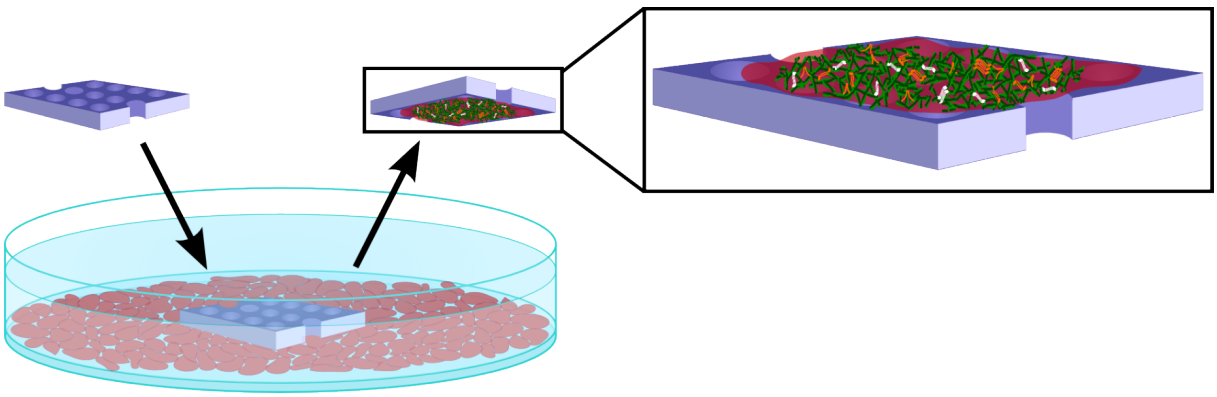

Figure 3.10: Schematic illustration the sandwich cleavage method. A porous silica substrate (purple) coated with the positively charged polymer PDL was placed on top of an osmotically swollen MDCK II cell monolayer (red) with a net negatively charged plasma membrane. After short incubation, the substrate was ripped off. Thereby, the strong adherent basal part of the MDCK II cells still remain on the petri-dish, while the apical cell cortex parts are transferred to the porous substrate. The cell membrane is shown in red, F-actin in green, myosin motors in white and possible cross-linking proteins in orange.

Immunostaining of Isolated Apical Cell Cortices

In order to stain the cell membrane, the MDCK II cell layer was rinsed twice with PBS and incubated for 10 min at 37 °C and 5% CO_2 with a CellMask Orange containing solution (1:500 in MEM) prior to sandwich cleavage.

After sandwich cleavage, samples used for AFM indentation experiments were additionally treated with LifeAct®-TagGFP (2 g/L, 1 h) – for staining of F-actin – and rinsed three times with PBS. Afterwards, the samples were stored at 4 °C overnight and AFM measurements were conducted the next day.

Isolated apical cell cortices used for fluorescence microscopy were fixed for 20 min with paraformaldehyde (PFA, 4% in PBS) and treated for 3 h with bovine serum albumin (BSA, 5% (*w*/*v*) in PBS) for blocking of unspecific antibody binding. Antibody staining of myosin II was performed by addition of the primary antibody anti-phospho-MRLC (Ser 19) mouse IgG (1:50 in PBS, 1 h). Thereafter, the secondary antibody Alexa Fluor 546 goat anti-mouse IgG (2 µg/mL) was incubated for 1 h. Filamentous actin was labeled using Alexa Fluor 488-Phalloidin (6.6 µM, 45 min). After each step, the sample was rinsed three times with PBS.

Apical cell cortices, which were used for STED imaging were also fixed for 20 min with 4% PFA and unspecific biding was avoid by adding BSA (5% (*w*/*v*) in PBS, 30 min). F-actin staining was performed by adding Abberior STAR RED (1.32 µM, 45 min). The sample was rinsed after each step three times with PBS. After rinsing, the sample was stored in Abberior Mount Liquid solution for STED measurements.

3.3 Biophysical Methods

In this work the following biophysical methods were used in order to investigate structure and mechanics of artificial actin networks and of native cell cortex fragments. A detailed list of devices and software used in this work and the corresponding suppliers can be found in the appendix (see chpt. 7.3).

3.3.1 Theoretical Basics of Fluorescence Microscopy

Fluorescence microscopy is a variant of light microscopy, based on the principle of fluorescence. Especially in biophysical chemistry, fluorescence microscopy is an important measuring technique, since this non-invasive method enables visualization of biomolecular structures as well as of dynamic biochemical processes. Fluorescence is the physical process of spontaneous light emission, occurring within nanoseconds during the transition of an electronically excited state back to the electronic ground state. For this, electrons of the molecule (fluorophore) have to be excited through photon absorption by light of a certain wavelength. During the returning process of excited electrons back to their ground state, not only photons (fluorescence light), but also heat will be emitted through non-radiative vibrational relaxation caused by interactions with surrounding solvent molecules. Here, both, collisions of the excited dipolar fluorophore with solvent molecules as well as reorganization of solvent molecules due to dipole moment changes of the fluorophore after electronic excitation lead to dissipation of energy.[114–116] Accordingly, the emitted photons possess a lower energy than the absorbed photons, which is mirrored in an energy difference between the absorption and emission spectrum of about 20 - 50 nm, called *Stokes* shift (see fig. 3.11).[117]

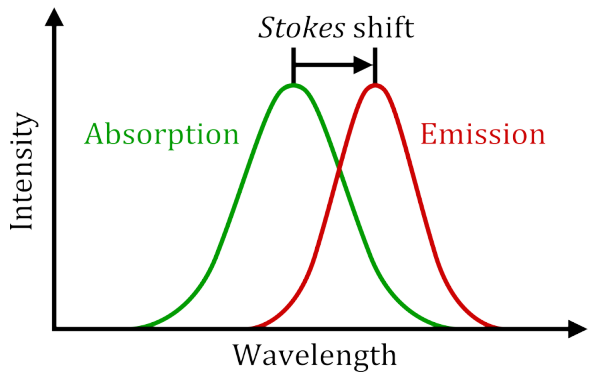

Figure 3.11: Schematic illustration of the *Stokes* shift between the absorption and emission spectrum of a fluorophore.

This phenomenon is used in fluorescence microscopy to excite fluorescent dyes coupled to biological material (see chpt. 3.1.2) at a certain wavelength and separately detect the red-shifted emitted light in order to examine architectures and dynamics of specific biomolecules.

In this work, three different types of microscopes – an epifluorescence, a confocal laser scanning microscope (CLSM) as well as a stimulated emission depletion (STED) microscope – were used to investigate the organization and mechanics of minimal actin cortices and native cell cortex fragments by visualizing localization of fluorescently labeled lipids and proteins.

3.3.2 Epifluorescence Microscopy

In epifluorescence microscopy, the effect of the Stokes shift is used to excite fluorophores with a specific wavelength and detect only the red-shifted emission. The schematic experimental setup and working principle of an epifluorescence microscope is shown in figure 3.12.

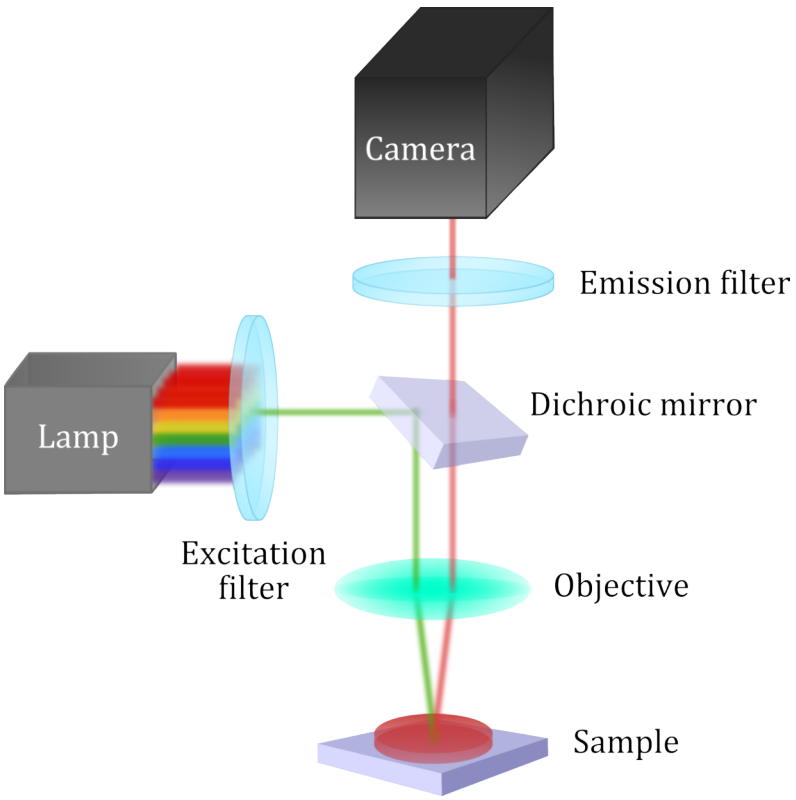

Figure 3.12: Schematic illustration of the experimental setup and light path of an epifluorescence microscope. The excitation light is shown in green and the emission light in red.

In epifluorescence microscopy often mercury lamps are used as light source for excitation. The emitted white light beam of the lamp first hits an excitation filter, which can only be passed by a chosen excitation wavelength. Then, the excitation light hits a dichroic mirror characterized by a critical wavelength λ_c Incoming light with a wavelength smaller than λ_c is reflected, while light with a wavelength larger than λ_c passes the dichroic mirror. The mirror possesses a critical wavelength in between the absorption and emission wavelength of the applied fluorescent dye. Thus, the short-wavelength excitation light is reflected at the dichroic mirror, passes the beam-focusing objective and excites fluorescent dyes within the sample. On the other hand, the Stokes shifted emission light has a larger wavelength and passes the objective and the dichroic mirror in the direction of the emission filter. Here, remaining excitation light is blocked and the emitted light reaches the detector recording the fluorescent specimen. The excitation light beam does not only illuminates a small point, but a certain section of the sample. This results also in partial excitations outside the focal plane. Hence, emitted light from above and below the focal plane is collected by the detector, leading to a loss of the image quality, which makes it difficult to recognize optical details. In epifluorescence microscopy the whole specimen is always illuminated, enabling high time resolution, while the lateral resolution is limited due to the diffraction of light at the optical components.[114,118] Generally, the lateral resolution limit d_{FWHM} describes the minimal distance to separate two points by the full width at half maximum (FWHM) of the intensity point spread function (PSF). This resolution limit d_{FWHM} is defined by *Abbe's* law,

$$d_{\mathrm{FWHM}} = \frac{0.51\,\lambda_{\mathrm{em}}}{n \sin\alpha} = \frac{0.51\,\lambda_{\mathrm{em}}}{\mathrm{NA}} \tag{3.1}$$

where λ_{em} is the emission wavelength, n is the refractive index, α is the opening angle and NA the numerical aperture of the objective.[119] The lateral resolution of epifluorescence microscopy is in the range of 200-300 nm for visible light, while axial resolution is in the range of about 500 - 700 nm.[120]

Darkfield Microscopy

A special illumination technique in epifluorescence microscopy is darkfield microscopy, where only scattered light from the specimen is captured, leading to an image with a dark background around the bright sample. A typical setup and light path of darkfield microscopy is shown in figure 3.13.

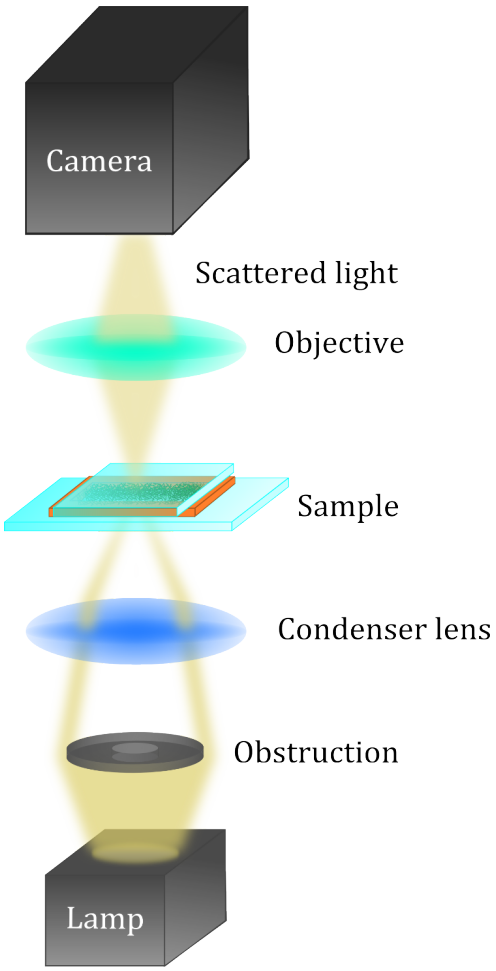

Figure 3.13: Schematic illustration of a typical setup and light path of darkfield microscopy.

In general, for the darkfield illumination technique, a darkfield condenser is mounted to an upright epifluorescence microscope. The obstruction of the darkfield condenser blocks incident light from the center of the light beam, forming an illuminated outer ring. This ring is focused onto the sample by a condenser lens. The light beam hits the specimen and is scattered or transmitted from it, whereby only the scattered light passes the objective. This technique enables high contrast visualization of unstained samples.[121]

Experimental Procedure

For quick analysis of the quality of solid supported membranes of 2D MAC (see chpt. 3.2.3) as well as of isolated cell fragments (see chpt. 3.2.4) the upright epifluorescence microscope BX 51 was applied with a 60 x water immersion objective. Furthermore, intact isolated cell fragments for AFM indentation experiments were localized using the BX 51 with a 40 x water immersion objective (see chpt 3.3.7). Image processing was done with the software GIMP 2.

To investigate local viscoelastic properties of 3D actin networks (see chpt. 3.2.2) and 2D MACs (see chpt. 3.2.3) video particle tracking (VPT, see chpt. 3.4.1) was performed. For this, carboxylate-modified beads were incorporated within the actin network (see chpt. 3.2.1) and tracked using a scientific complementary metal-oxide-semiconductor (sCMOS) camera (Zyla-5.5-CL-10). The camera was mounted on a fluorescence microscope (Olympus FluoView 1200, 60 x objective) or for VPT using darkfield illumination on an upright epifluorescence microscope (BX 51, 60 x objective) equipped with a darkfield condenser (U-DCW). Time series of 20 000 to 160 000 images were recorded of about 1 to 16 beads. The exposure time was between 10 ms to 40 ms and frame rates in the range of 20 fps to 50 fps. Particle tracking analysis was done using a MATLAB script written by *M. Kilfoil*[122] based on theory of *Weitz et al.*[123] and the tracking algorithm of *J. Crocker*.[123] Data evaluation is described in more detail in chapter 3.4.1.

3.3.3 Confocal Laser Scanning Microscopy

Confocal laser scanning microscopy (CLSM) is a more advanced version of epifluorescence microscopy. The schematic experimental setup as well as the light path of a CLSM are shown in figure 3.14.

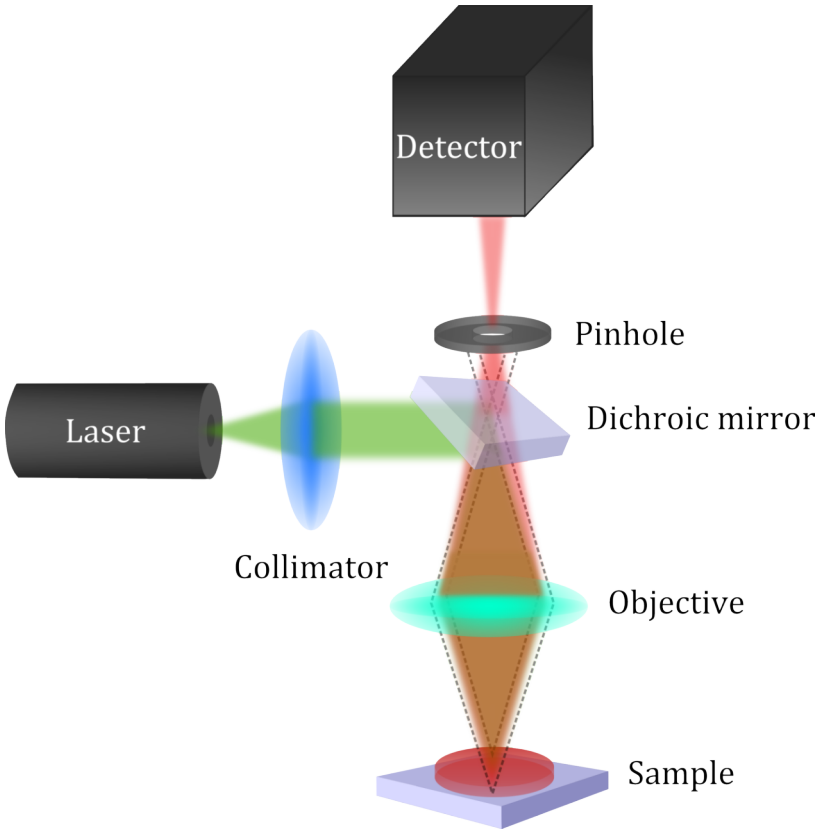

Figure 3.14: Schematic illustration of the experimental setup and light path of a confocal laser scanning microscope. The excitation light is shown in green, the emission light in red and the out-of-focus emitted light as grey dotted line.

In confocal microscopy monochromatic, collimated light generated by a laser source is directed onto the sample by a dichroic mirror and an objective. Contrary to epifluorescence microscopy, not the whole specimen, but only small focal volumes are illuminated and scanned spot-by-spot in the *x*-*y* plane. This is achieved by successive steering of the laser over the focal plane of the specimen through galvanometric scan-mirrors and imaging of the region of interest (ROI) by raster scan. The red-shifted fluorescence light passes the dichroic mirror and reaches an adjustable pinhole. Here, an ideal adjustment of the pinhole in the light path only allows the detection of light from the focal plane, while unfocused beams caused by fluorophores above and below the plane are blocked. The signal is detected by a photomultiplier, which converts the

light signal into an electrical voltage and enables sensitive detection with a high signal-to-noise ratio. Each detected signal belongs exactly to one point of the sample. By variation of the focal plane even three dimensional fluorescence micrographs can be recorded.[118,119,124] The detected focal volume can be adjusted through the diameter of the pinhole. If the pinhole diameter is large, the lateral resolution d_{FWHM} is in a similar range as for epifluorescence microscopy (see eq. 3.1), but depends on the excitation wavelength λ_{ex} as given in equation 3.2.[119]

$$d_{\mathrm{FWHM}} = \frac{0.51\,\lambda_{\mathrm{ex}}}{n \sin\alpha} = \frac{0.51\,\lambda_{\mathrm{ex}}}{\mathrm{NA}} \tag{3.2}$$

Here, n is the refractive index, α is the opening angle and NA the numerical aperture of the objective. The lateral resolution of a CLSM can be increased by a factor of about 1.4 by minimizing the pinhole diameter, but this is accompanied by a significant loss of the detected light intensity.[125] An advantage of this technique is minimization of fluorophore bleaching and photodamage, but on the other hand it slows down the image acquisition rate.

Fluorescence Recovery after Photobleaching

Fluorescence recovery after photobleaching (FRAP) is a method based on fluorescence microscopy, which allows to determine the lateral diffusion coefficient D of fluorescently labeled probes in cells or artificial biological model systems.[126] A schematic overview of a FRAP experiment performed on a lipid bilayer is shown in figure 3.15.

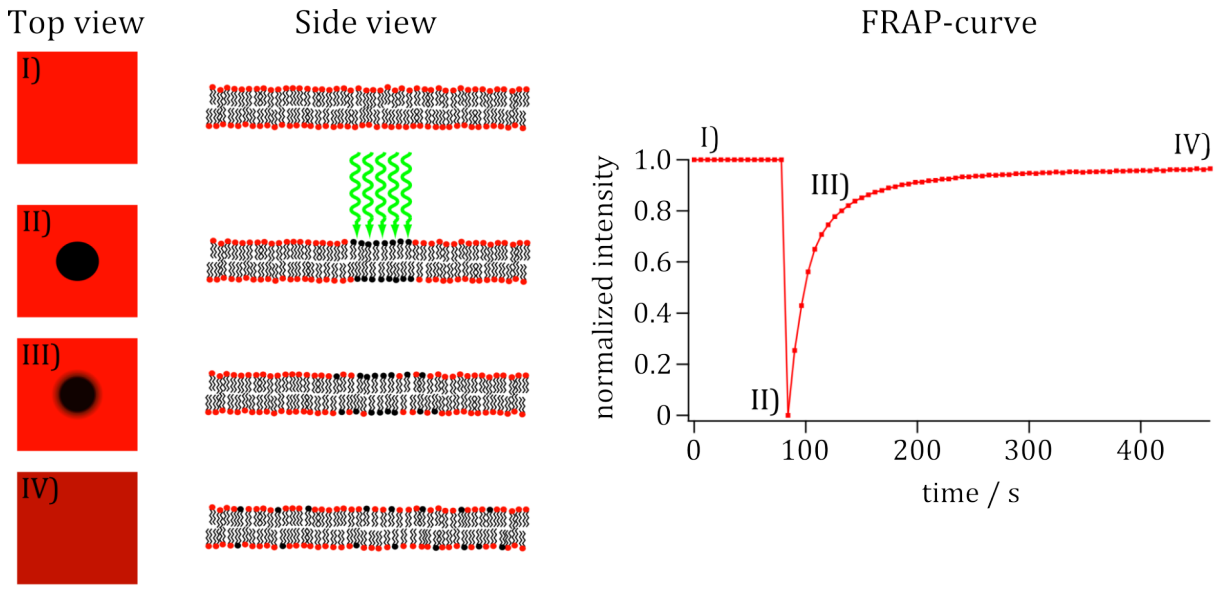

Figure 3.15: Schematic representation of a FRAP experiment performed on a lipid bilayer (top view and side view) and the corresponding FRAP-curve as normalized fluorescent intensity against the time. **I)** Fluorescent intensity before bleaching. **II)** Bleaching of fluorophores in ROI. **III)** Recovery of fluorescent intensity in ROI by diffusion. **IV)** Completely recovered fluorescent intensity in ROI with decreased intensity in contrast to **I)** due fluorophore bleaching. Modified from *MDougM*.[127]

In order to determine the diffusion coefficient of a fluorescently labeled lipid bilayer (see fig. 3.15, I), a high-energy laser pulse is irradiated on a ROI of the sample, leading to irreversible photochemical destruction (bleaching) of fluorescent dyes in this area (see fig. 3.15, II). If the bleached probes are laterally mobile molecules in the artificial membrane, diffusion of the bleached molecules out of the ROI occurs, while at the same time unbleached probes diffuse into the ROI. This process is called recovery (see fig. 3.15, III and IV).[126]

Data evaluation of FRAP experiments was performed using a MATLAB script (*frap_analysis*) written by *Jönsson et al.*[128] Here, they assume two dimensional diffusion of a fluorescence probe homogenously distributed in a lipid bilayer. The analytical method is based on the so-called Hankel transform, which is independent of the shape of the bleached area, reduces the noise effect and compensates temporal variations. FRAP data analysis was done by circular averaging, leading to reduced spatial noise and easier to handle data. In this work only artificial membranes with one diffusion component – SSMs composed of POPC and labeled with TxR-DHPE – were investigated. Therefore, a fit to *single component* was used. The fit function to the normalized Hankel transform *vs*. $4\pi^2 k^2 t$ is given in equation 3.3,

$$F(k,t)=F(k,0)\left[(1-\gamma_0)e^{-i\omega t}\exp\left(-4\pi^2 k^2 D_1 t\right)+\gamma_0\right] \qquad (3.3)$$

where k is the spatial frequency, D_1 the diffusion coefficients and γ_0 the immobile fraction of the components.[128] The fitted values for the diffusion coefficient D_1 were indicated in the program.

Experimental Procedure

In order to investigate 3D actin networks (see chpt. 3.2.2), 2D MAC (see chpt. 3.2.3) and cell cortex fragments (see chpt. 3.2.4) fluorescence micrographs were captured using an upright or inverted CLSM (Olympus FluoView 1200) equipped with a water immersion objective (60 x, NA = 1.0) or an oil immersion objective (100 x, NA = 1.3). More details about technical components are given in chapter 7.3 and about fluorescence probes and staining protocols in chapter 3.2. Image processing was done with the software GIMP 2.

For FRAP experiments lipid bilayers consisting of POPC and doped with 0.4 mol% TxRed-DHPE were prepared on glass supports as described in chapter 3.2.3. Each FRAP-curve was recorded at a different region of the respective SSM. The scanning mode was set to 2 µs/px and resolution to 63.46 µm x 63.43 µm (100 x magnification, zoom: 2.0). A ROI was determined with a circular shape and a diameter of 12.4 µm x 12.4 µm. Before bleaching 5 images of the chosen membrane area were taken. For bleaching a high-energy laser pulse emitting at 561 nm with 100% intensity was irradiated at the ROI for 15 s. After bleaching 45 images were taken to observe the recovery process.

3.3.4 Stimulated Emission Depletion Microscopy

Stimulated emission depletion (STED) microscopy is a super resolution microscopy technique developed by *Stefan Hell*, which overcomes the diffraction barrier (*Abbe* limit) of about 200 nm.[129,130] To achieve this, not only a laser beam for excitation of fluorophores in a diffraction limited focus is used, but also a second red-shifted depletion laser beam (STED beam) with high intensity. By passing through a phase plate, the STED beam is shaped like a torus in the focal plane.[131] A typical set-up for STED microscopy is illustrated in figure 3.16.

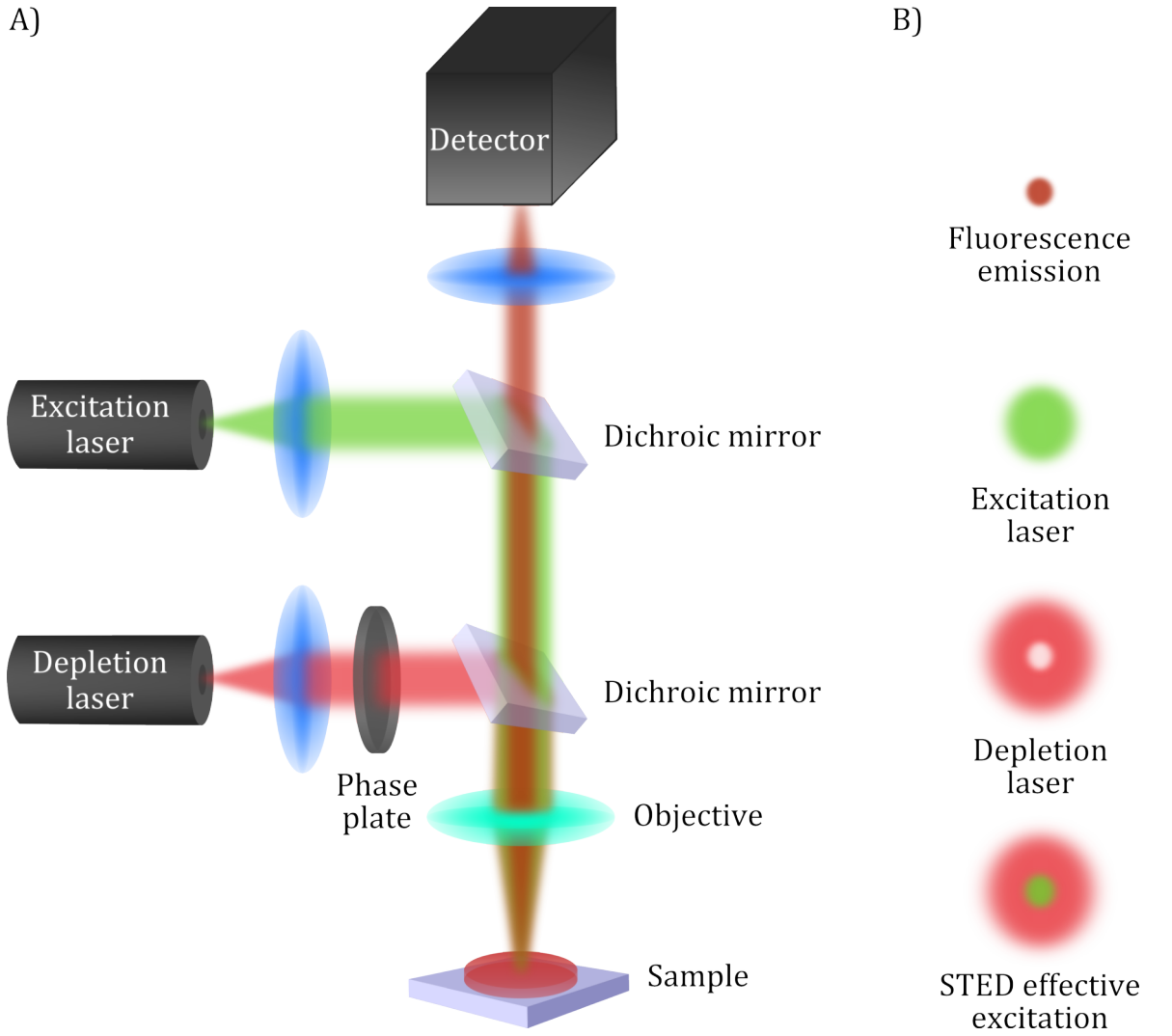

Figure 3.16: A) Schematic illustration of an experimental setup and light path of a stimulated emission depletion microscope. The excitation light is shown in green, the depletion light in bright red and the resulting effective emission light in dark red. **B)** Overview of the excitation laser spot, the torus shaped depletion laser spot, the effective STED excitation and the resulting fluorescence emission.

In short, the STED beam switches off fluorophores in the outer regions of the excitation focus by stimulated emission, while in the center of the excitation focus (a small observation volume determined by the pattern of the STED beam) fluorophores are still allowed to emit.[132,133] This emitted light is detected and by scanning the torus shaped beam across the sample, a high resolution image is generated. The lateral resolution improvement d can be described by a modified equation of *Abbe's* law.[134]

$$d = \frac{\lambda_{ex}}{2n\sin\alpha\sqrt{1+\varsigma}} = \frac{\lambda_{ex}}{2\,\mathrm{NA}\sqrt{1+\varsigma}} \qquad (3.4)$$

Here, λ_{ex} is the excitation wavelength, n is the refractive index, α is the opening angle and NA the numerical aperture of the objective. The saturation factor ς describes the ratio between the applied maximum STED intensity I_{max} and the saturation intensity I_s ($\varsigma = I_{max}/I_s$). The saturation intensity I_s corresponds to half the emission signal value and is determined by the rotational behavior of the fluorophore and properties of the STED beam, such as its wavelength and polarization.[134] By increasing the STED intensity, a smaller fluorescence focal width can be generated, which in turn enables the visualization of fluorescent objects with a lateral resolution of about 30 nm.[120]

Experimental Procedure

Native apical cell cortex fragments were prepared and stained for STED experiments as described in chapter 3.2.4. The samples were imaged using a Facility Line STED setup equipped with a pulsed 640 nm excitation laser and a pulsed 775 nm STED laser mounted on an IX83 inverted microscope. For imaging a 100 x oil immersion objective (NA = 1.4) was used.

3.3.5 Acoustic Force Spectroscopy

Acoustic force spectroscopy (AFS) is a novel technique developed by researchers at the Vrije University of Amsterdam, which enables manipulation of single biomolecules in a highly controlled manner by generating resonant acoustic waves.[135] This technique allows constant force, dynamic force and force extension measurements on a large number of molecules in parallel and therefore can be applied in a wide field of research, like for investigations of biopolymer mechanics, binding and unbinding kinetics of proteins as well as protein-protein interactions.[135,136] In this work, the AFS was only used for real-time parallel 2D tracking of microspheres embedded in an artificial actomyosin network and is therefore not described in more detail. A typical experimental setup for video particle tracking measurements by means of an AFS is shown in figure 3.17.

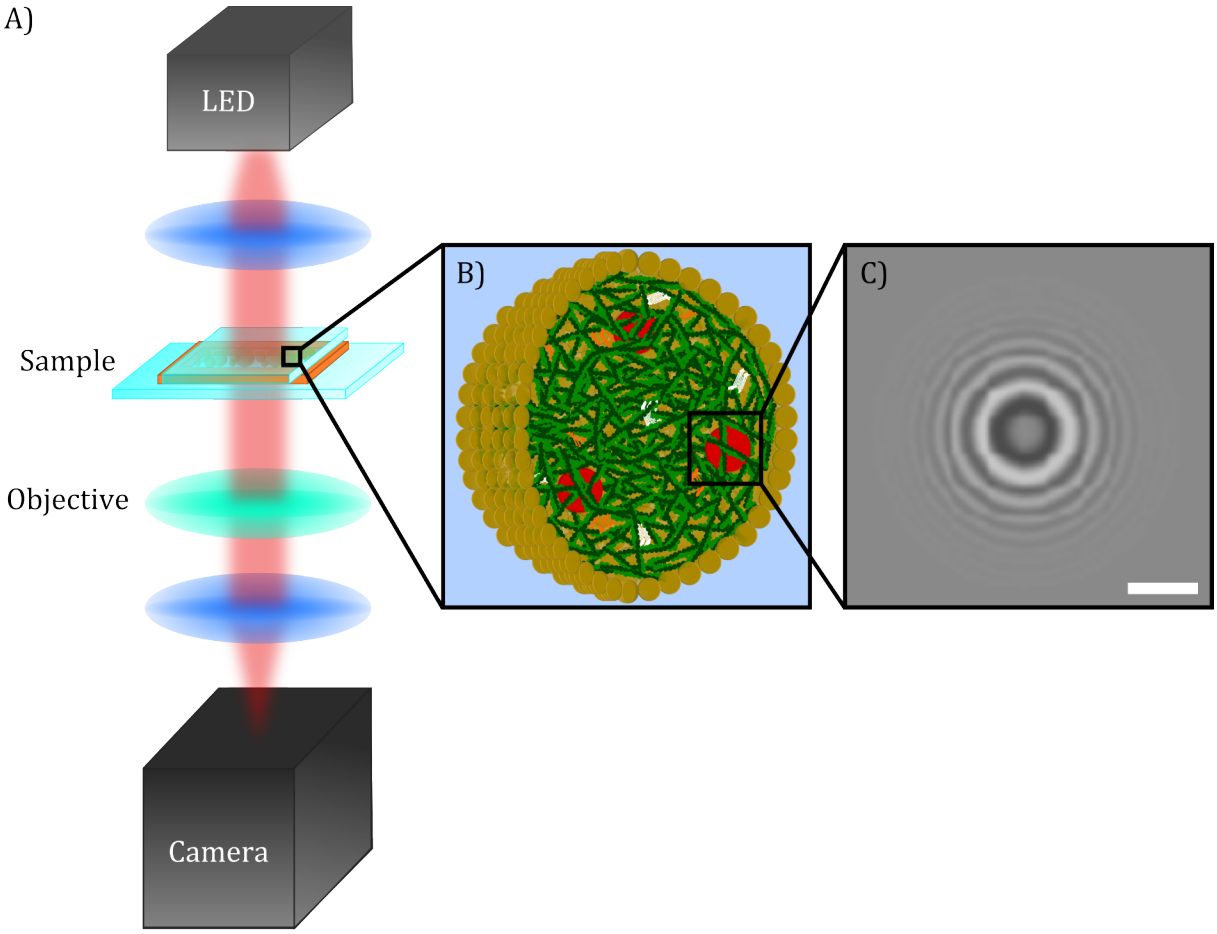

Figure 3.17: A) Schematic illustration of an AFS setup for video particle tracking measurements. The sample is placed in a glass channel chamber. Microspheres within the sample are illuminated using an LED light source and imaged by means of an objective and a camera. **B)** The sample contains water-in-oil droplets filled with polymerized actomyosin networks. F-actin is shown in green, myosin II in white, α-actinin in orange and the microspheres in red. **C)** Exemplary camera image of a microsphere with a radius of 1 µm. Scale bar: 2 µm.

For video particle tracking (VPT) measurements, the microspheres are illuminated with a light-emitting diode (LED) light source and their corresponding interference patterns resulting from the transmitted light, are imaged by means of an objective and a camera. These images are used to determine the position of the microspheres by analyzing their corresponding interference patterns with a TRACKING SOFTWARE written by *M. T. J. van Loenhout et al.,*[137] which is based on a quadrant-interpolation tracking algorithm. Trajectories of the microspheres in the *x*-*y*-plane are obtained with a high precision of about 1 nm.[137]

Experimental Procedure

Actin networks (c_A = 20 μM) in presence of myosin II bundles, α-actinin, ATP regeneration agents and tracer particles were polymerized within fluorosurfactant water-in-oil droplets and transferred into channel chambers as described in chapter 3.2.2. Tracer particles with a radius of 1 μm (see chpt. 3.2.1) within the actomyosin networks of immobile droplets were tracked in 2D by means of an AFS G2 setup (5 min, 140 Hz). AFS tracking measurements of 3 to 20 beads in parallel were performed 5 min after preparation, when there was still a sufficient stock of ATP was present within the droplets and 24 h after preparation, when the ATP stock was already consumed. For this, the particles were illuminated using an LED light source (685 nm) and imaged with a complementary metal-oxide-semiconductor (CMOS) camera USB 3.0 and a 40 x air objective (NA = 0.65). These images were used to analyze the position of the microspheres by means of a TRACKING SOFTWARE written by *M. T. J. van Loenhout et al.*[137] The obtained trajectories in *x*- and *y*-direction were further investigated using a PYTHON script (see chpt. 7.5) written by *I. P. Kuhlemann* (Institute of Physical Chemistry of the University of Göttingen, Germany), inspired by works from *Toyota et al*.[42] and using a MATLAB script written by *P. Nietmann* (Institute of Physical Chemistry of the University of Göttingen, Germany), which is based on a MATLAB script written by *M. Kilfoil.*[122] Data processing is described in more detail in chapter 3.4.1.

3.3.6 Oscillatory Rheometry

Rheometers are common measuring instruments in rheology – the study of the flow and deformation of matter in response to external stress – to investigate viscoelastic properties of soft materials. In general, rheometers possess two rotationally symmetrical components, in this work circular plates, which are arranged on a common axis and one of them is rotating. Between these rotationally symmetrical components, the sample is placed and linear viscoelastic properties are analyzed by shearing the material with a small deformation, as shown in simplified form in figure 3.18.[138,139]

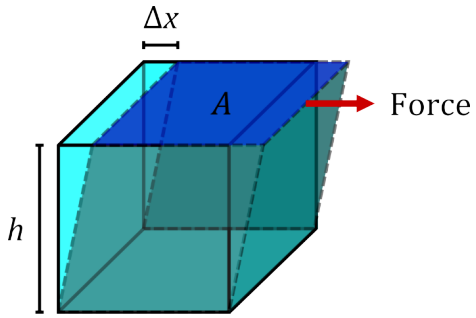

Figure 3.18: Schematic illustration of the shear deformation of a material applied by an external force. Here, h is the height of the sample, Δx the deflection and A the contact area (shown in blue).

In this representation, the sample is slightly deformed in one direction by an external force F. Therefore, only simplified uniaxial equations in the linear viscoelastic regime are considered. The quotient of the force F and the contact area A gives the shear stress σ, while the quotient of the deflection Δx and the height h of the sample is defined as the shear strain γ.

$$\sigma = \frac{F}{A} \tag{3.5}$$

$$\gamma = \frac{\Delta x}{h} \tag{3.6}$$

Mechanical properties of viscoelastic materials lie in between those of elastic solids and *Newtonian* liquids (viscous fluids). For elastic solids, the stress σ is proportional to the strain γ, equivalent to *Hook's* law.

$$\sigma = E\gamma \tag{3.7}$$

Here, E is the proportionality constant also known as the *Young's* modulus. In *Newtonian* liquids, the stress σ is proportional to the shear rate $\dot{\gamma}$ and the proportionality constant is the viscosity η of the liquid.[140–142]

$$\sigma = \eta\dot{\gamma} \tag{3.8}$$

By means of oscillatory rheometry it is possible to investigate both, elastic and viscous behavior of viscoelastic material, depending on the time scale of strain deformation. A typical experimental setup of a strain-controlled oscillating rheometer and the corresponding stress responses of different materials are shown in figure 3.19.[139]

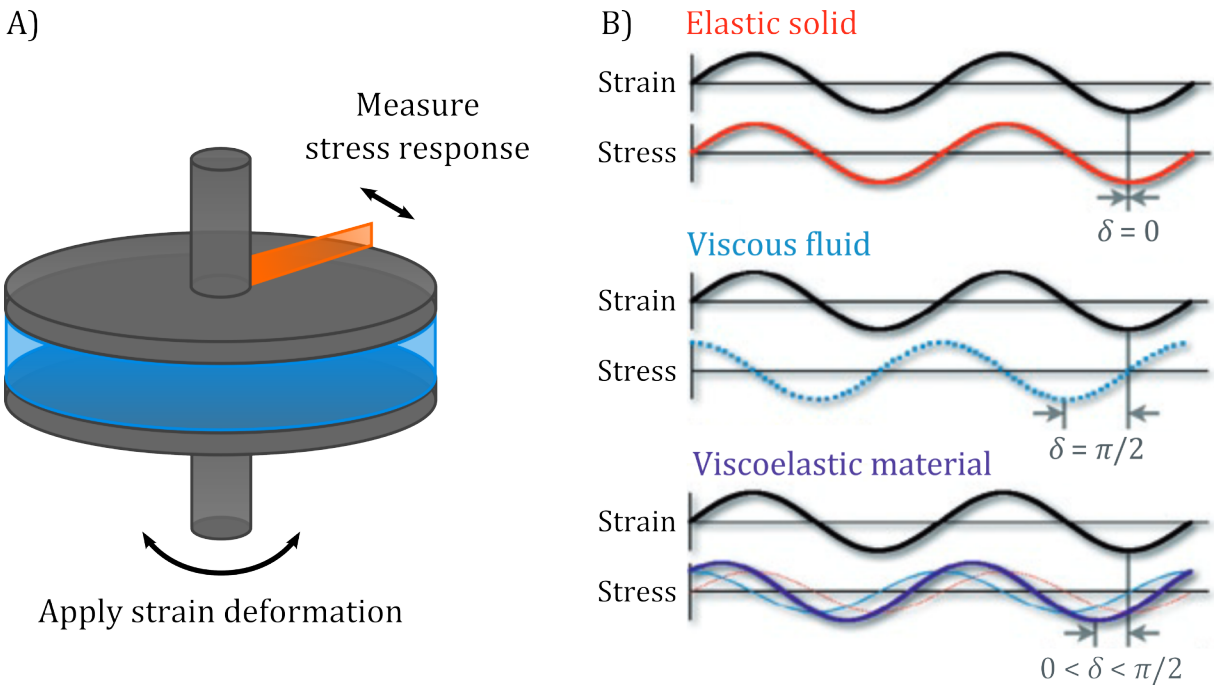

Figure 3.19: A) Schematic illustration of a strain-controlled oscillating plate-plate rheometer. The sample (blue) is loaded between the two plates (grey). An oscillatory strain is applied and the stress response of the sample is measured. **B)** Schematic representation of the stress response to an applied oscillatory strain for an elastic solid, a viscous fluid and a viscoelastic material. Modified from *Weitz et al.*[139]

For this, the specimen is placed between the two rheometer plates. A time-dependent sinusoidal shear deformation $\gamma(t)$ (see eq. 3.9) is induced in the specimen – by rotating the lower plate

with a motor, while the upper plate remains stationary – and the resulting stress response is measured (see fig. 3.19, A).[139]

$$\gamma(t)=\gamma_0 \sin(\omega t) \tag{3.9}$$

Here, ω is the oscillation angular frequency of the shear deformation and determines the probed time scale t. The time-dependent stress response $\sigma(t)$ is measured by calculating the torque that the specimen exerts on the upper plate. Schematic stress responses − of materials with different mechanical behavior to oscillatory strain deformation − at a single frequency are shown in figure 3.19, B. In case of elastic solids, the applied sinusoidal strain and the measured stress are exactly in phase, while in viscous liquids strain and stress are out of phase with a phase angle δ of $\pi/2$. For viscoelastic materials, the stress response lies between that of elastic solids and viscous liquids. Here, strain and stress are out of phase with a phase angle $0 < \delta < \pi/2$. The frequency-dependent viscoelastic behavior of the material is defined by the storage modulus $G'(\omega)$, describing the elastic contribution and the loss modulus $G''(\omega)$, describing the viscous dissipation. Using equation 3.7 for the elastic part and equation 3.8 for the viscous part, leads to the following relationship for the time-dependent stress response $\sigma(t)$ of a viscoelastic sample to a sinusoidal strain deformation (see eq. 3.9),[139]

$$\sigma(t)=G'(\omega)\gamma_0 \sin(\omega t)+G''(\omega)\gamma_0 \cos(\omega t) \tag{3.10}$$

where $G'(\omega)$ and $G''(\omega)$ can be written as:[142]

$$G'(\omega)=E=\frac{\sigma_0}{\gamma_0}\cos(\delta) \tag{3.11}$$

$$G''(\omega)=\eta\omega=\frac{\sigma_0}{\gamma_0}\sin(\delta) \tag{3.12}$$

Consequently, the storage modulus $G'(\omega)$ and the loss modulus $G''(\omega)$ of a viscoelastic material can be calculated by means of oscillatory rheometry via the preset strain γ_0, the subsequently measured stress response σ_0 and the phase angle δ.[142]

Experimental Procedure

Bulk rheology measurements of actin networks were performed using a strain-controlled oscillatory rheometer (Kinexus ultra+ Rheometer) with a plate-plate (r = 10 mm) geometry. The plates were cleaned with ultrapure water and ethanol before loading the sample. G-actin (19 µM) solutions in presence and absence of α-actinin and HMM (sample volume 125 µL) were polymerized for at least 30 min, as described in chapter 3.2.2, between the two rheometer plates with an adjusted gap distance of 300 µm. In order to investigate actin-HMM networks in active state, ATP (2 mM) was added and measurements were performed after 30 min of incubation. To prevent evaporation, a solvent trap with a reservoir filled with F-buffer (see chpt.3.2.1) was used. For rheometer experiments, the maximum applied strain was set at 1% to ensure that the measurements were performed in the linear viscoelastic regime. The frequency-dependent storage modulus $G'(f)$ and loss modulus $G''(f)$ were determined in the frequency range of 0.005 Hz to 4 Hz. Measurements and data analysis were done with the RSPACE SOFTWARE of the manufacturer of the rheometer *Malvern Panalytical.*

3.3.7 Atomic Force Microscopy

Atomic force microscopy (AFM) is a type of scanning probe microscopy (SPM), invented by *Binning*, *Quate* and *Gerber* in 1986 and is based on the principle of measuring forces exerted from a sample on a measuring probe, the so-called cantilever, during its approach to the sample.[143] This technique allows the investigation of surface topography with nanometer resolution by mechanical sensing, as well as the analysis of mechanical properties of a sample by local indentation. AFM measurements can be performed under different operating conditions. For example under ambient conditions, as well as in ultrahigh vacuum and – in contrast to other high resolution scanning techniques, like electron microscopy – measurements can also be carried out in liquid and are independent on the electrical conductivity of the specimen.[144–146] In comparison to super resolution microscopy techniques like STED,[120] three-dimensional projections can be generated with high resolution in axial (0.1 nm) and lateral (3 nm) direction, which, however, requires direct interaction between the sample surface and the scanning tip.[143] Due to these features, AFM has become an indispensable tool for investigations of biological samples under physiological conditions and is used in various scientific areas like surface-chemistry, solid-state physics, biophysics and other material sciences. A schematic setup and the working principle of an AFM are shown in figure 3.20.

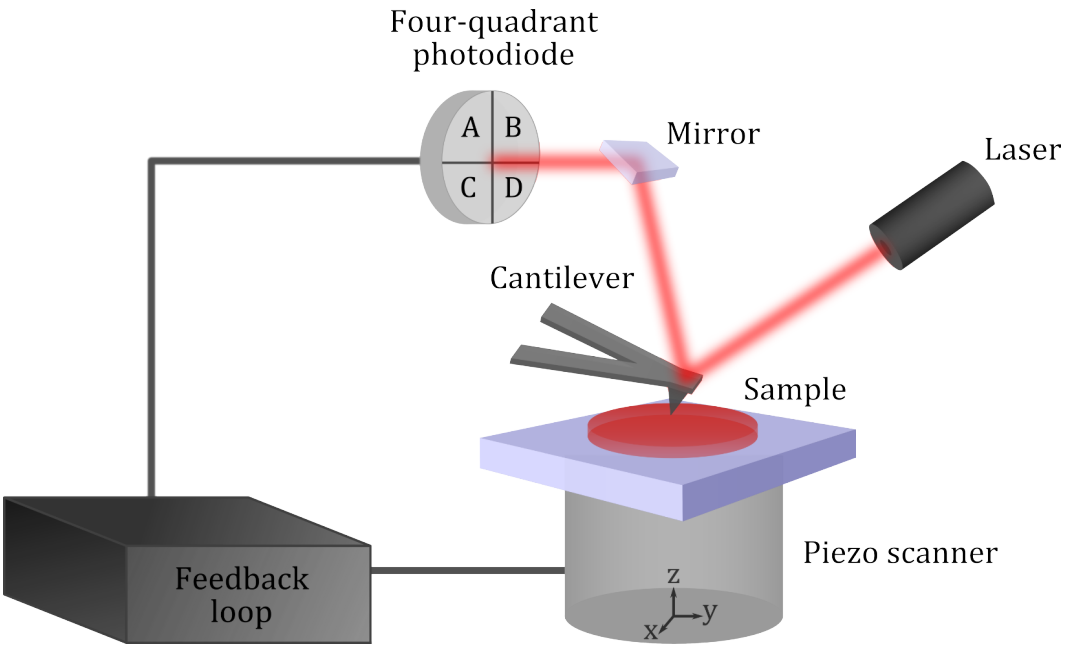

Figure 3.20: Schematic illustration of an AFM setup and its working principle according to the optical lever technique. A laser beam is reflected on the upper side of a cantilever and is directed via an adjustable mirror to a four-quadrant photodiode. The position of the signal on the photodiode controls the movement of the *z*-piezo scanner through a feedback loop.

In order to scan a sample surface, a nanometer sized sharp tip attached to the bottom side of the cantilever is moved over the surface using a piezoelectric scanner. The cantilever is approached to the surface via a *z*-piezo scanner until a pre-determined force value (the setpoint) is reached. In close contact, interactions between the tip and the surface occur, leading to bending of the cantilever, which can be detected by use of a laser beam focused on the reflective top of the cantilever (optical lever technique). By means of an adjustable mirror, the reflected laser beam is directed onto a four-segment photodetector. Due to the bending of the cantilever, vertical and lateral deflections are generated, leading to a changing position of the reflected laser beam on the four-quadrant photodiode. The vertical deflection A_{vert} can be calculated through photocurrent intensity changes of the single photodiode quadrants using the following equation.

$$A_{\mathrm{vert}} = \frac{I(A+B) - I(C+D)}{I(A+B) + I(C+D)} \tag{3.13}$$

The lateral deflection can be calculated in a similar way. The position of the resulting difference signal on the photodiode is used to control the movement of the piezoelectric scanner through a feedback loop. In brief, the feedback loop compares the actual measured value with a fixed value for the cantilever deflection, so-called setpoint, and corrects the *z*-piezo movement accordingly in order to keep the cantilever tip at a constant force. By controlling the *z*-position of the cantilever and scanning the sample surface in *x*-*y*-direction, a 3D projection is obtained.[144,147]

AFM Force Cycle Experiments

In addition to topographical imaging, the AFM also enables measurements of forces at microscopic level, which can be represented as a function of the distance between the cantilever tip and the sample, so-called force-distance curves (FDCs). FDCs are obtained by pushing the cantilever tip with a defined force onto the specimen and then removing the tip. The recorded deflection of the cantilever Z_{c} is converted into a force F by multiplication with the spring constant k_{c} of the cantilever according to *Hook's* law.[148]

$$F = k_{\mathrm{c}} Z_{\mathrm{c}} = \frac{E\, w_{\mathrm{c}} t_{\mathrm{c}}^{\,3}}{4 L_{\mathrm{c}}^{\,3}} Z_{\mathrm{c}} \tag{3.14}$$

Mechanical properties of the cantilever are mainly determined by its spring constant k_c, which depends on the *Young's* modulus E, the width w_c, the thickness t_c and the length L_c of the cantilever as shown in equation 3.14. Here, a rectangular geometry of the cantilever is assumed.[148] The most common procedure to calculate the spring constant of the cantilever is the thermal noise method, described by *Butt* and *Jaschke et al.*[148,149] and based on the theory of *Hutter* and *Bechhoefer et al.*[150] Here, the cantilever is modeled as a harmonic oscillator. For the practical determination of k_c, a force curve is recorded on an incompressible surface in order to calculate the sensitivity of the photodiode as a function of the deflection of the cantilever (voltage change of the photodiode per nanometer deflection). Afterwards, a thermal noise spectrum of the cantilever is recorded and fitted at the resonance frequency using a *Lorentzian* curve. Following integration of the *Lorentzian* curve gives the mean square deflection of the cantilever tip $\langle \Delta Z_c^2 \rangle$ at the first oscillation mode. Using the equipartition theorem, the spring constant of the cantilever is given by the following equation:

$$k_c = \beta \frac{k_B T}{\langle \Delta Z_c^2 \rangle} \tag{3.15}$$

Here, β is a correction factor, with a value of 0.971 for the first vibration mode of cantilever with a rectangular geometry, k_B is the *Boltzmann* constant and T the absolute temperature.[148] According to *Hook's* law, the determined spring constant can be used to calculate the force exerted by the sample on the cantilever (see eq. 3.14). A typical force-distance curve obtained for hard samples as well as a typical force-indentation curve received for soft samples – where the cantilever penetrates into the sample – are shown in figure 3.21.

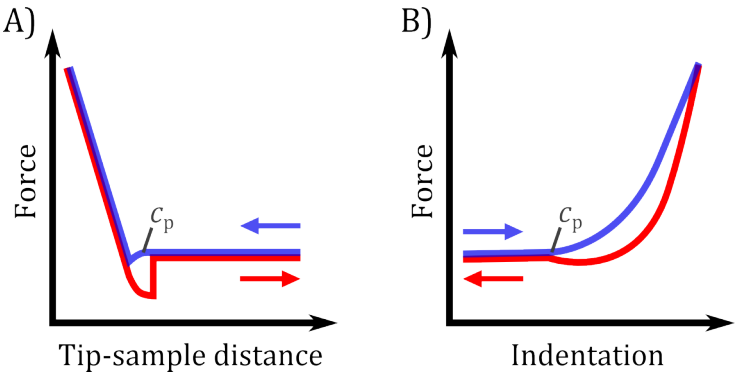

Figure 3.21: A) Schematic representation of a force-distance curve obtained by approaching and retracting a cantilever tip on a hard sample. **B)** Schematic representation of a force-indentation curve obtained by approaching and retracting a cantilever tip on a soft sample. The approach curve is shown in blue and the retraction curve in red. At the contact point c_p the cantilever tip is attached to the sample surface.

As long as the cantilever tip is not in contact with the sample, no forces – except for hydrodynamics – act on the cantilever and the plot of the force against the tip-sample distance shows a constant. Approaching the cantilever close to the sample often leads to a snap on effect, due to tip-sample interaction. As soon as the tip is attached to the surface at the contact point c_p, the cantilever is pushed upwards and a sharp linear increase of the FDC can be seen for hard samples until the set maximum force is reached (see fig. 3.21, A). For soft samples, however, so-called indentation occurs in the contact regime, because the cantilever penetrates into the specimen after reaching the contact point. This leads to a curvature of the force indentation curve (see fig. 3.21, B). Withdrawal of the cantilever results in a similar course of the curve, as when it is approached. Differences in the retraction curve can be attributed on the one hand to adhesive forces between the molecules of the tip and the sample, leading to a snap off effect of the cantilever (see fig. 3.21, A). On the other hand, a hysteresis can be observed, due to hydrodynamic resistance during measurements in liquid environment, as well as due to viscoelastic deformation of the sample in the contact regime (see fig. 3.21, B). With increasing tip-sample distance, the cantilever returns to its equilibrium position.[148]

Experimental Procedure

AFM indentation experiments on isolated apical cell cortices were performed applying a NanoWizard 4. In order to localize intact apical cell cortex fragments with a BX 51 upright epifluorescence microscope, the actin cortex was stained using LifeAct®-TagGFP, which is proclaimed to be non-toxic and to not interfere with actin dynamics.[151] A BioMat™ workstation was utilized as shuttle station between epifluorescence microscopy and AFM. For this, intact apical cell cortices were localized using fluorescent microscopy and the BioMat™ workstation enabled AFM indentation experiments at the same position of these localized intact apical cell cortices. Nanoindentation experiments were done using MLCT-cantilever (k_{nom} = 0.01 N/m), whose corresponding spring constant was determined before each measurement as aforementioned by the thermal noise method according to *Butt and Jaschke et al.*[148,149] based on the theory of *Hutter and Bechhoefer et al.*[150] Force-indentation curves were recorded with a constant velocity of 5 µm/s and a force setpoint of 0.5 nN. Maps of force-indentation curves with a lateral resolution of about 170 nm x 170 nm were recorded before and after addition of ATP (7 mM) or CytD (10 µM). More details concerning the preparation procedure can be found in chapter 3.2.4. Data analysis of the obtained force-indentation curves was performed using a JPK DATA PROCESSING SOFTWARE from the manufacturer of the AFM (*JPK Instruments*) and a

MATLAB script written by *I. P. Mey* (Institute of Organic and Biomolecular Chemistry of the University of Göttingen, Germany) and *A. Janshoff* (Institute of Physical Chemistry of the University of Göttingen, Germany). Data evaluation is described in more detail in chapter 3.4.2.

3.4 Data Evaluation

In this work the frequency-dependent viscoelastic behavior of artificial actin networks in different bottom-up model systems (see chpt. 3.2.2 and 3.2.3) was investigated. For this purpose, video particle tracking (VPT) microrheology was applied as described in chapter 3.3.2 and 3.3.5. Furthermore, in a top-down approach the mechanical properties as well as network architecture of apical cell cortices (see chpt. 3.2.4) were analyzed. The viscoelasticity of the apical cell cortices was studied by means of AFM indentation experiments (see chpt. 3.3.7) and their mesh size was determined from STED images (see chpt. 3.3.4). The corresponding evaluation of the data is described in the following.

3.4.1 Video Particle Tracking based Microrheology of F-actin Networks

Video particle tracking (VPT) is a passive microrheology method widely used in literature to investigate the frequency-dependent rheology of soft matter. For this purpose, tracer particles are incorporated in the probed material. The thermal fluctuations, responsible for *Brownian* motion of these particles, are recorded videographically and tracked by an algorithm. According to the fluctuation-dissipation theorem these fluctuations are connected − in equilibrium − to the material response in a predictable way. In an ergodic system, the generalized *Stokes-Einstein* equation connects the fluctuation's mean squared displacement with the shear modulus of the surrounding viscoelastic medium. Consequently, rheological properties can be calculated from the probe resistance, whereby the involved energies ($k_B T$) are very low and deformations remain in the linear viscoelastic regime, because no external stress is applied.[152] In this work the local viscoelasticity of 3D and 2D artificial F-actin networks (see chpt. 3.2.2 and 3.2.3) was examined. A schematic overview of a VPT measurement and the corresponding evaluation path is shown in figure 3.22.

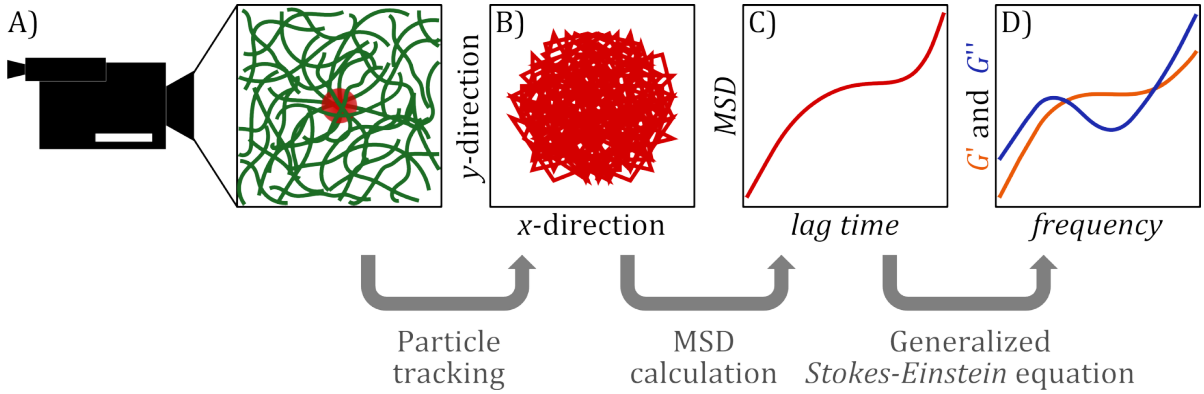

Figure 3.22: Schematic overview of video particle tracking (VPT) microrheology. **A)** Schematic illustration of a VPT measurement. Time series of a microsphere (red) embedded in an actin network (green) are recorded with a camera. **B)** The trajectory of the microsphere in *x*-*y*-direction is determined via a tracking algorithm. **C)** The mean square displacement (MSD, red line) of the microsphere is calculated. **D)** The generalized *Stokes-Einstein* equation is used to determine the frequency-dependent viscoelastic moduli of the actin networks. G' (orange line) is the storage modulus and G'' (blue line) the loss modulus.

Here, time series of thermally driven microspheres embedded in a homogeneous actin network were recorded with a camera (see fig. 3.22, A) and analyzed using a MATLAB script written by *M. Kilfoil*,[122] which is based on theory of *Weitz et al.*[123] and the tracking algorithm of *J. Crocker*.[123] In short, the position of the thermally fluctuating particles was tracked according to *Crocker's* tracking algorithm[123] to obtain the corresponding trajectories in the *x*-*y*-plane (see fig. 3.22, B). Trajectories with major artefacts, such as abrupt jumps or large changes in position over the time, were rejected since they would violate the requirement for ergodicity of the MSD. From the microsphere trajectories the mean square displacement $\langle \Delta x^2(\tau) \rangle$ (MSD, see fig. 3.22, C) was determined as an average of time,

$$\langle \Delta x^2(\tau) \rangle = \sum_i \left(x_i(t+\tau) - x_i(t) \right)^2 \tag{3.16}$$

where τ is the lagtime and i is the index of the time. Here, it is assumed that properties of the material do not change over time.[153] Tracer particle in a viscous fluid undergo normal diffusion, whereby the MSD $\langle \Delta x^2(\tau) \rangle$ is proportional to the number of dimensions N, the diffusion coefficient D and the lagtime τ.[154,155]

$$\langle \Delta x^2(\tau) \rangle = 2\,N D \tau \tag{3.17}$$

The diffusion coefficient D of a microsphere with the thermal energy $k_B T$ and the radius r immersed in a *Newtonian* fluid with a dynamic viscosity η can be described using the *Stokes-Einstein* equation, which is based on the fluctuation-dissipation theorem.[152]

$$D = \frac{k_B T}{6\pi\eta r} \tag{3.18}$$

In brief, the fluctuation-dissipation theorem states that the response of an equilibrium system to a minor external disturbance is equivalent with its response to a spontaneous fluctuation. In case of the *Stokes-Einstein* equation (see eq. 3.18), the random thermal fluctuation force of a particle in a viscous liquid − mirrored in D − and its dissipative frictional drag force due to the probe resistance− mirrored in $1/6\pi\eta r$ − have the same origin.[152,156] More complex materials, however, often show viscoelastic properties dominated by viscous or elastic behavior, depending on the time scale of the experiment. The *Brownian* motion of microspheres embedded in a viscoelastic medium strongly depend on the stiffness of the local microenvironment. Therefore, an important prerequisite for VPT microrheology is that the medium around the microsphere can be treated as a continuum. In continuum mechanics, two requirements must be satisfied. On the one hand, the material must contain sufficient micro-structural elements, like molecules, to behave in the same way at the micro-scale as at the macro-scale. On the other hand, the size of the incorporated particles must be larger than characteristic length scales of the material, such as its mesh size.[152] The MSD of particles within complex materials follows a power law described by the diffusive exponent α.

$$\left\langle \Delta x^2(\tau) \right\rangle \sim \tau^{\alpha} \tag{3.19}$$

A diffusive exponent of $\alpha = 1$ describes normal diffusion of a microsphere in a viscous fluid, while the particle undergoes sub-diffusion if $\alpha < 1$ and super-diffusion if $\alpha > 1$.[157] Here, the MSD of the microsphere trajectory was calculated as a time average (see eq. 3.16) and as an ensemble average, if multiple particles were tracked. The obtained MSD of the tracer particles was fitted using a local polynomial function of second-degree, which in turn was applied to determine the frequency-dependent complex shear modulus $G^*(\omega)$.[123] In order to optimize the fit to the MSD, single data points with artefacts (due to camera noise, inertia effects, drift processes or sudden drops of the beads) at the beginning or end of the measurement were carefully sorted out. The complex shear modulus quantifies the viscoelastic properties, by

reflecting different structural relaxation modes of the viscoelastic material occurring at different time scales. $G^*(\omega)$ can be separated in a real part and an imaginary part.[152]

$$G^*(\omega) = G'(\omega) + i\,G''(\omega) \tag{3.20}$$

Here, the storage modulus $G'(\omega)$ describes the elastic contribution and the loss modulus $G''(\omega)$ the viscous contribution of a viscoelastic material. In order to determine the complex shear modulus, the correspondence principle is used. This principle solves problems in continuum-mechanics in the linear response regime and is valid for incompressible viscoelastic materials, which are spatially isotropic and homogeneous. In short, the correspondence principle enables to obtain time-transformed linear viscoelastic flows around the microsphere from analogous solutions of elastic displacement field equations and viscous flows, by replacing the elastic shear modulus G and the viscosity η with the complex shear modulus $G^*(\omega)$ and the complex viscosity $\tilde{\eta}(\omega)$.[152] More details are given in literature by *Furst* and *Squires*,[152] *Nöding*[153] and *Gardel*.[157] In brief, viscoelastic moduli were calculated from the MSD of the microspheres, by using the generalized *Stokes-Einstein* equation (see fig. 3.22, D), which provides the relationship between the *Laplace* transform of the MSD $\langle \Delta\tilde{x}^2(s) \rangle$ and the complex viscosity $\tilde{\eta}(s)$,

$$\langle \Delta\tilde{x}^2(s) \rangle = \frac{N k_B T}{3\pi r s^2 \tilde{\eta}(s)} \tag{3.21}$$

whereby s is an expression of the frequency parameter in the *Laplace* domain. The complex viscosity $\tilde{\eta}(s)$ can be connected to the shear modulus $\tilde{G}(s)$,

$$\tilde{G}(s) = s\tilde{\eta}(s) \tag{3.22}$$

which leads together with equation 3.21 to the following relation between the shear modulus $\tilde{G}(s)$ and the MSD $\langle \Delta\tilde{x}^2(s) \rangle$:[153]

$$\tilde{G}(s) = \frac{N k_B T}{3\pi r s \langle \Delta\tilde{x}^2(s) \rangle} \tag{3.23}$$

Transformation in the *Fourier* space with $s = i\omega$ gives a relation between the frequency-dependent complex shear modulus $G^*(\omega)$ and the *Fourier* transform of the MSD $\langle \Delta\tilde{x}^2(\omega) \rangle$:[153]

$$G^*(\omega) = \frac{N k_B T}{3\pi r i\omega \langle \Delta \tilde{x}^2(\omega) \rangle} \tag{3.24}$$

Due to the fact, that the *Fourier* transform evaluation is non-trivial − because of a finite number of data points recorded during the VPT experiment and the non-convergent *Fourier* integral – an alternative form of the generalized *Stokes-Einstein* equation was used,[153] which was derived by *Dasgupta et al.*[123] and relies on a method established by *Mason et al.*[158] This results in the following relationships for the viscoelastic moduli:[153]

$$G^*(\omega) = \frac{N k_B T}{3\pi r \Gamma\left[1+\alpha(\omega)\right]\left[1+\frac{\beta(\omega)}{2}\right]} \frac{1}{\left\langle \Delta x^2\left(\frac{1}{\omega}\right)\right\rangle} = \frac{A}{\left\langle \Delta x^2\left(\frac{1}{\omega}\right)\right\rangle} \tag{3.25}$$

$$G'(\omega) = G^*(\omega)\left[\frac{1}{1+\beta'(\omega)}\right]\cos\left[\frac{\pi\alpha'(\omega)}{2} - \beta'(\omega)\alpha'(\omega)\left(\frac{\pi}{2}-1\right)\right] = G^*(\omega)B \tag{3.26}$$

$$G''(\omega) = G^*(\omega)\left[\frac{1}{1+\beta'(\omega)}\right]\sin\left[\frac{\pi\alpha'(\omega)}{2} - \beta'(\omega)\left(1-\alpha'(\omega)\right)\left(\frac{\pi}{2}-1\right)\right] = G^*(\omega)C \tag{3.27}$$

Here, $\alpha(\omega)$ and $\beta(\omega)$ are first and second order log-time derivatives of a local polynomial function obtained from a fit of the MSD against the lagtime. $\alpha'(\omega)$ and $\beta'(\omega)$ are first and second order log-time derivatives of a local polynomial function received by fitting the complex shear modulus against the frequency.[123]

In order to interpret the obtained frequency-dependent viscoelastic moduli of the F-actin networks, the theory of semiflexible polymers introduced by *Gittes*, *MacKintosh*[159] and *Morse*[160,161] was used. In short, the elastic response of semiflexible polymers, such as filamentous actin, to an external strain results from the stretching of the filaments, which can be treated like entropic springs.[153] A schematic illustration of typical curves of the frequency-dependent viscoelastic moduli of semiflexible F-actin networks is shown in figure 3.23.

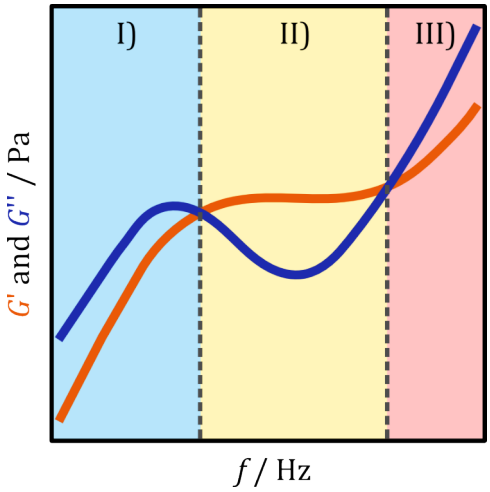

Figure 3.23: Schematic illustration of the frequency-dependent viscoelastic moduli of entangled F-actin networks. G' (orange line) is the storage modulus and G'' (blue line) the loss modulus. Three different frequency regimes can be distinguish: **I)** The low frequency regime (light blue), in which actin behaves like a liquid and filaments diffuse along their contour length. **II)** The intermediate frequency regime (light yellow), in which the network behaves like an elastic solid due to filament entanglement. **III)** The high frequency regime (light red), in which actin behaves again more liquid like and which is dominated by single filament bending modes.

Here, three different frequency regimes can be distinguish: the low, intermediate and high frequency regime. Within the low frequency regime (see fig. 3.23, I) F-actin networks behave like a viscous fluid, due to translational diffusive motions of the filaments along their own contour length, so-called reptation, which occurs on the time scale of seconds.[162,163] In this regime, the loss modulus G'' passes a maximum, while the storage modulus G' increases monotonously. *Bausch* and coworkers associated the maximum of G'' with energy dissipation, due to local stress releases caused by the diffusing filaments.[164,165] In the intermediate frequency regime (see fig. 3.23, II) actin meshworks behave like an elastic solid, since filament entanglements act as cross-links on these time scales. Here, G'' passes a minimum and G' reaches a plateau, characterized by the so-called plateau modulus G_0, which reports the stiffness of the system.[163,166] G_0 is determined at the minimum of G''.[54] The high frequency regime (see fig. 3.23, III) is dominated by single filament bending modes and actin networks behave again more like a liquid. The storage and loss modulus exhibit a typical ¾ power law scaling, which results from the bending of the single filaments and was observed in various studies.[167–170] More details can be found in the dissertation of *Nöding*.[153]

3.4.2 AFM Indentation Experiments of Isolated Apical Cell Cortices

– The theory in this chapter has been published in "Viscoelasticity of native and artificial actin cortices assessed by nanoindentation experiments" by H. Hubrich, I. P. Mey, B. R. Brückner, P. Mühlenbrock, S. Nehls, L. Grabenhorst, T. A. Oswald, C. Steinem and A. Janshoff, Nano Lett. ***2020****, 20 (9), 6329–6335.*[171] *–*

In order to investigate viscoelastic properties of cellular cortices, isolated apical cell cortices derived from MDCK II cells were transferred onto a porous substrate (see chpt. 3.2.4 and characterized by means of AFM indentation experiments (see chpt. 3.3.7). The data of the force indentation can be used, as described in the following section, to calculate mechanical parameters of the pore-spanning apical cell cortices. A schematic illustration of an AFM indentation experiment as well as of parameters, which are important for the evaluation – assuming the indentation of a planar, circular pore-spanning cortex with a cylindrical, flat punch – are shown in figure 3.24.

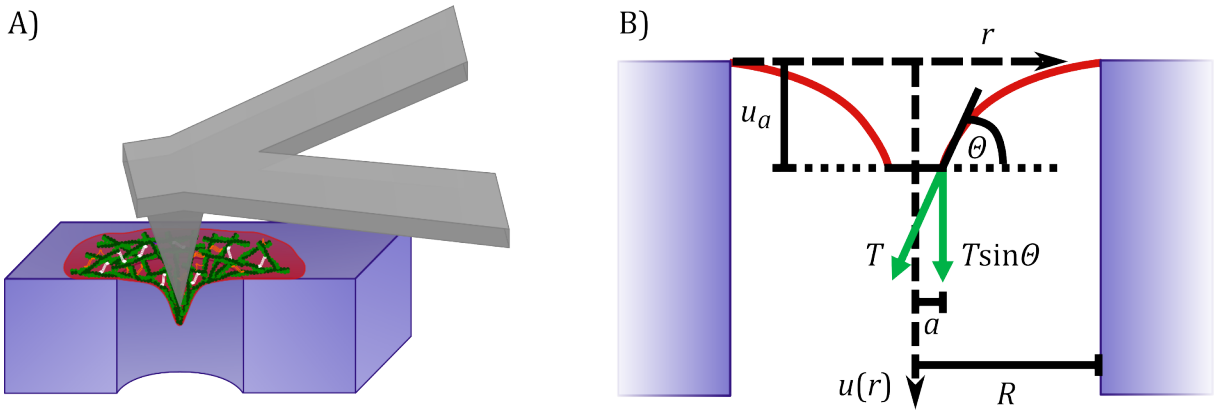

Figure 3.24: Overview of an AFM indentation experiment. **A)** Schematic illustration of an AFM indentation experiment of a pore spanning apical cell cortex with a conical indenter (grey). F-actin is shown in green, myosin motors in white, various cross-linkers in orange and the cell membrane in red. **B)** Schematic illustration of important parameters for the evaluation of the indentation of a flat punch into a flat circular cell cortex. Modified from *Hubrich et al.*[171]

In short, it is assumed that the resorting force upon indentation depends on the lateral tension of the cell membrane. Based on membrane theory, the contour of the membrane can be described as a function of the indentation depth.[5] The corresponding fitting function allows to determine the pre-stress T_0, the area compressibility modulus K_A^0 as well as the power law exponent β

(fluidity) of the cell cortices from experimental force indentation curves.[5,171] To determine the force response of the free-standing viscoelastic cell cortices, the following assumptions were made to simplify theoretical treatments: I) neglect of bending as well as shearing contributions to the energy function[172] and II) modelling of the indenter as a cylindrical flat punch with a radius a in the nanometer range, which represents the radius of the cantilever tip, close to a point load force (see fig. 3.24, B). More detailed descriptions on the solutions of the elastic case can be found in literature.[5,171] In principle, minimizing the energy is equivalent to identifying the minimal surface of the indented apical cell cortices. The corresponding force response f of an elastic pore-spanning apical cell cortex upon indentation is then in a first approximation:

$$f = 2\pi RT \frac{u(R)'}{\sqrt{1+u(R)'^2}} \tag{3.28}$$

whereby R is the pore radius and $u(R)'$ the spatial derivative of the membrane contour at the position $r = R$. The tension T of the membrane, which builds up with increasing area A_n during indentation can be written as:

$$T = T_0 + K_A \frac{A_n - A_0}{A_0} \tag{3.29}$$

Here, T_0 is the pre-stress, K_A the area compressibility modulus and A_0 the area before indentation, in this case simply $A_0 = \pi R^2$. The pre-stress T_0 of the pore-spanning apical cell cortex partly arises due to differences in chemical potential between the negatively charged plasma membrane adhering to the positively charged pore rim and the free-standing membrane, while T_0 in living cells reflects the contraction of the actomyosin network under consumption of ATP.[5,173] In order to account for in-plane stretching of the plasma membrane during indentation, the actual area A_n needs to be calculated as a function of the indentation depth u_a, which is the distance between the tip of the punch and the pore rim. The exact shape of the non-contact region corresponds to a catenoid, as this provides the required minimal surface between the radii R and a (see fig. 3.24, B). In order to calculate A_n by means of an analytically solvable surface integral, an approximation is used, which allows small indentation depths to be described with sufficient accuracy.

$$A_{\mathrm{n}} = \pi a^2 + 2\pi \int_a^R r \sqrt{1 + \left(\frac{u_{\mathrm{a}}}{r \ln\left(\frac{a}{R}\right)} \right)^2} \, \mathrm{d}r \tag{3.30}$$

It is assumed that viscoelasticity results from the time dependence of the area compressibility modulus $K_{\mathrm{A}}(t)$, which can be described best by a general power law representing the large distribution of relaxation times resulting from multiple transient actin cross-links in the cell cortices.

$$K_{\mathrm{A}}(t) = K_{\mathrm{A}}^0 \left(\frac{t}{t_0} \right)^{-\beta} \tag{3.31}$$

The power law exponent β is a description of the flow behavior in dependence on the relaxation time and in the range of $0 \leq \beta \leq 1$, whereby $\beta = 0$ describes an ideal elastic solid and $\beta = 1$ a *Newtonian* fluid. The time t_0 is set arbitrarily to 1 s. This results in the following relation for the time-dependent tension $T(t)$ under the assumption of the elastic-viscoelastic-correspondence principle:

$$T(t) = T_0 + \int_0^t K_{\mathrm{A}}^0 \left(\frac{t-\tau}{t_0} \right)^{-\beta} \frac{\partial}{\partial \tau} \left(\frac{A_{\mathrm{n}}(\tau) - A_0}{A_0} \right) \mathrm{d}\tau \tag{3.32}$$

It can be assumed that the contour of the membrane during indentation is identical to the contour of the elastic case, because the viscoelasticity of the plate only influences the in-plane area compressibility modulus. Thus, the force $f(t)$ that acts on the flat punch − or more precisely the cantilever tip of the AFM − during the approach with a constant velocity v_0 can be written as:

$$f(t) = 2\pi R T(t) \frac{u(R)'}{\sqrt{1 + u(R)'^2}} \approx 2\pi R T(t) u(R)' = 2\pi T(t) \frac{v_0 t}{\ln\left(\frac{a}{R}\right)} \tag{3.33}$$

whereby the indentation depth is $u_{\mathrm{a}} = v_0 t$. The insertion of equation 3.32 in equation 3.33 leads to the following expression for the force $f_{\mathrm{app}}(t)$ acting on the cantilever tip of the AFM during the approach:

$$f_{\mathrm{app}}(t)=2\pi T_0\frac{v_0 t}{\ln\left(\frac{a}{R}\right)}+2\pi\frac{v_0 t}{\ln\left(\frac{a}{R}\right)}\int_0^t K_{\mathrm{A}}^0\left(\frac{t-\tau}{t_0}\right)^{-\beta}\frac{\partial}{\partial\tau}\left(\frac{A_{\mathrm{n}}(\tau)-A_0}{A_0}\right)\mathrm{d}\tau \tag{3.34}$$

Substitution of $A_{\mathrm{n}}(t)$ as a function of $u_{\mathrm{a}}(t)=v_0 t$ for the indentation curve gives:

$$f_{\mathrm{app}}(t)=2\pi\frac{v_0 t}{\ln\left(\frac{a}{R}\right)}\left(T_0+\frac{2\pi}{\pi R^2}\int_0^t K_{\mathrm{A}}^0\left(\frac{t-\tau}{t_0}\right)^{-\beta}\frac{\partial}{\partial\tau}2\pi\int_a^R r\sqrt{1+\left(\frac{v_0\tau}{r\ln\left(\frac{a}{R}\right)}\right)^2}\,\mathrm{d}r\,\mathrm{d}\tau\right) \tag{3.35}$$

with $\tau=t_{\mathrm{m}}+t$. Supposing that at $t=t_{\mathrm{m}}$ indentation is reversed leads with $u_{\mathrm{a}}(t)=v_0(2t_{\mathrm{m}}-\tau)$ to the following expression for the force $f_{\mathrm{ret}}(t)$ of the retraction curve ($t>t_{\mathrm{m}}$):

$$\begin{aligned}f_{\mathrm{ret}}(t)=2\pi\frac{v_0(2t_{\mathrm{m}}-\tau)}{\ln\left(\frac{a}{R}\right)}&\left(T_0+\frac{2\pi}{\pi R^2}\int_0^{t_{\mathrm{m}}} K_{\mathrm{A}}^0\left(\frac{t-\tau}{t_0}\right)^{-\beta}\frac{\partial}{\partial\tau}2\pi\int_a^R r\sqrt{1+\left(\frac{v_0\tau}{r\ln\left(\frac{a}{R}\right)}\right)^2}\,\mathrm{d}r\,\mathrm{d}\tau\right.\\&\left.+2\pi\int_{t_{\mathrm{m}}}^t K_{\mathrm{A}}^0\left(\frac{t-\tau}{t_0}\right)^{-\beta}\frac{\partial}{\partial\tau}2\pi\int_a^R r\sqrt{1+\left(\frac{v_0(2t_{\mathrm{m}}-\tau)}{r\ln\left(\frac{a}{R}\right)}\right)^2}\,\mathrm{d}r\,\mathrm{d}\tau\right)\end{aligned} \tag{3.36}$$

Equation 3.35 and 3.36 were used as fitting functions for the approach and retraction curves of experimental force indentation curves to calculate the pre-stress T_0, the area compressibility modulus K_{A}^0 as well as the power law exponent β of pore-spanning cell membrane cortices. For this purpose, a MATLAB script written by *I. P. Mey* (Institute of Organic and Biomolecular Chemistry of the University of Göttingen, Germany) and *A. Janshoff* (Institute of Physical Chemistry of the University of Göttingen, Germany) was used. The script is attached in the appendix (see chpt. 7.4).

3.4.3 Mesh Size Analysis of Isolated Apical Cell Cortices

In order to determine the average mesh size of apical MDCK II cell cortex fragments, STED images were taken as described in chapter 3.3.4, subjected to an artificial retina analysis[65,174] and investigated by means of a bubble analysis.[175,176] An overview of a typical evaluation path is shown in figure 3.25.

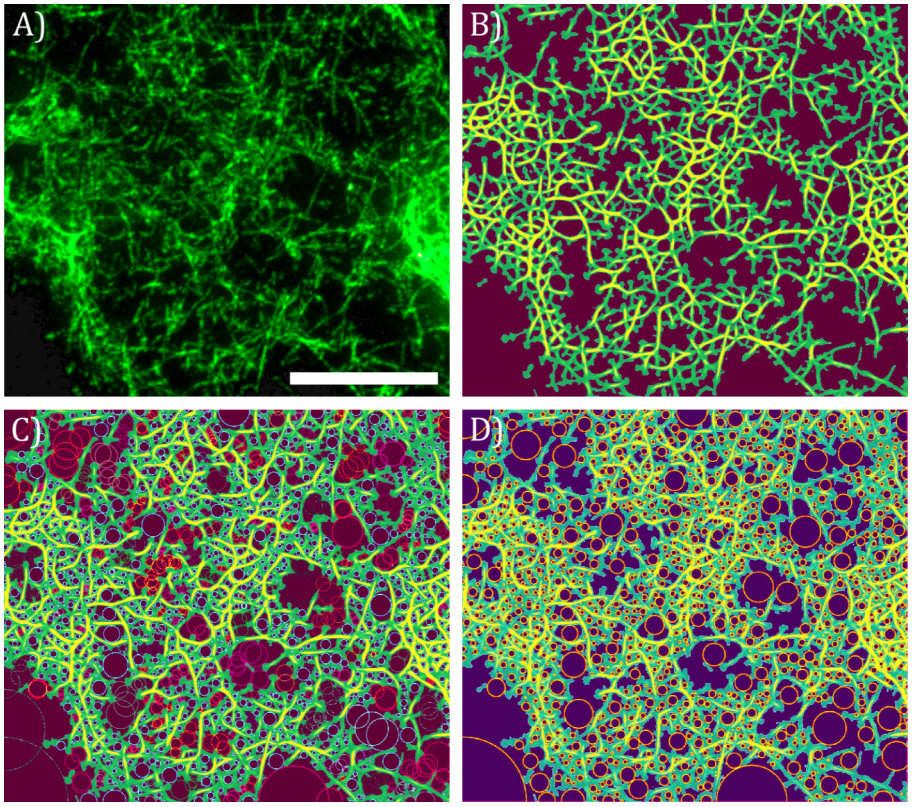

Figure 3.25: Overview of the evaluation pathway of the mesh size analysis of apical cell cortices. **A)** Exemplary STED image of apical cell cortices. F-actin was labeled with phalloidin STAR RED (here actin filaments are colored in green). **B)** The STED image was analyzed by means of an artificial retina. **C)** The mesh size was determined using a bubble analysis. For this, an *Euclidian* distance map (EDM) of the retina image was calculated. Local maxima in the EDM represent the center of the largest circle (multicolored) fitting into the mesh. **D)** In order to avoid various responses of one network pocket, overlapping circles were compared and only the largest circle (yellow) was taken to characterize the mesh size. Scale bar: 6 µm. Modified from *Hubrich et al.*[171]

The image processing by means of artificial retina was developed by *N. Dörrer* (Institute of Physical Chemistry of the University of Göttingen, Germany) and the underlying concept was described in detail by *Nöding* and *Schön et al*.[65] and by *Schön*.[177] In brief, each pixel of the STED image (see fig. 3.25, A) was classified as background or filament depending on the surrounding neighborhood of the pixels to obtain a retina image (see fig. 3.25, B) with smoother

filaments and less noise in comparison to the raw image. The retina image was used to calculate the average mesh size of the actin cortex. To achieve this, a bubble analysis − developed by *Molteni et al.*[167] and simplified by *Münster et al.*[168] − was applied, which in principle determines the largest circle that fits into the respective mesh pockets. For this purpose, an *Euclidian* distance map (EDM) of the actin cortex was calculated, which gives information about the distances of each pixel within the mesh pocket to the closest filament pixel. Local maxima within the EDM determine the centers of the largest diameter circles, which fit into the network pockets (see fig. 3.25, C). In order to avoid several responses of one pocket, overlapping circles were compared an only the circles with the largest diameter were used to characterize the mesh size of the pocket (see fig. 3.25, D). For the calculation of the EDM, as well as the determination of local maxima and comparison of overlapping circle a MATLAB script written by *I. P. Mey* (Institute of Organic and Biomolecular Chemistry of the University of Göttingen, Germany) was used, which is based on the open source code of *Münster et al.*[167] The MATLAB script can be found in the dissertation of *Schön*.[177]

4 Results and Discussion

The actin cortex is a highly complex construct, whose architecture and mechanics depend on many parameters, such as ion concentrations, pH, temperature, evaporation, measuring conditions and many more.[2,75–78,178,179] In order to characterize self-organization and viscoelasticity of native and artificial actin cortices, different bottom-up and top-down model systems were developed and analyzed as described in chapter 3.2 and 3.3.

4.1 Self-organization and Viscoelasticity of Artificial 3D Actin Networks

For a first simple mimic of the cell cortex, 3D actin networks were polymerized in a bottom-up approach – in presence of various actin binding proteins (ABPs) – between glass coverslips or rheometer plates and inside water-in-oil droplets (see chpt. 3.2.2). The self-organization and viscoelastic properties of the actin networks were investigated as a function of measurement conditions and in the presence of different ABPs.

4.1.1 Impact of the Experimental Setup on the Self-organization of Actin Networks

The viscoelasticity of actin networks strongly depends on their structure, which in turn can be influenced by several factors during the preparation and measurement procedure.[2,75–78,178,179] For artificial actin networks, the type of measuring chamber is decisive for the self-organization of actin filaments during the polymerization process. Therefore, the morphology of F-actin networks was investigated depending on the construction of the measuring chambers. For this purpose, *in vitro* actin networks were polymerized in different types of measuring chambers made of glass coverslips and double faced adhesive tape, which were further sealed with different techniques (see fig. 3.6) to prevent evaporation of the sample. F-actin was labeled with Alexa Fluor® 488-Phalloidin (AF 488-Phal) and imaged by confocal laser scanning microscopy (CLSM, see chpt. 3.3.3). An overview of the different kinds of measuring chambers used in this work and corresponding exemplary fluorescence micrographs are shown in figure 4.1.

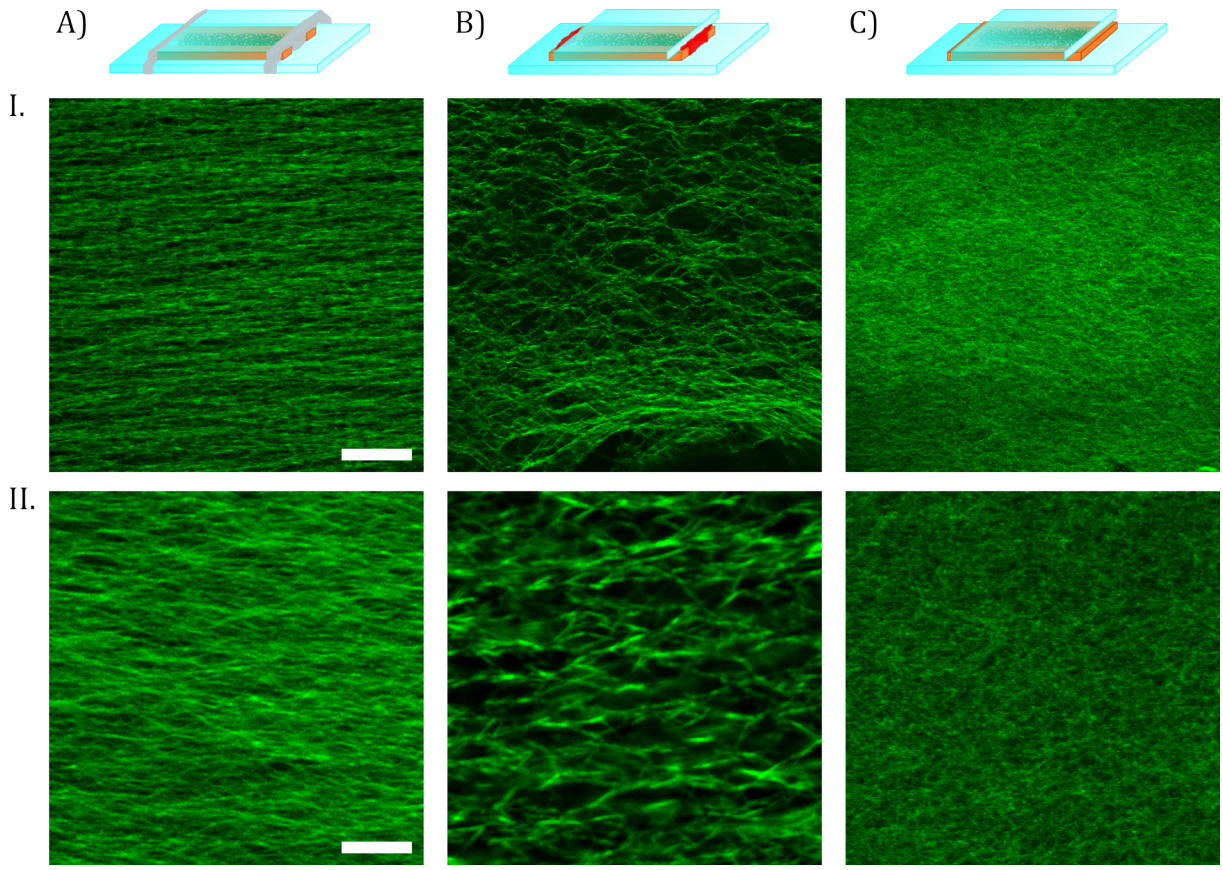

Figure 4.1: Schematic illustration of different glass chambers filled with F-actin solution and the corresponding fluorescence micrographs of the actin networks showing different network morphologies depending on the type of chambers. The glass chambers prepared by glass coverslips (cyan) and double faced adhesive tape (brown) were filled with actin solution (green) and closed in different ways. F-actin was labeled with AF 488-Phal at a concentration of c_A = 24 µM and imaged in the three different measuring chambers. **A)** Actin networks polymerized in a channel chamber closed with Parafilm® (grey) show anisotropic filament-like structures with a preferred orientation along the channel direction. **B)** Actin networks polymerized in a channel chamber closed with nail polish (red) show anisotropic bundle-like structures with a preferred orientation along the direction of the channel. **C)** If a rectangle was cut out of the double faced adhesive tape, glued onto a coverslip, filled with actin solution and closed by mounting a second coverslip on top (closed chamber), the actin networks show isotopically branched structures of filaments. Scale bars: **I.** 21 µm and **II.** 8 µm.

Depending on the type of measuring chamber and on the sealing technique, the fluorescence images of the corresponding actin networks show different morphologies. If actin was polymerized in channel chambers, an anisotropic network structure with a preferred orientation of the filaments along the channel direction was observed (see fig. 4.1, A and B) probably forced by capillary forces. The channel chambers were closed either with Parafilm® (see fig. 4.1, A) or nail polish (see fig. 4.1, B). The corresponding fluorescence micrographs show differences in fluorescence intensity of the filamentous structures, which might be due to different thicknesses of the filaments. While the networks in the chambers sealed with Parafilm® show rather thin filament-like structures (see fig. 4.1, A, I. and II.), the networks in chambers closed

with nail polish show big bundle-like structures (see fig. 4.1, B, I. and II), which is clearly visible in the magnification of the fluorescence images. The reason for the formation of bundle structures is attributed to the numerous substances contained in nail polish, such as diverse positively charged ions[180] that induce the cross-linking of several negatively charged actin filaments into a bundle.[78] The actin networks polymerized in a closed chamber − built by cutting out a rectangle from the double faced adhesive tape, sticking the constructed frame onto a glass coverslip, filling it with actin solution and closing it by mounting a second coverslip on top – show isotropic branched filament structures (see fig. 4.1, C). The preferred orientation of F-actin gels polymerized in channel chambers in contrast to actin networks polymerized in closed chambers without preferred orientations was also observed by *Schön*.[177] These spatially homogeneous and isotropic networks formed in a closed chamber are necessary for passive microrheology studies in order to fulfil the correspondence principle, which is essential for continuum mechanics (see chpt. 3.4.1).[152] Therefore, only viscoelastic properties of 3D actin networks polymerized in the closed chambers were investigated.

4.1.2 Impact of the Experimental Setup on the Viscoelastic Responses of Actin Networks

In order to investigate the frequency-dependent viscoelasticity of artificial 3D actin networks video particle tracking (VPT) based passive microrheology (PMR) was used. For this purpose, carboxylate-modified polystyrene beads ($r = 0.5$ μm) − which were found to bind weakly to actin networks and therefore react sensitively to changes in the local network stiffness[110] − were embedded in the actin gels. Tracking the beads incorporated in the F-actin network and analyzing their thermally fluctuating position allows the calculation of the local rheological properties of the network (see chpt. 3.4.1).[152] In this work, two different microscopy techniques were applied to track the beads. On the one hand, the fluorescently labeled particles were visualized via fluorescence microscopy (see chpt. 3.3.2) by recording the fluorescence light emitted by the beads. On the other hand, darkfield microscopy (see chpt. 3.3.2) – a technique, where only the scattered light from the beads is captured − was used to visualize the particles. To examine, whether the network stiffness is influenced by the different illumination used to visualize the beads, VPT measurements of different time lengths were performed with both fluorescence and darkfield microscopy and analyzed. The mean square displacements (MSDs) of the beads as well as the corresponding viscoelastic frequency spectra are shown in figure 4.2.

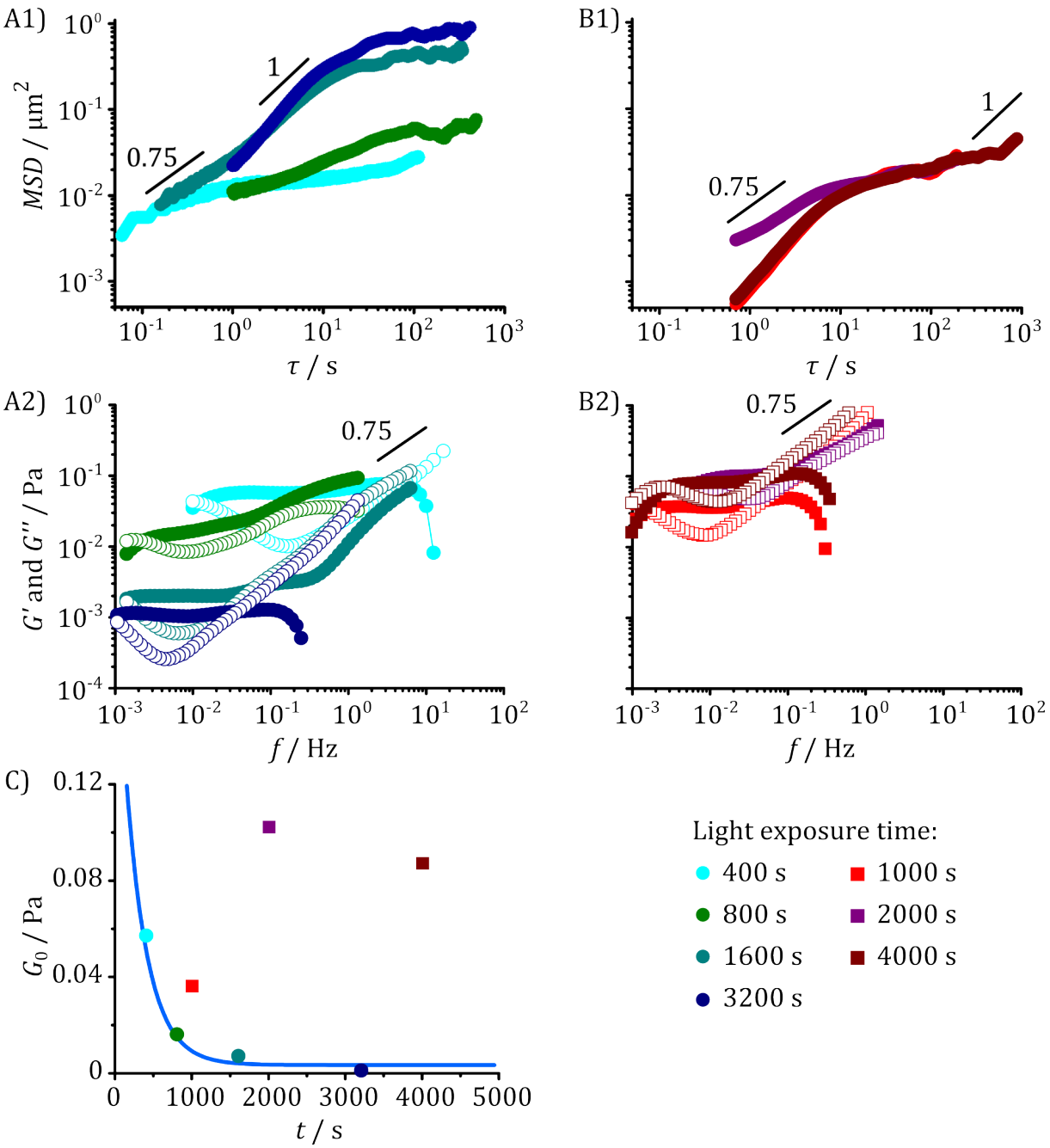

Figure 4.2: The MSD (time and ensemble averaged) and frequency-dependent viscoelastic properties of artificial 3D actin networks (c_A = 24 µM) measured with VPT using different microscopy techniques. The scaling behavior of the power law with an exponent of 0.75 and 1 are shown as black lines. **A1)** MSDs as well as **A2)** storage modulus G' (filled circles) and loss modulus G'' (open circles) of F-actin gels determined by means of VPT using fluorescent light to track tracer particles (r = 0.5 µm) at 50 fps for different time periods. Over a tracking period of 400 s (light cyan) a plateau modulus of G_0 = 57 mPa (N = 4) was determined, for 800 s (green) G_0 = 16 mPa (N = 4), for1600 s (dark cyan) G_0 = 7 mPa (N = 3) and over a period of 3200 s (blue) a plateau modulus of G_0 = 1 mPa (N = 2) was measured. **B1)** MSDs as well as **B2)** G' (filled squares) and G'' (open squares) of F-actin networks determined by VPT using the darkfield microscopy technique to track tracer particles (r = 0.5 µm) at 20 fps for different time periods. Over a tracking period of 1000 s (red) a plateau modulus of G_0 = 36 mPa (N = 3), over a period of 2000 s (purple) a modulus of G_0 = 102 mPa (N = 5) and for tracking over 4000 s (brown) G_0 = 87 mPa (N = 3) was determined. **C)** Overview of G_0 values of 3D F-actin networks measured over different time periods via VPT using fluorescence light (circles) or darkfield illumination (squares) in order to track tracer particles embedded within the networks. The solid light blue line shows the exponential fit $\left(G_0(t)=0.003+0.218\exp(-0.004t)\right)$ to the VPT data obtained via fluorescence microscopy.

MSDs of 3D Actin Networks determined by VPT Measurements using Fluorescence and Darkfield Microscopy

The time (see eq. 3.16) and ensemble averaged MSDs of beads incorporated in entangled F-actin networks (24 µM or 1 mg/mL) were calculated from the bead trajectories obtained from VPT measurements via fluorescence (see fig. 4.2, A1) or darkfield (see fig. 4.2, B1) microscopy. During evaluation, single data points with artefacts at the beginning or end of the measurement were sorted out in order to optimize the fit to the MSD, as described in more detail in chapter 3.4.1. Beads in complex materials follows a power law defined by the diffusive exponent α (see eq. 3.19). Normal diffusion of a bead within a viscous fluid is defined by a diffusive exponent of $\alpha = 1$, while sub-diffusion and super-diffusion are described by $\alpha < 1$ and diffusion $\alpha > 1$, respectively.[157] The MSDs of the 3D actin networks investigated exhibit different lagtime regimes with varying α, which will be discussed in the following.

In the low lagtime regime (τ in the range of about 10^{-1} - 10^{1} s) of the MSDs measured using fluorescence microscopy, a diffusive exponent α in the range of 0.45 to 1.27 was determined, while for MSDs measured by means of darkfield microscopy, a diffusive exponent α in the range of 0.67 to 1.22 was calculated. Thus, no significant difference between the two measuring techniques was found here. For semiflexible polymers such as F-actin a scaling behavior of ¾ is expected, due to single filament bending modes,[161,167–170,181] but in literature values for α in the range of 0.4 to 0.85 can be found.[76,182] One reason for the large deviations in the scaling behavior may be due to differences in the network properties of the entangled F-actin networks, such as the contour length L_c of the filaments. A dependency of the diffusive exponent α on L was observed by *Liu et al.* in one particle microrheology (1P-MR) measurements of entangled actin networks (24 µM) with contour length in the range of 0.5 µm to 17 µm.[182] For $L_c = 0.5$ µm a diffusive exponent of $\alpha = 0.85$ was determined, while longer filaments (2 - 17 µm) show a scaling behavior of $\alpha = 0.75$.[182] Accordingly, diffusive exponents in the range of $0.75 < \alpha < 1$ might be attributed to the presence of short filaments formed during the polymerization process or in the local environment of the tracked beads. On the other hand, super-diffusion ($\alpha > 1$) in purely entangled F-actin networks has not been observed so far and is attributed to artefacts.

At an intermediate lagtime (τ in the range of about 10^{0} - 10^{2} s) the MSDs of the beads within the entangled F-actin gels show a plateau. In case of fluorescence microscopy measurements, large variations were observed depending on the tracking time. With increasing tracking time the average movement of the beads in the plateau regime increases from about 130 nm to about 900 nm, while no dependence on the tracking time length was found for darkfield microscopy

measurements. Here, an average bead movement of 140 nm was observed. Within the intermediate lagtime regime, the motion of the beads is restricted by the entangled actin filaments. The increased bead movement with longer tracking times, in case of the fluorescence microscopy measurements, can be explained by a light-induced softening of the F-actin gels, as already observed by *Golde et al.*[178] For the plateau of the MSD of darkfield measurements a value of $1.9 \cdot 10^{-2}$ μm² was determined, which is in good agreement with literature, where values in the range of $5 \cdot 10^{-3}$ μm² to $8 \cdot 10^{-3}$ μm² were reported for actin networks with concentrations of about 0.9 mg/mL to 1.2 mg/mL.[76,181,182] The slightly higher value of the plateau of the MSD in comparison to literature might be due to in inhomogeneities of the F-actin network in the local bead environments. In contrast to the artificial systems, a much lower plateau value was observed in TC7 cells (~$5 \cdot 10^{-4}$ μm²).[183] This indicates a denser and stiffer actin cortex within living cells compared to the bottom-up approaches.

The high lagtime regime (τ in the range of 10^3 s) was only recorded for the darkfield measurement over a tracking period of 4000 s and shows a diffusive exponent of about one (see fig. 4.2, B1, brown line). This free diffusion of the beads may be due to the fact, that they were able to escape the constraints of the entangled filaments on these time scales. High lagtime regimes were hard to access using fluorescence microscopy for particle tracking. Here, the beads began to move more strongly and often drifted out of the record window, making further analysis of the data impossible. As already mentioned, the reason for this could be light-induced softening of the F-actin network, caused by the fluorescent beads, which increases with longer excitation times.[178]

Storage and Loss Moduli of 3D Actin Networks determined by VPT Measurements using Fluorescence and Darkfield Microscopy

The aforementioned MSDs of the beads incorporated in the F-actin networks (c_A = 24 μM) were used to determine the frequency-dependent complex shear modulus $G^*(f)$, which consists of a real part – so called storage modulus $G'(f)$ describing the elastic contribution – and an imaginary part – so-called loss modulus $G''(f)$ describing the viscous contribution – as described in chapter 3.4.1. The corresponding viscoelastic frequency spectra obtained by fluorescence microscopy measurements are given in figure 4.2, A2 and the spectra recorded by darkfield microscopy measurements are shown in figure 4.2, B2. According to the MSDs, low, intermediate and high frequency regimes (see fig. 3.23) can be distinguished.

The low frequency regime (f in the range of 10^{-3} Hz) is dominated by diffusive motions of the actin filaments along their contour length (reptation), which lead to local stress releases within the network and consequently to a more fluid-like behavior with $G'(f) < G''(f)$.[162–165] Reptation occurs on the time scale of seconds[162,163] and is defined by the reptation time τ_{rep}, which can be obtained from the intersection of $G'(f)$ and $G''(f)$ within the low frequency regime as reciprocal of the reptation frequency f_{rep}.[161]

$$\tau_{rep} = f_{rep}^{-1} \tag{4.1}$$

Reptation frequencies for fluorescence microscopy measurements were determined or extrapolated in a range of 0.011 Hz to 0.001 Hz (see fig. 4.2, A2) and for darkfield microscopy measurements in the range of 0.002 Hz to 0.005 Hz (see fig. 4.2, B2). The reptation frequency of semiflexible polymers is strongly dependent on the contour length L_c of the polymer.[161]

$$f_{rep} = \frac{\pi k_B T \ln\left(\frac{\xi}{d}\right)}{L_c^{\,3} 2\eta} \tag{4.2}$$

With the *Boltzmann* constant k_B of $1.38 \cdot 10^{-23}$ J/K, a temperature T of 298 K, a mesh size ξ of 300 nm (calculated according to *Schmidt et al.*[184] using $\xi[\mu m] = 0.3/\sqrt{c_A[mg/mL]}$), an F-actin diameter d of 7 nm[17], an assumed solvent viscosity η of about 1 mPa·s and actin contour lengths L_c in the range of 10 - 30 µm[10,162,185], theoretical reptation frequencies of about 0.001 - 0.024 Hz can be calculated. This is in good agreement with the experimentally determined values and clearly shows the strong dependence of the reptation frequency on the F-actin contour length with $f_{rep} \propto L_c^{-3}$ (see eq. 4.2). Also a broad range of f_{rep} values of actin filaments in entangled networks in the region of about $6 \cdot 10^{-4}$ - 0.1 Hz can be found in literature.[162,163,186] These findings imply that the self-organization and mechanics of entangled actin networks strongly depend on the preparation procedure as well as on conditions (see chpt. 4.1.1) and techniques of the measurement. In particular, the *in vitro* polymerization process is influenced by various parameters, such as temperature, pH, ion concentrations and measuring conditions.[2,75–78,178,179] Comparing the reptation frequencies obtained by fluorescence and darkfield microscopy measurements, it is noticeable that for the former method the f_{rep} values show a large scattering over a power of ten, whereas the f_{rep} values for the latter method are of the same order of

magnitude. Furthermore, a dependence of f_{rep} on the tracking time was observed in fluorescence microscopy measurements (a decrease of f_{rep} with increasing tracking time), while no dependence was found in darkfield microscopy measurements. This indicates an influence of the fluorescence illumination on the contour length of the actin filaments and thus also on the mechanical properties of the network. However, the decrease of f_{rep} with increasing tracking time cannot be explained within the thesis, because a degradation and consequently a shortening of the filaments with increasing excitation time was expected, due to light-induced softening processes,[178] which according to equation 4.2 should lead to an increase of f_{rep} with longer tracking times. As mentioned above, this frequency regime is experimentally difficult to access for actin networks, because the measurement at low frequencies takes a long time and therefore no clear evidence for filament reptation dynamics can be provided.

The intermediate frequency regime (f in the range of about 0.01 - 100 Hz) reflects time scales on which actin networks behave like elastic solids with $G'(f) > G''(f)$ due to entanglements of the filaments. Here, the loss modulus $G''(f)$ passes a minimum, while the storage modulus $G'(f)$ reaches a plateau. At the minimum of $G''(f)$, the plateau modulus G_0 can be determined,[54] which mirrors the stiffness of the actin network.[163,166] Comparing G_0 of microrheology experiments performed with fluorescence microscopy (see fig. 4.2, A2) and darkfield microscopy (see fig. 4.2, B2), a dependence of the network stiffness on the tracking time for the former method was observed, while the latter is independent. In fluorescence microscopy measurements, a decrease of G_0 with increasing excitation time (400 s up to 3200 s) from 57 mPa (mean, $N = 4$) to 16 mPa (mean, $N = 4$), 7 mPa (mean, $N = 3$) and 1 mPa (mean, $N = 2$) was measured (see fig. 4.2, C, circles). In contrast, no trend of G_0 on the excitation time was found in darkfield microscopy measurements (see fig. 4.2, C, squares). Here, tracking over 1000 s, 2000 s and 4000 s results in plateau moduli of 36 mPa (mean, $N = 3$), 102 mPa (mean, $N = 5$) and 87 mPa (mean, $N = 3$). These observations are consistent with findings of *Golde et al.*[178] They found light-induced softening of F-actin networks, probably caused by fluorescent beads. Presumably, the filaments are photochemically damaged by free radicals. In addition, they found increasing network softening with longer excitation times, as also observed in the microrheology measurements in this thesis using fluorescence imaging. *Golde et al.*[178] recommend non-fluorescent imaging techniques for microrheology experiments, which can be verified by measurements here and also by measurements performed on 2D minimal actin cortices (MACs, see chpt. 4.2.5).

Averaging the plateau moduli over all microrheology measurements leads in case of the fluorescence microscopy measurements to values of $\overline{G}_0 = (20 \pm 25)$ mPa (median: 12 mPa; $N = 13$, $n = 4$), which is in good accordance with the value $G_0 = 17$ mPa (mean, $N = 6$) determined by *Nöding*[153] for 3D actin networks (1 mg/mL) using the same microscopy technique. For the darkfield microscopy measurements an approximately four times higher value of $\overline{G}_0 = (75 \pm 35)$ mPa (median: 87 mPa; $N = 11$, $n = 3$) was calculated. This is in the same order of magnitude as plateau moduli for 3D actin networks (1 mg/mL) calculated by *Morse*[161] and *Hinner et al*[187] of about 100 mPa and supports the recommendation of *Golde et al.*[178] to use non-fluorescent imaging for microrheology experiments. *Gardel et al.*[76] measured a four times higher plateau modulus of about 300 mPa for entangled actin networks with a concentration of 1 mg/mL. Another closer look to the VPT data obtained by fluorescence microscopy measurements suggests an exponential decay of G_0 over time (see fig. 4.2, C, circles). An exponential fit to the data indicates a stiffness of the network of about 222 mPa at the time point 0 s, which is in good agreement with the aforementioned values for G_0 reported in the literature. Even higher values of the plateau modulus of actin networks (1 mg/mL) in the range of 1.5 Pa were reported by *Palmer et al.*[169] The variation of the reported stiffness of actin networks with a concentration of 1 mg/mL can be explained by heterogeneities of the actin network in the local bead environments, which lead to broad distributions of G_0 in case of VPT based microrheology measurements. Furthermore, differences in the preparation procedure can lead to varying network structures and thus to different mechanical properties. The formation of homogeneous and isotropic actin networks mainly depends on buffer conditions and actin monomer concentration.[2,75–78,178,179] An increased actin concentration leads to denser networks with smaller entanglement length and consequently smaller mesh sizes, which results in a higher network stiffness (see fig. 4.3).

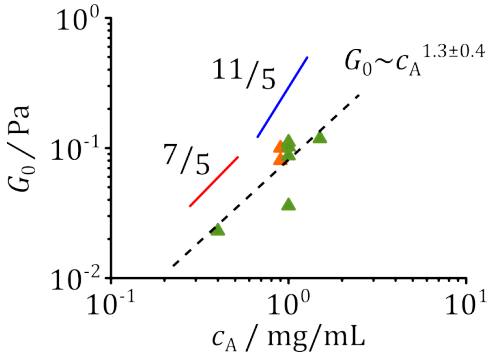

Figure 4.3: G-actin concentration c_A dependence of the plateau modulus G_0 obtained from one-particle microrheology of artificial 3D actin networks. Viscoelastic properties of actin networks were measured by means of VPT (green triangles: G_0(0.4 mg/mL) = 23 mPa (N = 6), G_0(1.0 mg/mL) = 111 mPa (N = 3), G_0(1.0 mg/mL) = 36 mPa (N = 3), G_0(1.0 mg/mL) = 102 mPa (N = 5), G_0(1.0 mg/mL) = 87 mPa (N = 3) and G_0(1.5 mg/mL) = 118 mPa (N = 6)) and by particle tracking using an AFS (orange triangles: G_0(0.9 mg/mL) = 100 mPa (N = 12) and G_0(0.9 mg/mL) = 80 mPa (N = 4)). The dashed black line displays a scaling of $c_A^{1.3}$, the solid red line a scaling of $c_A^{7/5}$, and the solid blue line a scaling of $c_A^{11/5}$.

According to *Isambert* and *Maggs*[185] a reciprocal scaling behavior of G_0 with the third power of the mesh size ξ is proposed.

$$G_0 \approx \frac{k_B T}{\xi^3} \tag{4.3}$$

Using the *Boltzmann* constant k_B of $1.38 \cdot 10^{-23}$ J/K, a temperature T of 298 K and a mesh size ξ of 300 nm (calculated according to *Schmidt et al.*[184]) for actin networks with a concentration of 1 mg/mL, a plateau modulus of 152 mPa is obtained. This value corresponds well to the experimental values of G_0 determined in this thesis using darkfield microscopy and with the plateau moduli reported in literature.[76,161,187]

The actin monomer concentration (c_A) dependence of the plateau modulus (G_0) of actin networks obtained by one-particle microrheology was determined with $G_0 \propto c_A^{1.3\pm0.4}$ (see fig. 4.3). Concentration dependencies in the same order of magnitude with $G_0 \propto c_A^{1.2\pm0.2}$ were reported by *Palmer et al.*[169] and with $G_0 \propto c_A^{7/5}$ by *Gurmessa et al.*[188] and *Hinner et al.*[187] In contrast, higher concentration dependencies were found by *Gardel et al.*[76] with $G_0 \propto c_A^{1.8\pm0.4}$ and by *MacKintosh et al.*[166] with $G_0 \propto c_A^{11/5}$. The origin of the different scaling behaviors can be explained by two different models, the affine and nonaffine model.[80] In the affine model the actin gels are densely cross-linked via entanglement points and deformations of the network are

evenly distributed over the specimen by these points, so that a homogeneous strain can be observed at all length scales.[80,189] Here, the plateau modulus is predicted to scale with $G_0 \propto c_A^{11/5}$ and corresponding actin networks show absolute stiffnesses of about 10 Pa[189] as reported by *MacKintosh et al.*[166] The nonaffine model describes loosely entangled actin gels with sparsely elastic connections, in which the network's response to deformation is dominated by filament bending, resulting in inhomogeneous strains within the gels.[80,189] For the nonaffine model, a scaling behavior of $G_0 \propto c_A^{7/5}$ with lower absolute stiffnesses in comparison to the affine actin networks is predicted.[189] This agrees well with results from *Gurmessa et al.*[188] and *Hinner et al.*[187] and also with the data presented here. Therefore, it can be assumed that nonaffine actin networks were produced here.

The high frequency regime (f in the range of about 10^{-1} - 10^{1} Hz) is dominated by bending of single actin filaments and the system behaves again more like a fluid with $G'(f) < G''(f)$. Here, $G'(f)$ and $G''(f)$ typically show a ¾ power law scaling.[167–170] In this regime a power law exponents in the range of 0.61 - 0.94 was determined independently on the microscopy technique of the VPT measurements and often a drop or lower exponent in the storage modulus compared to the loss modulus was observed. On the one hand, this might be due to actin bundle formation, which according to *Müller et al*.[190] lead to higher power law scaling in G' of about 0.93 and lower power law scaling in G'' of about 0.55. On the other hand, the differences in scaling of the storage modulus at high frequencies can be explained by inertia effects,[191] which is discussed in more detail in the dissertation of *Nöding*.[153]

Summarized, the viscoelastic properties of artificial actin networks are highly sensitive to measuring conditions as well as to the preparation method. For instance, a softening of the F-actin networks was found in microrheology experiments using fluorescence imaging, which increased with longer excitation times. In contrast, no effect on the stiffness was determined using darkfield microscopy. Furthermore, even small variations in the preparation procedure lead to differences in contour length, entanglement length and mesh size and therefore different network architectures and mechanics. In microrheology experiments, however, inhomogeneities of the network in the local bead environment can lead to dramatically different results. One method for measuring global instead of local properties of the actin networks is bulk rheology, which will be discussed in the next chapter.

4.1.3 Viscoelastic Responses of Cross-linked Actin-HMM Networks measured via Bulk Rheology

An important property of the cell cortex is the modification of its viscoelastic properties in order to maintain or change cell shape. The viscoelastic responses of F-actin networks are modified by various actin binding proteins (ABPs).[2–6] Here, the frequency-dependent viscoelasticity of artificial 3D actin networks in absence and presence of the cross-linking protein α-actinin (see chpt. 1.3) and the motor fragment protein heavy meromyosin (HMM, see chpt. 1.3.1) was analyzed via oscillatory rheometry (see chpt. 3.3.6). Oscillatory rheometry is a frequently used bulk rheology method, which in contrast to microrheology requires larger sample volumes as well as longer acquisition times and where the high frequency regime cannot be resolved.[152,192] However, bulk rheology offers the possibility to determine the global rheology of the actin networks instead of the local rheology as in case of microrheology, which is sensitive to network heterogeneities (see chpt. 4.1.2). The corresponding frequency spectra obtained by bulk rheology are shown in figure 4.4.

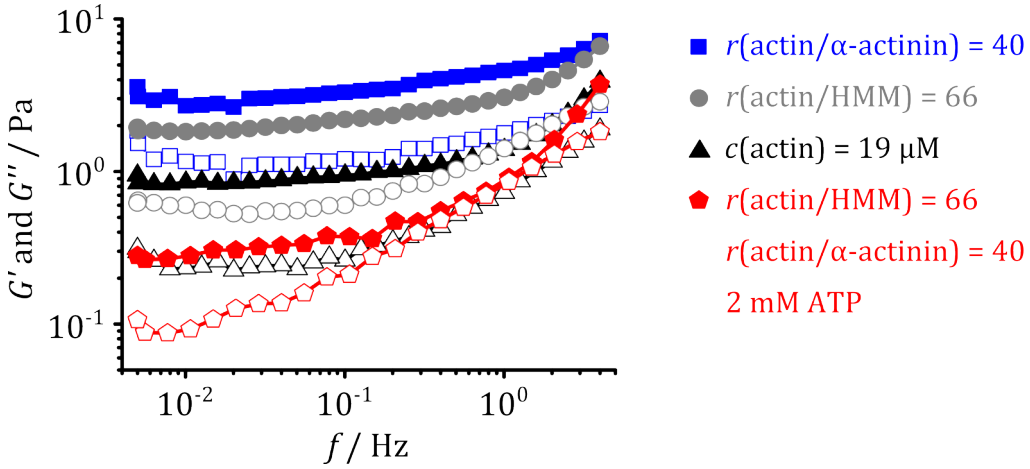

Figure 4.4: Frequency-dependent viscoelastic properties of artificial 3D actin networks (c_A = 19 µM) measured by means of a strain-controlled oscillating plate-plate rheometer (r = 10 mm) in a frequency range of 0.005 Hz to 4 Hz with a set shear strain of 1%. The storage modulus G' (filled symbols) and loss modulus G'' (open symbols) of F-actin gels in presence of different ABPs and additional agents were determined. An F-actin network cross-linked with α-actinin at a ratio of r(actin/α-actinin) = 40 (blue squares) show a plateau modulus of G_0 = 2.8 Pa (N = 1) and an actin network cross-linked with HMM at a ratio of r(actin/HMM) = 66 (grey circles) show a plateau modulus of G_0 = 1.9 Pa (N = 1). For a pure F-actin gel (black triangles), a modulus of G_0 = 0.9 Pa (N = 1) was measured. An Actin-HMM network (r(actin/HMM) = 66) cross-linked with α-actinin (r(actin/α-actinin) = 40) show a plateau modulus of G_0 = 0.3 Pa (N = 1) after activation of the HMM motor proteins by addition of 2 mM ATP (red pentagons).

For a pure F-actin network with a monomer concentration of 19 µM a plateau modulus G_0 of 0.9 Pa (see fig. 4.4, black triangles) was determined. *Tharmann* measured a plateau modulus of about 0.1 Pa[20] for an entangled actin network with a monomer concentration of 19 µM using torsional macrorheometry. The deviation in the measurement presented here can be attributed to differences in the preparation and measuring methods, which can dramatically influence the mechanical properties of actin networks, as discussed in chapter 4.1.2.

Compared to the pure actin network, cross-linking with α-actinin at a ratio of r(actin/α-actinin) = 40 results in an increased stiffening of the actin network with a concentration of 19 µM by a factor of 3 (G_0 = 2.8 Pa, see fig. 4.4, blue squares). The long and flexible cross-linker α-actinin is known to alter the structures and thus the mechanical response of F-actin networks depending on its concentration.[79,193–196] According to *Lieleg et al.*,[79] α-actinin can form three different structural phases of actin networks with distinct mechanical properties. At low concentrations (r(actin/α-actinin) > 200), a weakly cross-linked phase comparable to pure actin gels is formed with plateau moduli in the range of 0.03 - 0.9 Pa[79], which is in agreement with G_0 measured for the actin network without cross-linkers (G_0 = 0.9 Pa). Above a critical concentration (200 < r(actin/α-actinin) > 20), a composite phase is formed and a strong increase of G_0 is observed with increased α-actinin concentration.[79] For a ratio of r(actin/α-actinin) = 40 a plateau modulus of about 5 Pa was reported by *Lieleg et al.*,[79] which agrees well with the measurement in this thesis. At even higher concentrations of α-actinin (r(actin/α-actinin) < 20) a bundle-cluster phase is formed[79], which was not measured here.

Cross-linking of actin networks with the motor fragment protein HMM leads to the following results, depending on the ATP concentration. Under ATP depletion, a plateau modulus of 1.9 Pa (see fig. 4.4, grey circles) was measured for the actin-HMM network (r(actin/HMM) = 66 and actin monomer concentration of 19 µM), which is about twice as stiff as the actin network without cross-linkers. With addition of ATP (2 mM) a decrease in stiffness by one third was observed for the actin-α-actinin-HMM network (G_0 = 0.3 Pa, see fig. 4.4, red pentagons) in comparison to the purely entangled actin network. Comparable results were obtained in bulk rheology experiments by *Tharmann et al.* for actin-HMM networks under ATP depletion and ATP excess.[20,54] *Tharmann et al.* determined a plateau modulus of about $G_0 \approx 5$ Pa for an actin-HMM network at a ratio of r(actin/HMM) = 66 and an actin monomer concentration of 19 µM,[54] which is in the same order of magnitude as the measured value for the actin-HMM network in absence of ATP in this thesis. Here, HMM is suggested to be in its rigor state − where it

strongly binds to F-actin and behaves like a permanent cross-linker − forming an isotropically cross-linked network, whose stiffness rises with increasing HMM concentration.[54] With addition of ATP (~2 mM) to the actin-HMM network, *Tharmann* measured a reduction in the plateau modulus of about 70% compared to the pure actin network.[20] The addition of ATP is associated with an activation of the motor fragment protein HMM, which results in more transient cross-linking and consequently a higher fluidity induced by sliding of the filaments.[20] This fluidization is indicated by a decrease of G_0, which was also observed in experiments here, but due to additional cross-linking with α-actinin not to the same extent as in the experiments of *Tharmann*. In this thesis, the additional α-actinin cross-linking of the active actin-HMM network was used on the one hand to provide an optimal distance between actin filaments, allowing HMM molecules to assemble in between and produce forces by moving along the filaments.[2,28] On the other hand, cross-linking with α-actinin is proposed to prevent disassembly processes of F-actin caused by active motor proteins.[2,29–31] Furthermore, cross-linking of actomyosin networks prevents actin aggregations as well as phase separation (so-called superprecipitation) generated by contractile forces of active myosin motors.[45]

Humphrey et al.[41] performed similar bulk rheology experiments of actin networks with full-length myosin II motors in rigor and active state regulated by ATP. After addition of inactive myosin II to the actin networks an increase of G_0 by a factor of 6 ± 1 compared to pure actin networks was found. Activation of myosin II by addition of 500 μM ATP led to a decrease of G_0 of about $(40 \pm 10)\%$.[41] These findings are in good agreement with the data of HMM proteins presented here and show that the HMM motor protein fragment with its full motor activity[53] is suitable for bottom-up approaches. In contrast, *Mizuno et al.* observed that contractile activity of full-length myosin II motors in biotin-neutravidin cross-linked actin networks led to a stiffening of the system by a factor of about 100.[45] Here, it is assumed that the strong cross-links in combination with the active myosin motors allow the formation of tensile stresses in actin filaments between the cross-linking points.[45] Thus, relaxation of the network by filament sliding − as assumed in this thesis − is suppressed, making the network more rigid.

The regulation of the stiffness of actin networks by ATP shifting myosin motor proteins to their rigor or active state could also be observed in reconstituted actomyosin networks within water-in-oil droplets as a model of minimal cell compartments (see chpt. 4.1.4) and in apical cell cortex fragments obtained from living, intact MDCK II cells (see chpt. 4.3.3).

4.1.4 Viscoelastic Responses of Actin and Actin-Myosin II Networks in Minimal Cell Compartments measured via Passive Microrheology

To investigate the influence of compartmentation on the mechanics of artificial actin networks, nearly cell-sized minimal cell compartments (MCCs) were created in a bottom-up fashion. For this purpose, artificial actin networks were polymerized in the presence of tracer particles (r = 1 µm) within small water-in-oil droplets with diameters in the range of several hundred micrometers (see chpt. 3.2.2) and investigated via particle tracking using an acoustic force spectrometer (AFS, see chpt. 3.3.5).

Viscoelastic Responses of Entangled Actin Networks in MCCs

First analysis of water-in-oil droplets as a model system for MCCs were performed with pure actin networks (c_A = 22 µM or 0.9 mg/mL). An exemplary fluorescence micrograph and the MSD − of the beads embedded within the actin networks − obtained by particle tracking using an AFS, as well as the corresponding viscoelastic frequency spectra are shown in figure 4.5.

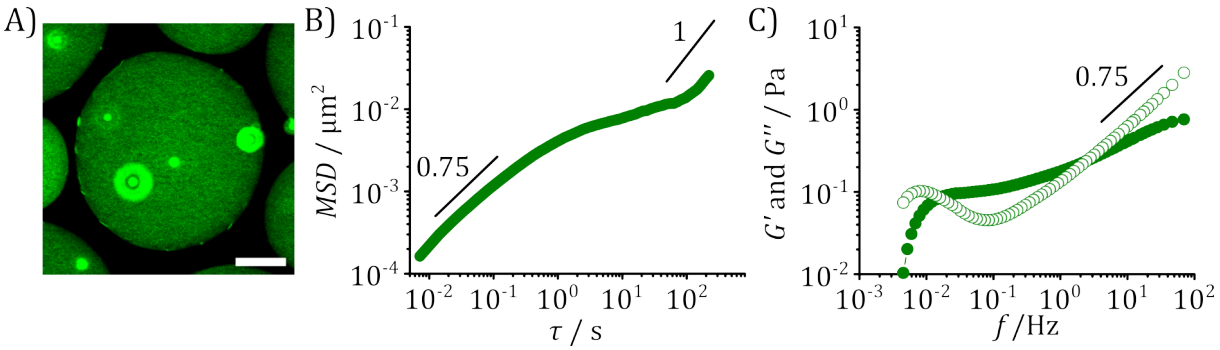

Figure 4.5: Frequency-dependent viscoelastic properties of artificial 3D actin networks (c_A = 22 µM) within water-in-oil droplets as MCCs measured by particle tracking using an AFS. **A)** Exemplary fluorescence micrograph of an artificial actin network with tracer particles (r = 1 µm) in MCCs. F-actin was labeled with AF 488-Phal. Scale bar: 24 µm. **B)** MSD (time and ensemble averaged) as well as **C)** storage modulus G' (filled circles) and loss modulus G'' (open circles) of F-actin gels within MCCs. The tracer particles were tracked at 140 Hz over a period of 240 s. A plateau modulus of G_0 = 100 mPa (N = 12, n = 6) was determined. The scaling behavior of the power law with an exponent of 0.75 and 1 are shown as black lines.

Within the water-in-oil droplets, a spatially homogeneous and isotropic actin network was formed (see fig. 4.5, A), which is a prerequisite for further microrheological evaluation based on continuum mechanics (see chpt. 3.4.1).[152] Due to the simple preparation method (see chpt. 3.2.2), droplets with diameters in the range of about 50 - 300 µm were produced. In this range,

no influences on the network mechanics by boundary confinement effects are to be assumed, because boundary effects are expected to occur in the order of magnitude of the persistence length of the actin filaments and thus for droplets with diameters in the range of about 10 µm. Consequently, the time averaged MSDs (see eq. 3.16) were also averaged over the ensemble of droplets with different sizes.

As discussed in detail in chapter 4.1.2, the MSD of the artificial actin networks exhibits three different regimes: the low, intermediate and high lagtime regime (see fig. 4.5, B). In the low lagtime regime (τ in the range of about 10^{-2} - 0.4 s) a diffusive exponent α of 0.74 was calculated, which is in good agreement with the expected ¾ scaling behavior of the semiflexible F-actin, resulting from bending modes of single filaments.[161,167–170,181] Within the intermediate lagtime regime (τ in the range of about 0.4 - 50 s) the MSD shows a plateau with an average bead motion of about 80 nm, due to restrictions caused by filament entanglement. The plateau value of $7 \cdot 10^{-3}$ µm^2 fits well with values reported in literature for artificial actin networks (0.9 mg/mL to 1.2 mg/mL) in the range of $5 \cdot 10^{-3}$ - $8 \cdot 10^{-3}$ µm^2.[76,181,182] In the high lagtime regime (τ >50 s) a diffusive exponent of nearly one was determined (0.93), which can be related to free diffusion of the beads at these time scales (see chpt. 4.1.2).

The MSD was used to calculate the frequency spectra in form of the storage $\left(G'(f)\right)$ and loss $\left(G''(f)\right)$ modulus with the characteristic low, intermediate and high frequency regimes (see fig. 4.5, C), as described in more detail in chapter 4.1.2. In the low frequency regime (f < 0.02 Hz) dynamic processes dominate, such as the diffusion of actin filaments. Here, the reptation frequency f_{rep} can be determined from the crossover of $G'(f)$ and $G''(f)$ with 0.016 Hz. Based on equation 4.2 and with a mesh size of 316 nm – calculated according to *Schmidt et al.*[184] applying $\xi[\mu\mathrm{m}] = 0.3/\sqrt{c_{\mathrm{A}}[\mathrm{mg/mL}]}$ – an actin contour length of about 12 µm was obtained. This corresponds well with F-actin contour length of about 10 µm to 30 µm given in the literature.[10,162,185] In the intermediate frequency regime (f in the range of about 0.02 - 2.5 Hz), the elastic response of actin networks predominate the viscous part due to filament entanglement, and the stiffness of the system is reflected by the plateau modulus G_0 (see chpt. 4.1.2). For pure actin networks in MCCs, a plateau modulus of 100 mPa (mean, N = 12, n = 6) was measured, which is in good agreement with values of about 100 mPa determined by *Morse*[161] and *Hinner et al.*[187] and the value of about 300 mPa calculated by *Gardel et al.*[76] for actin networks with a monomer concentration of 1 mg/mL. According to equation 4.3, a theoretical G_0 value of 130 mPa was calculated using the theoretical mesh size of 316 nm, which also agrees well with

the experimental value. The high frequency regime (f > 2.5 Hz) is governed by the mechanics of single actin filaments, which typically result in a power law scaling of ¾.[167–170] Here, a power law exponent of 0.74 was determined for $G''(f)$, which fits well with theory, while $G'(f)$ exhibits a power law scaling of 0.38. The deviation of the exponent of the storage modulus in the high frequency regime might be caused by inertia effects (see chpt. 4.1.2).[153,191]

Comparing microrheology experiments of *in vitro* actin networks in glass chambers (see chpt. 4.1.2) with those in MCCs shows that the latter are in better agreement with the results reported in literature for artificial 3D actin gels. The viscoelastic properties of actin networks strongly depend on the network architecture, which is mainly influenced by the preparation and measuring conditions, as discussed in detail in chapter 4.1.2. The polymerization of artificial actin networks in small sample volumes in the picoliter range, such as within the water-in-oil droplets, seems to lead to the formation of homogeneous and isotropic networks with less local heterogeneities than in the glass chambers with sample volumes of several microliters. Furthermore, it is possible to measure several independent MCC systems within one measurement, resulting in larger ensembles and better statistic. Therefore, the MCCs provide a stable and simple bottom-up model system for studying the microrheology of actin networks.

Viscoelastic Responses of Cross-linked Actin-Myosin II Networks in MCCs

− *Optical tweezer experiments and analysis have been carried out by Peter Nietmann* −

The motor protein myosin II is a mechanoenzyme, able to convert chemical energy into kinetic energy by hydrolysis of ATP and therefore plays an important role in many cell processes, like cell motility, morphogenesis and cell shape changes.[6,35,44,49] In order to analyze the impact of the myosin motor activity − controlled in an ATP-dependent manner − on actin network mechanics, a MCC bottom-up strategy was used. For this purpose, an artificial actin network (c_A = 22 µM) in presence of myosin II filaments, the cross-linker protein α-actinin and the ATP regeneration system creatine phosphokinase (see chpt. 3.2.1) was created in water-in-oil droplets (see chpt. 3.2.2). Tracer particles (r = 1 µm) were embedded within the actomyosin network and tracked by means of an AFS as described in chapter 3.3.5. A schematic illustration and a representative fluorescence micrograph of the reconstituted actomyosin networks within the MCCs are shown in figure 4.6.

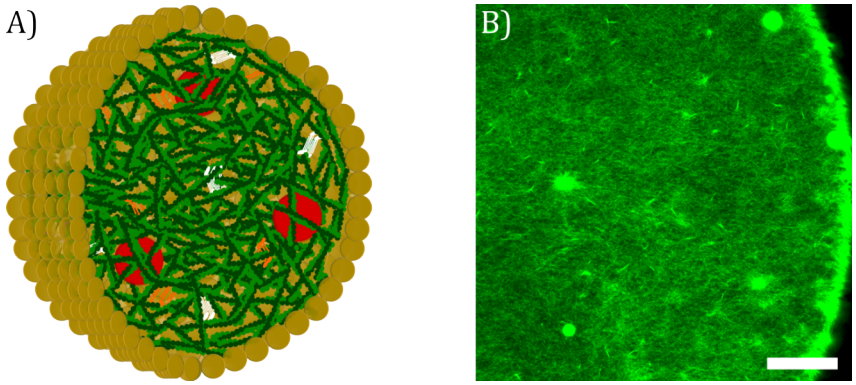

Figure 4.6: Reconstituted actomyosin networks within water-in-oil droplets as MCCs. **A)** Schematic illustration of 3D actomyosin networks in MCCs. F-actin is shown in green, myosin II in white, α-actinin in orange, tracer particles in red and the oil in yellow. **B)** Exemplary fluorescence micrograph of an artificial actomyosin network inside a MCC. F-actin was labeled with AF 488-Phal. Scale bar: 24 µm.

The fluorescence micrograph shows bundle-like structures (see fig. 4.6, B), which are formed due to the cross-linking of actin filaments via α-actinin and myosin II. AFS measurements of the MCCs were performed shortly after preparation, where a sufficient stock of ATP was present, and 24 h after preparation, where the ATP stock was already consumed. Exemplary trajectories as well as *van Hove* correlation functions for both cases are shown in figure 4.7.

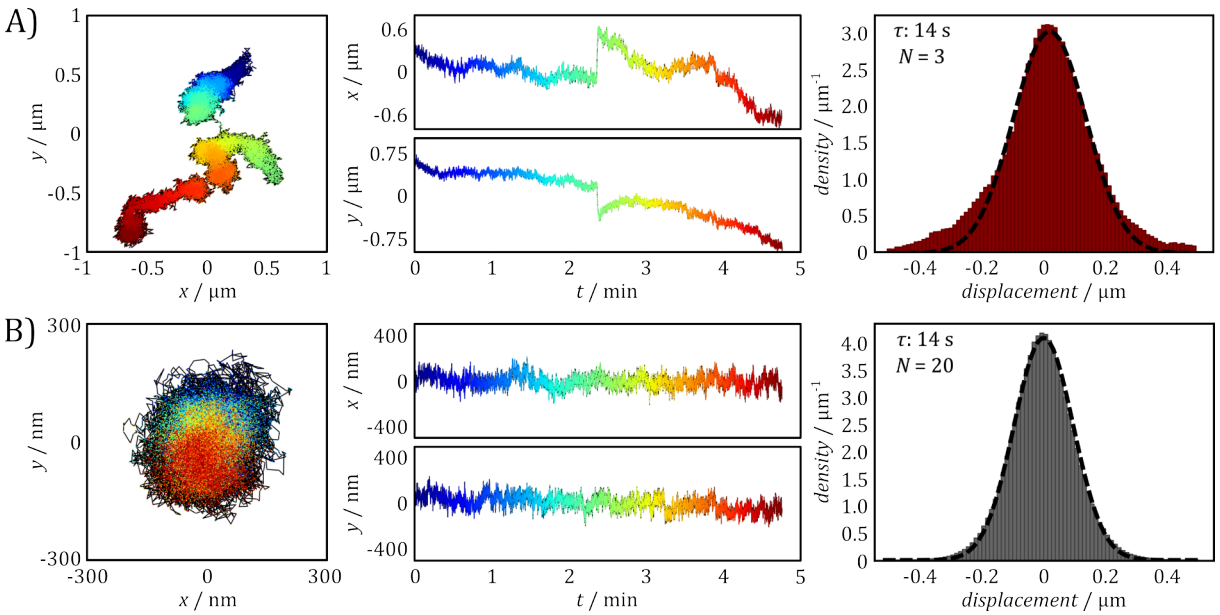

Figure 4.7: Exemplary trajectories and time-dependent *x*- and *y*-motions of beads (r = 1 µm) incorporated in an actomyosin network within MCCs, as well as ensemble averaged *van Hove* histograms of displacements and the corresponding *Gaussian* fit for small displacements (range [-0.2 µm, +0.2 µm]). The beads were tracked at 140 Hz over a time period of 300 s. **A)** Myosin II motor proteins in their active state under ATP excess. Non-equilibrium fluctuations due to active motors led to larger displacements than expected from thermal motions and were visible as deviations at the tails of the *Gaussian*. **B)** Myosin II motor proteins in their inactive state under ATP depletion (equilibrium system).

Bead trajectories measured directly after preparation (in excess ATP) show large movements with jumps in *x*- and *y*- direction of about 600 nm (see fig. 4.7, A), while bead trajectories after consumption of ATP (24 h after preparation) show constrained movements without jumps (see fig. 4.7, B). From the bead trajectories, *van Hove* correlation functions were calculated. For this, the distribution of the bead displacement along *x* and *y* was plotted against the displacement of the bead along *x* and *y* for a chosen lag time τ.[42] The ensemble averaged *van Hove* correlation function of beads measured shortly after preparation under ATP excess, exhibits large deviations from a *Gaussian* at its tails (see fig. 4.7, A), while the ensemble averaged *van Hove* correlation function of beads measured 24 h after preparation under ATP depletion, only exhibit small deviations from a *Gaussian* (see fig. 4.7, B). This was also observed by *Toyota et al*.[42] – for actin networks in presence of myosin II and ATP and for actin networks without myosin II – and can be explained by the fact that myosin motors can attain two different states depending on the ATP concentration (see chpt. 4.1.3). Under depletion of ATP, myosin is in its rigor state, where it acts as permanent cross-linker binding strongly to actin filaments.[36,41,42] Here, the actomyosin network is in an equilibrium state, where the *van Hove* correlation function agrees well with a *Gaussian* and small deviations can be attributed to local heterogeneities of the network structure.[42] On the other hand, under excess ATP myosin is in its active state and acts like a transient cross-linker leading to sliding movements of actin filaments and thus to contractile events.[36,41,42,45] In this state the actomyosin network is in non-equilibrium and active myosin motors generate athermal movements of the embedded beads with jump events in the range of about 500 nm,[42,45] similar to the measurements in this thesis. These athermal fluctuations are mirrored in a non-*Gaussian* behavior of the *van Hove* correlation function,[42] as observed in this thesis.

Another possibility to characterize the ATP dependent myosin activity, is to analyze the response function $A^*(\omega)$ of the actomyosin networks by bead tracking microrheology. The response function is determined from the displacement of the beads, whereby the following relation applies for simple homogeneous and incompressible materials:[45]

$$A^*(\omega) = \frac{1}{6\pi G^*(\omega) r} \tag{4.4}$$

Here, $G^*(\omega)$ is the complex shear modulus of the material and r the radius of the incorporated beads. For complex viscoelastic materials, $G^*(\omega)$ is composed of a real part, representing the elastic behavior and an imaginary part, representing the viscous behavior (see eq. 3.20). If the

beads are incorporated in an equilibrium system, only thermal forces act on them and the power spectral density function $C(\omega)$ of their displacement fluctuations $u(t)$ can be written as:[45]

$$C(\omega)=\int \langle u(t)u(0)\rangle e^{i\omega t}\,\mathrm{d}t \tag{4.5}$$

According to the fluctuation-dissipation theorem, $C(\omega)$ is directly connected to the imaginary part of the linear response function $A''(\omega)$ of a system in equilibrium,

$$A''(\omega)=\frac{\omega}{2k_{\mathrm{B}}T}C(\omega) \tag{4.6}$$

where $k_{\mathrm{B}}T$ is the thermal energy.[45] In order to characterize the myosin activity in actomyosin networks, $A''(\omega)$ was measured by active microrheology (AMR), while the normalized power spectrum $\omega C(\omega)/2k_{\mathrm{B}}T$ was measured by passive microrheology (PMR). In active actomyosin networks (non-equilibrium systems), additional fluctuations generated by motor activity are expected to increase the right side of equation 4.6 compared to the left side. This violation of the fluctuation-dissipation theorem is thus an indication for myosin activity.[45,192] Mechanical responses of actomyosin networks in equilibrium (inactive) and non-equilibrium (active) state measured via PMR as well as AMR are shown in figure 4.8.

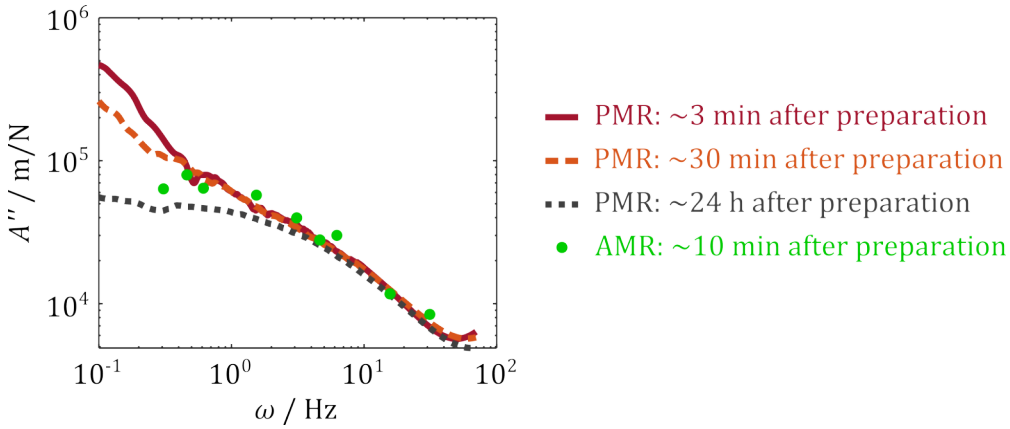

Figure 4.8: Imaginary part of the one-particle response function A'' of actomyosin networks as a function of the angular frequency ω. Response functions of active and inactive actomyosin networks polymerized inside MCCs measured via PMR at different time points after preparation using an AFS. The mean response function measured ~3 min after preparation, where myosin is in its active state, is shown as a red solid line (N = 3), the mean response function determined ~30 min after preparation (myosin is still active) as an orange dashed line (N = 46) and the mean response function calculated ~24 h after preparation, where myosin is in its inactive state, as a grey dotted line (N = 20). Mean response functions of an active actomyosin network polymerized inside MCCs measured ~10 min after preparation with AMR (sinusoidally oscillated optical trap with 100 mW generating a force at frequencies of 0.05 - 50 Hz, green circles, N = 9) using an optical tweezer (OT). The OT experiments and analysis were done by *Peter Nietmann*.

In PMR measurements, actomyosin networks under ATP excess – non-equilibrium system with myosin II in its active state – show enhanced fluctuations in the response function $A''(\omega)$ below 5 Hz (see fig. 4.8, red solid and orange dashed line) compared to actomyosin networks under ATP depletion (equilibrium system), where myosin is in its rigor state (see fig. 4.8, grey dotted line). This enhancement can be attributed to non-equilibrium fluctuations generated by the active myosin motors.[45,192] These non-equilibrium fluctuations were also found in an active actomyosin gel as disagreements in the response function $A''(\omega)$ between PMR (see fig. 4.8, red solid and orange dashed line) and AMR (see fig. 4.8, green circles) below 1 Hz. By combining PMR with AMR, it is possible to simultaneously measure the material response and low-frequency athermal fluctuations within the same active actomyosin gel as differences in the corresponding response spectra.[192] *Mizuno et al.* observed these differences between PMR and AMR in $A''(\omega)$ of a non-equilibrium actomyosin system at frequencies below 10 Hz,[45,192] which is in good agreement with the data presented here.

These results indicate ATP-dependent active processes in the actomyosin networks, which could be measured as athermal fluctuations. With excess ATP in the networks, athermal fluctuations were observed on the one hand in the *van Hove* plots, as deviations from a *Gaussian* at its tails, and on the other hand in the response functions measured via PMR and AMR, as violation of the fluctuation-dissipation theorem at low frequencies. It is assumed that these athermal fluctuations are induced by active myosin motors that bind to actin filaments and cause them to slide past each other under ATP consumption. However, according to *Mizuno et al.*[45] the ATP concentration should not be too high for active processes. At high ATP concentration of 3.5 mM they did not observe myosin activity in actomyosin networks, since the duty ratio of myosin motors to F-actin was too low to generate contraction. They measured active fluctuations for several hours at ATP concentrations of about 60 µM, which is in the same range as used in this thesis.[45] Furthermore, the contractile responses of active actomyosin gels strongly depends on the architecture and the connectivity of the networks, regulated by ABPs,[86,197] as also discussed in chapter 4.1.3. While in the absence of cross-linkers the myosin-induced sliding movements of the actin filaments lead to a fluidization of the network,[6,41–44] contractile stresses and thus a myosin-driven network stiffening can be observed if the cross-linking density is sufficiently high.[198,199] In literature, *Ennomani et al.* suggest different types of contractile responses of actomyosin networks – namely local sliding, global deformation or massive freezing − depending on the organization and connectivity of the actin filaments.[86] These studies highlight the importance of characterizing single-molecular interactions in order to interpret the molecular mechanisms of contraction in complex actomyosin structures such as the cellular

cortex. However, the artificial 3D actin networks do not mimic well the physiological conditions in living cells, where a quasi-2D actin cortex is dynamically attached to the plasma membrane. To better imitate the physiological situation in living cells, minimal actin cortices (MACs) − composed of an artificial actin layer coupled to a lipid bilayer − were designed and analyzed, as described in the following chapter.

4.2 Self-organization and Viscoelasticity of Artificial 2D Actin Networks attached to Lipid Bilayers

− Parts of the experiments have been carried out by Siqi Sun as part of his bachelor thesis −

The actin cortex – an important cell component for the regulation of dynamical and mechanical cellular properties – is a thin layer of actin filaments and several actin binding proteins (ABPs), which is dynamically linked to the plasma membrane by proteins from the ezrin-radixin-moesin (ERM) protein family, such as ezrin.[2–6] First investigations of separate actin cortex components were done in studies of artificial 3D actin networks, as discussed in detail in chapter 4.1. For a better mimic of the physiological conditions in living cells, minimal actin cortices (MACs) were designed, based on a model system developed by *Nöding* and *Schön et al.*[65,66] To achieve this, a quasi-2D F-actin layer was crowded by methylcellulose (MC) onto a solid supported membrane (SSM). Here, crowding refers to depletion forces. The actin layer was coupled to the SSM via the pseudophosphorylated ezrin mutant (ezrin T567D) and the receptor lipid phosphatidylinositol-4,5-bisphosphate (PIP_2, see chpt. 1.3.2), as described in chapter 3.2.3. The self-organization and viscoelastic responses of these 2D MACs were studied in dependence of the crowding agent MC, as well as in dependence of the pinning point density – regulated through the PIP_2 concentration within the SSM − and measuring conditions.

4.2.1 Diffusivity of Solid Supported Lipid Bilayers on Glass Coverslips

In this thesis, glass coverslips were used to form a planar SSM (see chpt. 3.2.3) − in contrast to *Nöding* and *Schön et al.*[65,66] using silicon dioxide coated silicon wafers – because a transparent support was a prerequisite for performing microrheological experiments using darkfield microscopy (see chpt. 4.2.5). In order to analyze, whether intact SSMs were formed on the glass coverslips, the membrane diffusivity was determined by fluorescence recovery after photo bleaching (FRAP) experiments (see chpt. 3.3.3). The corresponding lateral diffusion coefficients D were calculated using a MATLAB script (*frap_analysis*) written by *Jönsson et al.*,[128] as described in chapter 3.3.3. Exemplary fluorescence micrographs and diffusion coefficients of FRAP experiments of a SSM composed of 99.6 mol% POPC and 0.4 mol% TxR-DHPE are shown in figure 4.9.

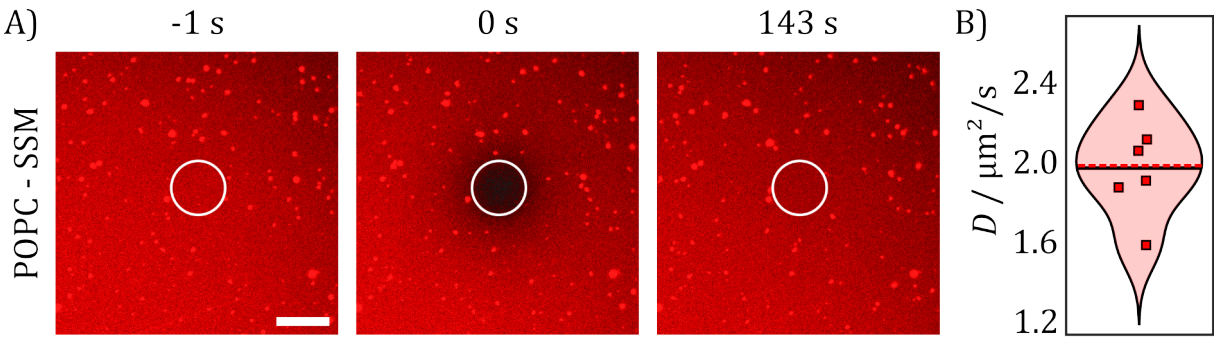

Figure 4.9: FRAP experiments performed on solid supported membranes (SSMs) consisting of 99.6 mol% POPC and 0.4 mol% TxR-DHPE. As solid support a glass coverslip cleaned with HELLMANEX® III was used. **A)** Exemplary time series of fluorescence micrographs of a TxR-DHPE labeled POPC-SSM during a FRAP experiment. In a region of interest (ROI, white circles) the fluorescence intensity of TxR-DHPE was measured as a function of time before (-1 s) and after bleaching (0 s and 143 s) to track the recovery process. Scale bar: 12 µm. **B)** Violin plot of the diffusion coefficients of POPC-SSMs determined according to *Jönsson et al.*[128] with a mean value (solid black line) of $\overline{D}$ = (1.99 ± 0.24) µm²/s and a median value (dashed red line) of 2.00 µm²/s (N = 6) at room temperature.

The fluorescence micrographs of the SSM show a uniform fluorescence signal – indicating an intact membrane – with some bright spots (see fig. 4.9, A) that could be caused by lipid material. The micrographs of FRAP experiments − before bleaching (see fig. 4.9, A, t = -1 s), immediately after bleaching the fluorophores in a region of interest (see fig. 4.9, A, white circle) with a high-energy laser pulse (see fig. 4.9, A, t = 0 s) and after the subsequent recovery (see fig. 4.9, A, t = 143 s) − were used to determine the diffusion coefficients D (see fig. 4.9, B). For the POPC lipid bilayers on the glass coverslips, a mean diffusion coefficient of $\overline{D}$ = (1.99 ± 0.24) µm²/s was measured at room temperature. This is in good accordance with values for diffusion coefficients reported by *Köchy et al.*[200] and *Vaz et al.*[201] for POPC supported bilayers. They found values of $\overline{D}$ = (2.1 ± 0.7) µm²/s at 10 °C and $\overline{D}$ = (4.0 ± 0.8) µm²/s at 30 °C using a nuclear-magnetic-resonance method[200] and values of $\overline{D}$ = (2.8 ± 0.3) µm²/s at 15 °C using the FRAP technique.[201] The small deviations in D might be caused by different preparation and measuring methods and are negligible. Consequently, it can be assumed that intact fluid lipid bilayers were formed on the glass coverslips, making it suitable as solid support for MACs and for further passive microrheology experiments (see chpt. 4.2.5).

In literature it was found that additional attachment of F-actin onto the SSM via ezrin and PIP_2 did not change lipid bilayer fluidity,[113,177] but reduced the mobility of the receptor lipid PIP_2.[113] In living cells, however, it is known that the actin cortex reduces the plasma membrane mobility by interacting with membrane proteins such as E-cadherin.[202] In this thesis, the influence of the actin cortex on membrane diffusivity in a MAC model system through additional agents like E-cadherins was not investigated, but this might be interesting in future research.

4.2.2 Attachment of Actin Networks to Lipid Bilayers

In its active state, the native protein ezrin acts as a linker between the actin cortex and the PIP_2 containing membrane (see chpt. 1.3.2).[27,56–58] In this thesis a permanently active pseudophosphorylated ezrin mutant (ezrin T567D) was used to prepare 2D MAC model systems (see fig. 3.9). Details on the isolation and characterization of ezrin T567D can be found in the dissertation of *Schön*.[177] In order to investigate the specific attachment of F-actin to the SSM via the linker ezrin T567D and the receptor lipid PIP_2, various control experiments were performed in the presence and absence of ezrin and PIP_2. The corresponding fluorescence micrographs of the SSMs and F-actin networks are shown in figure 4.10.

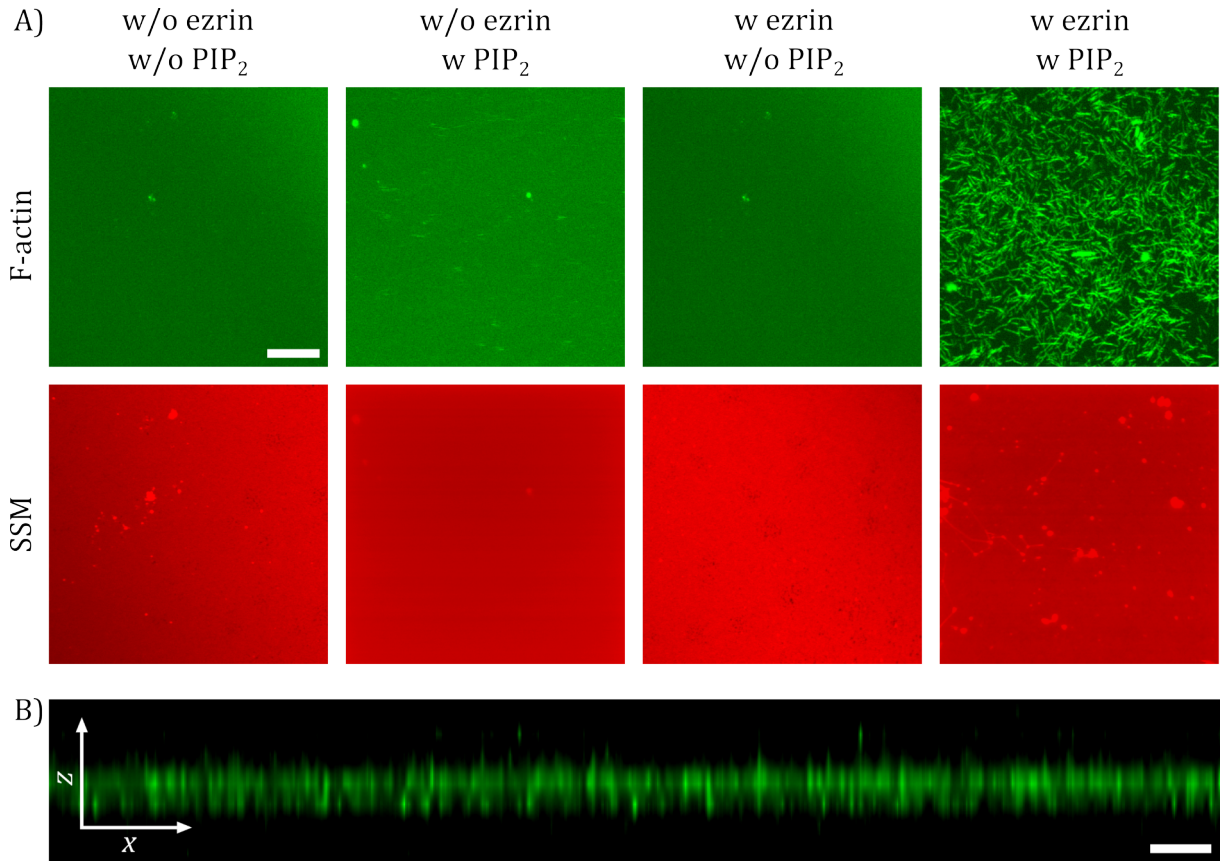

Figure 4.10: Fluorescence micrographs of actin filament attachment to SSMs in presence and absence of the receptor lipid PIP_2 and the linker protein ezrin T567D. F-actin was labeled with AF 488-Phal. **A)** SSMs in absence of PIP_2 consist of 99.6 mol% POPC and 0.4 mol% TxR-DHPE and SSMs in presence of PIP_2 consist of 94 mol% POPC, 5 mol% PIP_2 and 1 mol% Atto 390-DOPE (here colored in red). Pre-polymerized F-actin was crowded on the SSM with methylcellulose (MC, 0.02% (*w*/*v*)). After incubation and rinsing, F-actin attachment to the SSM was only observed in presence of PIP_2 and ezrin. Scale bar: 10 µm. **B)** Cross section of recorded *z*-stack images of an F-actin network attached to a SSM containing 5 mol% PIP_2 via ezrin T567D. The total height of the *z*-stack is 2.7 µm. Scale bar: 1 µm. Data was partially collected in the Bachelor thesis of *Siqi Sun* (2018).

The fluorescence micrographs of the SSMs show a uniform signal of fluorescence with some bright spots (see fig. 4.10, A), indicating that an intact lipid bilayer was formed (see chpt. 4.2.1). Pre-polymerized F-actin networks were crowded onto the intact SSMs by methylcellulose (MC, 0.02% (*w*/*v*)) and incubated for 4.5 h, followed by rinsing steps to remove unbound actin filaments (see chpt. 3.2.3). A specific binding of the F-actin network to the SSM was only observed in presence of ezrin and PIP_2 (see fig. 4.10, A, w ezrin and w PIP_2). Therefore, non-specific attachment of F-actin to the SSM due to membrane effects or the crowding agent MC can be excluded and the formation of the MAC can be attributed to the ezrin-PIP_2 interaction, as also observed by *Nöding* and *Schön et al.*[65,66]

The thickness of the membrane-attached actin network can be estimated from a cross section of *z*-stack images (see fig. 4.10, B). Due to the fact that the axial resolution limit is below 1 µm,[203] it can be assumed that the height of the actin layer is thinner than 1 µm and thus in the same order of magnitude as the averaged actin cortex thickness in living cells with about 200 nm.[48] The same was found by *Nöding* and *Schön et al.*[65] for the height of MACs without the depletion agent methylcellulose. The impact of MC on the self-organization of actin filaments attached to lipid bilayers will be discussed in the following chapter.

4.2.3 Impact of the Crowding Agent Methylcellulose on the Self-organization of Actin Networks attached to Lipid Bilayers

In this thesis, methylcellulose was used as a depletion agent for 2D MACs to localize the actin filaments near the SSM, thus enabling a stable coupling of the F-actin network to the membrane.[31,204] In order to investigate, whether MC influences the self-organization of the actin filaments, MACs were formed (see chpt. 3.2.3) using different amounts of the crowding agent. Fluorescence micrographs of F-actin networks crowded on lipid bilayers containing 5 mol% PIP_2 with different concentrations of MC are shown in figure 4.11.

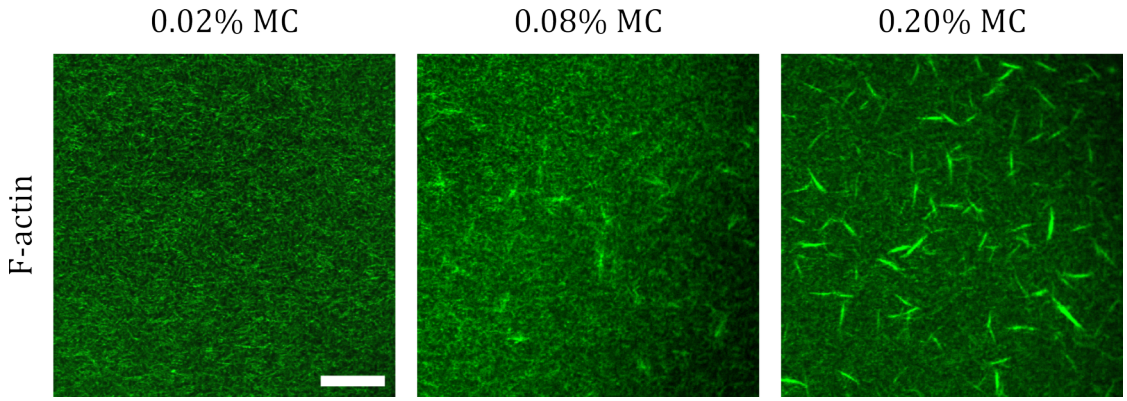

Figure 4.11: Fluorescence micrographs of F-actin attached via the linker ezrin T567D to SSMs consisting of 94 mol% POPC, 5 mol% PIP_2 and 1 mol% Atto 390-DOPE. F-actin was labeled with AF 488-Phal. Pre-polymerized F-actin was crowded on the SSMs with varying amounts of MC (0.02%, 0.08% and 0.20% (*w*/*v*)). After incubation and rinsing, different network morphologies can be observed depending on the amount of MC. At low concentration of MC (0.02% (*w*/*v*)) the actin network shows isotropic branched structures of filaments, while with increasing concentration of MC (0.08% and 0.20% (*w*/*v*)) more isotropic bundle-like structures can be observed. Scale bar: 12 µm. Data was partially collected in the Bachelor thesis of *Siqi Sun* (2018).

At low concentration of MC, a spatially homogeneous and isotropic F-actin network was formed on top of the SSM (see fig. 4.11, 0.02% MC). With increasing MC concentration, differences in the fluorescence intensity of the actin networks were observed in the micrographs, indicating the formation of filament structures with varying thickness. These bundle-like structures were observed at MC concentrations of 0.08% (*w*/*v*) in low amounts (see fig. 4.11, 0.08% MC) and at MC concentrations of 0.20% (*w*/*v*) in high amounts (see fig. 4.11, 0.20% MC). Therefore, it can be assumed that the crowding agent MC induces interaction between actin filaments, leading to bundling depending on its concentration. Consequently, an appropriate amount of MC must be applied to allow sufficient crowding of F-actin on the SSM on the one hand and to prevent bundling of the filaments on the other hand.

In literature, the reorganization of actin filaments into bundle-like structures induced by methylcellulose was reported by *Murrell* and *Gardel* at concentrations above 0.25% (*w*/*v*)[31] and by *Köhler et al.* at concentrations above 0.20% (*w*/*v*).[205] In the data presented here, bundle formation was already observed at MC concentrations of 0.08% (*w*/*v*). Since reorganization into bundles drastically changes the viscoelastic properties of actin networks and significant changes can occur even if the microstructure seems to be unaffected,[205] only MC concentrations of 0.02% (*w*/*v*) were used in this thesis for further experiments. These conditions allow the formation of homogeneous and isotropic F-actin network, which is an important prerequisite for passive microrheology studies (see chpt. 3.4.1).[152]

4.2.4 Impact of the Pinning Point Density on the Self-organization of Actin Networks attached to Lipid Bilayers

MACs were formed by the dynamic attachment of F-actin networks to PIP_2-containing lipid bilayers via ezrin T567D (see chpt. 4.2.2). The density of the F-actin attachment points – the so-called pinning point density − is regulated through the amount of PIP_2 in the lipid bilayer. In the plasma membrane of cells the amount of PIP_2 is generally in the range of 1 mol%, but can be enriched locally to concentrations of about 5 mol%.[59–61] To investigate the influence of PIP_2 on the morphology of membrane-attached actin networks, MAC with different amounts of PIP_2 − in a range compatible with the aforementioned reported values in literature – were studied using fluorescence microscopy. Exemplary fluorescence micrographs of MACs with PIP_2 concentrations of 0.5 mol%, 3 mol% and 5 mol% are shown in figure 4.12.

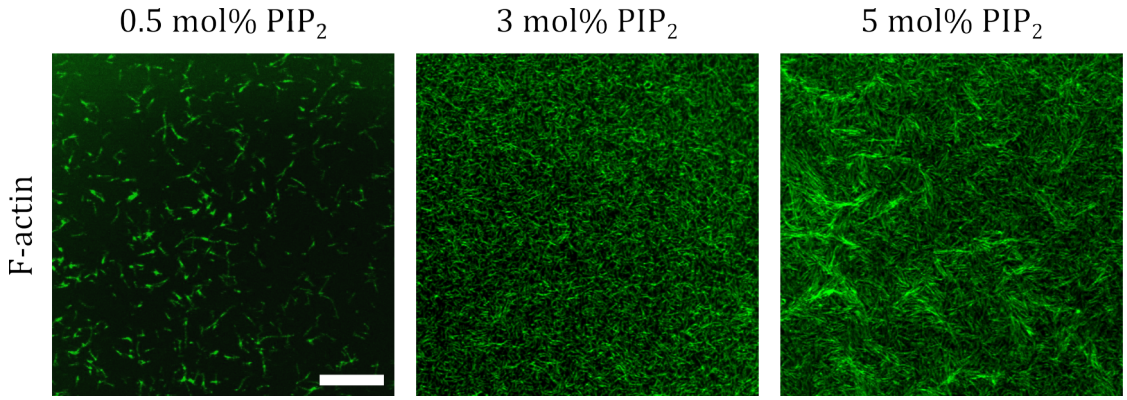

Figure 4.12: Fluorescence micrographs of F-actin attached via the linker ezrin T567D to SSMs with different amounts of PIP_2. F-actin was labeled with AF 488-Phal. Pre-polymerized F-actin was crowded on the SSMs with MC (0.02% (w/v)). After incubation and rinsing, different network morphologies can be observed depending on the concentration of PIP_2. On SSMs consisting of 99.1 mol% POPC, 0.5 mol% PIP_2 and 0.4 mol% TxR-DHPE only few filamentous structures are visible. Attachment of F-actin onto a SSM composed of 96.6 mol% POPC, 3.0 mol% PIP_2 and 0.4 mol% TxR-DHPE results in a dense, isotropic and branched network structure. On SSMs consisting of 94.6 mol% POPC, 5 mol% PIP_2 and 0.4 mol% TxR-DHPE a denser isotropic actin network with partial bundle-like structures can be observed. An increasing PIP_2 concentration in the SSM leads to more pinning points and therefore denser actin networks. Scale bar: 12 µm. Data was partially collected in the Bachelor thesis of *Siqi Sun* (2018).

For MAC with 0.5 mol% PIP_2, only few actin filaments were attached to the SSM (see fig. 4.12, 0.5 mol% PIP_2). At these concentrations, the pinning point density is too low to bind an intact network layer to the membrane. With increasing pinning point density, MACs with homogeneous isotropic actin networks were observed that completely covered the membrane (see fig. 4.12, 3 mol% PIP_2). A further increase of pinning points led to denser actin networks, in

which isotropic bundle-like structures began to form (see fig. 4.12, 5 mol% PIP_2). Thus, a clearly visible impact of the PIP_2 content on the F-actin architecture was found. An increasing PIP_2 concentration led to an increase of the ezrin surface coverage and consequently to the formation of denser actin networks, which was also reported by *Nöding* and *Schön et al.*[65] At concentrations of 6 mol% PIP_2 in the membrane, a maximal ezrin surface coverage was observed.[65] An influence of the pinning point density on the cortex thickness was not found in *z*-stack images recorded in this thesis, which is consistent with literature.[65]

Compared to 3D actin networks with filament contour lengths L_c of about 12 µm, calculated according to equation 4.2 (see chpt. 4.1.4), the filaments in the fluorescence micrographs of the MACs seems to be smaller (see fig. 4.12). Here, an evaluation of the network structure based on skeletonization using an artificial retina (see chpt. 3.4.3) was not possible, due to the low image resolution and the low number of the CLSM micrographs. Therefore, a manual filament contour length analysis based on human eye was performed with the IMAGEJ software using a simple line selection tool. This analysis could not be applied to the fluorescence micrographs of MACs with 3 mol% and 5 mol% PIP_2, because the start and end points of the individual filaments within the dense networks could not be identified. The filament contour length analysis of the fluorescence micrograph of a MAC containing 0.5 mol% PIP_2 (see fig. 4.12, 0.5 mol% PIP_2) is shown in figure 4.13.

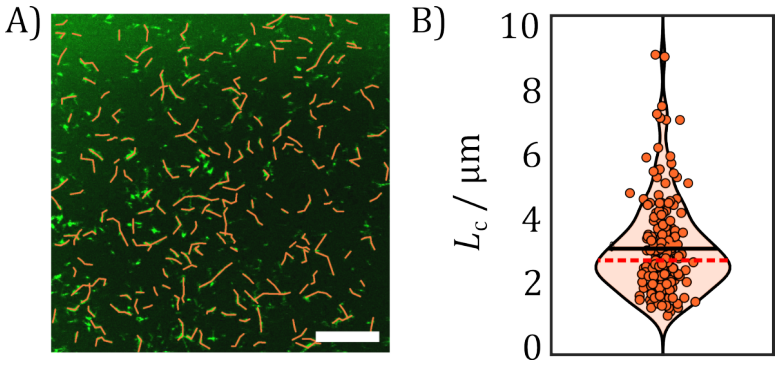

Figure 4.13: Manual analysis of the filament contour length L_c of a MACs containing 5 mol% PIP_2. **A)** Actin filaments on a fluorescence micrograph were identified by human eye and analyzed using the line selection tool of the IMAGEJ software (orange lines). Scale bar: 12 µm. **B)** Violin plot of the filament contour length analysis with a mean value (solid black line) of $\overline{L}_c$ = (3.1 ± 1.4) µm and a median value (dashed red line) of 2.7 µm (N = 190). Here, N displays the number of identified filaments.

For the identified single filaments on the MAC with a SSM containing 0.5 mol% PIP_2 (see fig. 4.13, A), a mean contour length of $\overline{L}_c = (3.1 \pm 1.4)$ µm (median: 2.7 µm, $N = 190$) was

determined (see fig. 4.13, B). This is about a quarter of the filament length calculated for 3D actin networks (see chpt. 4.1.4), and significantly below values given in literature for artificial actin gels, which are in the range of 10 - 30 µm.[10,162,185] Shorter filament contour length on MACs compared to 3D actin gels were also found by *Schön*.[177] He determined filament lengths of (3.8 ± 2.5) µm ($N = 397$) for MACs with SSMs containing 1 mol% PIP_2 using an artificial retina analysis and filament lengths of (17 ± 3) µm for 3D actin networks,[177] which is similar to the data presented here. Furthermore, he found a tendency to shorter actin filaments with increasing pinning point density in MACs.[177] Smaller contour lengths of about 2.2 µm ($N = 380$) were determined by *Vogel et al.* for actin filaments bound to a solid supported membrane via a biotin-neutravidin linkage.[30] The addition of myosin II filaments led to a further reduction of the F-actin length down to 0.7 µm ($N = 342$).[30] This shortening can be explained by filament fragmentation due to breakage processes induced by the active motor proteins.[2,30] These results indicate that a remodeling of F-actin might occur during binding processes. Consequently, the binding of F-actin to the membrane could also lead to a fragmentation of the filaments and thus to shorter contour length, as observed for the MACs in this thesis as well as in literature.[30,177] In the cortex of living HeLa and M2 cells *Fritzsche et al*. found even smaller contour lengths − for formin-nucleated and Arp2/3-nucleated actin filaments − in the range of 1.20 µm to 60 nm.[206] According to *Chugh et al*. this remodeling of the actin network architecture through filament shortening is important for the regulation of the plasma membrane tension.[48]

These findings imply that actin architecture is not only influenced by actin binding proteins, but also by the attachment of F-actin to the plasma membrane and thus the pinning point density, which is regulated in this thesis by the PIP_2 concentration in the SSM. The mechanical properties of membrane-attached actin networks in dependence of the pinning point density will be discussed in the next chapter.

4.2.5 Impact of the Experimental Setup on the Viscoelastic Responses of Actin Networks attached to Lipid Bilayers

The mechanical properties of actin cortices strongly depend on their architecture.[48,206,207] In 2D MACs it was found that the pinning point density – and thus the attachment points of the actin cortex on the membrane regulated by PIP_2 – modifies actin morphology (see chpt. 4.2.4) and consequently also actin mechanics. In order to analyze the viscoelastic behavior of MACs – in presence of the crowding agent methylcellulose (MC) – as a function of the pinning point density, video particle tracking (VPT) based passive microrheology (PMR) experiments were performed (see chpt. 3.4.1). Therefore, carboxylate-modified polystyrene beads (r = 1 µm) were incorporated in the pre-polymerized F-actin networks, which were attached to the SSMs – with different PIP_2 concentrations – via the linking protein ezrin T567D (see chpt. 3.2.3). A proper bead incorporation was only possible in dense actin layers, which formed at PIP_2 concentrations of 3 mol% and 5 mol% (see fig. 4.12), thus only MACs with these compositions were investigated. Exemplary fluorescence micrographs of the membrane-attached F-actin networks with incorporated beads are shown in figure 4.14.

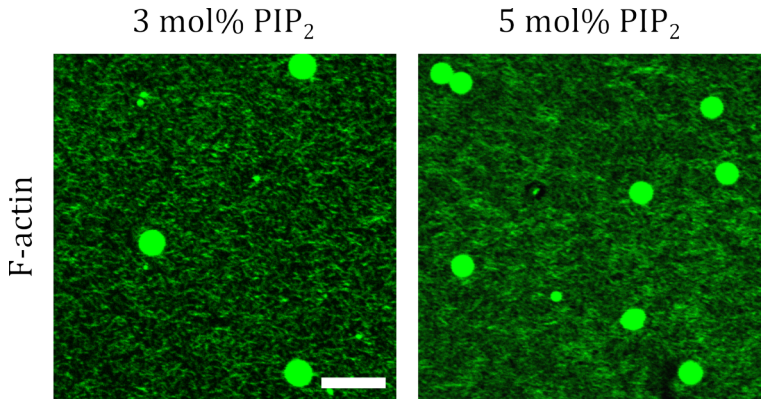

Figure 4.14: Fluorescence micrographs of AF 488-Phal labeled F-actin networks containing beads (r = 1 µm). F-actin was crowded to the SSM with MC (0.02% (w/v)) and attached via the linker ezrin T567D. The SSMs consist of 96 mol% POPC, 3 mol% PIP_2 and 1 mol% Atto 390-DOPE as well as of 94 mol% POPC, 5 mol% PIP_2 and 1 mol% Atto 390-DOPE. After incubation and rinsing, an isotropic branched actin network with incorporated beads can be observed, whereby the network density increases with a higher amount of PIP_2 in the SSM. Scale bar: 10 µm. Data was collected in the Bachelor thesis of *Siqi Sun* (2018).

The fluorescence micrographs of the MACs show intact actin cortex layers with incorporated beads. With increasing pinning point density, a denser network morphology was observed, as discussed in chapter 4.2.4. For microrheology investigations of the obtained MACs, VPT measurements were performed using two different microscopy techniques for bead

tracking – namely fluorescence microscopy (see chpt. 3.3.2) and darkfield microscopy (see chpt. 3.3.2) – to examine, whether the viscoelastic response of the network is influenced by the microscopy method. Similar experiments were carried out on 3D actin gels, as described in chapter 4.1.2. The obtained mean square displacements (MSDs) and viscoelastic frequency spectra of the MACs are shown in figure 4.15.

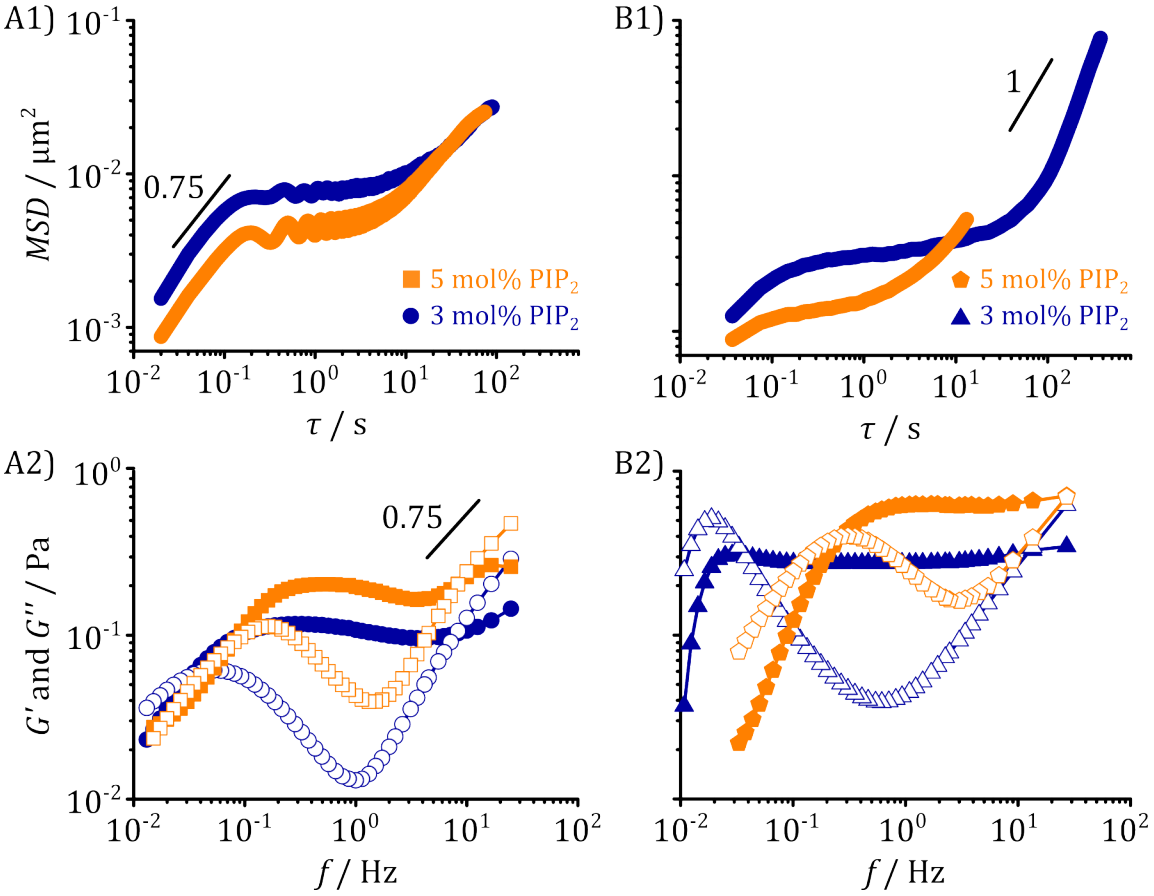

Figure 4.15: The MSD (time and ensemble averaged) and frequency-dependent viscoelastic properties of artificial 2D actin networks, attached via ezrin T567D to PIP_2 containing SSMs, measured by VPT using different microscopy techniques. The scaling behavior of the power law with an exponent of 0.75 and 1 are shown as black lines. The storage modulus G' is displayed as filled symbols and the loss modulus G'' as open symbols. **A1)** MSDs as well as **A2)** G' and G'' of MACs on SSMs were determined by means of VPT using fluorescent light to track beads (r = 1 µm) incorporated in the actin network at 50 fps over a tracking period of 800 s. The SSMs consist of 96 mol% POPC, 3 mol% PIP_2 and 1 mol% Atto 390-DOPE as well as of 94 mol% POPC, 5 mol% PIP_2 and 1 mol% Atto 390-DOPE. For MACs attached to a SSM doped with 3 mol% PIP_2 a plateau modulus of G_0 = 108 mPa (N = 1, blue circles) and for SSM containing 5 mol% PIP_2 a plateau modulus of G_0 = 189 mPa (N = 16, orange squares) was determined. **B1)** MSDs as well as **B2)** Storage and loss modulus of MACs attached to SSMs were measured by VPT using the darkfield microscopy technique to track tracer particles (r = 1 µm) within the actin network at 20 fps over a tracking period of 600 s. SSMs composed of 96.6 mol% POPC, 3.0 mol% PIP_2 and 0.4 mol% TxR-DHPE and of 94.6 mol% POPC, 5 mol% PIP_2 and 0.4 mol% TxR-DHPE were used. A plateau modulus of G_0 = 274 mPa (N = 4, blue triangles) was measured for SSMs containing 3 mol% PIP2 and G_0 = 615 mPa (N = 3, orange pentagons) for SSMs doped with 5 mol% PIP_2. Here, N represents the averaged tracer particle trajectories. Data was partially collected in the Bachelor thesis of *Siqi Sun* (2018).

As described in detail in chapter 4.1.2, the MSDs (see fig. 4.15, A1 and B1) of the semiflexible actin networks and thus the corresponding frequency spectra (see fig. 4.15, A2 and B2) exhibit three different regimes, which will be discussed in the following.

MSDs of 2D MACs determined by VPT Measurements using Fluorescence and Darkfield Microscopy

Independent of the microscopy technique of VPT measurements, a low, intermediate and high lagtime regime was found for the time (see eq. 3.16) and ensemble averaged MSDs of beads incorporated in 2D F-actin networks.

Within the low lagtime regime (τ in the range of about 10^{-2} - 10^{-1} s) of MSDs measured by fluorescence microscopy, a diffusive exponent α in the range of 0.81 to 0.86 was determined. The low τ regime for MSDs measured using darkfield microscopy are not completely resolved and only an α value of about 0.6 can be estimated from MACs with 3 mol% PIP_2 in the SSM. As already discussed in chapter 4.1.2, a theoretical power law scaling of ¾ is expected for semiflexible polymers like F-actin, induced by single filament mechanics.[161,167–170,181] In literature diffusion exponents between 0.4 and 0.85 can be found,[76,182] due to differences in network morphology, such as variations in contour length L_c.[182] According to *Liu et al.* contour length of 0.5 µm in 3D actin gels led to diffusion exponents of about 0.85.[182] Therefore, the α values of the fluorescence microscopy measurements might be an indication for the formation of short filaments on the MACs, which was also observed in fluorescence micrographs (see fig. 4.13). However, a direct comparison between the 3D and 2D networks is difficult, because the model systems have different binding and unbinding kinetics, which is associated with different rheological properties.[65] A comparison to the darkfield measurements cannot be done due to the low resolution.

At intermediate lagtimes (τ in the range of about 10^{-1} - 10^{1} s), a plateau regime was observed, where bead movements are constrained by entangled actin filaments. Here, for both microscopy techniques, a decrease of the averaged bead motion with increasing pinning point density was found. In fluorescence microscopy measurements, a MAC containing 3 mol% PIP_2 showed an averaged bead motion of about 89 nm, which decreased by about 20% with an increase of the PIP_2 concentration to 5 mol% (~71 nm). Similar experiments without the crowding agent MC performed by *Nöding* showed a decreased bead motion of 30% with larger PIP_2 amount from 3 mol% with around 80 nm to 5 mol% with around 55 nm. Darkfield microscopy measurements

even showed a 40% decrease in the averaged bead motion, when the PIP_2 amount was increased from 3 mol% (~55 nm) to 5 mol% (~32 nm). The reduced bead movement at higher PIP_2 concentrations can be explained by the formation of denser actin networks due to the increase in attachment points of the F-actin layer to the SSM (see chpt. 4.2.4). Comparing fluorescence and darkfield measurements, the latter showed about 38 - 55% lower averaged movements of the incorporated beads. This could be caused by light-induced softening of the F-actin layer induced by the fluorescent imaging technique, as reported by *Golde et al*.[178] and observed in this thesis for 3D actin gels (see chpt. 4.1.2). Furthermore, it is conceivable that the fluorescent light weakens the PIP_2-ezrin-actin binding, which would also soften the network and thus enable larger bead movements. A comparison between the darkfield measurements of 2D MACs and 3D F-actin gels showed that the averaged bead motion within the 3D actin networks is about three times larger (~140 nm, see chpt. 4.1.2) than in the actin layer. In living TC7 cells, however, even smaller bead movements of around 22 nm were found.[183] This clearly shows that the coupling of the actin cortex to a lipid bilayer plays an important role in the regulation of cortex stiffness in cells and that the binding of F-actin to the membrane via the lipid receptor PIP_2 and the linker ezrin T567D, which was used here for MACs, mimics the situation in living cells well.

Within the high lagtime regime ($\tau > 10^1$ s), large differences in the power law scaling can be observed in the range of 0.62 to 1.61. As discussed in chapter 4.1.2, this regime is experimentally difficult to access. Here, diffusion exponents of about one can be attributed to free diffusion of the beads – by overcoming the filament restrictions on these time scales – while super-diffusion ($\alpha > 1$) in F-actin networks without active components such as myosin motors has not been reported so far and might be an artefact.

Storage and Loss Moduli of 2D MACs determined by VPT Measurements using Fluorescence and Darkfield Microscopy

The frequency-dependent viscoelastic properties of MACs were determined from the corresponding MSDs of the fluorescence (see fig. 4.15, A2) and darkfield (see fig. 4.15, B2) microscopy measurements, similar to the microrheology experiments of 3D actin gels (see chpt. 4.1.2). For this purpose, the complex shear modulus $G^*(f)$ – consisting of the storage modulus $G'(f)$ for the description of the elastic contribution and the loss modulus $G''(f)$ for the description of the viscous contribution – was calculated (see chpt. 3.4.1). The resulting

frequency spectra showed the characteristic low, intermediate and high frequency regimes (see fig. 3.23), which will be discussed separately below with the focus on the intermediate frequency regime.

The low frequency regime (f in the range of 10^{-1} - 10^{-2} Hz) is determined by dynamic processes, such as binding kinetics of cross-linkers or diffusive motions of actin filaments, so-called reptation, which lead to dissipation of elastically stored energy and thus to $G'(f) < G''(f)$.[162–165] In MACs, the relaxation processes in the low frequency regime are mainly determined by the reptation movement of the actin filaments and the coupling of the actin filament to the membrane via ezrin T567D. Consequently, two peaks are expected in the loss modulus, but in the frequency spectra only one broadened peak was observed. A reason for this might be that the time scales of the relaxation of filament reptation and the unbinding kinetics of the PIP_2-ezrin-actin complex are too close and cannot be resolved by VPT measurements. The unbinding rate k_{off} of entangled actin filaments can be roughly obtained from the reptation frequency f_{rep} using the relation $k_{off} \approx 2\pi f_{rep}$,[164] which results in k_{off} rates of 0.50 s^{-1} (5 mol% PIP_2) and 0.19 s^{-1} (3 mol% PIP_2) for fluorescence microscopy measurements. For darkfield microscopy measurements higher unbinding rates of 1.70 s^{-1} (5 mol% PIP_2) and 0.25 s^{-1} (3 mol% PIP_2) were determined. Accordingly, the imaging technique might influence the binding kinetics and thus also viscoelastic properties of the material,[76] as already discussed in chapter 4.1.2. In addition, the k_{off} rates increase with rising pinning point density, possibly due to an increase in the confinement of actin filament movement with a higher number of attachment points.[65] For the k_{off} rate of the PIP_2-ezrin-actin complex, values in the range of 0.03 - 1.63 s^{-1} were reported in literature,[62,65,208] which overlap with the unbinding rate of filament reptation, thus only a broadened peak in the loss modulus was measured. In general, the interpretation of the VPT data in low frequency regime is difficult, because this regime is sensitive to slow motions, such as rocking movements of beads not properly incorporated into the actin network as well as drifting processes within the solid supported membrane.[153]

Within the intermediate frequency regime (f in the range of about 10^{-1} - 10^{1} Hz), the actin networks behave like elastic solids with $G'(f) > G''(f)$. This regime is characterized by the plateau modulus G_0, which mirrors the rigidity of the meshwork (see chpt. 4.1.2).[163,166] Independently of the microscopy technique used for the VPT experiments, a raised stiffness of the MACs was observed with an increase of the PIP_2 concentration in the SSMs from 3 mol% to 5 mol%. For darkfield microscopy measurements G_0 increased by a factor of 2.24 from 274 mPa

(3 mol%, $N = 4$) to 615 mPa (5 mol%, $N = 3$) and for fluorescence microscopy measurements, the plateau modulus grew by a factor of 1.75 from 108 mPa (3 mol%, $N = 1$) to 189 mPa (5 mol%, $N = 16$). The same was found by *Nöding* and *Schön et al.*[65] for MACs in absence of methylcellulose (MC) using VPT measurements with fluorescence microscopy. They determined a 1.73-fold increase of G_0 from 135 mPa (3 mol%, $N = 6$) to 233 mPa (5 mol%, $N = 9$).[65] Lower plateau moduli of about 100 mPa were calculated for entangled 3D actin networks (see chpt. 4.1.2 and 4.1.4), which indicates that attachment of F-actin to a membrane leads to a stiffening of the actin networks. Furthermore, these results show a clear influence of the pinning point density on the rigidity of the actin layer. With a higher amount of pinning points (higher PIP_2 concentrations in the SSM) not only the F-actin density increases (see fig. 4.12), but also the confinement of the actin filament movement through the ezrin linkage to the membrane, which results in stiffer MACs.[65] The comparison of the fluorescence and darkfield experiments showed lower absolute stiffnesses of the MACs measured by fluorescent imaging, as already observed for 3D actin gels (see chpt. 4.1.2). On the one hand, the fluorescent light is supposed to lead to a softening of the actin network by photochemical damage, as reported by *Golde et al*.[178] On the other hand, it is assumed that the coupling of F-actin to the SSM via erzin and PIP_2 is weakened, which might reduce the confinement of F-actin movements and thus the actin cortex stiffness. In order to express the ability of a cross-linker to strengthen F-actin networks, a power law scaling is usually applied in the form of $G_0 \propto R^x$, where R is the ratio of cross-linkers to G-actin concentration. According to *Nöding* and *Schön et al.*, R in MACs is equivalent to the pinning point density χ_{PIP_2} and consequently the concentration of PIP_2 in the membrane.[65] The scaling behavior of G_0 as a function of χ_{PIP_2} for fluorescence and darkfield microscopy measurements is shown in figure 4.16.

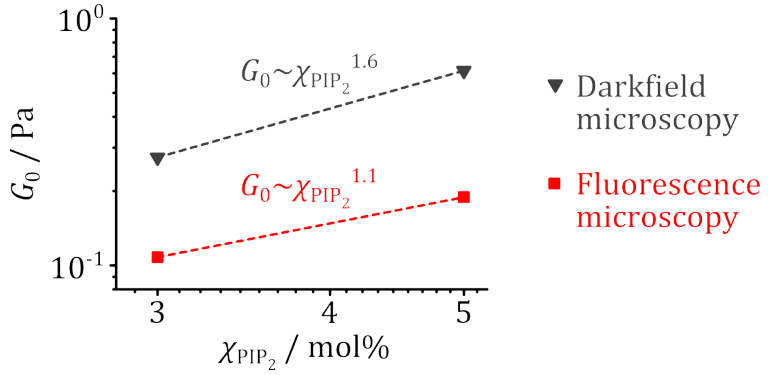

Figure 4.16: Power law scaling behavior of the plateau modulus G_0 as a function of the pinning point density χ_{PIP_2} in MACs determined via VPT using different microscopy techniques. For fluorescence microscopy measurements, a scaling of $G_0 \propto \chi_{PIP_2}^{1.1}$ (red squares) was calculated and for darkfield microscopy measurements $G_0 \propto \chi_{PIP_2}^{1.6}$ (grey triangles). The dashed lines show the corresponding power law fit.

A ratio of $G_0 \propto \chi_{PIP_2}^{1.1}$ was determined using fluorescence microscopy and of $G_0 \propto \chi_{PIP_2}^{1.6}$ for darkfield microscopy. *Nöding* and *Schön et al.* found a dependency of $G_0 \propto \chi_{PIP_2}^{1.5}$ for MACs without MC,[65] which agrees well with the data presented here. For cross-linked 3D F-actin networks, *Lieleg et al.*[79] reported a power law exponent of about 2 and *MacKintosh et al.*[166] of 2.5, which is higher compared to the quasi-2D MACs. However, a direct comparison between the two model systems is difficult, because the final concentration of the F-actin coupled to the SSM is not known and the influence of the attachment points on the filament confinement is hard to quantify. In contrast, lower power law exponent of 1 were reported by *Ershov et al.*[88] for actin networks coupled to a lipid monolayer through biotin-streptavidin and by *Head et al.*[209] for affinely deforming 2D networks in simulation studies. The power law scaling of the MACs measured here − with exponents in the range of 1.1 to 1.6 − is similar to the scaling behavior predicted for nonaffine 3D actin gels with $G_0 \propto c_A^{7/5}$ (see chpt. 4.1.2), which was also found by *Nöding* and *Schön et al.*[65]

Furthermore, a linear relationship was found for the pinning point density χ_{PIP_2} and the mesh size ξ of the actin cortices attached to the SSMs.[153] Consequently, there is also a connection between G_0 and ξ. In this thesis a network structure analysis based on skeletonization using an artificial retina could not be performed, as mentioned before. Therefore, mesh sizes of MACs without MC calculated by *Schön*[177] using an artificial retina analysis were used for further characterization of the model system. For MACs with a SSM containing 3 mol% PIP_2, a mesh size of (1.0 ± 0.6) µm was determined, which decreases to (0.8 ± 0.4) µm with an increase of the PIP_2 concentration to 5 mol%,[177] due to the formation of denser networks with a higher number

of pinning points (see fig. 4.12). According to *Gardel et al.*, smaller mesh sizes lead to a higher network stiffness:[80]

$$G_0 \approx \frac{k_B T l_p^{\,2}}{\xi^2 l_c^{\,3}} \tag{4.7}$$

Here, $k_B T$ is the thermal energy, l_p the persistence length and l_c the distance between cross-links, or for pure actin networks the so-called entanglement length. With a persistence length of 17 µm[4,9,10,80] and mesh sizes of 0.8 - 1 µm[177] l_c can be determined as follows.[76]

$$l_c \approx \xi^{\frac{4}{5}} l_p^{\frac{1}{5}} \tag{4.8}$$

Using equation 4.8, entanglement length in the range of 1.5 - 1.8 µm were calculated for the MACs, which is close to entanglement length of 1 µm reported by *Isambert and Maggs* for semidiluted solutions of F-actin.[185] Based on equation 4.7, this results in a theoretical plateau modulus of 217 mPa for MACs containing 3 mol% PIP_2 and 579 mPa for MACs with SSMs doped with 5 mol% PIP_2 at temperatures of 298 K. These theoretically determined values correspond well with the plateau moduli of darkfield microscopy measurements presented here. An overview of the scaling behavior of the plateau modulus (determined in different ways) in dependence of the mesh size for MACs is shown in figure 4.17.

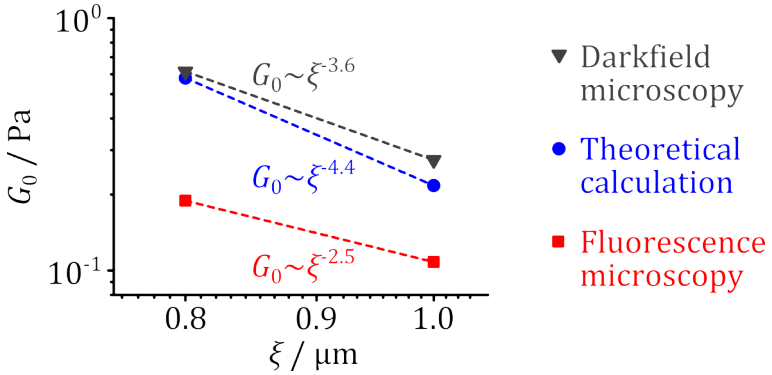

Figure 4.17: Power law scaling behavior of the plateau modulus G_0 as a function of the mesh size ξ in MACs determined via VPT using different microscopy techniques. The mesh size of MACs containing 3 mol% and 5 mol% PIP_2 was calculated by *Schön* using an artificial retina analysis.[177] For fluorescence microscopy measurements, a scaling of $G_0 \propto \xi^{-3.6}$ (red squares), for theoretically calculated plateau moduli according to *Gardel et al.*[80] of $G_0 \propto \xi^{-4.4}$ (blue circles) and for darkfield microscopy measurements of $G_0 \propto \xi^{-2.5}$ (grey triangles) was determined. The dashed lines show the corresponding power law fit.

The scaling of theoretically calculated plateau moduli as a function of the mesh size is $G_0 \propto \xi^{-4.4}$, while a lower dependency was found for darkfield microscopy measurements with $G_0 \propto \xi^{-3.6}$ and for fluorescence microscopy measurements with $G_0 \propto \xi^{-2.5}$. For purely entangled 3D actin networks a reciprocal scaling behavior of $G_0 \propto \xi^{-3}$ was reported by *Isambert* and *Maggs*[185] and an even higher dependency of $G_0 \propto \xi^{-5}$ was found by *MacKintosh et al.*[166] The power law scaling coefficients for 2D MACs determined in this thesis are exactly in between the values for the coefficients found in literature for 3D actin gels.

Within the high frequency regime ($f > 10^1$ Hz) the viscoelastic response is dominated by the relaxations of single filament bending modes, which usually leads to a power law exponent of ¾ in the storage and loss modulus.[167–170] Here, power law exponents of 0.80 - 0.92 were found for the loss modulus, independent on the microscopy technique used for the VPT measurements. A similar scaling behavior in the range of 0.80 - 0.84 was observed by *Nöding* and *Schön et al* for MAC without the crowding agent methylcellulose.[65] The power law scaling of the storage modulus, however, is much lower. This was also found for 3D actin gels (see chpt. 4.1.2) and can be attributed to inertia effects.[65,153,191] The high frequency regime for 2D MACs (see fig. 4.15) was more difficult to access compared to 3D actin networks (see fig. 4.2), because the frequency spectra shifted of about one order of magnitude towards higher frequencies. The increase of the pinning point density from 3 mol% to 5 mol% PIP_2 led to even higher cross-over frequencies of G' and G'', so-called entanglement frequencies. It is supposed that the restricted movement of F-actin through additional attachment points results in higher entanglement frequencies.[153]

Concluding, the viscoelastic response of minimal actin cortex model systems is governed by the dynamic coupling of F-actin to the SSM. Here, a successful linkage was achieved using the pseudophosphorylated ezrin mutant (ezrin T567D) and the receptor lipid PIP_2. With increasing PIP_2 concentration in the membrane and thus a higher number of attachment points, denser and stiffer actin networks form. Similar results were found by *Nöding* and *Schön et al.*[65] for MACs without the crowding agent methylcellulose, used in this thesis. Consequently, methylcellulose in low concentrations has no influence on the actin cortex mechanics, in contrast to the microscopy technique used for the VPT measurements. Using fluorescence imaging techniques resulted in a softening of the network in contrast to non-fluorescence imaging techniques, as also observed for 3D actin gels. However, compared to the stiffness reported for living cells in the range of several kPa,[96–99] the stiffness of the MACs with up to 615 mPa is significantly

lower. This indicates that not only the coupling of the actin cortex to the plasma membrane plays a key role in the regulation of the cell cortex stiffness, but also hundreds of ABPs, such as cross-linking proteins and motor proteins. In order to investigate the rheological properties of the entire biomolecular ensemble within the cellular cortex, top-down approaches are applied, where the actin cortex is isolated from living cells. A top-down model system of apical actin cortices isolated from living Madin-Darby canine kidney cells, strain II (MDCK II) will be discussed in the next chapter.

4.3 Architecture and Viscoelasticity of Actin Cortices

− The experiments in this chapter have been published in "Viscoelasticity of native and artificial actin cortices assessed by nanoindentation experiments" by H. Hubrich, I. P. Mey, B. R. Brückner, P. Mühlenbrock, S. Nehls, L. Grabenhorst, T. A. Oswald, C. Steinem and A. Janshoff, Nano Lett. ***2020****, 20 (9), 6329–6335.*[171] *−*

A variety of cellular processes, such as motility, adhesion and differentiation are regulated by the morphological dynamics as well as the resilience of the cell cortex and thus by its viscoelastic properties.[3,210–215] The cell cortex is a thin, transiently cross-linked actomyosin network reversibly bound to the plasma membrane via ezrin-radixin-moesin (ERM) proteins (see chpt. 1.3).[2–6] Architecture and mechanics of the actomyosin network are modulated by hundreds of actin binding proteins (ABPs) as well as by the dynamic attachment of the actin filaments to the membrane.[2,5,6,8,11,21,25–27,65] A first characterization of individual cortex components was performed using a bottom-up model system − so-called minimal actin cortex (MAC) − in which artificial actin cortices were coupled by ezrin T567D to a solid supported membrane (see chpt. 4.2). In order to study the mechanical properties of the entire biomolecule assembly in the cellular cortex, a top-down approach was used. For this purpose, apical cell cortex fragments were isolated from living, intact Madin-Darby canine kidney cells, strain II (MDCK II) and attached to a porous substrate using the sandwich cleavage method,[5,101] as described in chapter 3.2.4. This enables on the one hand to investigate the architecture and viscoelastic response of the apical cell cortex in absence of impeding intracellular contributions from the cytoplasm, organelles, the nucleus and other filament types. On the other hand, this top-down approach allows a simple external addition and directly following investigation of drugs that affect cortex mechanics. In this thesis, the viscoelastic responses of isolated apical cell cortices after treatment with different drugs were examined using force cycle experiments and compared to data obtained from MACs as well as from intact, living cells.

4.3.1 Verification of the Integrity of Isolated Apical Cell Cortices

Apical cell cortex fragments were obtained from intact, living MDCK II cells by applying the sandwich cleavage method (see chpt. 3.2.4).[5,101] In order to validate, whether intact apical cell cortex fragments were received after the isolation procedure, fluorescence microscopy measurements were performed. The corresponding staining protocols can be found in chapter

3.2.4. Exemplary confocal laser scanning microscopy (CLSM) micrographs of apical cell cortices deposited on porous substrates are shown in figure 4.18.

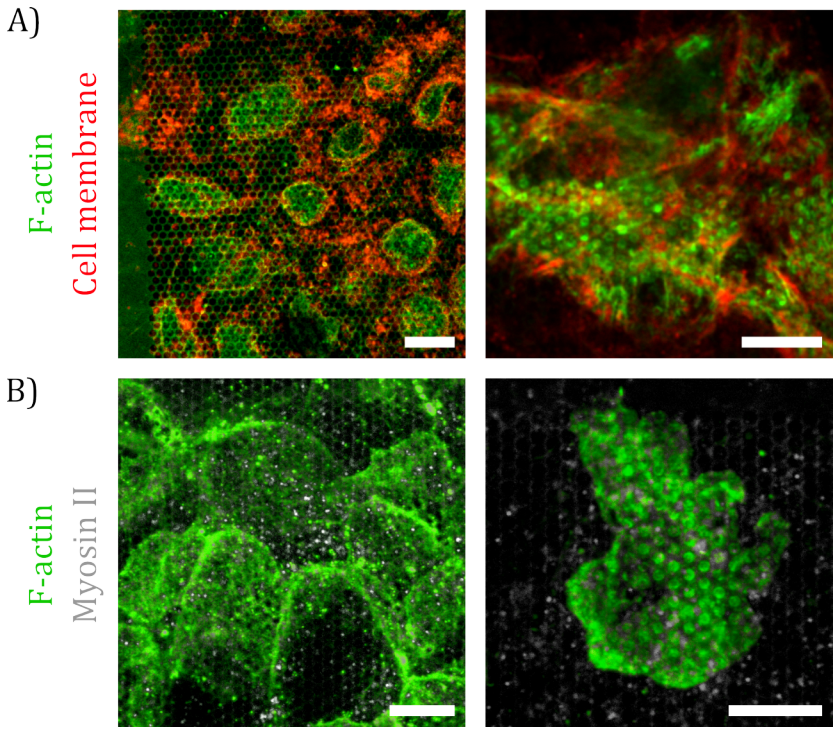

Figure 4.18: CLSM micrographs of apical MDCK II cell cortices on a porous silica substrate with a pore radius of 0.6 µm. **A)** The apical cell membrane was stained in red with CellMask Orange and F-actin in green with AF 488-Phal. **B)** Labeling of F-actin in green with AF 488-Phal and of myosin II in white using anti-phospho-MRLC (Ser 19) mouse IgG. Scale bars: 10 µm. Modified from *Hubrich et al.*[171]

The cell membrane was stained using CellMask Orange (see fig. 4.18, red), F-actin was labeled with AF 488 Phal (see fig. 4.18, green) and myosin II motor proteins were visualized using anti-phospho-MRLC (Ser 19) mouse IgG (see fig. 4.18, white). The micrographs show differences in the fluorescence intensity of the labeled actin filaments, indicating an inhomogeneous network structure. Some apical cell cortices show a dense actin morphology at the cell surface, while others exhibit dot-like filament structures, which might originate from microvilli. Microvilli are pronounced structures on the apical cell membrane of cultured MDCK II cells, which are formed and supported by actin filaments and linking proteins such as ezrin.[5] Thus, the dot-like structures in the fluorescence images indicate the presence of F-actin and ezrin on the surface of the cell membrane, which was also reported by *Nehls et al.*[5] Furthermore, myosin II motors were still present in the actin network after the preparation procedure. These results indicate a successful transfer of the apical cell cortices to the porous silica substrate and therefore a suitable top-down model system for further characterization of the actin cortex.

In addition, high resolution images of apical cell cortices were generated by means of stimulated emission depletion (STED) microscopy, as described in chapter 3.3.4. Exemplary STED images of apical cell cortices deposited on glass coverslips are shown in figure 4.19.

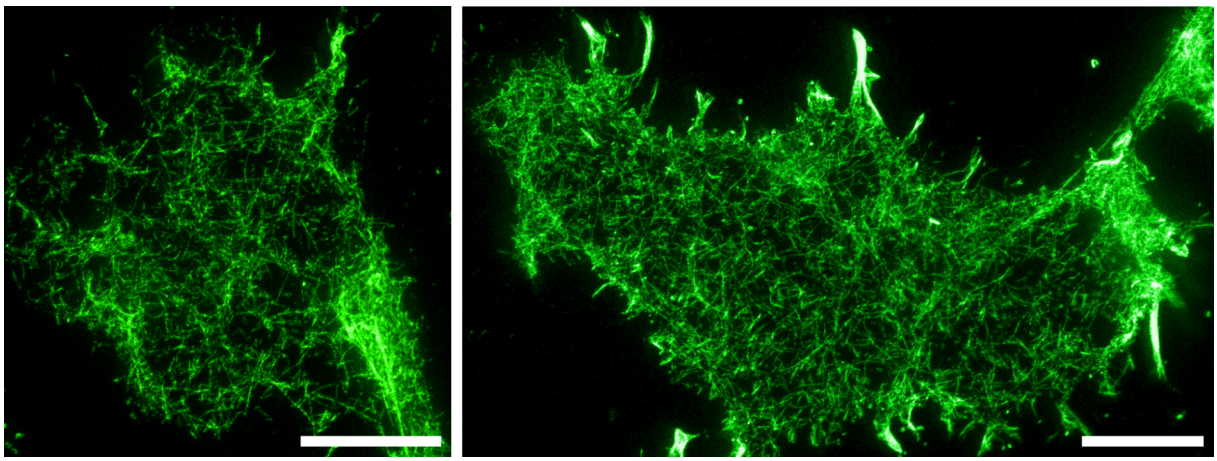

Figure 4.19: STED micrographs of apical cell cortices. F-actin was labeled with phalloidin STAR RED (here actin filaments are colored in green). Scale bars: 5 µm.

Similar to the CLSM micrographs (see fig. 4.18), intact apical cell cortex fragments with different actin network densities were observed. The high resolution STED images were used for mesh size analysis of the isolated actin cortices, which will be discussed in the following chapter.

4.3.2 Mesh Size Analysis of Isolated Apical Cell Cortices and Cortex Thickness Analysis of MDCK II Cells

− Cortex thickness experiments have been carried out by Tabea Oswald −

Important parameters for quantifying the actin cortex morphology − and thus also its mechanical properties − are the mesh size ξ and the cortex thickness d of the network layer. To calculate the average mesh size of apical cell cortex fragments isolated from MDCK II cells, high resolution STED images were converted to an artificial retina[65,174] and analyzed using a bubble analysis,[175,176] as described in chapter 3.4.3. The cortex thickness of confluent MDCK II cells was calculated from STED images by means of a self-written PYTHON script, as described by *Cordes et al.*[174] In short, the STED micrographs were smoothed by a *Gaussian* filter ($\sigma = 2$) for

noise reduction and binarized using an adaptive threshold algorithm for contrast enhancement. Structures in the micrographs were identified based on the pixel intensities of regions with areas larger than a cut-off value and then skeletonized. The cortex thickness was determined from the *Euclidian* distance between the skeleton and the edges of the identified structures.[174] The results of the mesh size and cortex thickness analysis are shown in figure 4.20.

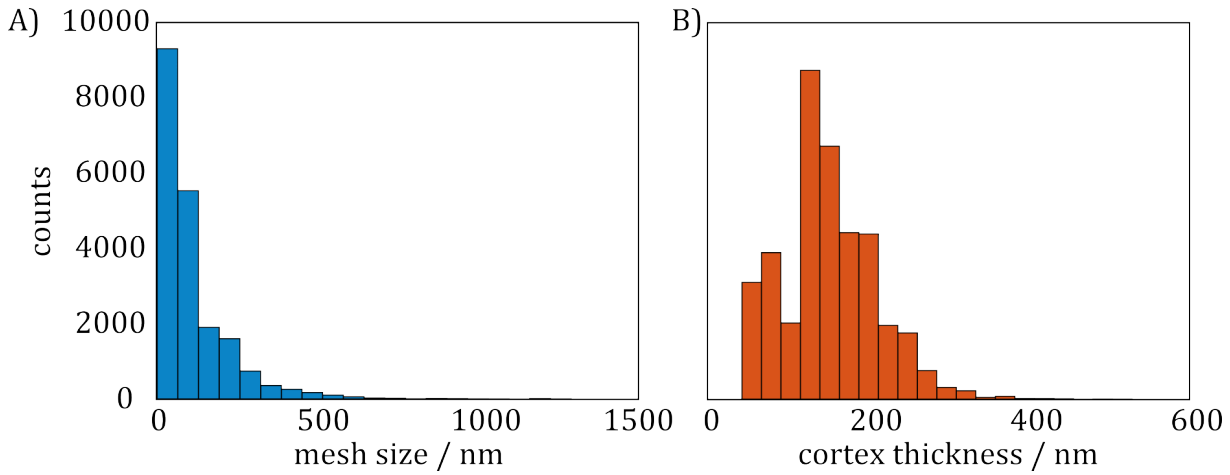

Figure 4.20: Analysis of mesh size and cortex thickness of MDCK II cells. **A)** Histogram of the mesh size of apical cell cortices (blue) obtained by an artificial retina analysis[65] of STED images of the apical cell cortices and investigated by means of a bubble analysis.[175,176] A mean mesh size of $\bar{\xi}$ = (114 ± 110) nm and a median mesh size of 80 nm was calculated. **B)** Histogram of the cortex thickness of confluent MDCK II cells (orange) determined by analysis of STED images using a self-written PYTHON sript.[174] A mean cortex thickness of $\bar{d}$ = (148 ± 62) nm and a median cortex thickness of 145 nm was calculated. Cortex thickness experiments and analysis were done by *Tabea Oswald*. Modified from *Hubrich et al.*[171]

For the mesh size of the apical MDCK II cell fragments a mean value of $\bar{\xi}$ = (114 ± 110) nm (median: 80 nm) was calculated (see fig. 4.20, A) and for the cortex thickness of living MDCK II cells, a mean value of $\bar{d}$ = (148 ± 62) nm with a median of 145 nm (see fig. 4.20, B). This is in good agreement with values reported by *Cordes et al.*[174] They found an averaged mesh size of about 130 nm for the apical cortex of MDCK II cells and an averaged cortex thickness of confluent MDCK II cells of around 220 nm.[174] A similar order of magnitude was determined by *Morone et al.*[216] for mesh sizes of fetal rat skin keratinocyte (FRSK) and normal rat kidney fibroblast (NRK) cell fragments, with values in the range of about 42 nm to 230 nm, and by *Chugh et al.*[48] for the cortex thickness of NRK cells of about 200 nm.

The results obtained here for the mesh size and cortex thickness of MDCK II cells were used for further analysis of apical cell cortex mechanics (see chpt. 4.3.3).

4.3.3 Viscoelastic Responses of Native as well as Isolated and Artificial Actin Cortices assessed by AFM Indentation Experiments

In order to investigate viscoelastic properties of cellular cortices – both in the context of living cells as well as in the absence of neighboring cells, non-cortical cytoskeletal filaments, the cytosol, the nucleus and other cell organelles − atomic force microscopy (AFM, see chpt. 3.3.7) nanoindentation experiments were performed on different model systems: confluent MDCK II cells, free standing apical cell cortices and artificial actin networks attached to free standing lipid bilayers. The experimental strategies to analyze the mechanical properties of the different model systems and the resulting cortex structures are illustrated in figure 4.21.

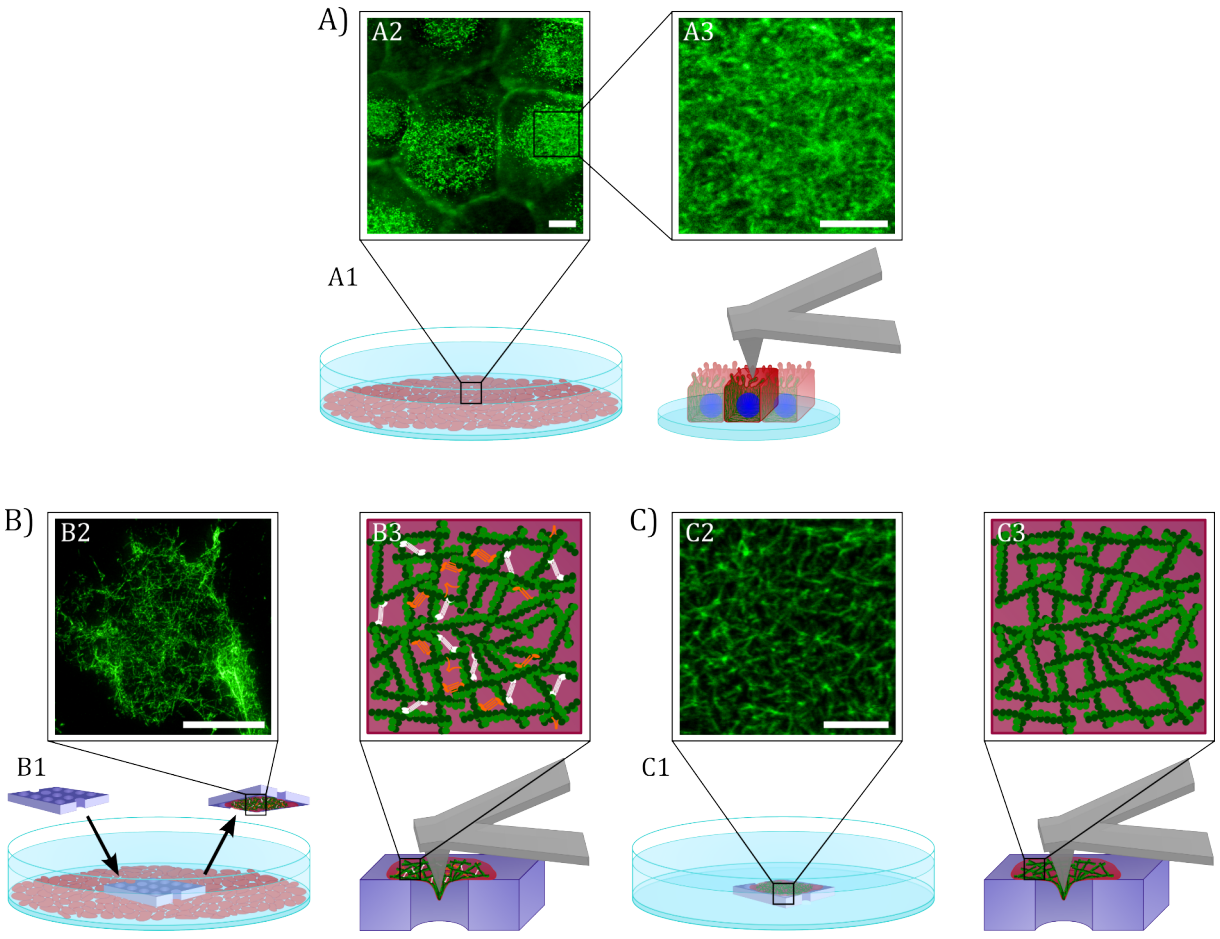

Figure 4.21: Overview of cortex preparation protocols, structure assessment and rheological properties obtained by AFM indentation experiments. **A)** *In vitro* MDCK II cell monolayer on a glass coverslip. **B)** Isolated apical MDCK II cell cortices on a porous substrate (r = 0.6 µm). **C)** Artificial minimal actin cortices (MACs) on a porous substrate (r = 0.6 µm and r = 2.5 µm). Schematic illustrations of the preparation protocols for the different model systems are shown in **A1**, **B1** and **C1**. Fluorescence micrographs of the actin cortex of the different model systems are shown in **A2-A3**, **B2** and **C2**. Schematic illustrations of the actin cortex composition of apical cell cortices and MACs are given in **B3** and **C3**. F-actin is shown in green, myosin II in white, various other cross-linkers in orange and cell membrane or lipid bilayer in red. Scale bars: 6 µm. Modified from *Hubrich et al.*[171]

The confluent MDCK II cell monolayers (see fig. 4.21, A), free standing apical MDCK II cell cortex fragments (see fig. 4.21, B) and minimal actin cortices (MACs) coupled to a pore-spanning membrane (PSM, see fig. 4.21, C) were deformed with conical indenters to obtain viscoelastic responses of the corresponding actin cortices. In STED micrographs of the cell cortex (see fig. 4.21, A1, F-actin was stained with Abberior STAR RED), actin protrusions are visible as dot-like structures at the cell surface (see fig. 4.21, A2 and A3), which indicates the presence of microvilli (see chpt. 4.3.1). The isolated apical cell cortices were obtained in a top-down fashion from living, intact MDCK II cells using the sandwich cleavage method[5,101] (see chpt. 3.2.4) and transferred to a porous substrate (see fig. 4.21, B1). STED images of apical cell cortices show an intact actin cortex with heterogeneous network densities (see fig. 4.21, B2, F-actin was stained with phalloidin STAR RED) and even microvilli-structures are preserved after cleavage, as already discussed in chapter 4.3.1. A schematic illustration of apical cell cortex composition is shown in figure 4.21, B3. In order to identify the essential composition to mimic viscoelastic properties of cellular cortices, MACs[65,66] were formed on PSMs. For this purpose, a PSM composed of DOTAP, DOPC and TxR-DHPE was prepared and pre-polymerized actin was deposited on top of the PSM by means of electrostatic interactions. PSMs possess two aqueous compartments and thus they can be indented using conventional conical cantilever tips (see fig. 4.21, C1). Since the pores are hydraulically coupled to the buffer solution, osmotic pressure gradient cannot form. An exemplary fluorescence micrograph of the F-actin network labeled with AF 488-Phal is shown in figure 4.21, C2 and a schematic illustration of the network in figure 4.21, C3.

All of the presented model systems were investigated regarding their viscoelastic properties by means of force cycle experiments using linear ramps. Before force measurements of the apical cell cortex fragments, cell membrane staining with CellMask Orange and F-actin labeling with LifeAct®-TagGFP (see chpt. 3.2.4) were used for localization of intact cell patches. Here, LifeAct®-TagGFP was used for staining of actin filament, because it is proclaimed to be non-toxic and to not interfere with actin dynamics.[151] Force indentation curves (FDCs) were recorded for each model system and fitted − for cells, as described in detail by *Hubrich et al.*[171] and for apical cell cortices and MACs according to equation 3.35 and 3.36 − to calculate the pre-stress T_0, the area compressibility modulus K_A^0 and the power law exponent β, describing their viscoelastic behavior (see chpt. 3.4.2). In order to be compliant with theory, the FDCs were acquired as close as possible to the center of the MDCK II cell or the PSM. Usually, deviations lead to slightly larger K_A^0 values and smaller β values, while T_0 remains almost unaffected.

Exemplary force time and force indentation curves and the corresponding fits of the different model systems are shown in figure 4.22.

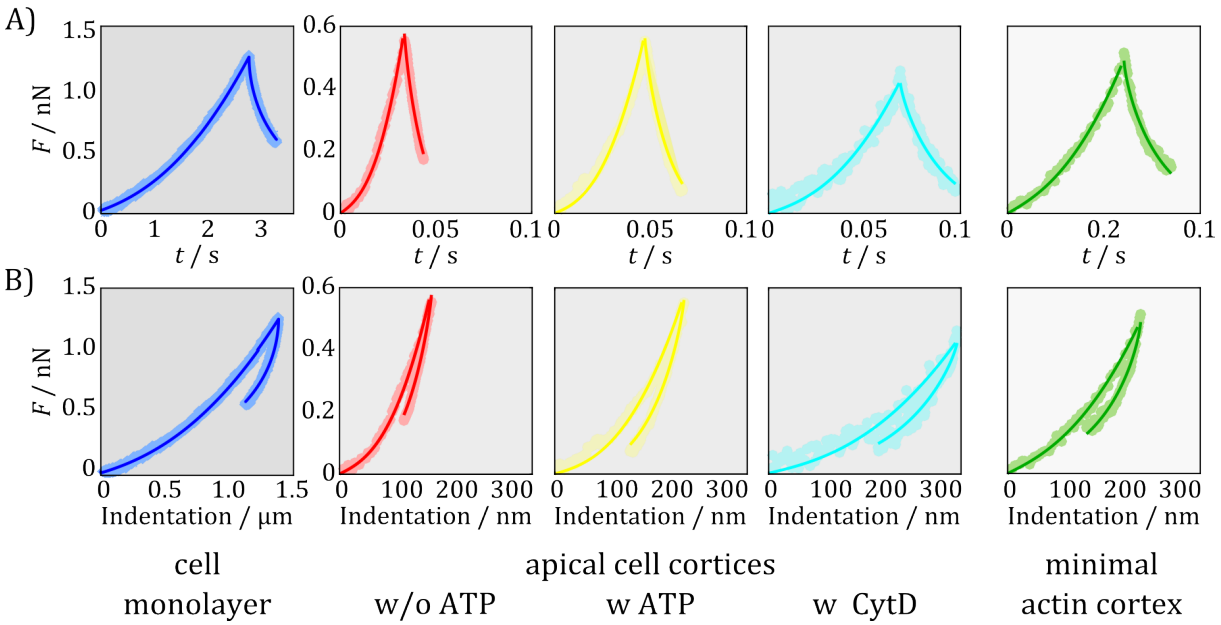

Figure 4.22: Exemplary force-time **A)** and force-indentation **B)** curves of an *in vitro* MDCK II cell monolayer (blue), of apical cell cortices in absence (red) as well as in presence of ATP (yellow) and CytD (cyan) and of MACs (green). The corresponding piecewise fit function to the single data points (filled circles) is shown as solid line. Data of the cell monolayers was collected by *Bastian Brückner* and of MACs by *Peter Mühlenbrock*. Modified from *Hubrich et al.*[171]

The piecewise fitting function comprises the approach curve $f\left(t \leq t_{\mathrm{m}}\right) = f_{\mathrm{app}}(t)$ and the retraction curve $f\left(t > t_{\mathrm{m}}\right) = f_{\mathrm{ret}}(t)$ (see chpt. 3.4.2), as illustrated in figure 4.22, A and B. In all model systems, a nonlinear force response to the indentation was observed (see fig. 4.22, B), as anticipated for area dilatation as the main contribution to the energy functional. Accumulated results of the different model systems for the pre-stress T_0, the area compressibility modulus K_{A}^{0} and the power law exponent β are presented as violin plots in figure 4.23.

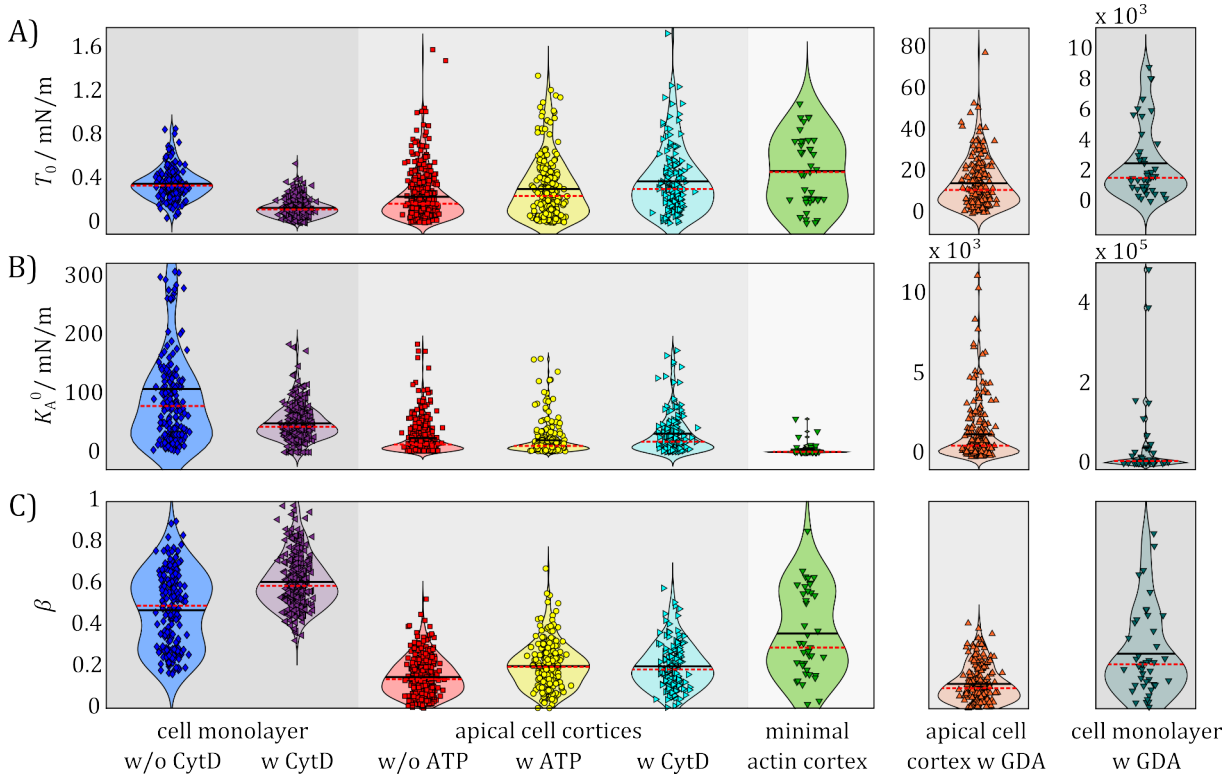

Figure 4.23: Violin plots of the pre-stress T_0 **A)**, the area compressibility modulus K_A^0 **B)** and the power law exponent β **C)** assessed from AFM indentation experiments for different model systems. Blue rhombuses represent data recorded on an *in vitro* MDCK II cell monolayer in absence ($N = 195$, $n = 20$) and purple triangles in presence of CytD ($N = 316$, $n = 8$). Red squares corresponds to data of apical cell cortices in absence ($N = 398$, $n = 4$) and yellow circles in presence of ATP ($N = 247$, $n = 4$). Cyan triangles represent data of apical cell cortices treated with CytD ($N = 149$, $n = 2$). Green triangles correspond to data of MACs ($N = 41$, $n = 6$). Orange triangles correspond to data of apical cell cortices after addition of GDA ($N = 205$, $n = 4$) and dark green triangles represent data recorded on an MDCK II cell monolayer after administration of GDA ($N = 43$, $n = 4$). The solid black lines represent the mean and the dashed red lines the median. Data of the cell monolayers was collected by *Bastian Brückner*, of MACs by *Peter Mühlenbrock* and of isolated apical cell cortices after treatment with GDA by *Stefan Nehls* and *Lennart Grabenhorst*. Modified from *Hubrich et al.*[171]

Due to their different complexity, the model systems contribute in varying manner to the pre-stress T_0, the area compressibility modulus K_A^0 and the power law exponent β. An overview of the mean, standard deviation and median of T_0, K_A^0 and β determined for each model system by AFM nanoindentation experiments is given in table 4.1.

Table 4.1: Overview of the mean and standard deviation as well as the median of the pre-stress T_0, the area compressibility modulus K_A^0 and the power law exponent β assessed from AFM indentation experiments for different model systems. MDCK II cell monolayers before (N = 195, n = 20) and after addition of CytD (N = 316, n = 8). Apical cell cortices in absence (N = 398, n = 4) and presence of ATP (N = 247, n = 4) as well as in presence of CytD (N = 149, n = 2). Minimal actin cortices (N = 41, n = 6). Apical cell cortices after addition of GDA (N = 205, n = 4) and MDCK II cell monolayers after treatment with GDA (N = 43, n = 4). Data of the cell monolayers was collected by *Bastian Brückner*, of MACs by *Peter Mühlenbrock* and of isolated apical cell cortices after treatment with GDA by *Stefan Nehls* and *Lennart Grabenhorst*.

	cell monolayer		apical cell cortices			minimal	apical cell	cell monolayer
	w/o CytD	w CytD	w/o ATP	w ATP	w CytD	actin cortex	cortex w GDA	w GDA
T_0 / mN/m								
mean:	0.36 ± 0.14	0.14 ± 0.08	0.24 ± 0.22	0.31 ± 0.28	0.39 ± 0.30	0.48 ± 0.32	14.8 ± 11.9	$(2.59 \pm 2.37)\cdot10^3$
median:	0.35	0.13	0.18	0.25	0.32	0.47	11.6	$1.65\cdot10^3$
K_A^0 / mN/m								
mean:	107 ± 120	49 ± 29	23 ± 28	19 ± 27	31 ± 36	5.2 ± 11	$(1.3 \pm 1.7)\cdot10^3$	$(40 \pm 98)\cdot10^3$
median:	78	43	12	9.3	18	1.1	$0.7\cdot10^3$	$7\cdot10^3$
β								
mean:	0.47 ± 0.18	0.61 ± 0.12	0.15 ± 0.09	0.20 ± 0.11	0.20 ± 0.11	0.36 ± 0.21	0.12 ± 0.09	0.26 ± 0.21
median:	0.49	0.59	0.14	0.20	0.19	0.29	0.10	0.21

The Pre-stress of Different Model Systems

For confluent MDCK II cells, an average cortical tension of $\overline{T}_0$ = (0.36 ± 0.14) mN/m (see fig. 4.23, A, blue rhombuses, median: 0.35 mN/m), after treatment with the F-actin depolymerization agent Cytochalasin D (CytD)[217] of $\overline{T}_0$ = (0.14 ± 0.08) mN/m (see fig. 4.23, A, purple triangles, median: 0.13 mN/m) and after treatment with the fixation agent glutardialdehyde (GDA)[5] of $\overline{T}_0 = (2.59 \pm 2.37) \cdot 10^3$ mN/m (see fig. 4.23, A, dark green triangles, median: $1.65 \cdot 10^3$ mN/m) was calculated. For apical cell cortices in absence of adenosine triphosphate (ATP) an average pre-stress of $\overline{T}_0$ = (0.24 ± 0.22) mN/m (see fig. 4.23, A, red squares, median: 0.18 mN/m), in presence of exogenous ATP of $\overline{T}_0$ = (0.31 ± 0.28) mN/m (see fig. 4.23, A, yellow circles, median: 0.25 mN/m), in presence of CytD of $\overline{T}_0$ = (0.39 ± 0.30) mN/m (see fig. 4.23, A, cyan triangles, median: 0.32 mN/m) and after treatment with GDA of $\overline{T}_0$ = (14.8 ± 11.9) mN/m (see fig. 4.23, A, orange triangles, median: 11.6 mN/m) was determined. When comparing tension data, precaution is needed, because the source of the pre-stress is different, depending on the model system. While in living cells T_0 originates from contraction of the actomyosin cortex under consumption of ATP, T_0 of the apical cell cortex fragments also mirrors the adhesion of the negatively charged plasma membrane to the positively charged pore rim.[5,101] Interestingly, a slight increase of T_0 was observed after external addition of ATP to the apical cell cortex fragments, which would be anticipated for higher contractility. For MACs a higher averaged pre-stress of

$\overline{T}_0$ = (0.48 ± 0.32) mN/m (see fig. 4.23, A, green triangles, median: 0.047 mN/m) was found compared to the untreated plasma membrane of living MDCK II cells and their apical cell cortex fragments obtained from top-down experiments. The larger pre-stress arises from higher differences of the chemical potential between the lipids adhering to the pore rim and the free-standing pore-spanning lipid bilayer.[173]

The Area Compressibility Modulus of Different Model Systems

The area compressibility modulus K_A^0 of the actin cortex is used to describe the linear-elastic resistance of the cortex shell against area dilatation. Area dilatation during indentation occurs inevitably either by compression of the living MDCK II cells at constant volume or by clamping of the apical cell cortices and the MACs at the pore rims. Both boundary conditions require the cortex to be stretched upon indentation. Since area dilatation is the main contribution to the free energy change, minimal surfaces are formed during indentation.[5,55,174] Due to the fact that the cortex is a composite structure, both, the plasma membrane as well as the actin network have to be considered in order to obtain a proper estimation for K_A^0 of the cellular cortex. If the plasma membrane is treated as a lipid bilayer, it is rather inextensible, with area compressibility moduli K_A in the range of 0.1 N/m to 0.5 N/m, depending on the lipid composition.[218] Here, a high amount of cholesterol results in larger K_A values, while a higher amount of unsaturated fatty acids leads to lower K_A values. But most importantly, epithelial cells possess a large amount of excess area, which is stored in microvilli, wrinkles and folds. The recruitment of these reservoirs is necessary to prevent cells from bursting when they are osmotically stressed. These membrane reservoirs effectively reduce the measured apparent compressibility modulus $\widetilde{K}_A = K_A A_0/(A_0+A_{ex})$, whereby the excess area A_{ex} might be 8 - 10 times the geometric area A_0, as reported by *Brückner et al.*[55] As already mentioned, not only the plasma membrane, but also the underlying actin cortex contribute to K_A. From the cortex thickness d and mesh size ξ of the cross-linked actin network, the elastic modulus can be estimated. According to *Gardel et al.*,[80] the shear modulus G of an actin network can be estimated from the persistence length l_p, mesh size ξ and the distance of the cross-linkers l_c. Using the relations $K_A = Ed$ and $E = 2G(1+\nu)$, with E the *Young's* modulus of the cortex, G the shear modulus and ν the *Poisson* ratio – here ν is assumed to be 0.5 – the area compressibility modulus can be determined as follows:[174]

$$K_A \approx \frac{3 k_B T {l_p}^2}{\xi^2} \frac{d}{{l_c}^3} \tag{4.9}$$

Based on equation 4.8, the distance between cross-links l_c in an actin cortex can be estimated using a persistence length l_p of 17 µm[4,9,10,80] and a mesh sizes of 80 nm (see chpt. 4.3.2). Assuming a cortex thickness of 145 nm (see chpt. 4.3.2) and a temperature of 298 K, equation 4.9 gives K_A values of about 6 mN/m. Thus, the area compressibility modulus K_A^0 is mainly affected by the area expansion of the membrane as well as the underlying actin cortex.

Comparing K_A^0 values of living MDCK II cells (see fig. 4.23, B, blue rhombuses, $\overline{K}_A^0$ = (107 ± 120) mN/m, median: 78 mN/m) with those of cells after treatment with CytD (see fig. 4.23, B, purple triangles, $\overline{K}_A^0$ = (49 ± 29) mN/m, median: 43 mN/m), apical cell cortex fragments treated with CytD (see fig. 4.23, B, cyan triangles, $\overline{K}_A^0$ = (31 ± 36) mN/m, median: 18 mN/m), apical cell cortices in absence of exogenous ATP (see fig. 4.23, B, red squares, $\overline{K}_A^0$ = (23 ± 28) mN/m, median: 12 mN/m) and after addition of exogenous ATP (see fig. 4.23, B, yellow circles, $\overline{K}_A^0$ = (19 ± 27) mN/m, median: 9.3 mN/m), as well as with MACs (see fig. 4.23, B, green triangles, $\overline{K}_A^0$ = (5.2 ± 11) mN/m, median: 1.1 mN/m), a successive decrease along this row was observed. These values are in the same order of magnitude as the K_A value theoretically calculated according to equation 4.9, showing that K_A^0 is mainly influenced by the cortex thickness and mesh size, as aforementioned. For the model systems investigated here, it is assumed that the cortex of the living MDCK II cells is the thickest and most densely cross-linked and thus exhibits the largest K_A^0 values according to equation 4.9, as found in this thesis. While no significant difference was found between apical cell cortices without exogenous ATP as well as after addition of exogenous ATP and CytD, MACs show the lowest K_A^0 values. One reason for this might be the absence of external cross-linkers in MACs as well as the lack of membrane stretching, because the membrane flows into the pore during indentation.[173]

GDA fixation of both, apical cell cortices (see fig. 4.23, B, orange triangles, $\overline{K}_A^0$ = (1.3 ± 1.7) · 10^3 mN/m, median: 0.7 · 10^3 mN/m) and living MDCK II cells (see fig. 4.23, B, dark green triangles, $\overline{K}_A^0$ = (40 ± 98) · 10^3 mN/m, median: 7 · 10^3 mN/m) resulted in a significant increase of K_A^0 compared to the untreated samples. The fixation agent GDA is known to lead to permanent cross-linking of protein domains within and on the plasma membrane.[5] This results in

a reduction of the accessible membrane reservoirs and thus to larger K_A^0 values, which was previously observed by *Nehls et al.*[5]

The considerable variance in K_A^0 is due to the heterogeneity of the actin network (see fig. 4.18 and fig. 4.19) − especially with respect to cortex thickness and mesh size (see chpt. 4.3.2) − and the accessibility of membrane reservoirs to buffer stretching.

The Power Law Exponent of Different Model Systems

The flow behavior of the actin cortex is characterized by the power law exponent β. An ideal elastic solid is defined by a β value of zero, while a *Newtonian* fluid is described by a β value of one.[219] For living MDCK II cells, a power law exponent of $\overline{\beta} = 0.47 \pm 0.18$ (see fig. 4.23, C, blue rhombuses, median: 0.49 mN/m) was calculated, which is in good accordance with previous findings by *Cordes et al.*[174] as well as theoretical predictions for transiently cross-linked actin networks by *Mulla et al.*[84] and *Broedersz et al.*[220] In more detail, *Broedersz et al.*[220] developed a microscopic model for long-time relaxation, which is controlled by cross-link dynamics. This model describes structural relaxation, resulting from unbinding or rebinding events of cross-linkers to actin filaments. Multiple independent events give rise to a power law in which $G \sim \omega^{1/2}$ below the characteristic frequency $\omega_0 = 2\pi/\tau_{off}$. Here, τ_{off} is the unbinding time of the linker, usually in the range of 0.1 s to 10 s. In contrast, lower β values of about 0.2 - 0.4 were found by *Kollmannsberger et al.*[219,221] using contact models derived from the *Hertz* model and β values of about 0.09 - 0.41 were reported by *Sousa et al.*[222] using a fractional *Kelvin-Voigt* model. The lack of including time-invariant pre-stress in contact models underestimates β, as recently reported by *Cordes et al.*[174] After treatment with CytD, an increase of the power law exponent to $\overline{\beta} = 0.61 \pm 0.12$ (see fig. 4.23, C, purple triangles, median: 0.59) was observed for living cells, due to the CytD-induced depolymerization of F-actin.[217] A CytD-driven softening of cells was also reported in literature.[223,224]

Compared to living cells, much lower power law exponents were determined for isolated apical cell cortex fragments, implying the presence of stiffer cortices with less transient cross-linking proteins in this model system. Note that for permanently cross-linked networks, $\beta = 0$ is expected.[219] Thus, the reduction of β is attributed partly to the preparation procedure of the top-down approach, where loosely bound proteins of the apical cortex might be rinsed away and myosin motor proteins devoid of ATP act as permanent cross-linkers. In order to quantify the latter contribution, exogenous ATP and CytD were added to the apical cell cortex fragments and

the viscoelastic response was re-examined. Comparing the power law exponents of apical cell cortices obtained in absence of ATP (see fig. 4.23, C, red squares, $\overline{\beta} = 0.15 \pm 0.09$, median: 0.14) with those obtained in presence of ATP (see fig. 4.23, C, yellow circles, $\overline{\beta} = 0.20 \pm 0.11$, median: 0.20) or CytD (see fig. 4.23, C, $\overline{\beta} = 0.20 \pm 0.11$, cyan triangles, median: 0.19), an increase of β was observed, which indicates successful fluidization of the actin cortex by activation of myosin motor proteins or by CytD-induced F-actin depolymerization. In absence of exogenous ATP, myosin proteins are in rigor state, in which the myosin heads are strongly bound to F-actin and behave like permanent cross-linkers. This results in a stiffening of the actin network. In contrast, under ATP consumption, myosin is in its active state, acting as a more dynamic and transient cross-linker. Here, fluidity of the isolated actin cortex is partially restored by sliding movements of the filaments through active myosin motors.[6,41–44] Similar results were also found for 3D actomyosin gels in rigor and active state, as discussed in chapter 4.1.3 and 4.1.4. A myosin-induced softening of non-adherent (suspended) cells was also reported by *Chan et al*.[223] In contrast, cells that adhere to solid substrates are stiffened by the activity of myosin motors, as the adhesions facilitate the formation of contractile pre-stress,[197,223] which also indicates the importance of the cell environment on the mechanical properties of cells. Furthermore, *Chan et al*.[223] measured a CytD-induces softening of cells, similar to the data presented here. The cytoskeleton disrupting drug CytD is known to inhibit the polymerization of actin by binding with high affinity to the growing end of F-actin,[217] which results in an increase of the viscous contribution, as reported by *Fabry et al.*[225]

The power law exponent β found for MACs (see fig. 4.23, C, green triangles, $\overline{\beta} = 0.36 \pm 0.21$, median: 0.29) is in between those for isolated apical cell cortices and living cells. However, there is considerable inhomogeneity in the actin cortices − reflected in a broad distribution of the β values – due to variations in cortex thickness, mesh size and differences in the density of cortex attachment points to the membrane. Furthermore, artificial MACs are less resilient compared to native apical membranes, which is reflected in their larger pre-stress T_0 (see fig. 4.23, A) and the absence of membrane reservoirs needed to buffer area dilatation. Thus, the PSM can easily be punctured during AFM indentation experiments. Furthermore, neither myosin motor proteins nor cross-linking proteins are present in the artificial actin cortex of the MACs, and actin filaments are not coupled to the membrane through adhesion proteins, such as from the ezrin-radixin-moesin protein family in case of the apical cell cortices and living cells.[27,226,227] In MACs, the negatively charged F-actin is attached by electrostatic interaction to the PSM containing positively charged DOTAP lipids. Consequently, it is assumed that the

fluidity of the artificial actin cortex in MACs is mainly determined by the entanglement of the actin filaments and the attachment points to the PSM.

Fixation of apical cell cortices and living cells with GDA led to a decrease of the power law exponent β in comparison to the untreated specimen. For isolated apical cell cortices, a reduction of β from 0.15 ± 0.09 (see fig. 4.23, C, red squares) to 0.12 ± 0.09 (see fig. 4.23, C, orange triangles, median: 0.10) was observed and for living cells an even stronger decrease from 0.47 ± 0.18 (see fig. 4.23, C, blue rhombus) to 0.26 ± 0.21 (see fig. 4.23, C, dark green triangles, median: 0.21). As already mentioned, GDA-fixation leads to permanent cross-linking of protein domains in the plasma membrane,[5] resulting in a stiffening of the actin cortex coupled to the membrane, which is mirrored in a decrease of β, as observed here.

The large deviations in β originate from the spread of the previously calculated area compressibility moduli K_A^0, since these two parameters are correlated.

The *Young's* Modulus of Native and Isolated Actin Cortices

In order to determine mechanical properties of cells, often AFM indentation experiments are performed and analyzed using common contact models. The elastic properties of cells are usually described by the so-called *Young's* modulus E. Here, the effective *Young's* modulus of living MDCK II cells was determined using a *Sneddon* fit to the AFM force cycle data.[228] For isolated apical MDCK II cell cortices the apparent *Young's* modulus was calculated via the area compressibility modulus K_A^0 obtained from force cycle experiments and the cortex thickness d (see chpt. 4.3.2) using the relation $K_A = Ed$.[174] The corresponding results for living cells and apical cell cortices after treatment with different drugs are shown in figure 4.24.

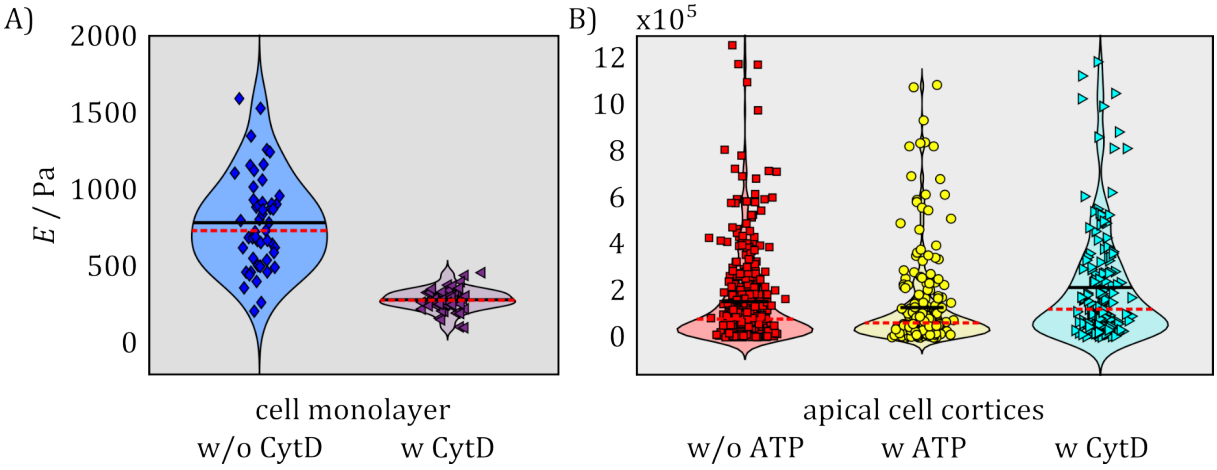

Figure 4.24: The *Young's* modulus E of *in vitro* MDCK II cell monolayers and apical cell cortices after treatment with different drugs. **A)** The effective *Young's* modulus of cell monolayers calculated by a *Sneddon* fit to the force indentation data. Blue rhombuses represent the *Young's* modulus before ($\overline{E}$ = (790 ± 308) Pa, median: 739 Pa, N = 51, n = 4) and purple triangles after treatment with CytD ($\overline{E}$ = (288 ± 70) Pa, median: 285 Pa, N = 57, n = 4). **B)** The apparent *Young's* modulus of apical cell cortices was determined by the quotient of the calculated area compressibility modulus K_A^0 and the median cortex thickness (d = 145 nm). Red squares represent data in absence of ATP ($\overline{E}$ = (1.56 ± 1.94) · 10^5 Pa, median: 8.07 · 10^4 Pa, N = 398, n = 4) and yellow circles in presence of ATP ($\overline{E}$ = (1.30 ± 1.89) · 10^5 Pa, median: 6.42 · 10^4 Pa, N = 247, n = 4). Cyan triangles correspond to data after treatment with CytD ($\overline{E}$ = (2.16 ± 2.47) · 10^5 Pa, median: 1.23 · 10^5 Pa, N = 149, n = 2). The solid black lines represent the mean and the dashed red lines the median. Data of the cell monolayers was collected by *Bastian Brückner.* Modified from *Hubrich et al.*[171]

Treating living cells with CytD resulted in a reduction of the effective *Young's* modulus compared to untreated samples from (790 ± 308) Pa (see fig. 4.24, A, blue rhombuses, median: 739 Pa) to (288 ± 70) Pa (see fig. 4.24, A, purple triangles, median: 285 Pa). CytD is known to lead to depolymerization of actin filaments,[217] which is mirrored in a reduction of E. The order of magnitude of the *Young's* modulus in the range of kPa found here for living cells is consistent with findings in literature.[174,206,219]

The apparent *Young's* modulus of isolated apical cell cortices was calculated from the quotient of the previously determined area compressibility moduli K_A^0 (see fig. 4.23, B) and the median cortex thickness d = 145 nm (see fig. 4.20, B). Here, treatment of the apical cell cortex fragments with various drugs did not lead to significant changes in the *Young's* modulus. For apical cell cortices in absence of ATP, an apparent *Young's* modulus of $\overline{E}$ = (1.56 ± 1.94) · 10^5 Pa (see fig. 4.24, B, red squares, median: 8.07 · 10^4 Pa) was determined, after addition of ATP a modulus of $\overline{E}$ = (1.30 ± 1.89) · 10^5 Pa (see fig. 4.24, B, yellow circles, median: 6.42 · 10^4 Pa) and after treatment with CytD of $\overline{E}$ = (2.16 ± 2.47) · 10^5 Pa (see fig. 4.24, B, cyan triangles, median: 1.23 · 10^5 Pa). In comparison to the living cells, these values are much larger, since only the material of the cortex is considered.

The Power Law Exponent of Isolated Actin Cortices as a Function of the Apparent Compressibility Modulus

According to *Kollmannsberger et al.*, the creep responses of cells with different stiffnesses show a common intersection point at short times, when plotted with double-logarithmic axes.[221] Consequently, a master equation is also expected here, to hold for the area compressibility modulus $K_A^0 = \kappa_A^0 (t/\tau_0)^{-\beta}$ with a common intersection point at κ_A and τ_0. In combination with $K_A(t) = K_A^0 (t/t_0)^{-\beta}$ the following relation results at $t_0 = 1$ s:

$$\beta = \frac{\ln K_A^0 - \ln \kappa_A^0}{\ln \tau_0} \tag{4.10}$$

The corresponding plots obtained from isolated apical cell cortices treated with different drugs are shown in figure 4.25.

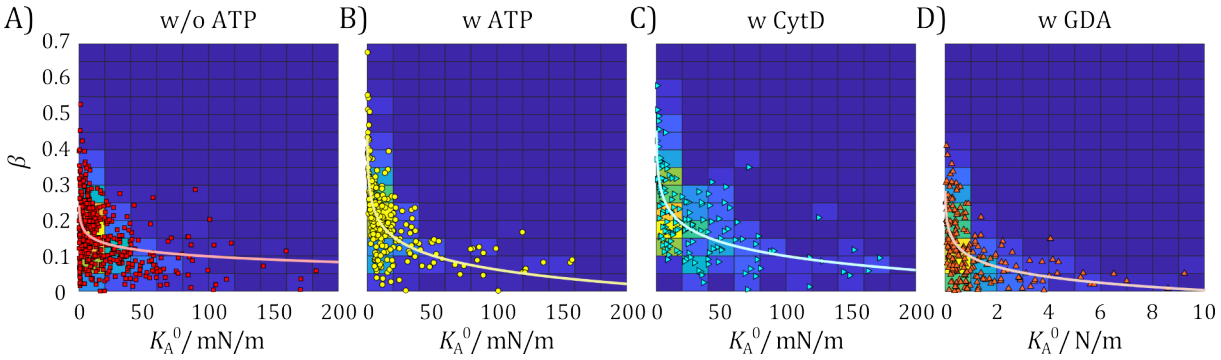

Figure 4.25: 2D histograms of the power law exponent β of apical cell cortices after treatment with different drugs as a function of their area compressibility modulus K_A^0 and the corresponding logarithmic fit function shown as solid line. **A)** Red squares correspond to data in absence of ATP ($\beta = -0.02 \log(K_A^0/7009)$, $N = 398$, $n = 4$). **B)** Yellow circles represent data after addition of ATP ($\beta = -0.06 \log(K_A^0/289)$, $N = 247$, $n = 4$). **C)** Cyan triangles show data after treatment with CytD ($\beta = -0.06 \log(K_A^0/570)$, $N = 149$, $n = 2$). **D)** Orange triangles correspond to data after administration of GDA ($\beta = -0.04 \log(K_A^0/(1.18 \cdot 10^4))$, $N = 205$, $n = 4$). Data of isolated apical cell cortices after treatment with GDA was collected by *Stefan Nehls* and *Lennart Grabenhorst*. Modified from *Hubrich et al.*[171]

While only a slight decrease of the power law exponent β with increasing area compressibility modulus K_A^0 was observed for apical cell cortices in absence of exogenous ATP (see fig. 4.25, A), the expected logarithmic behavior was shown in presence of exogenous ATP (see fig. 4.25, B) and CytD (see fig. 4.25, C). In comparison to living MDCK II cells, the isolated apical cell cortices display a shift towards smaller area compressibility moduli after addition of ATP.[174]

Without exogenous ATP, myosin motor proteins form permanent cross-links with F-actin, which results in stiffer and more solid-like cortices. Furthermore, it is assumed, that due to the increased stiffness of the membrane-attached actin cortex, existing reservoirs in the plasma membrane are not available for buffering indentation stresses. This effect is reflected in a correlated decrease of the power law exponent β and an increase of the area compressibility modulus K_A^0. After addition of exogenous ATP, myosin motors are shifted to their active state, with more transient cross-linking and thus a higher fluidity of the actin cortex, which is mirrored in an increase of β. The same fluidization effect was observed after treatment of apical cell cortices with the F-actin depolymerizing drug CytD. Furthermore, it is known that actomyosin contraction leads to blebbing,[229] which might enlarge accessible membrane reservoirs. This is mirrored in lower K_A^0 values, as observed in the data presented here. In contrast, the opposite effect was observed by fixation of apical cell cortices with GDA (see fig. 4.25, D). The GDA-induced permanent cross-linking of protein domains in the plasma membrane strengthens the actin cortex linked to the plasma membrane and leads to a reduction of the amount of accessible membrane reservoirs, which is reflected in a reduction of the β values to almost 0 and a substantial increase of the K_A^0 values.[5,101]

Concluding, AFM indentation experiments of living cells as well as of isolated apical cell cortices created in a top-down fashion and of MACs obtained in a bottom-up fashion, showed that the viscoelastic response of cells is dominated by the components of the membrane cortex. For this purpose, a viscoelastic cortex model was developed, in which the pre-stress of the actin network and the time-dependent resistance to area dilatation were considered. The shape of the deformed apical cell cortices and MACs assume minimal surfaces, since energy minimization is identical to area minimization. In particular, the actin cortex and myosin activity have a major impact on the viscoelastic behavior of cells. The fluidity of the cortex, represented by the power law exponent β, was larger in living MDCK II cells compared to isolated apical MDCK II cell cortices. In the presence of exogenous ATP, some myosin motors in the isolated apical cell cortices were reactivated, which enables the pre-stressed network to flow mirrored by slightly larger β values. Furthermore, the same logarithmic correlation between stiffness and fluidity was found as reported for living cells, indicating the existence of a master equation,[221] and consequently a correlation between elasticity and dissipative properties of cellular cortices.

5 Conclusion

The objective of this thesis was to investigate the contribution of the actin cortex to the viscoelastic properties of cells as an interplay of network architecture, myosin motor activity and adhesion to the plasma membrane. For this purpose, different model systems – namely entangled or cross-linked 3D actin gels and minimal actin cortices (MACs) created in a bottom-up fashion, as well as isolated apical cell cortex fragments obtained in a top-down fashion and intact living cells − were studied. Self-organization and viscoelastic responses derived from continuum mechanics of the different model systems were analyzed by means of fluorescence microscopy, video particle tracking (VPT) based passive microrheology (PMR), bulk rheology and nanoindentation experiments with an atomic force microscope (AFM).

The actin cortex is an active matter with a highly complex biological structure − regulated by an interplay of several hundreds of actin binding proteins (ABPs) − that constantly consumes energy in form of ATP hydrolysis to adapt its architecture and mechanics to its needs. To study this complex structure, the functions of individual, isolated components were initially examined in bottom-up strategies as imitations of living cells. First experiments were performed on entangled 3D actin gels, showing that preparation and measuring techniques were challenging, since F-actin network morphology and thus its mechanical properties were influenced by both the construction of the measuring chamber as well as by the choice of measuring method. Since in this thesis the linear viscoelastic response regime of the semiflexible polymer F-actin was investigated based on continuum mechanics, a prerequisite for microrheological studies was the formation of spatially isotropic and homogeneous networks. These network structures were successfully constructed within small water-in-oil droplets, so-called minimal cell compartments (MCCs), with volumes in the range of picoliters. Furthermore, the impact of the measuring method on the mechanics of actin networks was investigated. In PMR experiments using VPT, an impact of the illumination technique on the network stiffness – represented by the plateau modulus G_0 − of entangled 3D actin gels as well as of MACs was found. Here, a network softening was observed in PMR measurements using fluorescence imaging, which increased with longer light exposure time, while no effect on the rigidity of the actin network was determined using non-fluorescent imaging (darkfield microscopy). With the latter method, frequency spectra − in form of the storage $\left(G'(f)\right)$ and loss $\left(G''(f)\right)$ modulus – in the range of 10^{-3} - 10^{2} Hz, with the characteristic low, intermediate and high frequency regimes were

obtained, similar to results reported in literature. Furthermore, a dependence of the actin monomer concentration $\left(c_A\right)$ on the plateau modulus of entangled actin gels with $G_0 \propto {c_A}^{1.3\pm0.4}$ was obtained, indicating the formation of nonaffine actin networks.

In order to mimic cortex contractility, the motor protein myosin II and the cross-linking protein α-actinin were added to the *in vitro* F-actin networks. Under ATP excess, myosin motors are in their active state, driving the actin network out of equilibrium, which was reflected in non-*Gaussian* athermal fluctuations recorded by tracking of tracer particles embedded within the active gel. Furthermore, bulk rheology measurements with the motor fragment protein heavy meromyosin (HMM) showed significant fluidization of actin networks in the presence of active motors. Here, a reduction in stiffness by one third was measured for the active actin-HMM network compared to purely entangled actin gels. It is assumed that these fluctuations and fluidization are caused by sliding movements of the actin filaments induced by the active myosin motors under ATP consumption.

The remodeling of the actin network through motor activity is essential to build up tension. However, the role of the plasma membrane in the mechanics of the cytoskeleton is often overlooked. To better mimic the physiological conditions in living cells, MACs were crowded onto a solid supported membrane (SSM) by methylcellulose (MC) and coupled to the SSM via the pseudophosphorylated ezrin mutant (ezrin T567D) and the receptor lipid phosphatidylinositol-4,5-bisphosphate (PIP_2). MC was used to create more stable MACs, but a suitable concentration had to be found to avoid influencing the architecture and mechanics of the artificial actin cortices (here 0.02% (*w*/*v*)). A quasi-2D actin layer was formed with a thickness below 1 µm and thus the same order of magnitude as found for living MDCK II cells with $\overline{d}$ = (148 ± 62) nm. In fluorescence microscopy and VPT microrheology experiments, it was shown that network morphology and viscoelasticity can be modified by the number of pinning points to the SSM, regulated by the amount of the receptor lipid PIP_2. With increasing pinning points, the network stiffness increases with $G_0 \propto \chi_{PIP_2}{}^{1.6}$, similar to results in literature for MACs without MC, indicating that the crowding agent (in the concentration used here) does not affect MAC mechanics. Comparing the viscoelastic spectra of the MACs with the 3D actin gels, again three distinct frequency regimes were observed, but for the membrane-attached actin networks a significant increase of G_0 by a factor of about 6 was found. Furthermore, actin filaments in MACs were observed to be about a quarter shorter compared to in 3D entangled actin networks. These results indicate that actin cortex architecture and mechanics is mainly determined by the dynamic coupling of the actin network to the membrane. Thus, the bottom-up

model systems proved to be useful tools to characterize the contributions and functions of individual actin cortex components under controlled conditions.

In order to investigate the contribution of the whole biomolecular assembly of the cellular cortex to the viscoelasticity of the cell − in absence of the crowded and viscous cytoplasm and the much stiffer nucleus − apical membranes with an intact actin cortex were isolated from living MDCK II cells in a top-down fashion. These apical cell cortices were deposited on porous silica substrates, which permitted the probing of the cortices rheological properties in force cycle experiments with a sharp AFM tip. To analyze the force cycle data, a viscoelastic cortex model was developed that considers pre-stress of the actin network and a time-dependent resistance to area dilatation assuming power law rheology. The data obtained was compared with that of living MDCK II cells and also a bottom-up MAC model system. It was found that apical cell cortices and MACs show lower area compressibility moduli K_{A}^{0} and power law exponents β (reflecting the systems fluidity) in comparison to living cells, which indicates stiffer and less transient networks. This assumption was confirmed by rheological measurements. Here, stiffnesses of up to 615 mPa were measured for MACs, while significantly higher stiffnesses in the range of (790 ± 308) Pa were determined for living MDCK II cells. The reduced fluidity of the apical cell cortices was partially restored by addition of exogenous ATP, which shifts myosin from rigor state characterized by permanent cross-linking to a more dynamic state with transient cross-links between myosin and F-actin. Similar results were successfully reconstructed in simple bottom-up approaches of artificial 3D actomyosin networks as aforementioned. Fluidization of the actin cortex was also found after treatment of living cells and apical cell cortices with the F-actin depolymerization agent CytD, while the exact opposite was achieved by fixation of cells and apical cell cortices with GDA. In addition, apical cell cortices revived with exogenous ATP show the same power law as employed for living cells, which indicates the existence of a master equation. These results provide evidence that the viscoelastic response of living cells to external deformation is to a large extent generated in the apical cell cortex. In particular, the actin network architecture, its dynamic coupling to the plasma membrane as well as myosin motor activity driven by ATP consumption play a key role in the regulation of cell mechanics, as demonstrated by different bottom-up and top-down model systems.

6 Bibliography

(1) Clark, A. G.; Dierkes, K.; Paluch, E. K. Monitoring Actin Cortex Thickness in Live Cells. *Biophys. J.* **2013**, *105* (3), 570–580. https://doi.org/10.1016/j.bpj.2013.05.057.

(2) Blanchoin, L.; Boujemaa-Paterski, R.; Sykes, C.; Plastino, J. Actin Dynamics, Architecture, and Mechanics in Cell Motility. *Physiol. Rev.* **2014**, *94* (1), 235–263. https://doi.org/10.1152/physrev.00018.2013.

(3) Fletcher, D. A.; Mullins, R. D. Cell Mechanics and the Cytoskeleton. *Nature* **2010**, *463* (7280), 485–492. https://doi.org/10.1038/nature08908.

(4) Huber, F.; Boire, A.; López, M. P.; Koenderink, G. H. Cytoskeletal Crosstalk: When Three Different Personalities Team Up. *Curr. Opin. Cell Biol.* **2015**, *32*, 39–47. https://doi.org/10.1016/j.ceb.2014.10.005.

(5) Nehls, S.; Janshoff, A. Elastic Properties of Pore-Spanning Apical Cell Membranes Derived from MDCK II Cells. *Biophys. J.* **2017**, *113* (8), 1822–1830. https://doi.org/10.1016/j.bpj.2017.08.038.

(6) Banerjee, S.; Gardel, M. L.; Schwarz, U. S. The Actin Cytoskeleton as an Active Adaptive Material. *Annu. Rev. Condens. Matter Phys.* **2020**, *11* (1), 421–439. https://doi.org/10.1146/annurev-conmatphys-031218-013231.

(7) Medical School https://medicalschool.tumblr.com/search/cytoskeleton (accessed Mar 24, 2020).

(8) Rodriguez, M. L.; McGarry, P. J.; Sniadecki, N. J. Review on Cell Mechanics: Experimental and Modeling Approaches. *Appl. Mech. Rev.* **2013**, *65* (6). https://doi.org/10.1115/1.4025355.

(9) Ott, A.; Magnasco, M.; Simon, A.; Libchaber, A. Measurement of the Persistence Length of Polymerized Actin Using Fluorescence Microscopy. *Phys. Rev. E* **1993**, *48* (3), R1642–R1645. https://doi.org/10.1103/PhysRevE.48.R1642.

(10) Gittes, F.; Mickey, B.; Nettleton, J.; Howard, J. Flexural Rigidity of Microtubules and Actin Filaments Measured from Thermal Fluctuations in Shape. *J. Cell Biol.* **1993**, *120* (4), 923–934. https://doi.org/10.1083/jcb.120.4.923.

(11) Janmey, P. A.; Euteneuer, U.; Traub, P.; Schliwa, M. Viscoelastic Properties of Vimentin Compared with Other Filamentous Biopolymer Networks. *J. Cell Biol.* **1991**, *113* (1), 155–160. https://doi.org/10.1083/jcb.113.1.155.

(12) Otterbein, L. R.; Graceffa, P.; Dominguez, R. The Crystal Structure of Uncomplexed Actin in the ADP State. *Science* **2001**, *293*, 708–711. https://doi.org/10.2210/pdb1j6z/pdb.

(13) Reisler, E.; Egelman, E. H. Actin Structure and Function: What We Still Do Not Understand. *J. Biol. Chem.* **2007**, *282* (50), 36133–36137. https://doi.org/10.1074/jbc.R700030200.

(14) Pollard, T. D.; Blanchoin, L.; Mullins, R. D. Molecular Mechanisms Controlling Actin Filament Dynamics in Nonmuscle Cells. *Annu. Rev. Biophys. Biomol. Struct.* **2000**, *29*, 545–576. https://doi.org/10.1146/annurev.biophys.29.1.545.

(15) Dominguez, R.; Holmes, K. C. Actin Structure and Function. *Annu. Rev. Biophys.* **2011**, *40*, 169–186. https://doi.org/10.1146/annurev-biophys-042910-155359.

(16) Carlier, M. F.; Pantaloni, D.; Korn, E. D. The Mechanisms of ATP Hydrolysis Accompanying the Polymerization of Mg-Actin and Ca-Actin. *J. Biol. Chem.* **1987**, *262* (7), 3052–3059.

(17) Grazi, E. What Is the Diameter of the Actin Filament? *FEBS Lett.* **1997**, *405* (3), 249–252. https://doi.org/10.1016/S0014-5793(97)00214-7.

(18) Alberts, B.; Johnson, A.; Lewis, J.; Morgan, D.; Raff, M.; Roberts, K.; Walter, P. *Molekularbiologie der Zelle*; John Wiley & Sons, 2017.

(19) Korn, E. D.; Carlier, M. F.; Pantaloni, D. Actin Polymerization and ATP Hydrolysis. *Science* **1987**, *238* (4827), 638–644. https://doi.org/10.1126/science.3672117.

(20) Tharmann, R. Mechanical Properties of Complex Cytoskeleton Networks; 2006.

(21) Pollard, T. D.; Cooper, J. A. Actin, a Central Player in Cell Shape and Movement. *Science* **2009**, *326* (5957), 1208–1212. https://doi.org/10.1126/science.1175862.

(22) Pollard, T. D. Regulation of Actin Filament Assembly by Arp2/3 Complex and Formins. *Annu. Rev. Biophys. Biomol. Struct.* **2007**, *36*, 451–477. https://doi.org/10.1146/annurev.biophys.35.040405.101936.

(23) Uribe, R.; Jay, D. A Review of Actin Binding Proteins: New Perspectives. *Mol. Biol. Rep.* **2009**, *36* (1), 121–125. https://doi.org/10.1007/s11033-007-9159-2.

(24) Pollard, T. D.; Cooper, J. A. Actin and Actin-Binding Proteins. A Critical Evaluation of Mechanisms and Functions. *Annu. Rev. Biochem.* **1986**, *55*, 987–1035. https://doi.org/10.1146/annurev.bi.55.070186.005011.

(25) Gardel, M. L.; Kasza, K. E.; Brangwynne, C. P.; Liu, J.; Weitz, D. A. Chapter 19: Mechanical Response of Cytoskeletal Networks. *Methods Cell Biol.* **2008**. https://doi.org/10.1016/S0091-679X(08)00619-5.

(26) Bretscher, A.; Edwards, K.; Fehon, R. G. ERM Proteins and Merlin: Integrators at the Cell Cortex. *Nat. Rev. Mol. Cell Biol.* **2002**, *3* (8), 586–599. https://doi.org/10.1038/nrm882.

(27) Fehon, R. G.; McClatchey, A. I.; Bretscher, A. Organizing the Cell Cortex: The Role of ERM Proteins. *Nat. Rev. Mol. Cell Biol.* **2010**, *11* (4), 276–287. https://doi.org/10.1038/nrm2866.

(28) Vicente-Manzanares, M.; Ma, X.; Adelstein, R. S.; Horwitz, A. R. Non-Muscle Myosin II Takes Centre Stage in Cell Adhesion and Migration. *Nat. Rev. Mol. Cell Biol.* **2009**, *10* (11), 778–790. https://doi.org/10.1038/nrm2786.

(29) Reymann, A.-C.; Boujemaa-Paterski, R.; Martiel, J.-L.; Guérin, C.; Cao, W.; Chin, H. F.; De La Cruz, E. M.; Théry, M.; Blanchoin, L. Actin Network Architecture Can Determine Myosin Motor Activity. *Science* **2012**, *336* (6086), 1310–1314. https://doi.org/10.1126/science.1221708.

(30) Vogel, S. K.; Petrasek, Z.; Heinemann, F.; Schwille, P. Myosin Motors Fragment and Compact Membrane-Bound Actin Filaments. *eLife* **2013**, *2*, e00116. https://doi.org/10.7554/eLife.00116.

(31) Murrell, M. P.; Gardel, M. L. F-Actin Buckling Coordinates Contractility and Severing in a Biomimetic Actomyosin Cortex. *Proc. Natl. Acad. Sci.* **2012**, *109* (51), 20820–20825. https://doi.org/10.1073/pnas.1214753109.

(32) Campellone, K. G.; Welch, M. D. A Nucleator Arms Race: Cellular Control of Actin Assembly. *Nat. Rev. Mol. Cell Biol.* **2010**, *11* (4), 237–251. https://doi.org/10.1038/nrm2867.

(33) Pring, M.; Weber, A.; Bubb, M. R. Profilin-Actin Complexes Directly Elongate Actin Filaments at the Barbed End. *Biochemistry* **1992**, *31* (6), 1827–1836. https://doi.org/10.1021/bi00121a035.

(34) Prochniewicz, E.; Zhang, Q.; Janmey, P. A.; Thomas, D. D. Cooperativity in F-Actin: Binding of Gelsolin at the Barbed End Affects Structure and Dynamics of the Whole Filament. *J. Mol. Biol.* **1996**, *260* (5), 756–766. https://doi.org/10.1006/jmbi.1996.0435.

(35) Ruppel, K. M.; Spudich, J. A. Structure-Function Analysis of the Motor Domain of Myosin. *Annu. Rev. Cell Dev. Biol.* **1996**, *12* (1), 543–573. https://doi.org/10.1146/annurev.cellbio.12.1.543.

(36) Hartman, M. A.; Spudich, J. A. The Myosin Superfamily at a Glance. *J. Cell Sci.* **2012**, *125* (7), 1627–1632. https://doi.org/10.1242/jcs.094300.

(37) What is Myosin? https://www.mechanobio.info/cytoskeleton-dynamics/what-are-motor-proteins/what-is-myosin/ (accessed Mar 5, 2020).

(38) Howard, J. Molecular Motors: Structural Adaptations to Cellular Functions. *Nature* **1997**, *389* (6651), 561–567. https://doi.org/10.1038/39247.

(39) Linking molecular motors to membrane cargo https://www.ncbi.nlm.nih.gov/pmc/articles/PMC3393125/ (accessed Mar 6, 2020).

(40) Kühne, W. *Untersuchungen Über Das Protoplasma Und Die Contractilität /*; W. Engelmann,: Leipzig :, 1864; pp 1–192. https://doi.org/10.5962/bhl.title.46515.

(41) Humphrey, D.; Duggan, C.; Saha, D.; Smith, D.; Käs, J. Active Fluidization of Polymer Networks through Molecular Motors. *Nature* **2002**, *416* (6879), 413–416. https://doi.org/10.1038/416413a.

(42) Toyota, T.; A. Head, D.; F. Schmidt, C.; Mizuno, D. Non-Gaussian Athermal Fluctuations in Active Gels. *Soft Matter* **2011**, *7* (7), 3234–3239. https://doi.org/10.1039/C0SM00925C.

(43) Stam, S.; Alberts, J.; Gardel, M. L.; Munro, E. Isoforms Confer Characteristic Force Generation and Mechanosensation by Myosin II Filaments. *Biophys. J.* **2015**, *108* (8), 1997–2006. https://doi.org/10.1016/j.bpj.2015.03.030.

(44) Salbreux, G.; Charras, G.; Paluch, E. Actin Cortex Mechanics and Cellular Morphogenesis. *Trends Cell Biol.* **2012**, *22* (10), 536–545. https://doi.org/10.1016/j.tcb.2012.07.001.

(45) Mizuno, D.; Tardin, C.; Schmidt, C. F.; MacKintosh, F. C. Nonequilibrium Mechanics of Active Cytoskeletal Networks. *Science* **2007**, *315* (5810), 370–373. https://doi.org/10.1126/science.1134404.

(46) Roos, W. Biomimetic cytoskeleton assemblies and living cells on micropillar force sensor arrays https://archiv.ub.uni-heidelberg.de/volltextserver/5229/ (accessed Mar 9, 2020). https://doi.org/DOI:10.11588/heidok.00005229.

(47) Ishijima, A.; Doi, T.; Sakurada, K.; Yanagida, T. Sub-Piconewton Force Fluctuations of Actomyosin in Vitro. *Nature* **1991**, *352* (6333), 301–306. https://doi.org/10.1038/352301a0.

(48) Chugh, P.; Clark, A. G.; Smith, M. B.; Cassani, D. A. D.; Dierkes, K.; Ragab, A.; Roux, P. P.; Charras, G.; Salbreux, G.; Paluch, E. K. Actin Cortex Architecture Regulates Cell Surface Tension. *Nat. Cell Biol.* **2017**, *19* (6), 689–697. https://doi.org/10.1038/ncb3525.

(49) Chugh, P.; Paluch, E. K. The Actin Cortex at a Glance. *J. Cell Sci.* **2018**, *131* (14). https://doi.org/10.1242/jcs.186254.

(50) Tonomura, Y.; Appel, P.; Morales, M. On the Molecular Weight of Myosin. II*. *Biochemistry* **1966**, *5* (2), 515–521. https://doi.org/10.1021/bi00866a017.

(51) Howard, J. Mechanics of Motor Proteins and the Cytoskeleton Sunderland. In *Mechanics of Motor Proteins and the Cytoskeleton*; 2001; Vol. 55. https://doi.org/10.1115/1.1451234.

(52) Lodish, H.; Berk, A.; Zipursky, S. L.; Matsudaira, P.; Baltimore, D.; Darnell, J. *Molecular Cell Biology*, 4th ed.; W. H. Freeman, 2000.

(53) Heavy meromyosin protein https://www.cytoskeleton.com/mh01 (accessed Mar 9, 2020).

(54) Tharmann, R.; Claessens, M. M. A. E.; Bausch, A. R. Viscoelasticity of Isotropically Cross-Linked Actin Networks. *Phys. Rev. Lett.* **2007**, *98* (8), 088103. https://doi.org/10.1103/PhysRevLett.98.088103.

(55) Rouven Brückner, B.; Pietuch, A.; Nehls, S.; Rother, J.; Janshoff, A. Ezrin Is a Major Regulator of Membrane Tension in Epithelial Cells. *Sci. Rep.* **2015**, *5*, 14700. https://doi.org/10.1038/srep14700.

(56) Fievet, B. T.; Gautreau, A.; Roy, C.; Del Maestro, L.; Mangeat, P.; Louvard, D.; Arpin, M. Phosphoinositide Binding and Phosphorylation Act Sequentially in the Activation Mechanism of Ezrin. *J. Cell Biol.* **2004**, *164* (5), 653–659. https://doi.org/10.1083/jcb.200307032.

(57) Gary, R.; Bretscher, A. Ezrin Self-Association Involves Binding of an N-Terminal Domain to a Normally Masked C-Terminal Domain That Includes the F-Actin Binding Site. *Mol. Biol. Cell* **1995**, *6* (8), 1061–1075.

(58) Bosk, S.; Braunger, J. A.; Gerke, V.; Steinem, C. Activation of F-Actin Binding Capacity of Ezrin: Synergism of PIP2 Interaction and Phosphorylation. *Biophys. J.* **2011**, *100* (7), 1708–1717. https://doi.org/10.1016/j.bpj.2011.02.039.

(59) Martin, T. F. J. Role of PI(4,5)P(2) in Vesicle Exocytosis and Membrane Fusion. *Subcell. Biochem.* **2012**, *59*, 111–130. https://doi.org/10.1007/978-94-007-3015-1_4.

(60) McLaughlin, S.; Wang, J.; Gambhir, A.; Murray, D. PIP(2) and Proteins: Interactions, Organization, and Information Flow. *Annu. Rev. Biophys. Biomol. Struct.* **2002**, *31*, 151–175. https://doi.org/10.1146/annurev.biophys.31.082901.134259.

(61) Hammond, G. R. V. Does PtdIns(4,5)P2 Concentrate so It Can Multi-Task? *Biochem. Soc. Trans.* **2016**, *44* (1), 228–233. https://doi.org/10.1042/BST20150211.

(62) Braunger, J. A.; Brückner, B. R.; Nehls, S.; Pietuch, A.; Gerke, V.; Mey, I.; Janshoff, A.; Steinem, C. Phosphatidylinositol 4,5-Bisphosphate Alters the Number of Attachment Sites between Ezrin and Actin Filaments: A Colloidal Probe Study. *J. Biol. Chem.* **2014**, *289* (14), 9833–9843. https://doi.org/10.1074/jbc.M113.530659.

(63) Zhou, R.; Zhu, L.; Kodani, A.; Hauser, P.; Yao, X.; Forte, J. G. Phosphorylation of Ezrin on Threonine 567 Produces a Change in Secretory Phenotype and Repolarizes the Gastric Parietal Cell. *J. Cell Sci.* **2005**, *118* (Pt 19), 4381–4391. https://doi.org/10.1242/jcs.02559.

(64) Shabardina, V.; Kramer, C.; Gerdes, B.; Braunger, J.; Cordes, A.; Schäfer, J.; Mey, I.; Grill, D.; Gerke, V.; Steinem, C. Mode of Ezrin-Membrane Interaction as a Function of PIP2 Binding and Pseudophosphorylation. *Biophys. J.* **2016**, *110* (12), 2710–2719. https://doi.org/10.1016/j.bpj.2016.05.009.

(65) Nöding, H.; Schön, M.; Reinermann, C.; Dörrer, N.; Kürschner, A.; Geil, B.; Mey, I.; Heussinger, C.; Janshoff, A.; Steinem, C. Rheology of Membrane-Attached Minimal Actin Cortices. *J. Phys. Chem. B* **2018**, *122* (16), 4537–4545. https://doi.org/10.1021/acs.jpcb.7b11491.

(66) Schön, M.; Mey, I.; Steinem, C. Influence of Cross-Linkers on Ezrin-Bound Minimal Actin Cortices. *Prog. Biophys. Mol. Biol.* **2019**, *144*, 91–101. https://doi.org/10.1016/j.pbiomolbio.2018.07.016.

(67) Wieland, T.; Faulstich, H. Amatoxins, Phallotoxins, Phallolysin, and Antamanide: The Biologically Active Components of Poisonous Amanita Mushrooms. *CRC Crit. Rev. Biochem.* **1978**, *5* (3), 185–260. https://doi.org/10.3109/10409237809149870.

(68) Effects of Cytochalasin and Phalloidin on Actin. *J. Cell Biol.* **1987**, *105* (4), 1473–1478.

(69) Skillman, K. M.; Diraviyam, K.; Khan, A.; Tang, K.; Sept, D.; Sibley, L. D. Evolutionarily Divergent, Unstable Filamentous Actin Is Essential for Gliding Motility in Apicomplexan Parasites. *PLOS Pathog.* **2011**, *7* (10), e1002280. https://doi.org/10.1371/journal.ppat.1002280.

(70) Oda, T.; Namba, K.; Maéda, Y. Position and Orientation of Phalloidin in F-Actin Determined by X-Ray Fiber Diffraction Analysis. *Biophys. J.* **2005**, *88* (4), 2727–2736. https://doi.org/10.1529/biophysj.104.047753.

(71) Yanagida, T.; Nakase, M.; Nishiyama, K.; Oosawa, F. Direct Observation of Motion of Single F-Actin Filaments in the Presence of Myosin. *Nature* **1984**, *307* (5946), 58–60. https://doi.org/10.1038/307058a0.

(72) Steinmetz, M. O.; Stoffler, D.; Müller, S. A.; Jahn, W.; Wolpensinger, B.; Goldie, K. N.; Engel, A.; Faulstich, H.; Aebi, U. Evaluating Atomic Models of F-Actin with an Undecagold-Tagged Phalloidin Derivative11Edited by M. F. Moody. *J. Mol. Biol.* **1998**, *276* (1), 1–6. https://doi.org/10.1006/jmbi.1997.1529.

(73) Dancker, P.; Löw, I.; Hasselbach, W.; Wieland, Th. Interaction of Actin with Phalloidin:: Polymerization and Stabilization of F-Actin. *Biochim. Biophys. Acta BBA - Protein Struct.* **1975**, *400* (2), 407–414. https://doi.org/10.1016/0005-2795(75)90196-8.

(74) Adams, A. E. M.; Pringle, J. R. [51] Staining of Actin with Fluorochrome-Conjugated Phalloidin. In *Methods in Enzymology*; Guide to Yeast Genetics and Molecular Biology; Academic Press, 1991; Vol. 194, pp 729–731. https://doi.org/10.1016/0076-6879(91)94054-G.

(75) Xu, J.; Schwarz, W. H.; Käs, J. A.; Stossel, T. P.; Janmey, P. A.; Pollard, T. D. Mechanical Properties of Actin Filament Networks Depend on Preparation, Polymerization Conditions, and Storage of Actin Monomers. *Biophys. J.* **1998**, *74* (5), 2731–2740. https://doi.org/10.1016/S0006-3495(98)77979-2.

(76) Gardel, M. L.; Valentine, M. T.; Crocker, J. C.; Bausch, A. R.; Weitz, D. A. Microrheology of Entangled F-Actin Solutions. *Phys. Rev. Lett.* **2003**, *91* (15), 158302. https://doi.org/10.1103/PhysRevLett.91.158302.

(77) Strelnikova, N.; Herren, F.; Schoenenberger, C.-A.; Pfohl, T. Formation of Actin Networks in Microfluidic Concentration Gradients. *Front. Mater.* **2016**, *3*. https://doi.org/10.3389/fmats.2016.00020.

(78) Deshpande, S.; Pfohl, T. Real-Time Dynamics of Emerging Actin Networks in Cell-Mimicking Compartments. *PLOS ONE* **2015**, *10* (3), e0116521. https://doi.org/10.1371/journal.pone.0116521.

(79) Lieleg, O.; Claessens, M. M. A. E.; Bausch, A. R. Structure and Dynamics of Cross-Linked Actin Networks. *Soft Matter* **2010**, *6* (2), 218–225. https://doi.org/10.1039/B912163N.

(80) Gardel, M. L.; Shin, J. H.; MacKintosh, F. C.; Mahadevan, L.; Matsudaira, P.; Weitz, D. A. Elastic Behavior of Cross-Linked and Bundled Actin Networks. *Science* **2004**, *304* (5675), 1301–1305. https://doi.org/10.1126/science.1095087.

(81) Tseng, Y.; Fedorov, E.; McCaffery, J. M.; Almo, S. C.; Wirtz, D. Micromechanics and Ultrastructure of Actin Filament Networks Crosslinked by Human Fascin: A Comparison with Alpha-Actinin. *J. Mol. Biol.* **2001**, *310* (2), 351–366. https://doi.org/10.1006/jmbi.2001.4716.

(82) Gardel, M. L.; Nakamura, F.; Hartwig, J.; Crocker, J. C.; Stossel, T. P.; Weitz, D. A. Stress-Dependent Elasticity of Composite Actin Networks as a Model for Cell Behavior. *Phys. Rev. Lett.* **2006**, *96* (8), 088102. https://doi.org/10.1103/PhysRevLett.96.088102.

(83) Weirich, K. L.; Banerjee, S.; Dasbiswas, K.; Witten, T. A.; Vaikuntanathan, S.; Gardel, M. L. Liquid Behavior of Cross-Linked Actin Bundles. *Proc. Natl. Acad. Sci.* **2017**, *114* (9), 2131–2136. https://doi.org/10.1073/pnas.1616133114.

(84) Mulla, Y.; MacKintosh, F. C.; Koenderink, G. H. Origin of Slow Stress Relaxation in the Cytoskeleton. *Phys. Rev. Lett.* **2019**, *122* (21), 218102. https://doi.org/10.1103/PhysRevLett.122.218102.

(85) Murrell, M.; Oakes, P. W.; Lenz, M.; Gardel, M. L. Forcing Cells into Shape: The Mechanics of Actomyosin Contractility. *Nat. Rev. Mol. Cell Biol.* **2015**, *16* (8), 486–498. https://doi.org/10.1038/nrm4012.

(86) Ennomani, H.; Letort, G.; Guérin, C.; Martiel, J.-L.; Cao, W.; Nédélec, F.; De La Cruz, E. M.; Théry, M.; Blanchoin, L. Architecture and Connectivity Govern Actin Network Contractility. *Curr. Biol.* **2016**, *26* (5), 616–626. https://doi.org/10.1016/j.cub.2015.12.069.

(87) Barfoot, R. J.; Sheikh, K. H.; Johnson, B. R. G.; Colyer, J.; Miles, R. E.; Jeuken, L. J. C.; Bushby, R. J.; Evans, S. D. Minimal F-Actin Cytoskeletal System for Planar Supported Phospholipid Bilayers. *Langmuir* **2008**, *24* (13), 6827–6836. https://doi.org/10.1021/la800085n.

(88) Ershov, D.; Stuart, M. C.; Gucht, J. van der. Mechanical Properties of Reconstituted Actin Networks at an Oil–Water Interface Determined by Microrheology. *Soft Matter* **2012**, *8* (21), 5896–5903. https://doi.org/10.1039/C2SM25381J.

(89) Liu, A. P.; Fletcher, D. A. Actin Polymerization Serves as a Membrane Domain Switch in Model Lipid Bilayers. *Biophys. J.* **2006**, *91* (11), 4064–4070. https://doi.org/10.1529/biophysj.106.090852.

(90) Abu Shah, E.; Keren, K. Symmetry Breaking in Reconstituted Actin Cortices. *eLife* **2014**, *3*, e01433. https://doi.org/10.7554/eLife.01433.

(91) Liu, A. P.; Richmond, D. L.; Maibaum, L.; Pronk, S.; Geissler, P. L.; Fletcher, D. A. Membrane-Induced Bundling of Actin Filaments. *Nat. Phys.* **2008**, *4*, 789–793. https://doi.org/10.1038/nphys1071.

(92) Bement, W. M.; Capco, D. G. Analysis of Inducible Contractile Rings Suggests a Role for Protein Kinase C in Embryonic Cytokinesis and Wound Healing. *Cell Motil. Cytoskeleton* **1991**, *20* (2), 145–157. https://doi.org/10.1002/cm.970200207.

(93) Capco, D. G.; Tutnick, J. M.; Bement, W. M. The Role of Protein Kinase C in Reorganization of the Cortical Cytoskeleton during the Transition from Oocyte to Fertilization-Competent Egg. *J. Exp. Zool.* **1992**, *264* (4), 395–405. https://doi.org/10.1002/jez.1402640405.

(94) Kim, H. Y.; Davidson, L. A. Punctuated Actin Contractions during Convergent Extension and Their Permissive Regulation by the Non-Canonical Wnt-Signaling Pathway. *J. Cell Sci.* **2011**, *124* (4), 635–646. https://doi.org/10.1242/jcs.067579.

(95) Chaudhuri, O.; Parekh, S. H.; Fletcher, D. A. Reversible Stress Softening of Actin Networks. *Nature* **2007**, *445* (7125), 295–298. https://doi.org/10.1038/nature05459.

(96) Mahaffy, R. E.; Shih, C. K.; MacKintosh, F. C.; Käs, J. Scanning Probe-Based Frequency-Dependent Microrheology of Polymer Gels and Biological Cells. *Phys. Rev. Lett.* **2000**, *85* (4), 880–883. https://doi.org/10.1103/PhysRevLett.85.880.

(97) Alcaraz, J.; Buscemi, L.; Grabulosa, M.; Trepat, X.; Fabry, B.; Farré, R.; Navajas, D. Microrheology of Human Lung Epithelial Cells Measured by Atomic Force Microscopy. *Biophys. J.* **2003**, *84* (3), 2071–2079. https://doi.org/10.1016/S0006-3495(03)75014-0.

(98) Stamenovic, D.; Suki, B.; Fabry, B.; Wang, N.; Fredberg, J. J. Rheology of Airway Smooth Muscle Cells Is Associated with Cytoskeletal Contractile Stress. *J. Appl. Physiol. Bethesda Md 1985* **2004**, *96* (5), 1600–1605. https://doi.org/10.1152/japplphysiol.00595.2003.

(99) Fabry, B.; Maksym, G. N.; Butler, J. P.; Glogauer, M.; Navajas, D.; Fredberg, J. J. Scaling the Microrheology of Living Cells. *Phys. Rev. Lett.* **2001**, *87* (14), 148102. https://doi.org/10.1103/PhysRevLett.87.148102.

(100) Nakamura, F.; Osborn, E.; Janmey, P. A.; Stossel, T. P. Comparison of Filamin A-Induced Cross-Linking and Arp2/3 Complex-Mediated Branching on the Mechanics of Actin Filaments. *J. Biol. Chem.* **2002**, *277* (11), 9148–9154. https://doi.org/10.1074/jbc.M111297200.

(101) Pietuch, A.; Brückner, B. R.; Fine, T.; Mey, I.; Janshoff, A. Elastic Properties of Cells in the Context of Confluent Cell Monolayers: Impact of Tension and Surface Area Regulation. *Soft Matter* **2013**, *9* (48), 11490–11502. https://doi.org/10.1039/C3SM51610E.

(102) 16:0-18:1 PC (POPC) https://avantilipids.com/product/850457 (accessed Mar 20, 2020).

(103) Massey, J. B. Interaction of Ceramides with Phosphatidylcholine, Sphingomyelin and Sphingomyelin/Cholesterol Bilayers. *Biochim. Biophys. Acta BBA - Biomembr.* **2001**, *1510* (1), 167–184. https://doi.org/10.1016/S0005-2736(00)00344-8.

(104) Brain PI(4,5)P2 https://avantilipids.com/product/840046 (accessed Mar 20, 2020).

(105) Texas Red™ 1,2-Dihexadecanoyl-*sn*-Glycero-3-Phosphoethanolamine, Triethylammonium Salt (Texas Red™ DHPE) http://www.thermofisher.com/order/catalog/product/T1395MP (accessed Mar 20, 2020).

(106) ATTO-TEC GmbH - DOPE https://www.atto-tec.com/product_info.php?language=de&info=p132_dope.html (accessed Mar 20, 2020).

(107) ATTO-TEC GmbH - ATTO 390 https://www.atto-tec.com/product_info.php?language=de&info=p1_atto-390.html (accessed Mar 28, 2020).

(108) Alexa Fluor™ 488 Phalloidin http://www.thermofisher.com/order/catalog/product/A12379 (accessed Mar 20, 2020).

(109) AF488 Phalloidin [equivalent to Alexa Fluor® 488 phalloidin] | AAT Bioquest https://www.aatbio.com/products/af488-phalloidin-alexa-fluor-488-phalloidin (accessed Mar 20, 2020).

(110) Valentine, M. T.; Perlman, Z. E.; Gardel, M. L.; Shin, J. H.; Matsudaira, P.; Mitchison, T. J.; Weitz, D. A. Colloid Surface Chemistry Critically Affects Multiple Particle Tracking Measurements of Biomaterials. *Biophys. J.* **2004**, *86* (6), 4004–4014. https://doi.org/10.1529/biophysj.103.037812.

(111) Soares e Silva, M.; Depken, M.; Stuhrmann, B.; Korsten, M.; MacKintosh, F. C.; Koenderink, G. H. Active Multistage Coarsening of Actin Networks Driven by Myosin Motors. *Proc. Natl. Acad. Sci.* **2011**, *108* (23), 9408. https://doi.org/10.1073/pnas.1016616108.

(112) Lin, C.-M.; Li, C.-S.; Sheng, Y.-J.; Wu, D. T.; Tsao, H.-K. Size-Dependent Properties of Small Unilamellar Vesicles Formed by Model Lipids. *Langmuir* **2012**, *28* (1), 689–700. https://doi.org/10.1021/la203755v.

(113) Braunger, J. A.; Kramer, C.; Morick, D.; Steinem, C. Solid Supported Membranes Doped with PIP2: Influence of Ionic Strength and PH on Bilayer Formation and Membrane Organization. *Langmuir* **2013**, *29* (46), 14204–14213. https://doi.org/10.1021/la402646k.

(114) LP – Fluoreszenzmikroskopie https://lp.uni-goettingen.de/get/text/6741 (accessed Apr 6, 2020).

(115) Atkins, P. W.; Paula, J. de. *Physikalische Chemie*; John Wiley & Sons, 2006.

(116) Wedler, G.; Freund, H.-J. *Lehrbuch der Physikalischen Chemie*; John Wiley & Sons, 2012.

(117) Stokes Shift https://www.univie.ac.at/mikroskopie/3_fluoreszenz/definition/2_stoke.htm (accessed Apr 8, 2020).

(118) Cox, G. *Optical Imaging Techniques in Cell Biology*; CRC Press, 2006.

(119) ZEISS Microscopy Online Campus | Confocal References http://zeiss-campus.magnet.fsu.edu/referencelibrary/laserconfocal.html (accessed Apr 8, 2020).

(120) Huang, B.; Bates, M.; Zhuang, X. Super Resolution Fluorescence Microscopy. *Annu. Rev. Biochem.* **2009**, *78*, 993–1016. https://doi.org/10.1146/annurev.biochem.77.061906.092014.

(121) Optical Microscopy Application: Darkfield Illumination https://www.edmundoptics.de/knowledge-center/application-notes/microscopy/optical-microscopy-application-darkfield-illumination/ (accessed Apr 6, 2020).

(122) M. Kilfoil. 2D feature finding and tracking algorithms & microrheology algorithms. Matlab code, http://people.umass.edu/kilfoil/tools.php. (accessed Apr 8, 2020).

(123) Dasgupta, B. R.; Tee, S.-Y.; Crocker, J. C.; Frisken, B. J.; Weitz, D. A. Microrheology of Polyethylene Oxide Using Diffusing Wave Spectroscopy and Single Scattering. *Phys. Rev. E Stat. Nonlin. Soft Matter Phys.* **2002**, *65* (5 Pt 1), 051505. https://doi.org/10.1103/PhysRevE.65.051505.

(124) Roderfeld, M.; Matern, S.; Roeb, E. Konfokale Laserscanning-Mikroskopie: Der Blick in die Zelle. *DMW - Dtsch. Med. Wochenschr.* **2003**, *128* (48), 2539–2542. https://doi.org/10.1055/s-2003-44951.

(125) Amos, W. B.; White, J. G. How the Confocal Laser Scanning Microscope Entered Biological Research. *Biol. Cell* **2003**, *95* (6), 335–342. https://doi.org/10.1016/s0248-4900(03)00078-9.

(126) Axelrod, D.; Koppel, D. E.; Schlessinger, J.; Elson, E.; Webb, W. W. Mobility Measurement by Analysis of Fluorescence Photobleaching Recovery Kinetics. *Biophys. J.* **1976**, *16* (9), 1055–1069. https://doi.org/10.1016/S0006-3495(76)85755-4.

(127) MDougM. *English: Simulation and Schematic Diagram of the FRAP (Fluorescence Recovery after Photobleaching) Experimental Process*; 2008.

(128) Jönsson, P.; Jonsson, M. P.; Tegenfeldt, J. O.; Höök, F. A Method Improving the Accuracy of Fluorescence Recovery after Photobleaching Analysis. *Biophys. J.* **2008**, *95* (11), 5334–5348. https://doi.org/10.1529/biophysj.108.134874.

(129) Hell, S. W.; Wichmann, J. Breaking the Diffraction Resolution Limit by Stimulated Emission: Stimulated-Emission-Depletion Fluorescence Microscopy. *Opt. Lett.* **1994**, *19* (11), 780–782. https://doi.org/10.1364/OL.19.000780.

(130) The New Era Of Light Microscopy-STED; Nobel Prize 2014.

(131) Paës, G.; Habrant, A.; Terryn, C. Fluorescent Nano-Probes to Image Plant Cell Walls by Super-Resolution STED Microscopy. *Plants* **2018**, *7* (1). https://doi.org/10.3390/plants7010011.

(132) Stimulated Emission Depletion Microscopy (STED) | PicoQuant https://www.picoquant.com/applications/category/life-science/sted#description (accessed Apr 7, 2020).

(133) Vicidomini, G.; Bianchini, P.; Diaspro, A. STED Super-Resolved Microscopy. *Nat. Methods* **2018**, *15* (3), 173–182. https://doi.org/10.1038/nmeth.4593.

(134) Blom, H.; Brismar, H. STED Microscopy: Increased Resolution for Medical Research? *J. Intern. Med.* **2014**, *276* (6), 560–578. https://doi.org/10.1111/joim.12278.

(135) Sitters, G.; Kamsma, D.; Thalhammer, G.; Ritsch-Marte, M.; Peterman, E. J. G.; Wuite, G. J. L. Acoustic Force Spectroscopy. *Nat. Methods* **2015**, *12* (1), 47–50. https://doi.org/10.1038/nmeth.3183.

(136) Applications. *LUMICKS*.

(137) van Loenhout, M. T. J.; Kerssemakers, J. W. J.; De Vlaminck, I.; Dekker, C. Non-Bias-Limited Tracking of Spherical Particles, Enabling Nanometer Resolution at Low Magnification. *Biophys. J.* **2012**, *102* (10), 2362–2371. https://doi.org/10.1016/j.bpj.2012.03.073.

(138) Shenoy, A. V. *Rheology of Filled Polymer Systems*; Springer Science & Business Media, 1999.

(139) Weitz, D. A.; Wyss, H. H.; Larsen, R. J. Oscillatory Rheology Measuring the Viscoelastic Behaviour of Soft Materials; 2007.

(140) Tebel, K. H. An Introduction to Rheology. Von H. A. Barnes, J. F. Hutton Und K. Walters. Elsevier Science Publishers, Amsterdam – New York 1989. IX, 199 S., Zahlr. Abb. u. Tab., Geb., US-$60,50. *Chem. Ing. Tech.* **1990**, *62* (6), 457–457. https://doi.org/10.1002/cite.330620605.

(141) Macosko, C. W. *Rheology: Principles, Measurements, and Applications*; Wiley, 1994.

(142) Rubinstein, M.; Colby, R. H. *Polymer Physics*; Oxford University Press: Oxford, New York, 2003.

(143) Binnig, G.; Quate, C. F.; Gerber, Ch. Atomic Force Microscope. *Phys. Rev. Lett.* **1986**, *56* (9), 930–933. https://doi.org/10.1103/PhysRevLett.56.930.

(144) Jalili, N.; Laxminarayana, K. A Review of Atomic Force Microscopy Imaging Systems: Application to Molecular Metrology and Biological Sciences. *Mechatronics* **2004**, *14*, 907–945. https://doi.org/10.1016/j.mechatronics.2004.04.005.

(145) Ando, T.; Uchihashi, T.; Scheuring, S. Filming Biomolecular Processes by High-Speed Atomic Force Microscopy. *Chem. Rev.* **2014**, *114* (6), 3120–3188. https://doi.org/10.1021/cr4003837.

(146) Gerber, C.; Lang, H. P. How the Doors to the Nanoworld Were Opened. *Nat. Nanotechnol.* **2006**, *1* (1), 3–5. https://doi.org/10.1038/nnano.2006.70.

(147) Eaton, P.; West, P. *Atomic Force Microscopy*; Oxford University Press: Oxford, New York, 2018.

(148) Butt, H.-J.; Cappella, B.; Kappl, M. Force Measurements with the Atomic Force Microscope: Technique, Interpretation and Applications. *Surf. Sci. Rep.* **2005**, *59*, 1–152. https://doi.org/10.1016/j.surfrep.2005.08.003.

(149) Butt, H.-J.; Jaschke, M. Calculation of Thermal Noise in Atomic Force Microscopy. *Nanotechnology* **1995**, *6* (1), 1–7. https://doi.org/10.1088/0957-4484/6/1/001.

(150) Hutter, J. L.; Bechhoefer, J. Calibration of Atomic-force Microscope Tips. *Rev. Sci. Instrum.* **1993**, *64* (7), 1868–1873. https://doi.org/10.1063/1.1143970.

(151) Riedl, J.; Crevenna, A. H.; Kessenbrock, K.; Yu, J. H.; Neukirchen, D.; Bista, M.; Bradke, F.; Jenne, D.; Holak, T. A.; Werb, Z.; Sixt, M.; Wedlich-Soldner, R. Lifeact: A Versatile Marker to Visualize F-Actin. *Nat. Methods* **2008**, *5* (7), 605. https://doi.org/10.1038/nmeth.1220.

(152) Furst, E. M.; Squires, T. M. *Microrheology*; Oxford University Press, 2018.

(153) Nöding, H. Active and Passive Microrheology of F-Actin Membrane Composites. *From Minimal Cortex Model Systems to Living Cells* **2018**.

(154) Squires, T. M.; Mason, T. G. Fluid Mechanics of Microrheology. *Annu. Rev. Fluid Mech.* **2010**, *42* (1), 413–438. https://doi.org/10.1146/annurev-fluid-121108-145608.

(155) Wirtz, D. Particle-Tracking Microrheology of Living Cells: Principles and Applications. *Annu. Rev. Biophys.* **2009**, *38*, 301–326. https://doi.org/10.1146/annurev.biophys.050708.133724.

(156) Bonn, D.; Kegel, W. Stokes–Einstein Relations and the Fluctuation-Dissipation Theorem in a Supercooled Colloidal Fluid. *J. Chem. Phys.* **2003**, *118*. https://doi.org/10.1063/1.1532349.

(157) Gardel, M. L. Elasticity of F -Actin Networks. Ph.D., Harvard University, United States -- Massachusetts, 2004.

(158) Mason, T. G.; Ganesan, K.; van Zanten, J. H.; Wirtz, D.; Kuo, S. C. Particle Tracking Microrheology of Complex Fluids. *Phys. Rev. Lett.* **1997**, *79* (17), 3282–3285. https://doi.org/10.1103/PhysRevLett.79.3282.

(159) Gittes, F.; MacKintosh, F. C. Dynamic Shear Modulus of a Semiflexible Polymer Network. *Phys. Rev. E* **1998**, *58* (2), R1241–R1244. https://doi.org/10.1103/PhysRevE.58.R1241.

(160) Morse, D. C. Viscoelasticity of Concentrated Isotropic Solutions of Semiflexible Polymers. 1. Model and Stress Tensor. *Macromolecules* **1998**, *31* (20), 7030–7043. https://doi.org/10.1021/ma9803032.

(161) Morse, D. C. Viscoelasticity of Concentrated Isotropic Solutions of Semiflexible Polymers. 2. Linear Response. *Macromolecules* **1998**, *31* (20), 7044–7067. https://doi.org/10.1021/ma980304u.

(162) Käs, J.; Strey, H.; Tang, J. X.; Finger, D.; Ezzell, R.; Sackmann, E.; Janmey, P. A. F-Actin, a Model Polymer for Semiflexible Chains in Dilute, Semidilute, and Liquid Crystalline Solutions. *Biophys. J.* **1996**, *70* (2), 609–625.

(163) McLeish, T. C. B.; Cates, M. E.; Higgins, J. S.; Olmsted, P. D.; Keller, M.; Tharmann, R.; Dichtl, M. A.; Bausch, A. R.; Sackmann, E. Slow Filament Dynamics and Viscoelasticity in Entangled and Active Actin Networks. *Philos. Trans. R. Soc. Lond. Ser. Math. Phys. Eng. Sci.* **2003**, *361* (1805), 699–712. https://doi.org/10.1098/rsta.2002.1158.

(164) Lieleg, O.; Claessens, M. M. A. E.; Luan, Y.; Bausch, A. R. Transient Binding and Dissipation in Cross-Linked Actin Networks. *Phys. Rev. Lett.* **2008**, *101* (10), 108101. https://doi.org/10.1103/PhysRevLett.101.108101.

(165) Lieleg, O.; Kayser, J.; Brambilla, G.; Cipelletti, L.; Bausch, A. R. Slow Dynamics and Internal Stress Relaxation in Bundled Cytoskeletal Networks. *Nat. Mater.* **2011**, *10* (3), 236–242. https://doi.org/10.1038/nmat2939.

(166) MacKintosh, F. C.; Käs, J.; Janmey, P. A. Elasticity of Semiflexible Biopolymer Networks. *Phys. Rev. Lett.* **1995**, *75* (24), 4425–4428. https://doi.org/10.1103/PhysRevLett.75.4425.

(167) Gittes, F.; Schnurr, B.; Olmsted, P. D.; MacKintosh, F. C.; Schmidt, C. F. Microscopic Viscoelasticity: Shear Moduli of Soft Materials Determined from Thermal Fluctuations. *Phys. Rev. Lett.* **1997**, *79* (17), 3286–3289. https://doi.org/10.1103/PhysRevLett.79.3286.

(168) Schnurr, B.; Gittes, F.; MacKintosh, F. C.; Schmidt, C. F. Determining Microscopic Viscoelasticity in Flexible and Semiflexible Polymer Networks from Thermal

Fluctuations. *Macromolecules* **1997**, *30* (25), 7781–7792. https://doi.org/10.1021/ma970555n.

(169) Palmer, A.; Mason, T. G.; Xu, J.; Kuo, S. C.; Wirtz, D. Diffusing Wave Spectroscopy Microrheology of Actin Filament Networks. *Biophys. J.* **1999**, *76* (2), 1063–1071. https://doi.org/10.1016/S0006-3495(99)77271-1.

(170) Xu, J.; Palmer, A.; Wirtz, D. Rheology and Microrheology of Semiflexible Polymer Solutions: Actin Filament Networks. *Macromolecules* **1998**, *31* (19), 6486–6492. https://doi.org/10.1021/ma9717754.

(171) Hubrich, H.; Mey, I. P.; Brückner, B. R.; Mühlenbrock, P.; Nehls, S.; Grabenhorst, L.; Oswald, T.; Steinem, C.; Janshoff, A. Viscoelasticity of Native and Artificial Actin Cortices Assessed by Nanoindentation Experiments. *Nano Lett.* **2020**, *20* (9), 6329–6335. https://doi.org/10.1021/acs.nanolett.0c01769.

(172) Mey, I.; Steinem, C.; Janshoff, A. Biomimetic Functionalization of Porous Substrates: Towards Model Systems for Cellular Membranes. *J. Mater. Chem.* **2012**, *22* (37), 19348–19356. https://doi.org/10.1039/C2JM31737K.

(173) Mey, I.; Stephan, M.; Schmitt, E. K.; Müller, M. M.; Ben Amar, M.; Steinem, C.; Janshoff, A. Local Membrane Mechanics of Pore-Spanning Bilayers. *J. Am. Chem. Soc.* **2009**, *131* (20), 7031–7039. https://doi.org/10.1021/ja809165h.

(174) Cordes, A.; Witt, H.; Gallemí-Pérez, A.; Brückner, B.; Grimm, F.; Vache, M.; Oswald, T.; Bodenschatz, J.; Flormann, D.; Lautenschläger, F.; Tarantola, M.; Janshoff, A. Prestress and Area Compressibility of Actin Cortices Determine the Viscoelastic Response of Living Cells. *Phys. Rev. Lett.* **2020**, *125* (6), 068101. https://doi.org/10.1103/PhysRevLett.125.068101.

(175) Molteni, M.; Magatti, D.; Cardinali, B.; Rocco, M.; Ferri, F. Fast Two-Dimensional Bubble Analysis of Biopolymer Filamentous Networks Pore Size from Confocal Microscopy Thin Data Stacks. *Biophys. J.* **2013**, *104* (5), 1160–1169. https://doi.org/10.1016/j.bpj.2013.01.016.

(176) Münster, S.; Fabry, B. A Simplified Implementation of the Bubble Analysis of Biopolymer Network Pores. *Biophys. J.* **2013**, *104* (12), 2774–2775. https://doi.org/10.1016/j.bpj.2013.05.016.

(177) Schön, M. Self-Organization and Mechanics of Minimal Actin Cortices Attached to Artificial Bilayers. **2018**.

(178) Golde, T.; Schuldt, C.; Schnauß, J.; Strehle, D.; Glaser, M.; Käs, J. Fluorescent Beads Disintegrate Actin Networks. *Phys. Rev. E Stat. Nonlin. Soft Matter Phys.* **2013**, *88* (4), 044601. https://doi.org/10.1103/PhysRevE.88.044601.

(179) Alvarado, J.; Koenderink, G. H. Reconstituting Cytoskeletal Contraction Events with Biomimetic Actin-Myosin Active Gels. *Methods Cell Biol.* **2015**, *128*, 83–103. https://doi.org/10.1016/bs.mcb.2015.02.001.

(180) Lehmann, G.; Binkle, B.; Bell, V. Isolierung und Identifizierung von Farbstoffen in Nagellacken. *Fette Seifen Anstrichm.* **1984**, *86* (5), 208–210. https://doi.org/10.1002/lipi.19840860510.

(181) Mason; Gisler, T.; Kroy, K.; Frey, E.; Weitz, D. A. Rheology of F-Actin Solutions Determined from Thermally Driven Tracer Motion. *J. Rheol.* **2000**, *44*, 917–928.

(182) Liu, J.; Gardel, M. L.; Kroy, K.; Frey, E.; Hoffman, B. D.; Crocker, J. C.; Bausch, A. R.; Weitz, D. A. Microrheology Probes Length Scale Dependent Rheology. *Phys. Rev. Lett.* **2006**, *96* (11), 118104. https://doi.org/10.1103/PhysRevLett.96.118104.

(183) Massiera, G.; Van Citters, K. M.; Biancaniello, P. L.; Crocker, J. C. Mechanics of Single Cells: Rheology, Time Dependence, and Fluctuations. *Biophys. J.* **2007**, *93* (10), 3703–3713. https://doi.org/10.1529/biophysj.107.111641.

(184) Schmidt, C. F.; Baermann, M.; Isenberg, G.; Sackmann, E. Chain Dynamics, Mesh Size, and Diffusive Transport in Networks of Polymerized Actin: A Quasielastic Light Scattering and Microfluorescence Study. *Macromolecules* **1989**, *22* (9), 3638–3649. https://doi.org/10.1021/ma00199a023.

(185) Isambert, H.; Maggs, A. C. Dynamics and Rheology of Actin Solutions. *Macromolecules* **1996**, *29* (3), 1036–1040. https://doi.org/10.1021/ma946418x.

(186) Apgar, J.; Tseng, Y.; Fedorov, E.; Herwig, M. B.; Almo, S. C.; Wirtz, D. Multiple-Particle Tracking Measurements of Heterogeneities in Solutions of Actin Filaments and Actin Bundles. *Biophys. J.* **2000**, *79* (2), 1095–1106. https://doi.org/10.1016/S0006-3495(00)76363-6.

(187) Hinner, B.; Tempel, M.; Sackmann, E.; Kroy, K.; Frey, E. Entanglement, Elasticity, and Viscous Relaxation of Actin Solutions. *Phys. Rev. Lett.* **1998**, *81* (12), 2614–2617. https://doi.org/10.1103/PhysRevLett.81.2614.

(188) Gurmessa, B.; Fitzpatrick, R.; Falzone, T. T.; Robertson-Anderson, R. M. Entanglement Density Tunes Microscale Nonlinear Response of Entangled Actin. *Macromolecules* **2016**, *49* (10), 3948–3955. https://doi.org/10.1021/acs.macromol.5b02802.

(189) Frey, E.; Kroy, K.; Wilhelm, J. Physics of Solutions and Networks of Semiflexible Macromolecules and the Control of Cell Function. *ArXivcond-Mat9808022* **1998**.

(190) Müller, K. W.; Bruinsma, R. F.; Lieleg, O.; Bausch, A. R.; Wall, W. A.; Levine, A. J. Rheology of Semiflexible Bundle Networks with Transient Linkers. *Phys. Rev. Lett.* **2014**, *112* (23), 238102. https://doi.org/10.1103/PhysRevLett.112.238102.

(191) J, H. Comparison of Mathematical Models for Cat Lung and Viscoelastic Balloon Derived by Laplace Transform Methods from Pressure-Volume Data. *Bull. Math. Biophys.* **1969**, *31* (4), 651–667. https://doi.org/10.1007/bf02477779.

(192) Mizuno, D.; Head, D. A.; MacKintosh, F. C.; Schmidt, C. F. Active and Passive Microrheology in Equilibrium and Nonequilibrium Systems. *Macromolecules* **2008**, *41* (19), 7194–7202. https://doi.org/10.1021/ma801218z.

(193) Abe, S.; Maruyama, K. Effect of α-Actinin on F-ActinA Dynamic Viscoelastic Study. *J. Biochem. (Tokyo)* **1973**, *73* (6), 1205–1210. https://doi.org/10.1093/oxfordjournals.jbchem.a130192.

(194) Wachsstock, D. H.; Schwartz, W. H.; Pollard, T. D. Affinity of Alpha-Actinin for Actin Determines the Structure and Mechanical Properties of Actin Filament Gels. *Biophys. J.* **1993**, *65* (1), 205–214.

(195) Tempel, M.; Isenberg, G.; Sackmann, E. Temperature-Induced Sol-Gel Transition and Microgel Formation in \ensuremath{\alpha}-Actinin Cross-Linked Actin Networks: A Rheological Study. *Phys. Rev. E* **1996**, *54* (2), 1802–1810. https://doi.org/10.1103/PhysRevE.54.1802.

(196) Tharmann, R.; Claessens, M. M. A. E.; Bausch, A. R. Micro- and Macrorheological Properties of Actin Networks Effectively Cross-Linked by Depletion Forces. *Biophys. J.* **2006**, *90* (7), 2622–2627. https://doi.org/10.1529/biophysj.105.070458.

(197) Burla, F.; Mulla, Y.; Vos, B. E.; Aufderhorst-Roberts, A.; Koenderink, G. H. From Mechanical Resilience to Active Material Properties in Biopolymer Networks. *Nat. Rev. Phys.* **2019**, *1* (4), 249–263. https://doi.org/10.1038/s42254-019-0036-4.

(198) Koenderink, G. H.; Dogic, Z.; Nakamura, F.; Bendix, P. M.; MacKintosh, F. C.; Hartwig, J. H.; Stossel, T. P.; Weitz, D. A. An Active Biopolymer Network Controlled by Molecular Motors. *Proc. Natl. Acad. Sci. U. S. A.* **2009**, *106* (36), 15192–15197. https://doi.org/10.1073/pnas.0903974106.

(199) Alvarado, J.; Sheinman, M.; Sharma, A.; MacKintosh, F. C.; Koenderink, G. H. Molecular Motors Robustly Drive Active Gels to a Critically Connected State. *Nat. Phys.* **2013**, *9* (9), 591–597. https://doi.org/10.1038/nphys2715.

(200) Köchy, T.; Bayerl, T. M. Lateral Diffusion Coefficients of Phospholipids in Spherical Bilayers on a Solid Support Measured by $^{2}\mathrm{resonance}$ Relaxation. *Phys. Rev. E* **1993**, *47* (3), 2109–2116. https://doi.org/10.1103/PhysRevE.47.2109.

(201) Vaz, W. L. C.; Clegg, R. M.; Hallmann, D. Translational Diffusion of Lipids in Liquid Crystalline Phase Phosphatidylcholine Multibilayers. A Comparison of Experiment with Theory. *Biochemistry* **1985**, *24* (3), 781–786. https://doi.org/10.1021/bi00324a037.

(202) Iino, R.; Koyama, I.; Kusumi, A. Single Molecule Imaging of Green Fluorescent Proteins in Living Cells: E-Cadherin Forms Oligomers on the Free Cell Surface. *Biophys. J.* **2001**, *80* (6), 2667–2677.

(203) Cole, R. W.; Jinadasa, T.; Brown, C. M. Measuring and Interpreting Point Spread Functions to Determine Confocal Microscope Resolution and Ensure Quality Control. *Nat. Protoc.* **2011**, *6* (12), 1929–1941. https://doi.org/10.1038/nprot.2011.407.

(204) Linsmeier, I.; Banerjee, S.; Oakes, P. W.; Jung, W.; Kim, T.; Murrell, M. P. Disordered Actomyosin Networks Are Sufficient to Produce Cooperative and Telescopic Contractility. *Nat. Commun.* **2016**, *7*, 12615. https://doi.org/10.1038/ncomms12615.

(205) Köhler, S.; Lieleg, O.; Bausch, A. R. Rheological Characterization of the Bundling Transition in F-Actin Solutions Induced by Methylcellulose. *PLoS ONE* **2008**, *3* (7). https://doi.org/10.1371/journal.pone.0002736.

(206) Fritzsche, M.; Erlenkämper, C.; Moeendarbary, E.; Charras, G.; Kruse, K. Actin Kinetics Shapes Cortical Network Structure and Mechanics. *Sci. Adv.* **2016**, *2* (4), e1501337. https://doi.org/10.1126/sciadv.1501337.

(207) Fritzsche, M.; Li, D.; Colin-York, H.; Chang, V. T.; Moeendarbary, E.; Felce, J. H.; Sezgin, E.; Charras, G.; Betzig, E.; Eggeling, C. Self-Organizing Actin Patterns Shape Membrane Architecture but Not Cell Mechanics. *Nat. Commun.* **2017**, *8* (1), 14347. https://doi.org/10.1038/ncomms14347.

(208) Fritzsche, M.; Thorogate, R.; Charras, G. Quantitative Analysis of Ezrin Turnover Dynamics in the Actin Cortex. *Biophys. J.* **2014**, *106* (2), 343–353. https://doi.org/10.1016/j.bpj.2013.11.4499.

(209) Head, D. A.; Levine, A. J.; MacKintosh, F. C. Distinct Regimes of Elastic Response and Deformation Modes of Cross-Linked Cytoskeletal and Semiflexible Polymer Networks. *Phys. Rev. E* **2003**, *68* (6), 061907. https://doi.org/10.1103/PhysRevE.68.061907.

(210) Charrier, E. E.; Pogoda, K.; Wells, R. G.; Janmey, P. A. Control of Cell Morphology and Differentiation by Substrates with Independently Tunable Elasticity and Viscous Dissipation. *Nat. Commun.* **2018**, *9* (1), 449. https://doi.org/10.1038/s41467-018-02906-9.

(211) Janmey, P. A.; Fletcher, D. A.; Reinhart-King, C. A. Stiffness Sensing by Cells. *Physiol. Rev.* **2020**, *100* (2), 695–724. https://doi.org/10.1152/physrev.00013.2019.

(212) Rother, J.; Nöding, H.; Mey, I.; Janshoff, A. Atomic Force Microscopy-Based Microrheology Reveals Significant Differences in the Viscoelastic Response between Malign and Benign Cell Lines. *Open Biol.* **2014**, *4* (5), 140046. https://doi.org/10.1098/rsob.140046.

(213) Staunton, J. R.; Doss, B. L.; Lindsay, S.; Ros, R. Correlating Confocal Microscopy and Atomic Force Indentation Reveals Metastatic Cancer Cells Stiffen during Invasion into Collagen I Matrices. *Sci. Rep.* **2016**, *6*, 19686. https://doi.org/10.1038/srep19686.

(214) Garcia, P. D.; Garcia, R. Determination of the Viscoelastic Properties of a Single Cell Cultured on a Rigid Support by Force Microscopy. *Nanoscale* **2018**, *10* (42), 19799–19809. https://doi.org/10.1039/C8NR05899G.

(215) Wu, P.-H.; Aroush, D. R.-B.; Asnacios, A.; Chen, W.-C.; Dokukin, M. E.; Doss, B. L.; Durand-Smet, P.; Ekpenyong, A.; Guck, J.; Guz, N. V.; Janmey, P. A.; Lee, J. S. H.; Moore, N. M.; Ott, A.; Poh, Y.-C.; Ros, R.; Sander, M.; Sokolov, I.; Staunton, J. R.; Wang, N.; Whyte, G.; Wirtz, D. A Comparison of Methods to Assess Cell Mechanical Properties. *Nat. Methods* **2018**, *15* (7), 491–498. https://doi.org/10.1038/s41592-018-0015-1.

(216) Morone, N.; Fujiwara, T.; Murase, K.; Kasai, R. S.; Ike, H.; Yuasa, S.; Usukura, J.; Kusumi, A. Three-Dimensional Reconstruction of the Membrane Skeleton at the Plasma Membrane Interface by Electron Tomography. *J. Cell Biol.* **2006**, *174* (6), 851–862. https://doi.org/10.1083/jcb.200606007.

(217) Casella, J. F.; Flanagan, M. D.; Lin, S. Cytochalasin D Inhibits Actin Polymerization and Induces Depolymerization of Actin Filaments Formed during Platelet Shape Change. *Nature* **1981**, *293* (5830), 302–305. https://doi.org/10.1038/293302a0.

(218) Daily, B.; Elson, E. L.; Zahalak, G. I. Cell Poking. Determination of the Elastic Area Compressibility Modulus of the Erythrocyte Membrane. *Biophys. J.* **1984**, *45* (4), 671–682. https://doi.org/10.1016/S0006-3495(84)84209-5.

(219) Kollmannsberger, P.; Fabry, B. Linear and Nonlinear Rheology of Living Cells. *Annu. Rev. Mater. Res.* **2011**, *41* (1), 75–97. https://doi.org/10.1146/annurev-matsci-062910-100351.

(220) Broedersz, C. P.; Depken, M.; Yao, N. Y.; Pollak, M. R.; Weitz, D. A.; MacKintosh, F. C. Cross-Link-Governed Dynamics of Biopolymer Networks. *Phys. Rev. Lett.* **2010**, *105* (23), 238101. https://doi.org/10.1103/PhysRevLett.105.238101.

(221) Kollmannsberger, P.; Mierke, C. T.; Fabry, B. Nonlinear Viscoelasticity of Adherent Cells Is Controlled by Cytoskeletal Tension. *Soft Matter* **2011**, *7* (7), 3127–3132. https://doi.org/10.1039/C0SM00833H.

(222) de Sousa, J. S.; Freire, R. S.; Sousa, F. D.; Radmacher, M.; Silva, A. F. B.; Ramos, M. V.; Monteiro-Moreira, A. C. O.; Mesquita, F. P.; Moraes, M. E. A.; Montenegro, R. C.; Oliveira, C. L. N. Double Power-Law Viscoelastic Relaxation of Living Cells Encodes Motility Trends. *Sci. Rep.* **2020**, *10* (1), 4749. https://doi.org/10.1038/s41598-020-61631-w.

(223) Chan, C. J.; Ekpenyong, A. E.; Golfier, S.; Li, W.; Chalut, K. J.; Otto, O.; Elgeti, J.; Guck, J.; Lautenschläger, F. Myosin II Activity Softens Cells in Suspension. *Biophys. J.* **2015**, *108* (8), 1856–1869. https://doi.org/10.1016/j.bpj.2015.03.009.

(224) Ekpenyong, A. E.; Whyte, G.; Chalut, K.; Pagliara, S.; Lautenschläger, F.; Fiddler, C.; Paschke, S.; Keyser, U. F.; Chilvers, E. R.; Guck, J. Viscoelastic Properties of Differentiating Blood Cells Are Fate- and Function-Dependent. *PLOS ONE* **2012**, *7* (9), e45237. https://doi.org/10.1371/journal.pone.0045237.

(225) Fabry, B.; Maksym, G. N.; Butler, J. P.; Glogauer, M.; Navajas, D.; Taback, N. A.; Millet, E. J.; Fredberg, J. J. Time Scale and Other Invariants of Integrative Mechanical Behavior in Living Cells. *Phys. Rev. E* **2003**, *68* (4), 041914. https://doi.org/10.1103/PhysRevE.68.041914.

(226) Shrivastava, R.; Köster, D.; Kalme, S.; Mayor, S.; Neerathilingam, M. Tailor-Made Ezrin Actin Binding Domain to Probe Its Interaction with Actin In-Vitro. *PLOS ONE* **2015**, *10* (4), e0123428. https://doi.org/10.1371/journal.pone.0123428.

(227) McClatchey, A. I. ERM Proteins at a Glance. *J. Cell Sci.* **2014**, *127* (15), 3199–3204. https://doi.org/10.1242/jcs.098343.

(228) Brückner, B. R.; Nöding, H.; Janshoff, A. Viscoelastic Properties of Confluent MDCK II Cells Obtained from Force Cycle Experiments. *Biophys. J.* **2017**, *112* (4), 724–735. https://doi.org/10.1016/j.bpj.2016.12.032.

(229) Loiseau, E.; Schneider, J. A. M.; Keber, F. C.; Pelzl, C.; Massiera, G.; Salbreux, G.; Bausch, A. R. Shape Remodeling and Blebbing of Active Cytoskeletal Vesicles. *Sci. Adv.* **2016**, *2* (4), e1500465. https://doi.org/10.1126/sciadv.1500465.

7 Appendix

7.1 List of Symbols and Abbreviations

2D	two dimensional
3D	three dimensional
a	radius of the flat punch
A	area
$A^*(\omega)$	response function
A''	imaginary part of the response function
A_0	area before indentation, geometric area
A_{ex}	excess area
A_n	actual area during indentation
A_{vert}	vertical deflection
ABP	actin binding protein
ADP	adenosine diphosphate
AF	actin filament
AF 488-Phal	Alexa Fluor® 488-Phalloidin
AFM	atomic force microscope
AFS	acoustic force spectroscopy
AMR	active microrheology
ATP	adenosine triphosphate
Atto 390-DOPE	Atto 390 1,2-dioleoyl-*sn*-glycero-3-phosphoethanolamine
BSA	bovine serum albumin
c	concentration
C	power spectral density
C-ERMAD	*C*-terminal ezrin-radixin-moesin associated domain
CLSM	confocal laser scanning microscopy
c_p	contact point
CMOS	complementary metal-oxide-semiconductor
CP	creatine phosphate
CPK	creatine phosphokinase
CytD	Cytochalsin D

D	diffusion coefficient
d	physical thickness, F-actin diameter, cortex thickness
d_{FWHM}	lateral resolution
DOPC	1,2-dioleoyl-*sn*-glycero-3-phosphocholine
DOTAP	1,2-dioleoyl-3-trimethylammonium-propane
DTT	dithiolthreitol
E	*Young's* modulus
E. coli	Escherichia coli
EDM	*Euclidian* distance map
ERM	ezrin-radixin-moesin
F	force
f	frequency
f, f_{app}, f_{ret}	force that acts on a flat punch, during approach or during retraction
F-actin	filamentous actin
FCS	fetal calf serum
FDC	force-distance curve
fps	frames per second
FRAP	fluorescence recovery after photobleaching
f_{rep}	reptation frequency
FRSK	fetal rat skin keratinocyte
FV	FluoView
g	gramm
G^*, G', G''	shear, storage and loss moduli
G_0	plateau modulus
G-actin	globular actin
GDA	glutardialdehyde
GSER	generalized Stokes Einstein relation
GUV	giant unilamellar vesicle
h	hour
h	height
HEPES	2-[4-(2-hydroxyethyl)piperazin-1-yl]ethanesulfonic acid
His_n-tag	polyhistidine-tag with n histidine residues
HMM	heavy meromyosin
I	intensity, light

I_{max}	maximum STED intensity
I_s	saturation intensity
IF	intermediate filaments
k	rate constant or spatial frequency
K_A, K_A^0	area compressibility modulus
$\widetilde{K}_A$	apparent compressibility modulus
k_c	spring constant
k_B	*Boltzmann* constant
KCl	potassium chloride
K_D	dissociation constant
kDa	kilo Dalton
k_{off}	unbinding rate constant
L	filament length
L	liter
L_c	length of the cantilever, contour length
l_c	distance between cross-links or entanglement length
LASER	light amplification by stimulated emission of radiation
LED	light-emitting diode
LMM	light meromyosin
l_p	persistence length
M	molar mass
M	molar
MAC	minimal actin cortex
MCC	minimal cell compartment
MDCK II	Madin-Darby Canine Kidney epithelial cell line
MEM	minimum essential medium
$MgCl_2$	magnesium chloride
min	minute
MR	microrheology
MSD	mean square displacement
MT	microtubule
n	refractive index
N	number of dimensions or number of beads

NA	numerical aperture
NaCl	sodium chloride
N-ERMAD	*N*-terminal ezrin-radixin-moesin associated domain
nm	nanometer
NRK	normal rat kidney fibroblast
N-WASP	neuronal Wiskott-Aldrich syndrome protein
OT	optical tweezer
PBS	phosphate-buffered saline
PD	probability density
PDL	poly-D-lysine
P_i	inorganic phosphate
PID	proportional-integral-differential controller
PIP_2	L-α-phosphatidylinositol-4,5-bisphosphate
POPC	1-palmitoyl-2-oleoyl-glycero-3-phosphocholine
PSF	point spread function
PSLB	pore spanning lipid bilayer
PSM	pore spanning membrane
r	radius or ratio
R	radius of the pore, ratio of cross-linkers to G-actin concentration
ROI	region of interest
RT	room temperature
s	second
s	expression of the frequency parameter in the *Laplace* domain
SAM	self-assembled monolayer
sCMOS	scientific complementary metal-oxide-semiconductor
SLB	supported lipid bilayer
SPM	scanning probe microscopy
SSM	solid supported membrane
STED	stimulated emission depletion
SUV	small unilamellar vesicle
t, t_0, t_m	time
T	absolute temperature or Tension of the membrane
T_0	pre-stress
t_c	thickness of the cantilever

TxR-DHPE	Texas Red® 1,2-dihexadecanoyl-*sn*-glycero-3-phosphoethanolamine
u_a	indentation depth
$u(R)'$	spatial derivative of the membrane contour at the position $r=R$
$u(t)$	displacement fluctuations
UV	ultraviolet
V	volume
v_0	constant velocity
VASP	vasodilator-stimulated phosphoprotein
vis	visible
VPT	video particle tracking
WAVE	Wiskott-Aldrich Syndrome protein
w_c	width of the cantilever
$\langle \Delta x^2(\tau) \rangle$	mean square displacement
Z_c	deflection of the cantilever
$\langle \Delta Z_c^2 \rangle$	mean square deflection of the cantilever tip at the first oscillation mode
α	opening angle of the objective or diffusive exponent
β	correction factor or power law exponent
γ	strain
$\dot{\gamma}$	shear rate
γ_0	immobile fraction or preset strain
δ	phase angle
η, $\tilde{\eta}$	viscosity, complex viscosity
λ	wave length
λ_c	critical wavelength
λ_{em}	emission wavelength
λ_{ex}	excitation wavelength
μ	micro
ν	*Poisson* ratio
ξ	mesh size
σ	stress
ς	saturation factor
τ	lagtime
τ_{off}	unbinding time

τ_{rep}	reptation time
χ_{PIP_2}	pinning point density
ω	oscillation angular frequency
ω_0	characteristic frequency

7.2 List of Chemicals and Consumables

008-fluorosurfactant	*RAN Biotechnologies,* Berverly, MA, USA
1 µm carboxylate-modified polystyrene beads, fluorescent yellow-green	*Sigma-Aldrich*, Taufkirchen, Germany
2 µm carboxylate-modified polystyrene beads, fluorescent red	*Sigma-Aldrich*, St. Louis, MO, USA
α-actinin protein	*Cytoskeleton*, Denver, CO, USA
Abberior STAR RED	*Abberior*, Göttingen, Germany
Abberior Mount Liquid solution	*Abberior*, Göttingen, Germany
Alexa Fluor® 488-phalloidin	*Thermo Fisher Scientific*, Waltham, MA, USA
AlexaFluor 546 gotat anti-mouse IgG	*Thermo Fisher Scientific*, Waltham, MA, USA
Anti-phospho-MRLC (Ser 19) mouse IgG	*Cell Signaling Techlology Europe*, Frankfurt am Main, Germany
ATP	*Sigma-Aldrich*, Taufkirchen, Germany
Atto390-DOPE	*Atto-tec*, Siegen, Germany
BSA	*Carl Roth GmbH*, Karlsruhe, Germany
$CaCl_2$	*Merck KGaA*, Darmstadt, Germany
CellMask Orange	*Thermo Fisher Scientific*, Waltham, MA, USA
Creatine phosphate	*Sigma-Aldrich*, Taufkirchen, Germany
Creatine phosphokinase	*Sigma-Aldrich*, Taufkirchen, Germany
Chloroform	*VWR International*, Darmstadt, Germany
Cytochalasin D	*Thermo Fisher Scientific*, Waltham, MA, USA
Double faced adhesive tape	*Tesa SE*, Norderstedt, Germany
DOPC	*Avanti Polar Lipids*, Alabaster, AL, USA

DOTAP	*Avanti Polar Lipids*, Alabaster, AL, USA
DTT	*Sigma-Aldrich*, Taufkirchen, Germany
EDTA	*Carl Roth GmbH*, Karlsruhe, Germany
EGTA	*Sigma-Aldrich*, Taufkirchen, Germany
Eppendorf-Cups	*Eppendorf*, Hamburg, Germany
Eppendorfpipettes	*Eppendorf*, Hamburg, Germany
Ethanol p.a.	*VWR International*, Darmstadt, Germany
ezrin T567D	isolated and purified by *N. L. Liebe* from the Institute of Organic and Biomolecular Chemistry of the University of Göttingen, Germany
FCS	*BioWest*, Nuaillé, France
G-actin protein (rabbit skeletal muscle)	*Cytoskeleton*, Denver, CO, USA
G-actin protein (human platelet non-muscle)	*Cytoskeleton*, Denver, CO, USA
Glass coverslips No. 1 (0.13 - 0.16 mm, 22 x 22 mm)	*Carl Roth GmbH*, Karlsruhe, Germany
Glass coverslips No. 1 (0.13 - 0.16 mm, 24 x 50 mm)	*Carl Roth GmbH*, Karlsruhe, Germany
Guanidine carbonate	*Sigma-Aldrich*, Taufkirchen, Germany
H_2O_2 (25%)	*Merck KGaA*, Darmstadt, Germany
HCl	*Merck KGaA*, Darmstadt, Germany
Hellmanex® III	*Hellma,* Müllheim, Germany
HMM protein	*Cytoskeleton*, Denver, CO, USA
KCl	*Carl Roth GmbH*, Karlsruhe, Germany
KOH	*Merck KGaA*, Darmstadt, Germany
LifeAct®-TagGFP	*Ibidi*, Gräfling, Germany
MatTek 35 mm dish, No. 1.5 (0.17 mm, 14 mm diameter)	*MatTek Corporation*, Ashland, MA; USA

MDCK II cells	*European Collection of Authenticated Cell Cultures*, Salisbury, UK
MEM	*Life Technologies*, Paisley, UK
Methylcellulose	*Merck KGaA*, Darmstadt, Germany
$MgCl_2$	*Merck KGaA*, Darmstadt, Germany
Microscopy slides	*Thermo Fisher Scientifi*c, Waltham, MA, USA
MLCT-cantilever (k_{nom} = 0.01 N/m)	*Bruker AFM Probes*, Camarillo, CA, USA
Myosin II protein (rabbit skeletal muscle)	*Cytoskeleton*, Denver, CO, USA
Na-citrate	*Merck KGaA*, Darmstadt, Germany
NaCl	*VWR International*, Darmstadt, Germany
NaN_3	*Merck KGaA*, Darmstadt, Germany
NH_3 (30%)	*VWR International*, Darmstadt, Germany
Parafilm®	*Pechiney Plastic Packaging*, Chicago, IL, USA
PBS	*Biochrom,* Berlin, Germany
Petridishes	*VWR International*, Darmstadt, Germany
PIP_2	*Avanti Polar Lipids*, Alabaster, AL, USA
PDL	*Sigma-Aldrich*, Taufkirchen, Germany
POPC	*Avanti Polar Lipids*, Alabaster, AL, USA
Porous SI_3N_4 substrates (diameter: 1.2 µm)	*Aquamarijn*, Zutphen, Netherlands
Silicone grease	*VWR International*, Darmstadt, Germany
Tris/HCl	*Carl Roth GmbH*, Karlsruhe, Germany
Trypsin	*Biochrom*, Berlin, Germany
TxR-DHPE	*Sigma-Aldrich*, Taufkirchen, Germany
Ultrapure H_2O	*Millipore*, Billerica, MA, USA

7.3 List of Devices and Software

7.3.1 Devices

Atomic Force Microscope

NanoWizard 4	*JPK Instruments*, Berlin, Germany

Fluorescence Microscopy

Olympus BX51	*Olympus*, Tokyo, Japan
IX83 inverted microscope	*Olympus*, Tokyo, Japan
Olympus FluoView 1200 CLSM	*Olympus Europe SE & Co. KG*, Hamburg, Germany
405 nm diode laser (50 mW)	*Olympus Europe SE & Co. KG*, Hamburg, Germany
480 nm diode laser (50 mW)	*Olympus Europe SE & Co. KG*, Hamburg, Germany
561 nm diode pumped solid state laser (20 mW)	*Olympus Europe SE & Co. KG*, Hamburg, Germany
Facility Line STED setup	*Abberior Instruments*, Göttingen, Germany
775 nm STED laser	*Abberior Instruments*, Göttingen, Germany
640 nm pulsed excitation laser	*Abberior Instruments*, Göttingen, Germany
100x oil immersion objective (UPLFLN100XO2PH, NA = 1.3)	*Olympus*, Tokyo, Japan
100x oil immersion objective (UPLSAPO100XO, NA = 1.4)	*Olympus*, Tokyo, Japan
60x water immersion objective (LUMFLN, NA = 1.1)	*Olympus*, Hamburg, Germany
40x water immersion objective (LUMFLN, NA = 0.8)	*Olympus*, Hamburg, Germany
40x air objective (CFI Achromat, NA = 0.65)	*Nikon Instruments Europe B.V.*, Amsterdam, Netherlands
Darkfield condenser (U-DCW, NA: 1.2 – 1.4)	*Olympus*, Hamburg, Germany

Other Devices

AFS G2	*LUMICKS B.V.*, Amsterdam, Netherlands
BioMat™ workstation	*JPK Instruments*, Carpinteria, CA, USA
CMOS camera USB 3.0 (DCC3260M)	*Thorlabs Inc*, Newton, NJ, USA
Kinexus ultra+ Rheometer (KNX2312)	*Malvern Panalytical GmbH*, Kassel, Germany
NanoTracker 2 optical tweezer	*JPK Instruments*, Berling, Germany
pH-meter Calimatic 766	*Thermo Fisher Scientifi*c, Waltham, MA, USA
sCMOS camera (Zyla-5.5-CL-10)	*Andor Oxford Instruments*, Belfast, UK
Ultrasonic bath Sonorex RK 255H	*Bandelin*, Berlin, Germany
Ultrapure water system	*Millipore*, Billerica, MA, USA
Vacuum drying oven VD23	*Binder*, Truttlingen, Germany
Zepto plasma cleaner	*Diener Electronic*, Ebbhausen, Germany

7.3.2 Software

ANDOR SOLIS	*Oxford Instruments plc,* Abingdon, UK
GIMP 2	https://www.gimp24.de
IMAGEJ (FIJI) 1.51F	http://www.fiji.sc
JPK DATA PROCESSING 6.0	*JPK Instruments*, Berlin, Germany
MATLAB2014A & 2018	*Math Works*, Natick, MA, USA
ORIGINPRO 8.5G	*OriginLab Cooperation*, Northampton, MA, USA
PYTHON 2.7.14	*Python Software Foundation*, Beaverton, OR, USA
RSPACE SOFTWARE	*Malvern Panalytical GmbH*, Kassel, Germany
TRACKING SOFTWARE	http://ceesdekkerlab.tudelft.nl/download

7.4 MATLAB Script of the Viscoelastic Cortex Model

– This script was written by I. P. Mey and A. Janshoff from the University of Göttingen –

```
function varargout = ViscoAna(varargin)
% VISCOANA MATLAB code for ViscoAna.fig
%      VISCOANA, by itself, creates a new VISCOANA or raises the existing
%      singleton*.
%
%      H = VISCOANA returns the handle to a new VISCOANA or the handle to
%      the existing singleton*.
%
%      VISCOANA('CALLBACK',hObject,eventData,handles,...) calls the local
%      function named CALLBACK in VISCOANA.M with the given input arguments.
%
%      VISCOANA('Property','Value',...) creates a new VISCOANA or raises the
%      existing singleton*.  Starting from the left, property value pairs are
%      applied to the GUI before ViscoAna_OpeningFcn gets called.  An
%      unrecognized property name or invalid value makes property application
%      stop.  All inputs are passed to ViscoAna_OpeningFcn via varargin.
%
%      *See GUI Options on GUIDE's Tools menu.  Choose "GUI allows only one
%      instance to run (singleton)".
%
% See also: GUIDE, GUIDATA, GUIHANDLES

% Edit the above text to modify the response to help ViscoAna

% Last Modified by GUIDE v2.5 15-Apr-2019 09:15:58

% Begin initialization code - DO NOT EDIT
gui_Singleton = 1;
gui_State = struct('gui_Name',       mfilename, ...
                   'gui_Singleton',  gui_Singleton, ...
                   'gui_OpeningFcn', @ViscoAna_OpeningFcn, ...
                   'gui_OutputFcn',  @ViscoAna_OutputFcn, ...
                   'gui_LayoutFcn',  [] , ...
                   'gui_Callback',   []);
if nargin && ischar(varargin{1})
    gui_State.gui_Callback = str2func(varargin{1});
end

if nargout
    [varargout{1:nargout}] = gui_mainfcn(gui_State, varargin{:});
else
    gui_mainfcn(gui_State, varargin{:});
end
% End initialization code - DO NOT EDIT

% --- Executes just before ViscoAna is made visible.
function ViscoAna_OpeningFcn(hObject, eventdata, handles, varargin)
% This function has no output args, see OutputFcn.
% hObject    handle to figure
% eventdata  reserved - to be defined in a future version of MATLAB
% handles    structure with handles and user data (see GUIDATA)
% varargin   command line arguments to ViscoAna (see VARARGIN)
% Choose default command line output for ViscoAna
handles.output = hObject;
handles.instruct.String='load jpk-force file';
```

```
guidata(hObject, handles);
% Update handles structure
guidata(hObject, handles);

% UIWAIT makes ViscoAna wait for user response (see UIRESUME)
% uiwait(handles.figure1);

% --- Outputs from this function are returned to the command line.
function varargout = ViscoAna_OutputFcn(hObject, eventdata, handles)
% varargout  cell array for returning output args (see VARARGOUT);
% hObject    handle to figure
% eventdata  reserved - to be defined in a future version of MATLAB
% handles    structure with handles and user data (see GUIDATA)

% Get default command line output from handles structure
varargout{1} = handles.output;

% --- Executes on button press in load.
function load_Callback(hObject, eventdata, handles)
% hObject    handle to load (see GCBO)
% eventdata  reserved - to be defined in a future version of MATLAB
% handles    structure with handles and user data (see GUIDATA)

[fn,pn]=uigetfile('*.jpk-force');
handles.fn=fn;
handles.pn=pn;
data=Curve(pn,fn)
handles.force_data=data.force_time;
handles.distance_data=data.distance_time;
handles.time_data=handles.force_data(1,:)
handles.force_data=handles.force_data(2,:).*1e6;
handles.distance_data=handles.distance_data(2,:);

%data.velocity
%(handles.distance_data(1)-handles.distance_data(end))./
(handles.time_data(1)-handles.time_data(end))

a=diff(handles.time_data);
wind=150;
[~,idxmax]=max(handles.force_data);

axes(handles.axes1);
plot(handles.time_data,handles.force_data,'b.');
guidata(hObject, handles);
handles.instruct.String='jpk-force file loaded. BL Offset calculation next!';
guidata(hObject, handles);

% --- Executes on button press in selectTrace.
function selectTrace_Callback(hObject, eventdata, handles)
% hObject    handle to selectTrace (see GCBO)
% eventdata  reserved - to be defined in a future version of MATLAB
% handles    structure with handles and user data (see GUIDATA)
handles.instruct.String='Click and Hold to select approach contact point!';
guidata(hObject, handles);
axes(handles.axes1)
plot(handles.time_data,handles.force_data,'b.');
axes(handles.axes1);
p1=selectdata('SelectionMode','Closest','Verify','on');
handles.instruct.String='Click and Hold to select last point for evaluation
on retraction curve.!';
guidata(hObject, handles);
p2=selectdata('SelectionMode','Closest','Verify','on');
```

```
axes(handles.axes1);
plot(handles.time_data,handles.force_data,'b.');
hold on
plot(handles.time_data(p1:p2),handles.force_data(p1:p2),'r.');
hold off
handles.force_selected=handles.force_data(p1:p2);
handles.time_selected=handles.time_data(p1:p2);
[~,idx_max]=max(handles.force_selected);
handles.ReTrace_force=handles.force_selected(idx_max:end)+handles.BL_Offset;
handles.Trace_force=handles.force_selected(1:idx_max-1);
handles.ReTrace_time=handles.time_selected(idx_max:end);
handles.Trace_time=handles.time_selected(1:idx_max-1);
length(handles.Trace_force)
length(handles.ReTrace_force)
if length(handles.ReTrace_force)>1.5.*length(handles.Trace_force)
    resize=ceil(length(handles.ReTrace_force)/length(handles.Trace_force))

handles.force_selected=[handles.Trace_force,handles.ReTrace_force(1:resize:en
d)];

handles.time_selected=[handles.Trace_time,handles.ReTrace_time(1:resize:end)]
;
elseif length(handles.ReTrace_force).*1.5<length(handles.Trace_force)

resize=ceil(1./(length(handles.ReTrace_force)/length(handles.Trace_force)))
    length(handles.ReTrace_force)/length(handles.Trace_force)

handles.force_selected=[handles.Trace_force(1:resize:end),handles.ReTrace_for
ce];

handles.time_selected=[handles.Trace_time(1:resize:end),handles.ReTrace_time]
;
else
    resize=1
    handles.force_selected=[handles.Trace_force,handles.ReTrace_force];
    handles.time_selected=[handles.Trace_time,handles.ReTrace_time];
end
handles.instruct.String='Data Selected and Baseline Corrected. Caution to
ensure good fitting points might be thrown away at apporach or retract part!
Next delete unnecesary point at the return point!';
guidata(hObject, handles);
plotSelected_Callback(hObject, eventdata, handles)

guidata(hObject, handles);

% --- Executes on button press in selectReTrace.
function selectReTrace_Callback(hObject, eventdata, handles)
% hObject    handle to selectReTrace (see GCBO)
% eventdata  reserved - to be defined in a future version of MATLAB
% handles    structure with handles and user data (see GUIDATA)
% axes(handles.axes1)
% plot(handles.time_data,handles.force_data,'b.');
% axes(handles.axes1);
% p1=selectdata('SelectionMode','Closest','Verify','on')
% p2=selectdata('SelectionMode','Closest','Verify','on')
% axes(handles.axes1);
% plot(handles.time_data,handles.force_data,'b.');
% hold on
% plot(handles.time_data(p1:p2),handles.force_data(p1:p2),'r.');
% hold off
% handles.ReTrace_force=handles.force_data(p1:p2)+handles.BL_Offset;
% handles.ReTrace_time=handles.time_data(p1:p2);
```

```
%
% if length(handles.ReTrace_force)>length(handles.Trace_force)
%     resize=ceil(length(handles.ReTrace_force)/length(handles.Trace_force))
%
handles.force_selected=[handles.Trace_force,handles.ReTrace_force(1:resize:en
d)];
%
handles.time_selected=[handles.Trace_time,handles.ReTrace_time(1:resize:end)]
;
% elseif length(handles.ReTrace_force)<length(handles.Trace_force)
%
resize=1/(ceil(length(handles.ReTrace_force)/length(handles.Trace_force)))
%
handles.force_selected=[handles.Trace_force(1:resize:end),handles.ReTrace_for
ce];
%
handles.time_selected=[handles.Trace_time(1:resize:end),handles.ReTrace_time]
;
% elseif length(handles.ReTrace_force)==length(handles.Trace_force)
%     handles.force_selected=[handles.Trace_force,handles.ReTrace_force];
%     handles.time_selected=[handles.Trace_time,handles.ReTrace_time];
% end
%
% guidata(hObject, handles);

% --- Executes on button press in plotSelected.
function plotSelected_Callback(hObject, eventdata, handles)
% hObject    handle to plotSelected (see GCBO)
% eventdata  reserved - to be defined in a future version of MATLAB
% handles    structure with handles and user data (see GUIDATA)

axes(handles.axes1);
plot(handles.time_selected,handles.force_selected,'g.');
guidata(hObject, handles);

% --- Executes on button press in blOffset.
function blOffset_Callback(hObject, eventdata, handles)
% hObject    handle to blOffset (see GCBO)
% eventdata  reserved - to be defined in a future version of MATLAB
% handles    structure with handles and user data (see GUIDATA)
handles.instruct.String='Choose first a baseline region on the approach part
of the data';
guidata(hObject, handles);
axes(handles.axes1)
plot(handles.time_data,handles.force_data,'b.');
axes(handles.axes1);
off1_idx=selectdata('SelectionMode','rect','Verify','on');
handles.instruct.String='Now choose first baseline region on the retraction
part of the data';
guidata(hObject, handles);
off2_idx=selectdata('SelectionMode','rect','Verify','on');
handles.BL=mean(handles.force_data(off1_idx));
handles.force_data=handles.force_data-handles.BL;
handles.BL_Offset=abs(mean(handles.force_data(off1_idx))-
mean(handles.force_data(off2_idx)));
guidata(hObject, handles);
set(handles.bloffset_text,'String',num2str(handles.BL_Offset));
handles.instruct.String='baselines are done. Next is select Data!';
guidata(hObject, handles);

% --- Executes on button press in Fitting.
function Fitting_Callback(hObject, eventdata, handles)
```

```
% hObject    handle to Fitting (see GCBO)
% eventdata  reserved - to be defined in a future version of MATLAB
% handles    structure with handles and user data (see GUIDATA)
ys=handles.force_selected';
xs=handles.time_selected';
red=str2num(handles.nrRed.String);
xs=xs(1:red:end); %data reduction by red
ys=ys(1:red:end);
xs=xs-xs(1);
ymax = max(ys);
index = find(ys==ymax);
tm = xs(index);
par.R = str2num(get(handles.Rpore,'String')); %micrometer
par.vo = str2num(get(handles.v0,'String'));  %micrometer pro sekunde
par.beta = str2num(get(handles.betaStart,'String')); % Keine Einheit
par.Ka = 0.016; % N/m
par.T0 = 0.0002; % N/m
par.a = 0.02; % Tipsize (Radius) in micrometer
par.tm = tm; % Turning point
par.inc = 0.0001;
par.fn=handles.fn;
par.pn=handles.pn;
fitFDC(xs,ys,par)

function nrRed_Callback(hObject, eventdata, handles)
% hObject    handle to nrRed (see GCBO)
% eventdata  reserved - to be defined in a future version of MATLAB
% handles    structure with handles and user data (see GUIDATA)

% Hints: get(hObject,'String') returns contents of nrRed as text
%        str2double(get(hObject,'String')) returns contents of nrRed as a
double

% --- Executes during object creation, after setting all properties.
function nrRed_CreateFcn(hObject, eventdata, handles)
% hObject    handle to nrRed (see GCBO)
% eventdata  reserved - to be defined in a future version of MATLAB
% handles    empty - handles not created until after all CreateFcns called

% Hint: edit controls usually have a white background on Windows.
%       See ISPC and COMPUTER.
if ispc && isequal(get(hObject,'BackgroundColor'),
get(0,'defaultUicontrolBackgroundColor'))
    set(hObject,'BackgroundColor','white');
end

function Rpore_Callback(hObject, eventdata, handles)
% hObject    handle to Rpore (see GCBO)
% eventdata  reserved - to be defined in a future version of MATLAB
% handles    structure with handles and user data (see GUIDATA)

% Hints: get(hObject,'String') returns contents of Rpore as text
%        str2double(get(hObject,'String')) returns contents of Rpore as a
double

% --- Executes during object creation, after setting all properties.
function Rpore_CreateFcn(hObject, eventdata, handles)
% hObject    handle to Rpore (see GCBO)
% eventdata  reserved - to be defined in a future version of MATLAB
% handles    empty - handles not created until after all CreateFcns called

% Hint: edit controls usually have a white background on Windows.
```

```
%       See ISPC and COMPUTER.
if ispc && isequal(get(hObject,'BackgroundColor'),
get(0,'defaultUicontrolBackgroundColor'))
    set(hObject,'BackgroundColor','white');
end

function v0_Callback(hObject, eventdata, handles)
% hObject    handle to v0 (see GCBO)
% eventdata  reserved - to be defined in a future version of MATLAB
% handles    structure with handles and user data (see GUIDATA)

% Hints: get(hObject,'String') returns contents of v0 as text
%        str2double(get(hObject,'String')) returns contents of v0 as a double

% --- Executes during object creation, after setting all properties.
function v0_CreateFcn(hObject, eventdata, handles)
% hObject    handle to v0 (see GCBO)
% eventdata  reserved - to be defined in a future version of MATLAB
% handles    empty - handles not created until after all CreateFcns called
% Hint: edit controls usually have a white background on Windows.
%       See ISPC and COMPUTER.
if ispc && isequal(get(hObject,'BackgroundColor'),
get(0,'defaultUicontrolBackgroundColor'))
    set(hObject,'BackgroundColor','white');
end

% --- Executes on button press in selectDelete.
function selectDelete_Callback(hObject, eventdata, handles)
% hObject    handle to selectDelete (see GCBO)
% eventdata  reserved - to be defined in a future version of MATLAB
% handles    structure with handles and user data (see GUIDATA)
handles.instruct.String='Click and Hold to mark points to be deleted.';
guidata(hObject, handles);
axes(handles.axes1);
plot(handles.time_selected,handles.force_selected,'g.');
idx=selectdata('SelectionMode','Brush','Verify','on');
handles.time_selected(idx)=[];
handles.force_selected(idx)=[];
handles.instruct.String='Done, good luck for the fitting!';
guidata(hObject, handles);
plotSelected_Callback(hObject, eventdata, handles)

function betaStart_Callback(hObject, eventdata, handles)
% hObject    handle to betaStart (see GCBO)
% eventdata  reserved - to be defined in a future version of MATLAB
% handles    structure with handles and user data (see GUIDATA)
% Hints: get(hObject,'String') returns contents of betaStart as text
%        str2double(get(hObject,'String')) returns contents of betaStart as a
double

% --- Executes during object creation, after setting all properties.
function betaStart_CreateFcn(hObject, eventdata, handles)
% hObject    handle to betaStart (see GCBO)
% eventdata  reserved - to be defined in a future version of MATLAB
% handles    empty - handles not created until after all CreateFcns called

% Hint: edit controls usually have a white background on Windows.
%       See ISPC and COMPUTER.
if ispc && isequal(get(hObject,'BackgroundColor'),
get(0,'defaultUicontrolBackgroundColor'))
    set(hObject,'BackgroundColor','white');
end
```

7.5 PYTHON Script for the *van Hove* Histograms

− This script was written by I. P. Kuhlemann from the University of Göttingen −

```
import os
import numpy as np
import matplotlib.pyplot as plt
from scipy.optimize import curve_fit
import read_data
"""
Erstellt sowohl individuelle van Hove Plots für alle Dateien in den drei Kategorien:
  * Active Sample 1 = "weniger aktiven", da zu einem späteren Zeitpunkt aufgenommen
  * Active Sample 2 = Sehr aktive Systeme
  * Inactive Sample 1 = Inaktive Systeme
Außerdem noch ensemble Vanhove Plots für diese 3 Kategorien.
Zum Skript Ausführen einfach im Terminal in den Ordner ``Auswertung`` navigieren (wo das
Skript ``plot_vanhove.py`` liegt) und mit ``python plot_vanhove.py`` ausführen.
Ergebnisse landen im Ordner ``Auswertung/plots/vanhove``.
Parameter wie lag in frames (durch frame rate teilen um lag in Zeiteinheit zu erhalten)
und Anzahl bins können in den ersten Zeilen verändert werden. Mit max_displacement kannst
du die Grenzen der x-Achse festlegen (in positive und negative Richtung derselbe Wert).

ÄNDERUNG 2020-10-13: Gauss-Fit hinzugefügt.
"""
def gauss(x, A, sigma):
    return A*np.exp(-x**2/2/sigma**2)


def gauss_mu(x, A, sigma, mu):
    return gauss(x-mu, A, sigma)


def _plot_individual_i(bin_edges, hist, width, files, i, dir_individual):
    fig, ax = plt.subplots(1, 1)
    ax.bar((bin_edges[1:] + bin_edges[:-1])/2, hist, width=width)
```

```
    fname = os.path.split(files[i])[1]
    ax.set(
        title=files[i][3:],
        xlabel='displacement/$\mu$m',
        ylabel='density'
    )
    figname = os.path.join(dir_individual, os.path.splitext(fname)[0])
    fig.savefig(figname + '.svg')
    fig.savefig(figname + '.pdf')
    fig.savefig(figname + '.png')
    plt.close(fig)


def _plot_ensemble_with_gauss(fit_function, centers, hist, width,
                              gauss, p_opt, label, lag, dir_ensemble):
    function_name = fit_function.__name__
    print(f'plotting ensemble with {function_name}')

    p0 = [hist.max(), hist.std()]
    if function_name == 'gauss_mu':
        p0.append(0.0)
    p_opt, varmatrix = curve_fit(fit_function, centers[range_mask],
                                 hist[range_mask], p0=p0)

    fig, ax = plt.subplots(1, 1)
    ax.bar(centers, hist, width=width)
    ax.plot(centers, fit_function(centers, *p_opt), '--k', lw=3.5)
    ax.set(
        title=label + ', lag {}'.format(lag),
        xlabel='displacement/$\mu$m',
        ylabel='density'
    )
```

```
    figname = os.path.join(dir_ensemble, label + '_fit_' + function_name)
    fig.savefig(figname + '.svg')
    fig.savefig(figname + '.pdf')
    fig.savefig(figname + '.png')
    plt.close(fig)

if __name__ == "__main__":

    lag = 500 # lag in frames
    n_bins = 80
    # only True possible here at the moment, let me know
    # if you need x and y separated:
    combine_x_and_y = True
    # in micro meter
    max_displacement = 0.5

    # default: plots only ensembles.
    # set this true if you want individual plots as well
    PLOT_INDIVIDUAL = False
    # range for gauss fit in microns
    fit_range = [-0.2, 0.2]

    files_active_sample1, files_active_sample2 = read_data.get_files_active('..')
    files_inactive = read_data.get_files_inactive('..')

    dir_ensemble = os.path.join('plots', 'vanhove', 'ensemble', 'lag_{:04}'.format(lag))
    os.makedirs(dir_ensemble, exist_ok=True)

    for files, label in  [
            (files_active_sample1, 'Active Sample 1'),
            (files_active_sample2, 'Active Sample 2'),
```

```
        (files_inactive, 'Inactive Sample 1')
    ]:
        print('-'*80)
        print('files', label)
        data = read_data.load_files(files)
        displacements = data[lag:] - data[:-lag]

        bin_edges = np.linspace(-max_displacement, max_displacement, n_bins+1)
        width = bin_edges[1] - bin_edges[0]

        split_arrays = []

        dir_individual = os.path.join('plots', 'vanhove', 'individual', label)
        os.makedirs(dir_individual, exist_ok=True)
        # individual Vanhove plots
        for i in range(displacements.shape[1]):
            print('reading', files[i])
            if not combine_x_and_y:
                msg = "Habe erstmal X und Y Displacements zusammengeschmissen! "
                msg += "Sag bescheid, wenn du die auch noch getrennt betrachten möchtest!"
                raise NotImplementedError(msg)
            concatenated_i = np.concatenate([displacements[:, i, 0], displacements[:, i, 1]])
            split_arrays.append(concatenated_i)
            hist, edges = np.histogram(
                concatenated_i,
                bins=bin_edges,
                density=True
            )
            assert (edges == bin_edges).all()
```

```
    if PLOT_INDIVIDUAL:
        _plot_individual_i(bin_edges, hist, width, files, i, dir_individual)


concatenated = np.concatenate(split_arrays)
hist, edges = np.histogram(
    concatenated,
    bins=bin_edges,
    density=True
)
assert (edges == bin_edges).all()

print('performing Gauss fit on ensemble displacements')

centers = (bin_edges[1:] + bin_edges[:-1]) / 2

range_mask = (centers >= fit_range[0]) & (centers <= fit_range[1])

for fit_method in [gauss, gauss_mu]:
    _plot_ensemble_with_gauss(fit_method, centers, hist,
                              width, gauss, range_mask, label, lag, dir_ensemble)
```

Curriculum Vitae

Personal Data

Name:	Hanna Hubrich
Date of birth:	24.04.1993
Place of birth:	Uelzen, Germany
Citizenship:	German

Career

since 02/2017 **Ph.D. thesis** at the Georg-August University in Göttingen, entitled *"Active matter in confined geometries – biophysics of artificial minimal cortices",* under leadership of PROF. DR. A. JANSHOFF.

10/2014–11/2016 **Graduate studies** in chemistry at the Georg-August University in Göttingen, degree: Master of Science, grade: 1.3, title of the master thesis: *"Characterisation of glycosphingolipid interactions in membranes by means of atomic force microscopy"*, grade: 1.0

10/2011–08/2014 **Undergraduate studies** in chemistry at the Georg-August University in Göttingen, degree: Bachelor of Science, grade: 1.7, title of the bachelor thesis: *"Analysis of Collybistin-Phosphatidylinositolphosphate interactions by means of surface plasmon resonance spectroscopy"*, grade: 1.3

08/2004–07/2011 **Allgemeine Hochschulreife** at Lessing Gymnasium in Uelzen, degree: Abitur (advanced courses: Chemistry, Physics, Mathematics), grade: 1.7

Scientific Contributions

Peer-reviewed Publication

08/2020 Hubrich, H.; Mey, I. P.; Brückner, B. R.; Mühlenbrock, P.; Nehls, S.; Grabenhorst, L.; Oswald, T.; Steinem, C.; Janshoff, A. Viscoelasticity of Native and Artificial Actin Cortices Assessed by Nanoindentation Experiments. *Nano Lett.* **2020**, *20* (9), 6329–6335.

Selected Poster Presentations

07/2019 12th EBSA and 10th IUPAP Biophysics Congress in Madrid, Spain. Title: "Active matter in confined geometries – biophysics of artificial minimal cortices"

12/2019 Status-Symposium on "Life? – A Fresh Scientific Approach to the Basic Principles of Life", Hannover, Germany. Title: "Living foams: from artificial cells to synthetic tissues"

Danksagung

Zuerst möchte ich mich ausdrücklich bei *Prof. Dr. Andreas Janshoff* für die gute Betreuung dieser Doktorarbeit, die zahlreichen fachlichen Diskussionen und die Unterstützung während der gesamten Promotionszeit bedanken.

Auch *Prof. Dr. Sarah Köster* möchte ich danken für die Übernahme der Zweitkorrektur und den guten wissenschaftlichen Austausch in den Thesis Committee Meetings. Ich danke auch *Dr. Sarah Adio, Prof. Dr. Michael Meinecke, Prof. Dr. Jörg Großhans* und *Prof. Dr. Silvio O. Rizzoli* für die Bereitschaft Mitglieder meiner Prüfungskommission zu sein.

Der *VolkswagenStiftung* danke ich für die finanzielle Unterstützung meiner Doktorarbeit und das interessante Symposium. An dieser Stelle möchte ich mich auch für die staatliche *BAföG*-Unterstützung während des Bachelor- und Masterstudiums bedanken, die mir dieses Studium erst ermöglicht hat. Auch wenn 9 Jahre Studium eine lange Zeit sind und Forschung manchmal frustrierend sein kann, ist mir durchaus bewusst, dass Bildung ein Privileg ist und ich bin froh, dass mir diese Ausbildung in Deutschland ermöglicht wurde!

Weiterhin möchte ich mich bei meinem Bachelorstudenten *Sun* und meinem Masterstudenten *Peter* bedanken für die Unterstützung bei Projekten dieser Arbeit.

Ganz herzlich möchte ich mich auch bei *Peter, Marian*, *Ingo, Nils* und vor allem bei *Tabea* bedanken für die stetige Unterstützung und Hilfsbereitschaft bei meinen Projekten und für das Korrekturlesen dieser Arbeit! Speziell bei *Ingo* und *Peter* möchte ich mich nochmal bedanken, die mir immer mit Rat und Tat zur Seite standen, zahlreiche Fragen beantwortet haben und mich immer wieder motivieren konnten, auch wenn die Experimente mal nicht so gut liefen! *Tabea, Angela, Basti* und *Stefan* möchte ich speziell für die Unterstützung bei den Zellexperimenten danken. Bei *Helen, Markus* und *Nils* möchte ich mich für Tipps und Tricks zur Präparation der MACs bedanken und für die stetige Hilfsbereitschaft. *Ilyas* möchte ich herzlich für die Hilfe bei den *van Hove* Plots danken!

Für die Unterstützung beim Ausfüllen und Einreichen zahlreicher Formulare möchte ich mich herzlich bei *Petra* bedanken.

Bei dem gesamten Arbeitskreis bedanke ich mich für die herzliche Aufnahme und die gute Zeit!

Ein besonderer Dank geht auch an meine Familie und Freunde für die Unterstützung auf den Weg hierher! Speziell den Göttingern *Jonathan, Raphael, Danilo, Pia* und *Krishya*, der

Klettercrew *Stefi, Kai, Paddy* und *Diana* und den ganzen Beachvolleyballern danke ich für die gute, lustige und vor allem sportliche Zeit!

Ein ganz besonderer Dank geht an *Vanessa*! Du bist seit dem Bachelor an meiner Seite und hast mich immer unterstützt und mir immer Rückhalt gegeben. Wir haben stressige und entspannte Zeiten, faule und sportliche Zeiten, traurige und lustige Zeiten, aber vor allem schöne Zeiten zusammen erlebt. Ich bin dir sehr dankbar für alles!

Micha, dir danke ich für deine Unterstützung, deine Geduld und dein Verständnis gerade in der anstrengenden letzten Phase meiner Promotion! Vor allem danke ich dir für die zuverlässige Schokoladenversorgung in der Schreibphase − auch wenn ich manchmal suchen musste − und für die täglichen Witze ☺ … aber natürlich auch für deine zahlreichen motivierenden Worte!!!